02
11/25/91 am (2)

ANL-91/26

Nuclear Technology Programs Semiannual Progress Report

April-September 1989

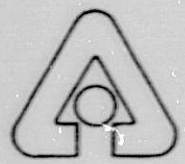

Argonne National Laboratory, Argonne, Illinois 60439
operated by The University of Chicago
for the United States Department of Energy under Contract W-31-109-Eng-38

Reproduced from the best available copy.

Available to DOE and DOE contractors from the
Office of Scientific and Technical Information
P.O. Box 62
Oak Ridge, TN 37831
Prices available from (615) 576-8401, FTS 626-8401

Available to the public from the
National Technical Information Service
U.S. Department of Commerce
5285 Port Royal Road
Springfield, VA 22161

Distribution Category:
General, Miscellaneous, and Progress
Reports (Nuclear) (UC-500)

ANL--91/26

DE92 003358

ANL-91/26

ARGONNE NATIONAL LABORATORY
9700 South Cass Avenue
Argonne, IL 60439

NUCLEAR TECHNOLOGY PROGRAMS SEMIANNUAL PROGRESS REPORT

April-September 1989

Chemical Technology Division

M. J. Steindler, Director
J. E. Battles, Associate Director
J. E. Harmon, Editor

August 1991

Previous Reports in this Series

October 1988-March 1989	ANL-90/16
April 1988-September 1988	ANL-90/15
October 1987-March 1988	ANL-89/29
April 1987-September 1987	ANL-88-49

TABLE OF CONTENTS

TABLE OF CONTENTS (contd)

TABLE OF CONTENTS (contd)

TABLE OF CONTENTS (contd)

NUCLEAR TECHNOLOGY PROGRAMS
SEMIANNUAL PROGRESS REPORT
April-September 1989

ABSTRACT

This document reports on the work done by the Nuclear Technology Programs of the Chemical Technology Division, Argonne National Laboratory, in the period April-September 1989. These programs involve R&D in three areas: applied physical chemistry, separation science and technology, and nuclear waste management. The work in applied physical chemistry includes investigations into the processes that control the release and transport of fission products under accident-like conditions, the thermophysical properties of metal fuel and blanket materials of the Integral Fast Reactor, and the properties of selected materials in environments simulating those of fusion energy systems. In the area of separation science and technology, the bulk of the effort is concerned with developing and implementing processes for the removal and concentration of actinides from waste streams contaminated by transuranic elements. Another effort is concerned with developing a process for separating the organic and inorganic constituents of the red-water waste stream generated in production of 2,4,6-trinitrotoluene. In the area of waste management, investigations are underway on the performance of materials in projected nuclear repository conditions to provide input to the licensing of the nation's high-level waste repositories.

SUMMARY

Applied Physical Chemistry

Calculational and experimental efforts are underway to investigate the release of refractory fission products (Sr, Ba, and La) and uranium during the core-concrete interaction phase of a degraded-core accident. In the experimental effort, mixtures of urania, zirconia, and concrete are vaporized at 2150 or 2400 K into flowing H_2 or He-6% H_2 gas. Three different concretes having silica contents ranging from 7 to 69 wt % were used to reflect the known range of reactor-basemat compositions. The total mass of material that was vaporized was determined by weighing the condensates; the masses of individual elements were determined by chemical analyses of the condensates. The phases present in the heated mixtures were inferred from an electron probe microanalysis and X-ray diffraction analyses. Equilibrium calculations were also performed using the SOLGASMIX computer code and a thermodynamic data base containing 112 gaseous and 108 condensed species. The partial molar free energy of oxygen was calculated from the equilibrium oxygen pressure established in the high-temperature reaction zone between the gas and the sample. Using the experimental data, we estimated the release fractions to be expected in a severe nuclear-reactor accident for Sr, Ba, La, and U, and for total mass (aerosols). The release of these four elements was less than 1% for the basemat concrete of low silica content (7 wt %) and decreased to less than 0.01% for the basemat concrete of high silica content (69 wt %). These values are much lower than those reported in the literature. The total mass release was about 0.5% for all three concretes.

Measurements are being performed to provide needed thermodynamic and transport property data for Integral Fast Reactor (IFR) fuels. As part of our investigation on fuel-cladding compatibility, we performed differential thermal analysis (DTA) experiments with mixtures of U-Pu-Zr fuel and steel

claddings (HT9, D9, and 316SS). The DTA curves on initial heating indicated solid-state transitions in the fuel at 600-700°C and an exothermal reaction forming more stable products (probably an Fe_2Zr-like phase) at 1200°C. On subsequent cooling, the DTA curve indicated primary precipitation at 1220°C and a freezing transition at 700°C. The DTA curves were used to estimate the "onset-of-melting" temperature with an accuracy of ±10-20°C. Scanning electron microscopy of the residues from these experiments indicated the following reaction sequence on heating: primary precipitation of a Fe_2Zr-like phase, followed by secondary precipitation of Fe_2U, followed by formation of Fe_2U-FeU_6 eutectic. Other studies on metal fuel properties involved calculations of the Pu-U phase diagram, which will be used to refine the U-Pu-Zr phase diagram, and DTA experiments with U-Fe mixtures, which will be used to obtain a better understanding of the phase relations involved in fuel-cladding systems.

A critical element in the development of a fusion reactor is the blanket for breeding tritium fuel. Several studies are underway with the objective of determining the feasibility of using lithium-containing ceramics as breeder material. In one such study, temperature programmed desorption (TPD) measurements are in progress to provide data that describe the kinetics of desorption of $H_2O(g)$ and $H_2(g)$ from $LiAlO_2(s)$. Blank experiments (no $LiAlO_2$ present) were performed to gain information on the behavior of the empty stainless steel sample tube exposed to a flowing gas mixture, He-100 ppm H_2O-500 ppm H_2. Reactivity with the steel was demonstrated: H_2O was consumed and $H_2(g)$ was produced, and there was the suggestion of dissolution/reaction of $H_2(g)$ in the steel. Nevertheless, in the absence of $H_2(g)$, the sample tube can be stabilized so that useful measurements with $H_2O(g)$ can be made. Fresh samples of $LiAlO_2(s)$ contain large amounts of adsorbed H_2O. We obtained TPD spectra for $LiAlO_2$ samples that had been equilibrated with 200 ppm $H_2O(g)$ at temperatures of 200, 300, 400, and 500°C. The spectra exhibited different shapes suggestive of differing and/or multiple processes taking place as H_2O is desorbed from the solid.

In a continuing collaboration with Canadian researchers, we have been involved in analyzing tritium release data from CRITIC, an experimental study of tritium release from Li_2O breeder material. Of particular interest is the tritium release at low temperatures. For temperature decreases to final temperatures below 450°C, the tritium release appeared to reach a plateau below the steady-state release. Initially, it was believed that this may have been a result of some instrumental problem, possibly due to a change in the sensitivity of the proportional counter used for tritium measurements at different temperatures or gas compositions. However, the data from the proportional counters and data from the scintillation counting of tritium collected in glycol traps indicated that release was below steady-state release for substantial periods of time. After considering other possible instrumental or measurement errors and ruling them out, we arrived at a hypothesis that the plateau region may be caused by a second phase of LiOT precipitating in the Li_2O. In related work, we calculated the tritium inventory during pulsed operation for a lithium oxide blanket and investigated methods for increasing tritium release in breeder materials. With regard to the latter, our calculations indicated that doping will increase the lithium vacancy concentration in $LiAlO_2$, which would increase its tritium diffusivity.

Within the solid breeder material, tritium may be found as LiOT, which may transport lithium (and tritium) to cooler parts of the blanket. This process may cause loss of lithium from the blanket, blocking of flow paths, and increase of the tritium inventory. Experiments were, therefore, undertaken to investigate the transport of LiOH from a lithium oxide solid breeder with a helium purge stream containing water vapor. The gas velocity was varied from 50 to 2600 cm/s at 850°C. The fractional saturation product for $H_2O(g)$ diffusion from the flowing helium to the lithium oxide and LiOH(g) diffusion into the flowing helium was calculated from the experimental results. Our results were in general agreement with those reported by others. This work established conditions for calculating LiOH undersaturation in helium as a function of the blanket purge channel dimensions and velocity of the purge gas.

Earlier experiments indicated that substantial increase of tritium release occurs when a small amount of H_2 (about 0.1%) is added to the helium purge stream. We are using a quantum cluster approach with the extended Huckel method to investigate the interaction between $H_2(g)$ and the $Li_2O(110)$ surface. Three types of sites were investigated: midway between the nearest neighbor O-O, O-Li, and Li-Li. We found that all three are sites for H_2 nondissociative adsorption. The binding energetics are around 0.2-0.3 eV, and the equilibrium height is around 2 Å.

The International Thermonuclear Experimental Reactor (ITER) is an international project whose purpose is to produce a conceptual design of a tokamak reactor which can be used to test components for a prototype power reactor. Designs of each of the reactor systems are being generated by the ITER partners in the U.S., U.S.S.R., Japan, and the European community. In this report period, we prepared a design of the tritium processing system for the U.S. ITER aqueous salt blanket design and provided it to the staff at the Tritium Systems Test Assembly, the designated coordinator of the U.S. tritium systems design for ITER. This information was incorporated into a total tritium systems design for ITER, which includes the plasma exhaust processing system plus the blanket streams. Also, the effects of radiolysis and electrolytic decomposition were examined for the borated water shield and water coolant for a ceramic solid breeder.

The Breeding Blanket Interface (BBI) is that system which performs the necessary processing and recycle of the tritium recovered from a fusion reactor blanket. Although considerable attention has been given to studies of tritium breeding and recovery and also many aspects of tritium processing, very little work has been done on the BBI. In this report period, preconceptual designs of the BBI were developed for two types of blankets: aqueous salt solution and solid breeder blanket. A summary of the major design features of the two BBI systems is given.

In neutron dosimetry and damage analysis, fusion materials are being irradiated in a variety of facilities, including fission reactors, 14 MeV neutron sources, and higher energy accelerator-based neutron sources. We are determining the neutron energy spectrum, flux levels, and damage parameters for the materials irradiated in these facilities, along with exposure parameters for each irradiation. In this report period, neutron dosimetry and radiation damage calculations were performed for three short irradiations by Battelle Pacific National Laboratory in the Omega West Reactor at Los Alamos National Laboratory. The dosimetry capsules contained small wires of Ni, Fe, Ti, 0.1% Co-Al, and 80.2% Mn-Cu. The samples were irradiated at 200°C and a maximum neutron fluence of 8.3×10^{19} n/cm^2. Data are reported for activation rates, neutron flux and fluence, and radiation damage parameters. Using the SPECOMP computer code, we also calculated the production of atomic displacement damage in the superconducting material $YBa_2Cu_3O_7$. The results have been added to the SPECTER computer code for routine calculation of damage in any specified neutron spectrum.

Separation Science and Technology

The Division's work in separation science and technology is mainly concerned with removing and concentrating actinides from waste streams contaminated with transuranic (TRU) elements by use of the TRUEX solvent extraction process. The extractant found most satisfactory for the TRUEX process is octyl (phenyl)-N,N-diisobutylcarbamoylmethylphosphine oxide, which is abbreviated CMPO. This extractant is combined with tributyl phosphate (TBP) and a diluent to formulate the TRUEX process solvent. The diluent is typically a normal paraffinic hydrocarbon (NPH) or a nonflammable chlorocarbon such as tetrachloroethylene (TCE). Another project was initiated to develop a process for converting the hazardous red-water waste stream from TNT manufacturers to forms that are readily disposable or acceptable for recycling.

The major effort involves development of a generic data base and modeling capability for the TRUEX solvent extraction process. The Generic TRUEX Model (GTM) will be directly useful for site-specific flowsheet development directed to (1) establishing a TRUEX process for specific waste streams, (2) assessing the economic and facility requirements for installing the process, and (3) improving, monitoring, and controlling on-line TRUEX processes. Versions of the model are now available for use with Macintosh and IBM-compatible personal computers. A more powerful and faster second-generation GTM will be available in 1990. Improvements will include the ability to calculate flowsheets and predict space and cost requirements for any type of solvent extraction equipment, including pulsed columns, and to estimate solvent degradation during processing caused by radiolysis and hydrolysis of the extractant (CMPO).

One of the sections in the GTM, the Spreadsheet Algorithm for Stagewise Solvent Extraction (SASSE), was modified so that (1) it can now handle large amounts of other-phase carryover, (2) residence time is explicit rather than implicit, and (3) the volume of each phase in each stage in a TRUEX flowsheet can be specified. This modified worksheet is being used to evaluate a new model for solvent extraction in columns. In the future, it will be used to model time-dependent chemical reactions in the solvent extraction equipment. By restricting the worksheet to steady-state solutions, convergence problems have been eliminated and the worksheet runs much faster.

A mathematical correlation is being developed for the GTM to treat changes in density resulting from changes in temperature. Data are given for determining densities of complex aqueous solution as a function of temperature. The species considered include Al^{3+}, Cr^{3+}, $H_2C_2O_4$, H_3PO_4, NpO_2^+, Pd^{2+}, Pu^{3+}, Pu^{4+}, Rh^{3+}, $Ru(NO)^{3+}$, and Zr^{4+}. A check on the accuracy of the GTM density predictions is in progress. Methods are being developed for estimating aqueous electrolyte thermodynamic activities at elevated temperature and thermodynamic activities of aluminum in solution.

In laboratory studies to obtain data for the GTM, we determined oxalic acid extraction data for TRUEX-TCE and TRUEX-NPH as a function of aqueous nitric acid concentration at 25°C. These data will be used in developing models to predict the influence of organic-phase oxalic acid on the partitioning of metal species in the scrub and strip sections of a TRUEX flowsheet. Data were also derived for extracting actinides (Pu^{4+}, Th^{4+}, Np^{4+}, NpO_2^+, Am^{3+}, Cm^{3+}), fission-product rare earths (Y, La, Ce, Pr, Nd, Sm, Eu, and Gd), and iron over a range of conditions of solute composition, solvent composition, and temperature (25 and 50°C). The need for this information results from our continuing efforts to test the GTM and increase its applicability to a wider range of process conditions and waste streams. Much of the extraction data generated at CMT through September 1989 have been entered into the GTM data base. Additions will be made as further data are generated.

Earlier data on hydrolysis and radiolysis of TRUEX-NPH solvent in contact with aqueous HNO_3 solution have been correlated in the forms of a rate law. The G value representative of irradiation of TRUEX-NPH solution in contact with aqueous solutions of acidity ranging from 0.25 to 6M HNO_3 was determined to be 0.66 molecules of CMPO destroyed per 100 eV absorbed.

Investigations are underway to develop a method for analyzing aqueous aluminum nitrate solutions (an important constituent of many high-level and TRU-containing waste streams), to assess the use of $AlOH(NO_3)_2$ or $Al(OH)_2NO_3$ as scrub feed solutions in the TRUEX process, and to investigate the incorporation of an evaporator-concentrator into the TRUEX process.

A series of laboratory verification tests is in progress to develop a better understanding of the TRUEX process chemistry, test and verify process modifications, and verify the results from GTM predictions. Five verification tests with 16-stage 4-cm centrifugal contactors were completed during this

report period: three with TRUEX-TCE and two with TRUEX-NPH solvent. Variations between tests included changes in the extraction-section feed composition, the temperature, the feed-stream flow rates, and/or the TRUEX solvent composition. Experimental results were then compared with GTM predictions. The findings from this comparison are being used to refine the GTM.

Centrifugal contactor development continues to be an important part of the TRUEX process development. Relatively simple vibration criteria have been developed to aid the design of the motor/rotor system for the centrifugal contactor. Using these criteria was made easier by incorporating them in an Excel worksheet called Beam. Bearing stiffness data needed to support these criteria were obtained from experimental tests of motors and motor/rotor systems by using a Zonic Real Time Spectrum Analyzer. Evaluation of the experimental results are done using the BEAM IV computer program developed at Virginia Polytechnic Institute and State University. This program was also used to check the operation of the Beam worksheet. With this new vibrational model, we can easily determine how a change in the rotor design will affect the critical speed of the motor/rotor system. The new model will be used to modify existing units and design new contactors.

A 4-cm centrifugal contactor was designed, built, and tested for use at the Y-12 plant (Oak Ridge, TN) in the evaluation of various flowsheets for recovering uranium scrap. The design, which builds on earlier contactor designs, especially the remote-handled 4-cm unit, allows hands-on use of the contactor in the Y-12 plant and permits many solvents to be evaluated over a wide range of organic-to-aqueous flow ratios. We also consulted with Westinghouse Hanford on the final design of a 10-cm contactor for processing of Plutonium Finishing Plant wastes.

A project was initiated to develop a new and cost-effective process for converting the hazardous red-water waste stream from TNT manufacture to forms that are readily disposable or acceptable for recycling. The ANL conceptual process for red-water treatment consists of separating the inorganic salts from the organic nitrosulphonic acids before the latter are biodegraded to nonhazardous compounds. This separation, which appears necessary for biodegradation of the organics, is accomplished by a biphasic solvent extraction process. Research to date has concentrated on the polyethylene glycol (PEG)/Na_2SO_4 system. At room temperature, a concentration of 7.5% PEG and 6% Na_2SO_4 forms an aqueous two-phase system. Increasing temperature to 80°C results in biphase formation at significantly lower salt and PEG concentrations.

High Level Waste/Repository Interactions

The volcanic tuff beds of Yucca Mountain, Nevada, are being studied as a potential repository site for isolating spent reactor fuel and high-level defense and commercial waste. The reprocessed high-level wastes will be incorporated into a borosilicate glass matrix prior to the emplacement in the repository. The behavior of this waste in the host environment must be sufficiently well understood to project its stability over very long time periods. As part of the waste package study group of the Yucca Mountain Project, CMT has been studying the corrosion behavior of simulated nuclear waste glass and spent fuel in aqueous environments relevant to the Yucca Mountain site.

In an ongoing study, simulated waste glasses (SRL 165 and ATM-10) have been intermittently contacted with dripping well water (J-13) using an unsaturated test method. These tests have been in progress for 182 weeks with SRL 165 glass and 117 weeks with ATM-10 glass. The releases of actinides and selected cations are given.

Parametric unsaturated tests with SRL 165 and ATM-10 glasses are in progress to determine the effect of varying the volume of water contacting the waste, the interval between water injection periods,

the ratio of glass surface area in contact with water to water volume (SA/V), and the condition of the stainless steel in contact with the glass. Under conditions where evaporative processes dominate (e.g., extended drop interval or no metal retainer), release from the glass is minimized and calcium-rich secondary phases are the dominant reaction products. When varying degrees of sensitization are imparted to the metal retaining sections in the experimental apparatus, elemental release increases by up to twofold, compared to tests performed with nonsensitized metal. Also, iron-rich phases become common. However, when the top and bottom glass surfaces remain wet, the elemental release from the waste package is increased up to a factor of ten. This increase results from the exfoliation of reacted glass layers, followed by transport of these released layers from the glass by intermittent water contact.

Experiments are in progress to investigate the effect of SA/V ratio (10, 50, 100 m^{-1}), as well as the initial silicon concentrations (deionized water, 60 ppm Si, and 120 ppm Si), on the final steady-state conditions of a static leach test. The test results indicated that the leach rate is directly proportional to the SA/V ratio, provided that the solution pH does not change and no secondary mineral phases form.

The experimental alteration of obsidian (Coso 4-1, Mule Creek, Orito Quarry) in water vapor is being investigated in support of similar experiments with simulated waste glasses. These experiments are performed at 60 to 100% relative humidity (RH) and temperatures of 150-175 °C for up to 30 days. The results demonstrate that RH significantly affects the obsidian hydration rates. This finding supports the assertions of others that careful measurement of temperature and RH are necessary to successfully use obsidian hydration dating. Work is in progress to better understand the compositional effects of obsidians on both their sorptive and reactive properties.

In addition to glass studies, experiments designed to determine radionuclide release rates by exposing spent fuel to repository-relevant groundwater are being performed. Preliminary experiments with UO_2 powders and monoliths in liquid water and small amounts of dripping water are underway in preparation for spent fuel studies. A set of experiments, whereby Zircaloy clad-UO_2 pellets have been contacted by dripping EJ-13 water, has been in progress for over 4.5 years. A pulse of uranium released from the UO_2 solid, combined with the formation of schoepite and dehydrated schoepite on the sample surface, characterizes reactions during the first 30-100 weeks. Thereafter, the uranium pulse subsided and a second set of secondary phases formed on the top UO_2 surfaces.

The effect of ionizing gamma radiation on the host environment and on waste package components has also been experimentally studied. Radiolytic yields of ammonia were determined at temperatures up to 152 °C in three oxygen-containing gaseous environments: N_2/H_2 with 0.1% O_2, N_2/H_2O with 0.1% oxygen, and bubbled air. The results indicated that ammonia formation under repository-relevant conditions is possible. The results also indicate that hydrogen and/or hydrogeneous transients compete much more effectively with oxygen for atomic nitrogen than previously believed.

The Product Consistency Test (PCT) was developed by Savannah River Laboratory (SRL) to provide confirmation of the consistency of radioactive glass produced by the glass melter of the Defense Waste Processing Facility (DWPF) at Westinghouse Savannah River Co. Three glasses supplied by SRL have been tested: two radioactive, one nonradioactive. The radiation levels associated with the radioactive glasses required that many of the test-related operations be conducted in a shielded facility with remote handling capabilities. The results indicate that good precision was obtained for replicate samples, and that the PCT could distinguish between the different glasses.

Prior to DWPF startup, the glass producers must demonstrate that they can produce a consistent product, and DOE must indicate how the glass will perform in the storage environment. To assist with the second requirement, we are undertaking two tasks: a critical review of parameters that affect glass

reaction in an unsaturated environment, and long-term testing of fully radioactive glasses made from actual waste taken from Westinghouse Savannah River.

The technique of laser photoacoustic spectroscopy (LPAS) is being applied to the study of radionuclide speciation in groundwater-like systems. The work in this period was focused on continued development of the LPAS technique, with emphasis on improving the spectral sensitivity and stability of the LPAS system at temperatures up to 90°C.

We are developing a strategy for validating performance-assessment modeling codes for near-field waste package/groundwater interactions over a range of conditions applicable to the proposed Yucca Mountain site. The basis for near-field performance assessment depends on the coupling of sub-models that describe three events: ingress of groundwater, reaction of groundwater with the waste package, and transport of radionuclides through the near-field environment. The experimental strategy revolves around (1) identifying those independent variables that affect each of the three events, (2) identifying the dependent variables that describe the data needs to assess the repository performance, (3) simplifying the overall approach through the use of bounding assumptions, and (4) establishing whether the dependent and independent variables can be measured and/or controlled during experimentation.

Program on Plutonium Recovery from Residue

The objective of this program is to develop an effective pyrochemical process for recovering plutonium from intractable residues. Lawrence Livermore National Laboratory (LLNL) is working with ANL to (1) devise a single economical pyrochemical process capable of recovering plutonium from all the types of scrap and residue now being generated or in storage from previous DOE weapons production operations, (2) minimize waste volumes, (3) remove and concentrate other TRU materials from the wastes so that the bulk of the pyrochemical process effluents can be classified as nonTRU wastes, and (4) provide a basis for upgrading recycled weapons materials. Savannah River Site (SRS) is also working with ANL to develop pyrochemical steps that can be applied in conjunction with existing aqueous processing facilities at SRS to recover plutonium from residues efficiently.

This report covers work in process development; experiments on calcium reduction, calcium electrowinning, and reference electrode development; calculation of americium distribution between liquid plutonium and molten NaCl- KCl; and design work on transfer lines for liquid metals and molten salts used with pyrochemical equipment.

The process development activities look at reference processes from feed to final products to obtain an overview of the process and help define its major features. A reference flowsheet for residue processing with a Zn-Ca solvent/reductant system is presented, and the major process features are defined. A material balance flowsheet is also presented for an ash-heel feed.

Results are reported for reduction experiments with two types of residues, bomb reduction slag and ash heel, with calcium reductant. Zinc-based and aluminum-based reductant alloys were investigated.

Ten experimental runs were conducted to investigate the recovery of plutonium from the slag remaining in crucibles after bomb reductions. In these experiments, $CaCl_2$ was added to modify the slag composition to one that is molten at 800°C, and either a zinc or an aluminum phase was introduced to dissolve and consolidate the remaining plutonium. Because at least a portion of the plutonium was expected to be present as an oxide or fluoride, agitation was provided to promote reduction by calcium. In some runs, the residual calcium from the bomb reduction was supplemented by additional calcium.

The slag fragments were liquefied within 15 min by the added $CaCl_2$, and balls of metallic calcium floated to the surface of the melt. Six separate slag samples were processed. The material balances for the runs ranged from 57 to 141%, which does not lend confidence in the results. However, two runs with zinc and two runs with aluminum indicated plutonium recoveries of over 99%. One sample was reacted four separate times with the same aluminum alloy at ever-increasing agitator intensity. These runs indicate that the violent agitation that was used in the other runs is required to recover the plutonium in the metal phase. The salt from the least successful run was recontacted with a fresh zinc-calcium melt. Even after the two contacts, about 14% of the plutonium remained in the salt. The reason for this unsuccessful run has not been identified.

The recovery of plutonium from ash heels in an ingot that can be dissolved readily in nitric acid was investigated. Two runs were made with Zn-Ca alloys under a program supported by LLNL, and one was made with an Al-Ca alloy, under an SRS-supported effort. The material balances were all low (61 to 83% of the charge) for these runs. The reductions appear to be sensitive to the calcium concentration of the melts. The extent of reductions, based on salt analysis, was 99.5, 97.5, and 95.9% for calcium concentrations of 14.8, 9.0, and 6.3 at. %, respectively. Americium behavior was similar to plutonium behavior in these runs. The expected final CaO concentration in the $CaCl_2$-CaF_2 reduction salt is about 12 wt %, whereas the solubility is about 9.3 wt %. There is mounting evidence that reductions with calcium are hindered markedly when the salt is saturated with CaO. Faster reductions can be expected if more salt is used. In any case, salt recovery and recycle are important to avoid excessive salt wastes.

The calcium electrowinning experiments were based on recovery of calcium and salt from reduction steps using Zn-Ca alloys. Accordingly, the electrolytic cells employed a liquid zinc cathode for calcium recovery. The zinc provides an effective collection medium for the calcium and promotes the electrolytic reaction (reduces the reversible decomposition potential by about 0.5 V) by lowering the zinc activity at the cathode. The resulting alloy can be recycled directly to the reduction step. If successful, a calcium electrowinning process step could markedly decrease the volume of waste salt from pyrochemical reductions by allowing recycle of the salt and calcium reductant. Runs were made at the saturation level (17 mol %) of CaO in the salt and at about 5 mol %. Based on calcium analysis of filtered zinc samples, current efficiencies were from 23 to 72% for the higher CaO concentration and 22% for the low concentration. For the latter case, stirring was required to avoid excessive anode polarization.

During most of each run, the cell potential was maintained below 2.7 V, the calculated value for reversible decomposition of $CaCl_2$ under the experimental conditions. Both CO and CO_2 were observed in the effluent gas; however, even when cell potentials as high as 3.3 V were allowed toward the end of some runs, no chlorine was observed. Some fine carbon was released from the anode and accumulated on the salt surface during every run.

Future experiments will investigate the many parameters affecting the electrowinning. These include concentrations, current densities, electrode design, and cell design. Design features to avoid carbon contamination of melts must be developed.

Reference electrodes are being developed as a necessary instrument in monitoring and controlling reduction and separation processes. Results are reported for two scoping experiments with zinc-alloy/molten-salt systems. These experiments were performed to test a simple zinc electrode contained in a porous MgO tube, which has pores that fill with salt but will not permit metal entry. A concentration cell is established between the reference electrode and alloy of interest. The first experiment monitored the potential difference between two pools of molten zinc with differing concentrations of dissolved calcium and connected by a salt bridge through a porous ceramic wall. Test results showed that the concentration cell concept was feasible and the results agreed well with predictions; however, the ceramic

porosity should be reduced to slow down the diffusion of the calcium through the wall to obtain a longer and more stable sensor. It also showed that the zinc-alloy composition should have sufficient calcium concentration so that the potential change in the reference electrode will be small. The second experiment showed that the reference electrode is a useful instrument for monitoring and controlling the extraction of Ca, Mg, and Al from a Ca-Mg-Al-Zn alloy using incremental $ZnCl_2$ additions.

Calculations were made to verify the valence state of americium and estimate its activity coefficient in a NaCl-KCl mixture. This information is needed to understand and predict PuRR process parameters. The results confirm that $AmCl_2$ is the main product formed by the extraction of americium from liquid plutonium by $PuCl_3$ dissolved in a molten equimolar mixture of NaCl-KCl and indicates that the activity coefficient of $AmCl_2$ is about ten times that of $PuCl_3$. The analysis method developed for these experiments should be useful in understanding salt effects observed using different diluent salts.

In practical pyroprocessing schemes, it is often desirable to transfer molten metals or salts from a crucible in one furnace to one in another furnace for additional process steps or to a mold. The purpose of the development effort undertaken for SRS was to design, build, and test a transfer line for the pyroprocessing facilities at SRS. We developed a preliminary design of a transfer line suitable for use in a glovebox under construction for SRS, based on preliminary heat transfer tests at ANL. The initial phase also included effort to obtain Mo-30 wt % W tubing needed for the design.

I. APPLIED PHYSICAL CHEMISTRY
(C. E. Johnson)

The program in applied physical chemistry involves studies of the thermochemical, thermophysical, and transport behavior of selected materials in environments simulating those of fission and fusion energy systems.

A. Fission Product Vaporization from Core-Concrete Mixtures
(M. F. Roche, L. Leibowitz, and J. L. Settle)

1. Introduction

In a severe nuclear reactor accident involving loss of coolant, molten core debris may melt through the reactor vessel and react with the concrete basemat beneath the vessel. The literature contains conflicting information about the fraction of the more refractory fission products that would be released to the environment under these extreme conditions. In the Reactor Safety Study,[1,2] recommended release fractions (the source term) are 0.02 to 0.06 for the alkaline-earth fission products (strontium and barium) and 0.003 to 0.004 for the rare-earth fission products such as lanthanum. Much larger release fractions for strontium (up to 0.84), barium (up to 0.60), and lanthanum (up to 0.06) have been proposed in more recent studies.[3,4] As a result of the debate, alternative assumptions in calculating release fractions have been explored. Among these are

1. Equilibrium condensed phases (oxide and metal) with the fission product release being controlled by equilibrium between the condensed phases and the gas phase,[5]

2. Non-equilibrium condensed phases with the fission product release being controlled by equilibrium between the metal phase and the gas phase,[5]

3. Non-equilibrium condensed phases with the fission product release being controlled by equilibrium between the oxide phase and the gas phase.[5,6]

The last alternative yields low release fractions for the alkaline-earth and rare-earth fission products, while the first two yield high release fractions.

Resolving this issue is important because even small fractional releases of the refractory fission products can have a significant impact on the consequences of a severe reactor accident,[2] but there are few experimental data with which to test the proposed models. Our experiments employed controlled gas-phase oxygen potentials, well-characterized materials, and detailed computer modeling of the partial pressures of all species. They were performed using a transpiration method in which mixtures of urania (doped with oxides of Sr, Ba, La, and Zr), zirconia, concrete, and (in a few experiments) stainless steel were vaporized at 2150 or 2400 K into flowing H_2 or He-6% H_2. Concretes having silica contents ranging from 7 to 69 wt % were employed to reflect the known range of reactor-basemat compositions. The transpiration method was used to measure the vapor pressures of Sr, Ba, La, and U.

Equilibrium vaporization calculations were performed using the SOLGASMIX computer code,[7,8] which was modified to allow for more elements (up to 25) and species (up to 250) and to adapt its input and output to our needs. The 19 elements now included are H, He, O, Na, Mg, Al, Si, K, Ca, Cr, Mn, Fe, Ni, Sr, Zr, Sn, Ba, La, and U. The data base currently contains free energies of formation of 220 species (112 elemental, oxide, and hydroxide species in the gas phase and 108 in the solid and liquid

oxide and solid and liquid metal phases). In the SOLGASMIX calculations, the 112 gas-phase species were treated as ideal mixtures, as were the 17 liquid-metal species and the 3 solid metals (Fe, Cr, and Zr). Thirty-seven species were incorporated in an ideal liquid-oxide mixture, and fifty-one species were incorporated in an ideal solid-oxide mixture. The approach of employing a variety of species in a phase to model an element's chemical behavior originated with Bottinga and Richet[9] and is called the speciation model.[10,11] The advantage of this model is that mixing between the species is generally close to ideal.[10] Most of the free-energy data were taken from the literature. Other free-energy data were estimated using extrapolation techniques and thermodynamic properties at 298 K. The thermodynamic data are tabulated elsewhere.[12]

2. Experimental

The samples consisted of various amounts of urania (doped with 1 mol % SrO, 0.4 mol % BaO, 1 mol % La_2O_3, and 2 mol % ZrO_2), zirconia, Type 304 stainless steel, and concrete. The concrete types used in this study were a limestone-aggregate concrete, a limestone-sand concrete, and a siliceous concrete. The compositions of the concretes are given in Table I-1. Each sample was heated at the bottom of a Mo-30 wt % W furnace tube (46-cm long x 2.9-cm OD x 2.4-cm ID) in a Brew Model 1064-C High Temperature Vacuum Furnace (Richard D. Brew, Inc.). Materials vaporized from the sample were condensed in a molybdenum tube (54-cm long x 0.8-cm OD x 0.5-cm ID) whose entrance lay within a crucible a few centimeters above the sample surface. The temperature gradient was such that the condensates were deposited about 10-15 cm beyond the tube entrance.

Table I-1. Compositions of Concretes Used in Experiments

	Composition, wt %			
	Limestone Concrete	Limestone-Sand Conc.	Siliceous Concrete	Basalt Concrete
Na_2O	0.034	1.09	0.69	3.06
K_2O	0.40	0.57	1.41	1.41
MgO	7.44	9.62	0.70	3.03
CaO	42.96	26.02	13.47	12.51
SrO	0.030	0.031	0.023	0.046
BaO	0.007	0.032	0.021	0.07
Al_2O_3	1.91	3.48	4.04	11.26
SiO_2	7.13	28.27	68.99	52.80
TiO_2	0.097	0.143	0.81	1.35
V_2O_5	0.011	0.012	0.0	0.045
Cr_2O_3	0.006	0.009	0.007	0.016
MnO	0.014	0.054	0.028	0.137
Fe_2O_3	0.80	1.64	1.00	8.58
CoO	0.003	0.003	0.0	0.006
NiO	0.004	0.005	0.0	0.006
CuO	0.011	0.005	0.0	0.008
ZnO	0.005	0.007	0.0	0.024
ZrO_2	0.004	0.019	0.0	0.026
CO_2+H_2O	40.64	27.54	7.91	4.36
CO_2	33.63	21.41	4.23	----
Sum:	101.5	98.6	99.1	98.7

The samples were held in either calcia-stabilized zirconia crucibles (1.6-cm ID x 1.9-cm OD x 3.8-cm height) or molybdenum crucibles (1.7-cm ID x 1.9-cm OD x 3.8-cm height). Experiments with mixtures of limestone-aggregate concrete (2 g), doped urania (3 g), and steel (3 g) were conducted in zirconia crucibles at 2150 K. The zirconia crucibles were resistant to attack by the steel, but they were partially dissolved by the concretes due to the formation of calcium zirconate. In subsequent experiments, molybdenum crucibles were employed with mixtures of urania, zirconia, and concrete at 2150 and 2400 K (steel was omitted because it would have dissolved the molybdenum).

The transpiration gas was either He-6% H_2-0.06% H_2O or H_2-0.03% H_2O. The H_2O-to-H_2 ratios were equivalent to O_2 partial molar free energies of -420 kJ/mol (-100 kcal/mol) and -550 kJ/mol (-130 kcal/mol), respectively. The flow rate of the gas was either 100 or 200 cm^3/min at 25 °C. The experiments lasted for 73 min at the higher flow rate and 146 min at the lower flow rate. The usual amount of gas was 0.6 mol when the sample was at the desired test temperature.

After the experiments, four of the crucibles were cross-sectioned, mounted, polished, and examined by electron probe microanalysis (EPM). After cross-sectioning, small samples were analyzed by X-ray diffraction (XRD). To determine the total mass transpired, the molybdenum condenser tube was weighed before and after the experiment. The condensates were extracted from the molybdenum tubes with up to four acid washes (first 1:1 HCl-H_2O, then a series of washes with 1:4 HNO_3-H_2O, which chemically attacks molybdenum). The acids were evaporated to dryness, and the residues were digested in 10-15 mL of hot HCl (1:1) or HNO_3 (1:1). The samples were then diluted to 100 mL, making the solutions 1M in HCl or HNO_3 for subsequent analysis. The solutions were analyzed by the Analytical Chemistry Laboratory for metals by inductively coupled plasma/atomic emission spectroscopy (ICP-AES) and for uranium by laser fluorescence spectroscopy.

3. Results and Discussion

The calculated and measured masses of the deposits in the molybdenum tubes are presented in Table I-2 for limestone-aggregate (LL), limestone-sand (LS), and siliceous (SI) concrete. The masses of the deposits in experiments 55-LL and 62-LL agree reasonably well with each other, as do those in experiments 75-LL and 79-LL. These two comparisons establish a lack of significant flow-rate dependence and indicate that the gas is being saturated by the samples. In SOLGASMIX, the masses of the gas-phase species were summed, excluding the hydrogen mass in each species. Oxygen was included because very little oxygen was found in the exit-gas stream; the water vapor concentration in the exit gas decreased to very low levels during these experiments (generally less than 10 ppm). Figure I-1 is a plot of the calculated vs. measured deposit masses; for limestone-aggregate concrete, these masses are in good agreement, while for limestone-sand and siliceous concrete the calculated values are about 50% larger than those measured.

One of the samples examined by EPM and XRD was from an experiment at 2150 K (62-LL) in which the test material contained limestone concrete, doped urania, and stainless steel. It was examined because of the inefficient Fe, Cr, and Ni vaporization in experiments 55-LL and 66-LL. Examination of the cross-sectioned crucible revealed that the steel phase was approximately spherical and embedded within the concrete-urania mixture. Apparently, the steel could not equilibrate with the gas. The data for experiments 55-LL and 62-LL were omitted from Fig. I-1 because the calculated masses include a significant amount of steel (75 mg of Fe + Cr + Ni) and the steel transport was hindered.

The EPM scans of two oxide regions of 62-LL were presented in the previous report in this series. The major phases present at ambient temperature in this experiment were deduced from the overlap of the elemental images in the photomicrographs and a knowledge of the system chemistry and

thermodynamics. The phases were (1) urania containing mainly calcia and zirconia, (2) calcium zirconate, (3) a calcium-magnesium silicate, (4) magnesia associated with the calcium-magnesium silicate, and (5) a metal phase. The presence of $CaZrO_3$ and a major face-centered-cubic (fcc) phase with a lattice constant of 5.375 Å (consistent with known lattice constants for urania-calcia-zirconia phases) was confirmed by XRD. A melting point as low as 1763 K is reported[13] for the $MgO-CaZrO_3-CaSiO_3$ section of the $MgO-CaO-ZrO_2-SiO_2$ system. Therefore, the calcium-magnesium-silicate, magnesia, and calcium zirconate phases all crystallized from a liquid phase.

Table I-2. Total Mass Deposited in Molybdenum Condenser Tube

Expt. No.[a]	$\Delta G(O_2)$, kJ/mol	Temp., K	Gas[b]	Flow Rate, cm^3/min	Mass, mg	
					Measured	SOLGASMIX
55-LL	-431	2150	He-5% H_2	200	129	149
62-LL	-431	2150	He-6% H_2	100	98	149
75-LL	-381	2150	He-6% H_2	200	86	44
79-LL	-381	2150	He-6% H_2	100	91	44
98-LL	-326	2400	He-6% H_2	200	182	133
106-LL	-400	2400	H_2	200	368	338
111-LL	-445	2150	H_2	100	153	136
89-LS	-361	2150	He-6% H_2	100	76	101
93-LS	-306	2400	He-6% H_2	200	156	258
101-LS	-377	2400	H_2	200	430	708
109-LS	-427	2150	H_2	100	210	329
119-SI	-336	2400	H_2	200	987	1433
124-SI	-331	2400	H_2	200	858	1274

[a]LL is limestone-aggregate, LS is limestone-sand, and SI is siliceous concrete.
[b]The added water, usually 0.06% for He-6%H_2 and 0.03% for H_2, is not shown in this column.

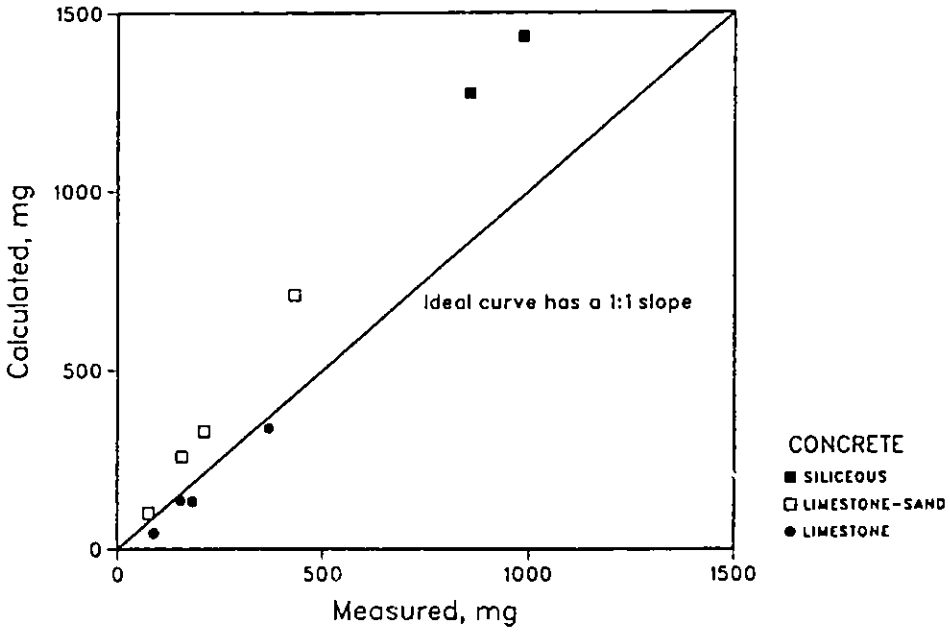

Fig. I-1. Calculated and Measured Masses of Deposits

The above information led us to conclude that the sample phases present during experiment 62-LL (2150 K) were (1) gas phase; (2) liquid oxide phase containing most of the calcia, zirconia, silica, and magnesia (this liquid yielded three solid phases on cooling); (3) solid oxide phase containing most of the urania; and (4) liquid metal phase (stainless steel).

The other samples that were examined by EPM were from experiments performed at 2400 K (106-LL, 101-LS, and 119-SI). All three samples exhibited a pronounced meniscus and wetted the molybdenum beakers. The EPM studies suggested that the two higher silica samples (101-LS and 119-SI) were mostly liquid at 2400 K; these samples exhibited an alternating-layer structure typical of crystallization from a liquid. One layer was richer in urania and zirconia, while the other was richer in silica, calcia, and magnesia. The EPM studies for the limestone-aggregate sample (106-LL) indicate that it was at least partially liquid at 2400 K, but it did not exhibit the pronounced alternating-layer structure seen in the higher-silica samples. The phases in 106-LL appeared to be similar to those described for the 62-LL sample.

The XRD results for the 106-LL sample indicated a fcc phase with a lattice constant of 5.39 to 5.42 Å. Also detected by XRD were calcium zirconate (with a slightly larger lattice constant than in the sample from experiment 62-LL) and a minor phase (possibly a calcium silicate). The XRD results for the 101-LS sample indicated two fcc phases with lattice constants of 5.415 Å and 5.29 Å. The XRD results for the 119-SI sample also indicated two fcc phases with lattice constants of 5.415 Å and 5.21 Å. The cubic phase having the larger lattice constant (5.37 to 5.42 Å) is a urania-rich solid solution because its lattice constant is consistent with those for urania-calcia-zirconia solid solutions (a range of lattice constants is possible for a solid solution). This phase is present in all four samples: 62-LL, 106-LL, 101-LS, and 119-SI. The cubic phase having the smaller lattice constant (5.21 to 5.29 Å) is present in 101-LS and 119-SI and is probably the phase richer in silica, calcia, and magnesia.

These data indicated that the samples consisted of a gas phase, a solid oxide phase, a liquid oxide phase, and (in two cases: 55-LL and 62-LL) a liquid metal phase at test temperature. Upon cooling, the liquid oxide phase was found to segregate into as many as three phases.

Spot-analysis data from the EPM are listed in Tables I-3 through -6 for the four samples from Experiments 62-LL, 106-LL, 101-LS, and 119-SI. Below the data in each table are the linear correlation coefficients between the data for each pair of elements. High positive correlations of Sr and La with Zr in sample 62-LL are indicated in Table I-3; these elements are mainly present in the calcium zirconate that crystallized from the liquid oxide phase on cooling. Calcium is also correlated with zirconium, but the data exhibit significant scatter. This result is understandable because calcium is present in significant concentration in more than one phase. Barium was detected in only three of the spots analyzed; its concentration was generally too low for a reliable analysis.

The data for sample 106-LL in Table I-4 are largely uncorrelated. The positive correlation of La with U is the only interesting one. It indicates that the lanthanum oxide, which was initially in solid solution in the urania, remained with the urania throughout the experiment. The high variability of the spot analyses indicates that this sample is not a homogeneous solid solution, but we were unable to detect any obvious pattern.

The data for sample 101-LS in Table I-5 show strong positive correlations of Mg with Ca and Zr with U. Strong negative correlations of Ca, Mg, and Si with Zr and U indicate that Ca, Mg, and Si tend to be in different phases than Zr and U. In addition, the data for the trace element Sr are correlated with the data for Si. From the correlation data, the Ba appears to be associated with a phase rich in Si.

Table I-3. Spot Assays and Linear Correlation Coefficients from EPM Studies of Sample from Experiment 62-LL

Spot assays, wt %							
Ca	Mg	Si	Ba	La	Sr	Zr	U
20.5	6.8	4.2	0	0.44	0.3	21.4	21.7
20.6	0.7	0	0	0.69	0.46	45.1	6.6
16.5	4.2	3.7	0	0.31	0.16	10.7	17.2
25.1	0.62	0	0	0.69	0.46	46.0	6.2
10.7	2.4	1.2	0	0.40	0.17	25.4	36.2
17.3	0.44	0.44	0.14	0.57	0.25	29.0	27.8
18.3	1.1	0.24	0	0.72	0.44	38.1	21.1
19.1	0.49	0	0	0.79	0.44	44.0	6.9
19.6	11.4	3.1	0	0.61	0.42	31.3	7.6
9.4	0.63	2.0	0.26	0.23	0	3.9	74.9
7.3	3.9	2.0	0.12	0.22	0	5.8	62.4
26.6	0.47	0	0	0.73	0.41	45.5	6.1
25.4	0.49	0.12	0	0.74	0.47	44.7	6.1
Linear correlation coefficient matrix for above spot assays							
	Mg	Si	Ba	La	Sr	Zr	U
Ca→	-0.114	-0.357	-0.623	0.819	0.878	0.826	-0.878
	Mg→	0.785	-0.200	-0.274	-0.080	-0.320	-0.046
		Si→	0.093	-0.678	-0.489	-0.718	0.291
			Ba→	-0.594	-0.724	-0.640	0.848
				La→	0.956	0.972	-0.831
					Sr→	0.943	-0.911
						Zr→	-0.836

Table I-4. Spot Assays and Linear Correlation Coefficients from EPM Studies of Sample from Experiment 106-LL

Spot assays, wt %							
Ca	Mg	Si	Ba	La	Sr	Zr	U
17.8	24.2	1.6	0	0.29	0.16	11.4	13.9
9.0	0.0	1.9	0	0.59	0.08	1.7	50.5
51.3	0.05	8.5	0.14	0.50	0.14	0.68	25.6
41.9	0.03	8.7	0.08	0.33	0.22	4.6	27.0
17.7	0.05	0.14	0	0.36	0.02	1.6	35.9
67.4	0.11	0.12	0	0.10	0.05	0.7	12.2
50.0	0.08	10.9	0.05	0.19	0.26	0.27	1.9
47.3	0.02	9.7	0.06	0.26	0.16	0.91	41.2
48.7	0.05	10.8	0.06	0.20	0.22	3.1	8.1
36.8	0.14	0.2	0	0.28	0.06	2.1	23.3
22.6	0.0	0.67	0	0.49	0.24	24.4	36.9
59.0	0.08	0.7	0	0.12	0.11	2.6	5.1
Linear correlation coefficient matrix for above spot assays							
	Mg	Si	Ba	La	Sr	Zr	U
Ca→	-0.362	0.358	0.382	-0.709	0.111	-0.429	-0.630
	Mg→	-0.196	-0.225	-0.043	0.063	0.310	-0.198
		Si→	0.808	-0.086	0.674	-0.311	-0.184
			Ba→	0.167	0.422	-0.297	-0.045
				La→	-0.006	0.329	0.781
					Sr→	0.415	-0.259
						Zr→	0.176

Table I-5. Spot Assays and Linear Correlation Coefficients from EPM Studies of Sample from Experiment 101-LS

Spot assays, wt %							
Ca	Mg	Si	Ba	La	Sr	Zr	U
23.0	1.6	15.3	0.02	0.73	0.21	5.7	22.7
28.8	1.4	19.5	0.10	0.93	0.34	4.9	5.3
25.3	1.4	21.0	0.12	0.92	0.35	3.5	1.4
34.0	2.0	18.5	0.05	0.56	0.33	0.67	0.63
36.8	2.3	17.5	0.01	0.66	0.31	0.39	0.26
13.4	0.73	10.7	0.01	0.69	0.19	12.1	25.3
14.9	0.67	9.0	0	0.61	0.23	15.2	34.0
25.0	1.3	16.8	0	0.57	0.20	7.1	10.3
33.5	1.6	17.5	0.01	0.70	0.29	1.2	0.74
21.6	0.93	15.0	0	0.59	0.28	7.3	20.6

Linear correlation coefficient matrix for above spot assays							
	Mg	Si	Ba	La	Sr	Zr	U
Ca→	0.922	0.769	0.229	0.061	0.667	-0.944	-0.899
	Mg→	0.682	0.196	0.036	0.521	-0.905	-0.788
		Si→	0.681	0.480	0.758	-0.860	-0.903
			Ba→	0.830	0.716	-0.344	-0.493
				La→	0.470	-0.174	-0.288
					Sr→	-0.677	-0.742
						Zr→	0.918

Table I-6. Spot Assays and Linear Correlation Coefficients from EPM Studies of Sample from Experiment 119-SI

Spot assays, wt %							
Ca	Mg	Si	Ba	La	Sr	Zr	U
10.0	0.50	17.8	0.01	0.70	0.18	4.9	35.5
12.0	0.61	24.2	0.21	0.79	0.27	5.6	3.9
10.6	0.45	19.0	0.06	0.58	0.17	10.2	12.6
0.44	0.15	0.38	0	0.33	0.06	10.1	48.6
1.8	0.06	6.5	0	0.22	0.07	6.4	65.6
6.2	0.28	7.5	0.01	0.52	0.14	13.2	26.4
6.0	0.20	12.2	0	0.32	0.08	7.0	52.5
12.5	0.44	24.2	0.16	0.69	0.32	6.1	4.0
11.7	0.46	25.2	0.18	0.68	0.22	5.6	3.8
12.4	0.43	25.4	0.12	0.79	0.28	5.8	4.2
11.8	0.47	25.4	0.15	0.74	0.23	8.3	4.6
12.0	0.46	23.8	0.16	0.70	0.19	5.2	7.9
10.9	0.31	20.0	0.12	0.61	0.18	15.2	22.2
8.6	0	24.0	0.12	0.58	0.16	15.0	11.2
11.7	0	22.2	0.13	0.86	0.23	6.4	5.1

Linear correlation coefficient matrix for above spot assays							
	Mg	Si	Ba	La	Sr	Zr	U
Ca→	0.589	0.943	0.798	0.907	0.887	-0.244	-0.886
	Mg→	0.459	0.437	0.489	0.569	-0.403	-0.459
		Si→	0.858	0.837	0.841	-0.227	-0.866
			Ba→	0.762	0.812	-0.197	-0.867
				La→	0.881	-0.259	-0.896
					Sr→	-0.329	-0.867
						Zr→	0.068

This association of the trace element Ba with the major element Si is more significant than its apparent correlation with the trace element La.

The data for sample 119-SI in Table I-6 indicate strong positive correlations of Mg, Si, Sr, and La with Ca. The data for Ba are also correlated with Ca but are even more strongly correlated with Si. Thus, the trace elements Sr, Ba, and La are present in 119-SI, mainly in the silicate phase along with the major elements Mg and Ca. SOLGASMIX calculations for this sample also indicate that the condensed-phase chemistry of Sr, Ba, and La is dominated by the silicate species.

In summary, the spot-analysis data, particularly for samples 62-LL, 101-LS, and 119-SI, demonstrate that zirconates and silicates play an important role in the condensed-phase chemistry of Sr, Ba, and La oxides in core-concrete mixtures under reactor-accident conditions.

4. Release during Severe Reactor Accidents

Analytical data and SOLGASMIX calculations for Mg, Ca, Sr, Ba, La, and U transport during the experiments listed in Table I-2 were presented in the previous report in this series (Sec. I.A). The data and calculations can be used to estimate the release of Sr, Ba, La, and U and the total mass release during the molten core-concrete interaction (MCCI) phase of a severe reactor accident. To make these estimates, we used experiment 106-LL for the limestone-aggregate concrete, experiment 101-LS for the limestone-sand concrete, and experiments 119-SI and 124-SI for the siliceous concrete. These experiments, which were at the highest temperature (2400 K) and employed the most reducing conditions (H_2 gas), gave releases for Sr, Ba, La, and U that were a factor of ten higher than those of the experiments at 2150 K with the most reducing conditions. Although our calculations of release fractions ignore the changes in temperature and composition of the core-concrete mixtures that are expected to occur as a reactor accident progresses (for example, Ref. 4), we believe that they are reasonable because the temperature and reducing power of the gas are comparable to the conditions expected in a severe reactor accident.[3]

To calculate the release for a hypothetical reactor accident, we divided the amount of each element transported by its initial inventory in the sample and multiplied by 100 to give the percent released to the gas. This percentage was multiplied by the number of moles of gas (CO_2 plus H_2O) that would have evolved from the concrete as it decomposed, and the product was then divided by the number of moles of gas (usually 0.6 mol) used in our experiments. Additionally, the total mass transported (deposit masses from Table I-2) was converted to release fractions (as a percent of the initial mass of uncalcined concrete, doped urania, and zirconia). These deposit masses, which arise from vapor condensation, are believed to be the major contributors to the aerosol mass.[4]

The results of the calculations using the experimental values and SOLGASMIX values are plotted in Fig. I-2. The measured release fractions for Sr, Ba, and La are less than 1% for the limestone-aggregate concrete, which is low in silica (7.13 wt %), and they are further reduced as the silica content of the concrete is increased. The U release shows little sensitivity to concrete type. This result is reasonable, since the urania was a major fraction of the samples and forms no compounds with silica or zirconia. The curves in Fig. I-2 are smooth fits to the SOLGASMIX calculations for the three concretes. For La, the SOLGASMIX calculations deviate from the measurements by the greatest amount (up to a factor of forty), but we believe that the thermodynamic values in SOLGASMIX are poorest for lanthanum. We estimated the thermodynamics of lanthanum silicates and lanthanum zirconate by using values calculated for barium silicates and zirconates. For Ba and Sr, the SOLGASMIX calculations are within a factor of four of the measurements. For U and total mass, the SOLGASMIX calculations are within a factor of two of the measurements, which we consider good agreement.

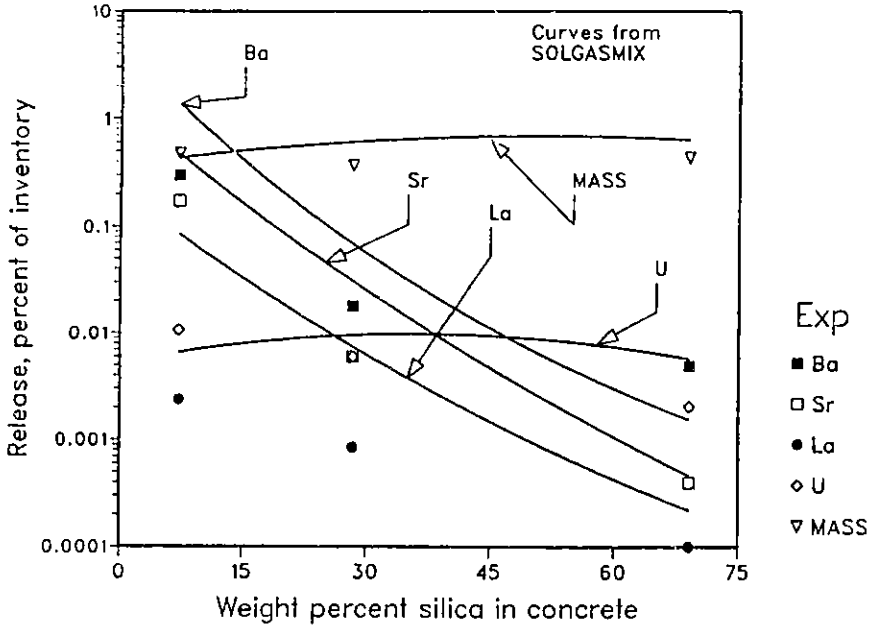

Fig. I-2. Release of Fission Products, Uranium, and Total Mass from Mixtures of Urania, Zirconia, and Three Concretes at 2400 K

Figures I-3 through -5 show smooth curves through SOLGASMIX calculations for four values (-250, -350, -450, and -550 kJ) of the partial molar free energy of oxygen and for the three concrete types. Also shown are the experimental data, which are the same as in Fig. I-2; they are plotted at the partial molar free energy of oxygen calculated by SOLGASMIX. This free energy is close to the minimum in the mass curve of each figure. The increase in predicted mass at the left of Figs. I-3 through -5 is due largely to the very high fraction of water vapor in the gas phase that is needed to set the partial molar free energy at a value of -250 kJ (the mole fraction H_2O at 2400 K is about 33%). Since the calculated mass release includes all the oxygen present in the gas phase at 2400 K, the oxygen in this water vapor is included. We have not developed a satisfactory alternative to the present calculation at this point. The measured and calculated masses agree well for the limestone-aggregate concrete (Fig. I-3). However, the masses calculated by SOLGASMIX are about 50% higher than the experimental masses for the limestone-sand concrete (Fig. I-4) and the siliceous concrete (Fig. I-5). This discrepancy was noted previously in connection with Fig. I-1.

Figures I-3 through -5 reveal that no other partial molar free energy of oxygen would have resulted in a better fit of SOLGASMIX to the experiments. As an extreme example, the partial molar free energy of oxygen in the inlet gas, -550 kJ/mol, leads to very high calculated releases for Ba, Sr, La, and total mass. These values are seen to be a particularly poor representation of the experimental data.

A significant feature of the gas-phase chemistry is the magnitude of the change in partial molar free energy of oxygen from the inlet-gas value (-550 kJ/mol) to the equilibrium value over the sample. The calculated equilibrium value is at the center of the horizontal axis in Fig. I-3 (-400 kJ/mol), further to the left in Fig. I-4 (-376 kJ/mol), and even further to the left in Fig. I-5 (-333 kJ/mol). This shift toward the left is caused by increasing amounts of water vapor in the gas phase over the samples. The calculated values are about 12,000 ppm for the limestone-aggregate concrete, 21,000 ppm for the limestone-sand concrete, and 57,000 ppm for the siliceous concrete. The reaction responsible for increasing amounts of water with increasing amounts of silica in the sample is reduction of the silica by hydrogen to form silicon monoxide. The effect tends to suppress the release of Sr, Ba, and La with

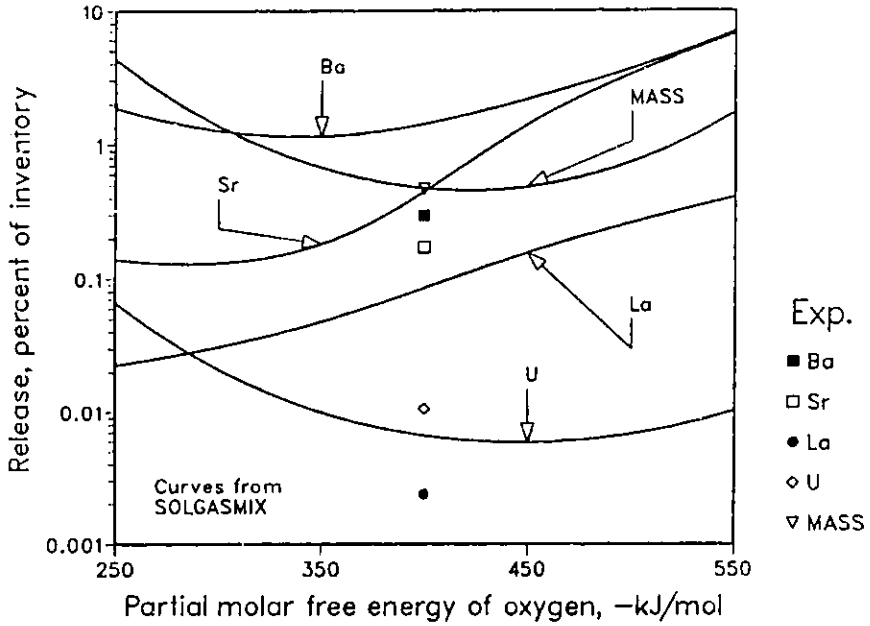

Fig. I-3. Release of Fission Products, Uranium, and Total Mass from Urania, Zirconia, and Limestone Concrete at 2400 K

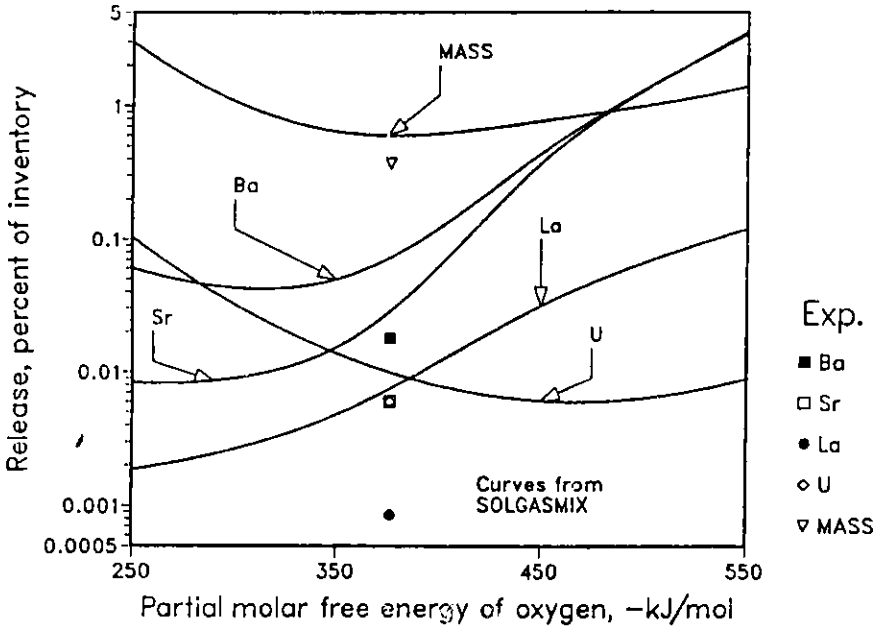

Fig. I-4. Release of Fission Products, Uranium, and Total Mass from Urania, Zirconia, and Limestone-Sand Concrete at 2400 K

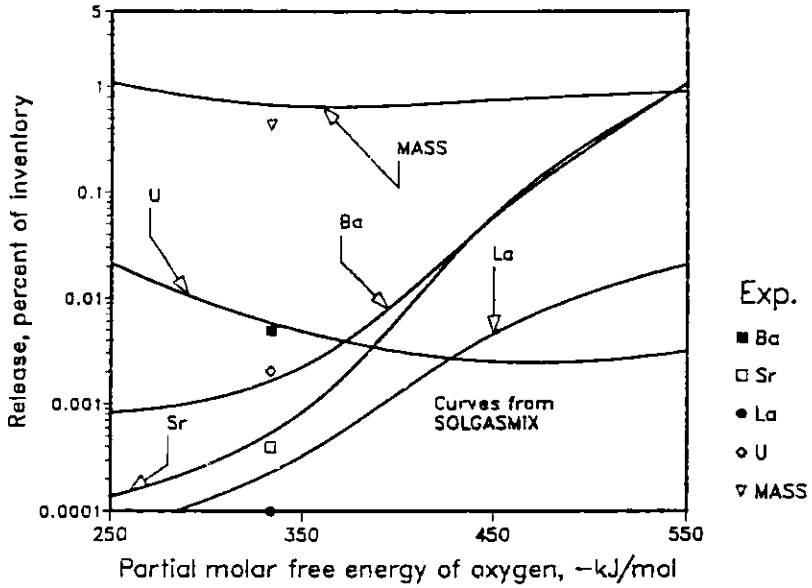

Fig. I-5. Release of Sr, Ba, La, U, and Total Mass from Mixtures of Urania, Zirconia, and Siliceous Concrete at 2400 K

increasing silica concentration. The high levels of water vapor calculated by SOLGASMIX to be in equilibrium with the samples were balanced by large amounts of species such as Na(g), Mg(g), SiO(g), and K(g). These species reacted with the water vapor during the condensation process to form oxides and hydroxides so that the exit gas stream contained less than 10 ppm H_2O. Thus, it is appropriate to include in the mass release nearly all the oxygen from the water vapor that is present at 2400 K in equilibrium with the samples.

The SOLGASMIX calculations indicated that the dominant gas-phase species in the limestone-concrete experiment (106-LL) were Sr and SrOH for strontium, Ba and BaO for barium, LaO for lanthanum, and UO_2 and UO_3 for uranium. In the limestone-sand concrete experiment (101-LS), these species were Sr and SrOH for strontium; Ba, BaO, and BaOH for barium; LaO for lanthanum; and UO_2 and UO_3 for uranium. In the siliceous concrete experiments (119-SI and 124-SI), they were Sr, SrOH, and $Sr(OH)_2$ for strontium; BaO, BaOH, and $Ba(OH)_2$ for barium; LaO and $La(OH)_2$ for lanthanum; and UO_2 and UO_3 for uranium. The hydroxides of strontium, barium and lanthanum thus increased in concentration as the partial molar free energy of oxygen became more positive.

In summary, we observed three major chemistry effects that tended to suppress the release of the refractory fission products. They were

1. Shifts in the partial molar free energy of oxygen in the gas phase toward more positive values as a result of reactions between the gas phase and the core-concrete mixture,

2. Formation of silicates of the refractory fission products in the condensed oxide phases,

3. Formation of zirconates of the refractory fission products in the condensed oxide phases.

5. Conclusions

Our results indicate that the releases of Sr, Ba, La, and U in a severe reactor accident will be less than 1% of their inventory. These results are as low as, or lower than, the source-term values in the Reactor Safety Study[1,2] and are lower than values proposed in a more recent study.[3] We conclude, further, that aerosol release will be about 0.5% of the total core-concrete mass.

During the MCCI phase of a severe reactor accident, an oxide phase (concrete, urania, and zirconia) will lie over a metallic phase containing zirconium and stainless steel.[4] Our work leads us to conclude that the gas emanating from this molten core-concrete mixture will have a partial molar free energy of oxygen that is in equilibrium with the overlying oxide phase. The recommended calculational procedure is to equilibrate the gas (H_2O and CO_2 arising from decomposition of the concrete basemat) first with the metallic phase (reducing most of the H_2O and CO_2 to H_2 and CO) and then with the oxidic phase (partially oxidizing the H_2 and CO to H_2O and CO_2). This approach, which leads to low calculated release fractions for barium, strontium, and lanthanum, has been explored in recent theoretical work[5,6] although the details of the calculations differ in some respects.

Accurate source-term calculations are not yet possible with the existing thermodynamic data base. Needed refinements include measurements of high-temperature thermodynamic properties for liquid and solid silicates and zirconates, the alkaline earths, and the rare earths, as well as improved calculational methods to predict the relative amounts of solid-oxide and liquid-oxide phases. Currently, the calculations predict more solid oxide than is found experimentally; minor changes in the free energy data base may correct this problem. The release of certain radiologically important fission products (particularly Te, Ru, Ce, and Pu) from core-concrete mixtures has not been addressed in this study; transpiration studies of these elements are also needed to understand their behavior in a severe reactor accident.

B. Thermophysical Properties of Metal Fuels

(L. Leibowitz and R. A. Blomquist)

Measurements and calculational analyses are being performed to provide needed information on the thermodynamic and transport properties of Integral Fast Reactor (IFR) fuels. A summary is given below of our work on (1) fuel-cladding compatibility, (2) the U-Pu-Zr phase diagram, and (3) phase relations in the U-Fe system.

1. Fuel-Cladding Compatibility

An important area in the IFR development is chemical interaction between the U-Pu-Zr alloy fuel and the steel cladding. Because there are low melting eutectics in the U-Fe and Pu-Fe systems, cladding integrity could be compromised by formation of liquid phases during irradiation of fuel. As part of our investigation of fuel-cladding compatibility, we performed differential thermal analysis (DTA) experiments with several mixtures of U-Pu-Zr fuel and stainless steel cladding alloys (HT9, D9, and 316). The compositions for the fuel-cladding mixtures were chosen to yield a nearly constant fuel (U + Zr + Pu) atom fraction of about 0.5 in each mixture, which is the ratio of fuel to cladding in a section of an actual fuel pin. Fuels containing U-10 wt % Zr and U-10 wt % Zr plus 8, 19, or 26 wt % Pu were tested. Each fuel-cladding mixture was heated at 10°C/min to about 1570°C in a yttria crucible, after which several cooling/heating cycles were initiated at various rates.

Overall, similar DTA results were obtained with the various mixtures that we studied. Figure I-6 gives the DTA curves on heating and cooling for a U-10 wt % Zr/HT9 mixture. At about 600-

700°C on initial heating, small peaks in the DTA curve (uppermost one in Fig. I-6) corresponding to solid-state transitions in the fuel were seen. Then, at about 1200°C, there was a large exothermal peak, which is indicative of a reaction forming more stable products (probably an Fe_2Zr-like phase). On subsequent cooling, the DTA curve indicated primary precipitation in the neighborhood of 1220°C. At about 700°C, there was a marked DTA peak, which we attribute to a freezing transition. The appearance of this peak suggests significant subcooling. Transitions which would be expected at intermediate temperatures were difficult to identify unequivocally from these data. As shown by the bottom curve in Fig. I-6, the peak indicating sample melting was sharp and narrow and suggested formation of a eutectic. As the plutonium content increased, this major peak became wider and smaller. It appears that the temperature range between solidus and liquidus had progressively increased.

Of primary interest to IFR development is the so-called "onset-of-melting" temperature found from heating curves. We found that this temperature fell as the plutonium content of the fuel increased. Reproducibility of the values with repeated heating and cooling cycles was very good, typically within 2-4°C. It is difficult to judge the absolute accuracy of these temperatures, however, and we estimate that our onset-of-melting temperatures are probably reliable to about ±10-20°C, with the larger uncertainty being associated with the 19 and 26 wt % Pu fuels.

Scanning electron microscope (SEM) examination of the residues from these tests showed three types of precipitates, and the results qualitatively support the following reaction sequence: primary precipitation of a Fe_2Zr-like phase, followed by secondary precipitation of Fe_2U, followed by formation of a Fe_2U-FeU_6 eutectic. A matrix found in the SEM examination of these samples had a eutectic-like appearance and contained a phase with a very high uranium content, close to FeU_6. The major peak found in the DTA curves is believed to correspond to a three-phase region of Fe_2U-Fe_2Pu, FeU_6-$FePu_6$, liquid in the phase diagram.

An evaluation of the applicability of these data to IFR development must await further experiments in which the rate of attainment of equilibrium is evaluated. For example, whole-pin heating tests, which will help define this rate, are planned.

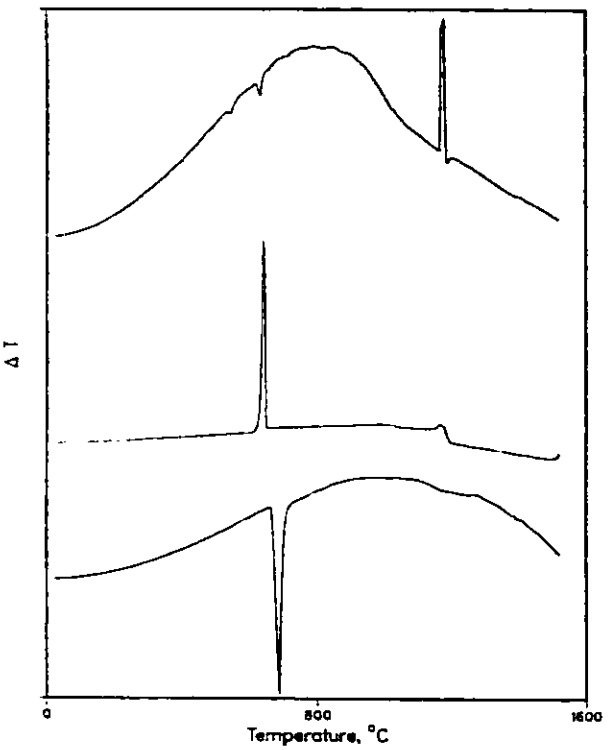

Fig. I-6.

Differential Thermal Analysis Curves for U-10 wt % Zr/HT9 Mixture (top curve, initial heating; middle curve, initial cooling; bottom curve, subsequent heating)

2. U-Pu-Zr Phase Diagram

The chief source of information on the important U-Pu-Zr phase diagram is the work of O'Boyle and Dwight.[14] There are significant uncertainties in their published diagrams, however, and we have undertaken to improve this situation by a combination of phase diagram calculation and experimental measurement. Calculation of a ternary phase diagram requires thermodynamic functions for all phases existing in the three binary subsystems; the ternary phase diagram can be calculated from these functions. We have already completed an analysis of the U-Zr system[15] and have begun a similar analysis of the Pu-U system. A recent assessment of the Pu-U system was published by Peterson and Foltyn[16]; these authors, however, did not provide thermodynamic data adequate for phase diagram calculations.

In comparing the 500°C isothermal section of the U-Pu-Zr phase diagram of O'Boyle and Dwight with the Pu-U phase diagram of Peterson and Foltyn, we found that a wide two-phase $\alpha + \zeta$ field in the former was absent in the latter. At about 500°C that field extends roughly from 14 to 29 at. % Pu. It would be expected, therefore, that a much more extensive three-phase $\delta + \alpha + \zeta$ field would exist in the ternary phase diagram than is indicated by O'Boyle and Dwight. This region is of particular importance to IFR fuel development and represents just one area that should be investigated further.

In assessing the Pu-U system, we expanded our previous work on calculation of the solidus-liquidus in the U-Pu-Zr system.[17] The present evaluation essentially confirmed the earlier findings with only minor modifications. The main conclusion was that the published solidus-liquidus for the Pu-U[16] system is not consistent with the accepted enthalpy of fusion of uranium. It is known that, for a melting transition in an alloy (A-B), as the composition approaches a pure component (X_B), the difference between the slopes of the liquidus and solidus curves is determined by just the enthalpy of fusion, ΔH_f°, and the melting point, T_f, of that component. That is,

$$\lim_{X_B \to 1} \left[\frac{dX_B^{\ell}}{dT} - \frac{dX_B^{s}}{dT} \right] = \frac{\Delta H_f^\circ}{RT_f^2} \qquad \text{(I-1)}$$

where the superscripts ℓ and s indicate liquidus and solidus, respectively. Our calculated Pu-U diagram shows the correct limiting slopes if we accept the value for the enthalpy of fusion of uranium given by the International Atomic Energy Agency.[18]

The Pu-U system is unusual in that, in addition to the large number of phase transitions in the constituent elements, there are two intermediate phases, η and ζ, which have very broad fields in the phase diagram. We are currently developing an approach for thermodynamic analysis of the unusual features of this system.

3. Phase Relations in Fuel-Cladding Systems

Considerable effort has been expended in analysis of fuel-cladding compatibility (Sec. I.B.1). We are also directing our efforts toward gaining a more thorough understanding of the phase relations involved in fuel-cladding systems. Our initial experiments were directed toward the important U-Fe binary system. In the published phase diagram,[19] the liquidus curve over much of the diagram is interpolated; indeed, there are no data whatever in the literature defining that curve. The chief sources of experimental data for the U-Fe diagram are given in the literature.[19-21]

Our initial efforts involved DTA studies of a U-Fe mixture containing 50 at. % U in a beryllia crucible. That container material was chosen because it was used, with apparent success, by Gordon and Kaufmann.[20] We found a very sharp eutectic peak in our DTA curve at the same temperature as had been reported in the literature (725 °C),[22] but we observed that the initial liquidus temperature was quite high compared with the estimated liquidus and, more importantly, increased as the sample underwent heating/cooling cycles. After considerable work with this container material, we changed to a yttria crucible (because of its greater stability at high temperatures) and prepared a new alloy sample of the same composition. We found a stable liquidus temperature with cycling, but the eutectic peak appeared at 722 °C. Although the liquidus peak was very small, the temperature was clearly about 60-70 °C higher than the published diagram indicates. In view of these conflicting findings, we are proceeding with an examination of several other U-Fe alloy compositions and with SEM examination of the residues from these tests.

C. Desorption Characteristics of the $LiAlO_2$-H_2-H_2O(g) System

(A. K. Fischer)

Temperature programmed desorption (TPD) measurements are in progress to determine the activation energies of desorption for H_2O(g) and H_2(g) from γ-$LiAlO_2$, a candidate ceramic tritium breeder for fusion reactors. Since the species directly released from the surface in irradiation tests can be considered to be dominantly the oxidized form (HTO or T_2O, with the appearance of HT often being ascribable to post-release interactions of HTO with metallic walls or exchange with H_2), measurements of the activation energy for desorption of H_2O(g) are especially relevant to the development of a firm understanding of the release process.

Measurements of H_2(g) adsorption and desorption are also needed to describe the purge gas chemistry and to define an optimal balance between the beneficial effects from adding H_2(g) as a tritium release promoter and the need for minimizing the amount of protium that must be separated from tritium in processing the recovery stream. The experimental program will, therefore, address both gaseous species. Insofar as H_2O(g) is concerned, the new study, with its emphasis on kinetics of desorption, complements our earlier study on adsorption, which culminated in designer-usable adsorption data for the $LiAlO_2$-H_2O system.[23]

The TPD measurement employs mass spectrometry as the principal method for detection of the release of gaseous species. These preliminary results provide the first direct desorption data and are useful for assessing the performance of the TPD apparatus.

1. Blank Experiments

An apparatus for TPD measurements with a stainless steel sample tube was designed and constructed. Preliminary blank experiments (no $LiAlO_2$ present) were performed to gain information on the behavior of the empty stainless steel sample tube exposed to a flowing gas mixture of He, H_2O, and H_2. The gas-carrying lines were maintained at 200 °C to minimize holdup of H_2O(g). Figure I-7 shows the response to a step change in gas composition from pure helium to He-100 ppm H_2O-500 ppm H_2 and back again to pure helium. (Often 1000 ppm H_2 is used in tritium release tests, and lower concentrations are of interest; thus, the mixture used here is a realistic one in this respect.) The curves in Fig. I-7 clearly indicate that the steel is not an inert material, because H_2O is consumed and H_2 is produced. In the first 5 min, the lag in the H_2 curve suggests that some dissolution/reaction of H_2 in the steel occurs.

At the moment of the switch from pure helium (after ~2 min), a 200 to 700 °C linear temperature ramp (~33 °C/min) for the sample tube was started, shown in Fig. I-8. It is evident that, with

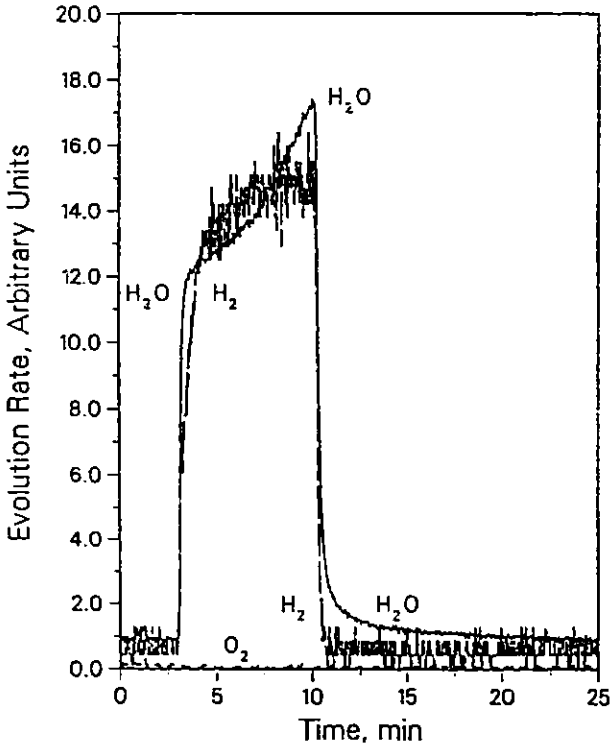

Fig. I-7.

Response of Stainless Steel Sample Tube at 200°C (473 K) to Step Change from Pure Helium to Mixture of Helium with 100 vppm H_2O and 500 vppm H_2 Followed by Return to Pure Helium

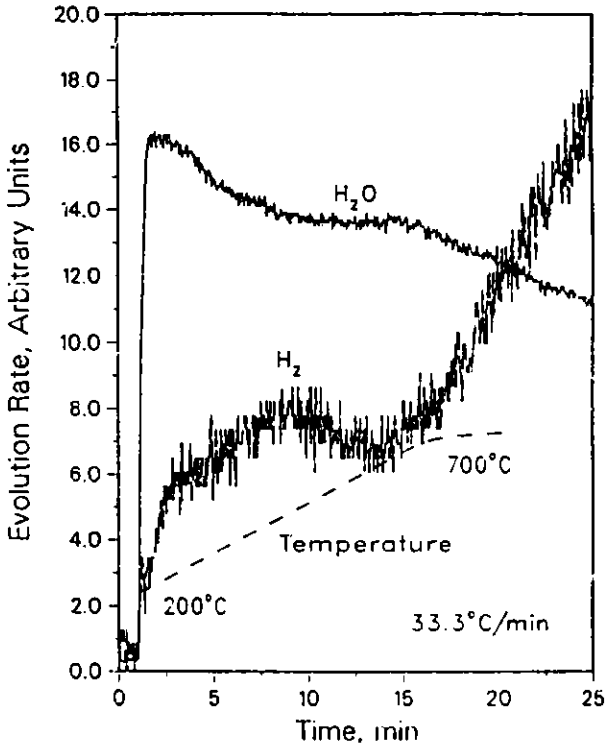

Fig. I-8.

Temperature Programmed Reaction Spectrum of Stainless Steel Sample Tube for a Step Change from Pure Helium to He-H_2O-H_2 Mixture and a Temperature Ramp from 200 to 700°C

increasing temperature, the consumption of H_2O and the dissolution and production of H_2 proceed in a complex way. In TPD measurements with $LiAlO_2$, these tube-related processes would be superimposed on processes relating to the sample itself. However, by treating the sample tube for a sufficient time with helium containing only H_2O(g) at temperatures up to 400°C, "featureless" TPD spectra (i.e., no desorption peaks) for temperature ramps of 200 to 600°C were obtained. This result indicates that the sample tube can be stabilized so that it will not affect the release gases.

2. Measurements on $LiAlO_2$

Initial TPD measurements on $LiAlO_2$ reflected the large amount of water borne by the ceramic material from its earlier exposure to air. The TPD spectrum also revealed the reaction between evolved H_2O and the fresh steel surface that had not yet stabilized. After further drying of the sample (for 2 days at 200°C in pure helium), the TPD data for a 200 to 700°C ramp showed that little H_2O is evolved below 600°C, and that no reaction with the steel is evident from the H_2 trace. However, substantial H_2O is released on approaching 700°C and, also, substantial H_2 is formed. In subsequent runs, only peaks in the lower temperature region (200 to 500°C) were used for evaluation of the desorption process.

Figure I-9 shows a TPD spectrum for $LiAlO_2$ equilibrated with 200 ppm H_2O(g) at 200°C. The peak was analyzed using the width of the peak at half-peak height to calculate a desorption activation energy. The equation is

$$E_d/RT_p = 2[-1 + (1 + 3.11\ T_p^2\ /W_{1/2}^2)^{1/2}] \qquad (I\text{-}2)$$

where T_p is the temperature at maximum rate of H_2O evolution, E_d is the activation energy of desorption, and $W_{1/2}$ is the width at half-peak height.[24] The calculated activation energy (15 kcal/mol, 63 kJ/mol) was of a magnitude consistent with weak chemisorption.

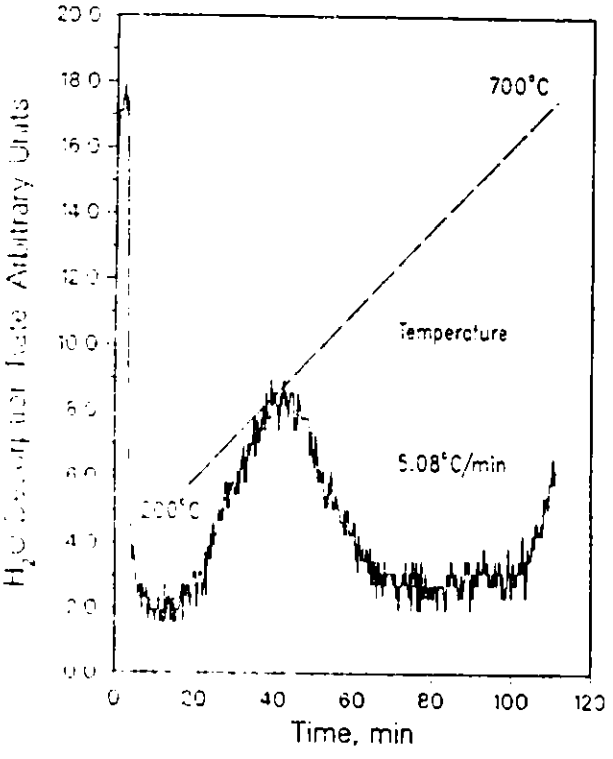

Fig. I-9.

Temperature Programmed Desorption Spectrum for $LiAlO_2$ Sample Equilibrated at 200°C (473 K) with Helium Containing 200 vppm H_2O(g) at 1 atm. Temperature ramp is 200 to 700°C (473 to 973 K) at rate of 5.08 deg/min.

In TPD runs where samples were equilibrated at 300°C with 200 ppm H_2O, the spectra peaks, though sharp, showed evidence of being composites of two or more smaller ones. Such overlap of peaks was also possible for samples equilibrated at 400°C. However, in this case, if one assumed that the peak represented a single phenomenon, the calculated desorption activation energy approximated that reported by Kudo for the decomposition of LiOH [meaning $H_2O(g)$ evolution].[25] In Kudo's case, the decomposing LiOH produced a surface of Li_2O with scattered OH^- groups, so that the fraction of surface covered by OH^-, θ, steadily decreased from 1. In the present work, the initial θ was roughly 0.05 (estimated from our earlier adsorption isotherm data). It appears reasonable to explore further the hypothesis that, considering this apparent similarity with Li_2O, some sites on $LiAlO_2$ resemble sites on Li_2O in their H_2O-evolving behavior. Only one TPD spectrum has been recorded so far for a sample equilibrated at 500°C with 200 ppm H_2O. Though the TPD peak was not well defined, the width analysis suggested a desorption activity energy significantly higher than the ones previously calculated.

3. Future Work

Work on activation energies of desorption of $H_2O(g)$ from $LiAlO_2$ will be completed by examining TPD spectra at lower temperature ramp rates and lower initial coverages. This will allow us to resolve peaks appearing below about 600°C. For the peaks at higher temperatures, stabilization of the steel at these temperatures will be necessary. We will then measure the desorption kinetics of H_2, paying attention to the interactions of H_2 with the tubing material. The other candidate materials for a tritium breeder (Li_2O, Li_4SiO_4, and Li_2ZrO_3) will also need to be characterized in terms of the desorptive behavior of H_2O and H_2.

D. Modeling of Tritium Behavior in Ceramic Breeder Materials

(J. P. Kopasz and J. Kwasny*)

1. Analysis of Results from Tritium Release Experiments

In a continuing collaboration with the Canadians, we have been involved in analyzing data from CRITIC, an experimental study of tritium release from Li_2O breeder material.[26] Of particular interest is the tritium release at low temperatures. For temperature decreases to final temperatures below 450°C, the tritium release appeared to reach a plateau below the steady-state release. Initially, this plateau was believed to have resulted from some instrumental problem, possibly a change in the sensitivity of the proportional counter at different temperatures or gas compositions. However, the data from the proportional counters and from the tritium collected in the glycol traps both indicated that release was below steady-state values for substantial periods of time. After considering many possible instrumental or measurement errors, we arrived at the hypothesis that the plateau region is caused by the precipitation of a second phase of LiOT in the Li_2O.

Hydrogen solubility in Li_2O has been observed to follow the relation

$$\log X_{LiOH} = (0.495 + 13.4/T)\log P_{H_2O}(\text{atm}) + (1.238 - 3738/T) \qquad \text{(I-3)}$$

from 973 to 1273 K.[27] Using this relationship and the equations describing the partial pressure of water over diphasic Li_2O-LiOH found by Tetenbaum and Johnson,[28] one can estimate a maximum tritium concentration in the solid or a maximum vapor pressure of water above the solid before second-phase

---

*Institute for Reactor Materials, Nuclear Research Centers, Julich, Federal Republic of Germany.

formation begins. The water partial pressure at which precipitation is expected to occur is 294 vppm at 400°C but only 46.4 vppm at 350°C. In the CRITIC experiment, the water vapor pressure was measured to be as high as 842 vppm (due to a leaking capsule condition).[26] This result suggested that, at least in this condition, a second-phase LiOH/LiOT forms in the CRITIC experiment. The moisture concentration in the solid which leads to second-phase formation was estimated to be 0.7 ppm at 400°C and 0.01 ppm at 300°C. Inventory calculations for Li_2O have shown the inventory at 400°C to be above this solubility limit. This result suggests that second-phase formation should also occur in other tritium release experiments at low temperature. Indeed, similar release curves were also observed for some tests on Li_2O in the MOZART experiment.

The MOZART experiment is an in-pile tritium release experiment[29] similar to the CRITIC and TRIO experiments. There appears to be some inconsistency between the reported results of the MOZART experiment and our calculations of tritium inventory based on thermodynamic considerations. The calculations suggest that tritium inventory at temperatures below about 400-450°C increases rapidly due to the formation of a second phase of LiOT. For the MOZART experiment, Briec et al.[29] report that the inventory at 300°C is associated with one-day production, and that no drastic increase in inventory occurred with decreasing temperature near 400°C. This apparent disagreement has given us cause to review the calculations and the data from the MOZART experiment.

To study second-phase formation of LiOT, we analyzed the tritium release curves for MOZART experiments with He + 0.1% H_2 as the purge gas. Our analysis indicated that the experimental data reported contain residence times calculated where steady state was not reached after a temperature decrease. The release reached a plateau below steady-state release for temperature-decrease experiments, where the final temperature was below 400°C. For temperature-decrease experiments where the final temperature was above 400°C, steady-state release was attained. Residence times calculated from experiments where steady state is not attained are not a good indication of the tritium inventory in the sample.

The residence time is dependent on the mechanism of tritium release. For diffusion-controlled release, the residence time is the time to regain 66% of the change in release, while for desorption-controlled release, the residence time is the time to regain 62% of the change. Since we are dealing with diffusion and desorption, we chose a value of 65% for regaining the change in release. For a temperature decrease, the tritium release decreases to a minimum, then rises back to steady state. The inventory change associated with a temperature decrease is the difference between the observed tritium release curve and the tritium generation curve (steady-state release). To calculate an inventory from a residence time, one assumes that the release continues toward steady state along the same curve that it followed to get to the 65% recovery point. However, for the MOZART experiment at temperatures below 400°C, the release curves reach a plateau near to, but do not reach, steady state. The inventory calculated from the residence time will then be less than the true inventory, as illustrated in Fig. I-10 for a temperature decrease from 400 to 350°C. The solid line in the figure represents the curve that the release would be expected to follow if it returned to steady state. The open circles represent the observed release. The shaded area represents the difference between the true inventory and that calculated from the residence time. As can be deduced from the figure, the inventory calculated from the residence time greatly underestimates the true inventory (overestimates tritium release). This suggests that residence times should not be calculated for experiments which do not reach steady state, since the residence time will lead to a calculated inventory which may be much less than the true inventory. The inventory at 300°C in the MOZART experiment appears to have been calculated from the residence times. Since the release curves at 300°C reached a plateau below the steady state, these inventories are underestimated.

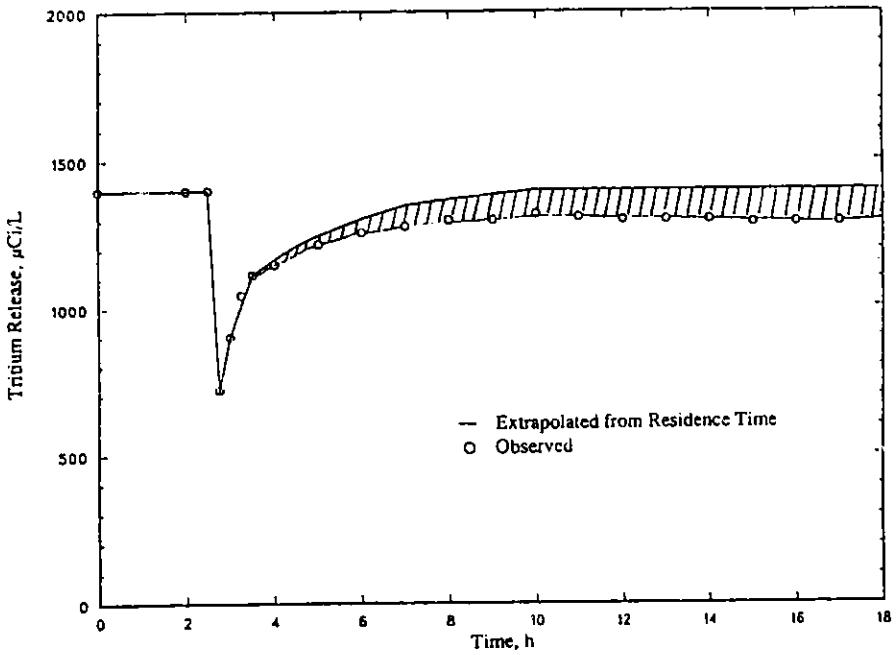

Fig. I-10. Observed and Calculated Tritium Release vs. Residence Time in MOZART Li_2O Experiment (400-350 °C)

In an effort to learn more about the tritium release processes from the MOZART experiment, we plotted the time to regain 65% of the change in release from steady state versus the inverse temperature (Fig. I-11). The 65% value is taken as a reference point below the plateau region for the release peaks that were analyzed. The activation energy for the portion of the curve below the LiOH melting point (471 °C) is 27.8 kcal/mol (116 kJ/mol). This is in fair agreement with the activation energy for desorption observed by Bertone,[30] 28.5 kcal/mol (119 kJ/mol), and the activation energy that we calculated from Tetenbaum's data[28] for the equilibrium water pressure above a two-phase system of LiOH-Li_2O, 30.7 kcal/mol (129 kJ/mol). This result suggests that in the MOZART experiment, tritium release at low temperatures (below 471 °C) may be controlled by the partial pressure of HTO above diphasic LiOT-Li_2O.

The tritium pressures corresponding to the non-steady-state plateau regions observed in the MOZART and CRITIC experiments were calculated and compared to the equilibrium pressure above a diphasic Li_2O-LiOH system calculated from Tetenbaum's data.[28] The results are shown in Fig. I-12. As can be seen from the figure, pressures from the plateau regions reached in the MOZART and CRITIC experiments do not correspond to the pressures calculated from the Tetenbaum data. In addition, the temperature dependence of the experimental pressures is significantly different from that calculated for the diphasic system. The curve for Tetenbaum's data shows a break in the equilibrium pressure above the diphasic system occurring at the LiOH melting point, with the slope corresponding to 30.7 kcal/mol (129 kJ/mol) below the melting point and 20.2 kcal/mol (85 kJ/mol) above the melting point. The curves for the experimental pressures show no break at the LiOH melting point and have slopes corresponding to 3.3 kcal/mol (14 kJ/mol) for the CRITIC experiment and 5 kcal/mol (20 kJ/mol) for the MOZART experiment. The lack of a break at the LiOH melting point and the large difference between the activation energies calculated from these experiments and those for the diphasic system indicate that the tritium pressure above Li_2O in the plateau regions is not determined by the Li_2O-LiOT equilibrium.

Further analysis of the MOZART and CRITIC data shows what may be a slight dependence of the tritium pressure in the plateau regions on the hydrogen pressure in the purge gas. In the Li_2O MOZART experiment, the apparent activation energy increases from 2.3 to 3.3 kcal/mol (10 to 14 kJ/mol)

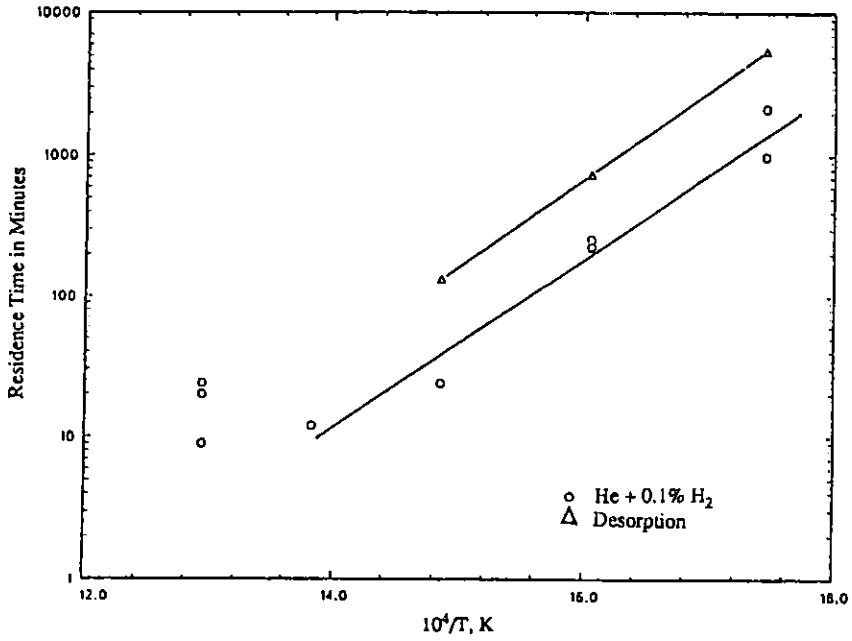

Fig. I-11. Residence Time as Function of Inverse Temperature in MOZART Li_2O Experiment

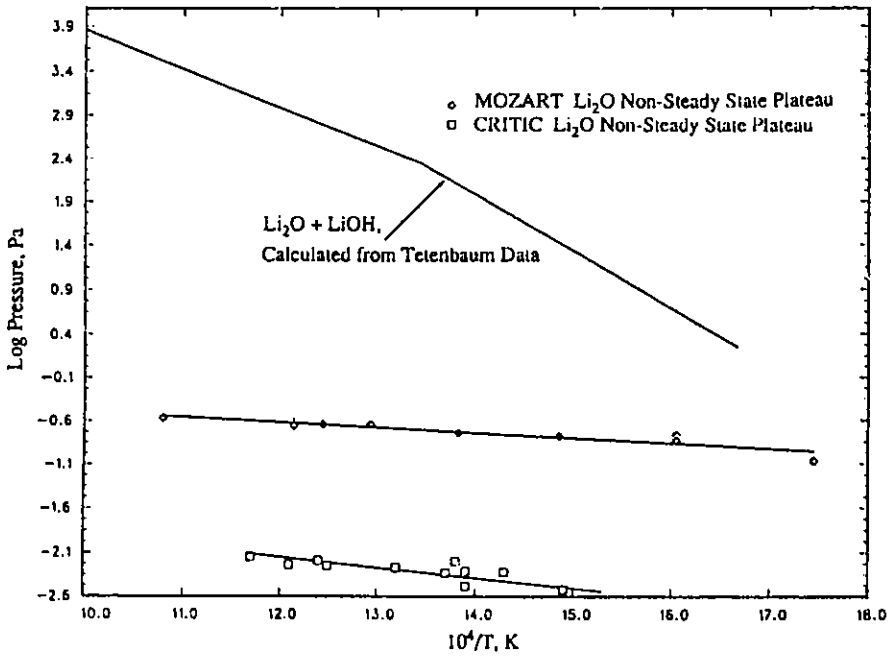

Fig. I-12. Tritium/Hydrogen Pressure vs. Inverse Temperature for CRITIC and MOZART Experiments

when the hydrogen concentration of the purge gas is increased from 0.01 to 0.1% (see Fig. I-13). In the CRITIC experiment, the activation energy decreased from 5.8 to 5.0 kcal/mol (24 to 21 kJ/mol) when the H_2 content of the purge gas was increased from 0.01 to 0.1% (see Fig. I-14). Due to the larger scatter in the CRITIC data, however, the change in activation energy in this case is believed to be insignificant.

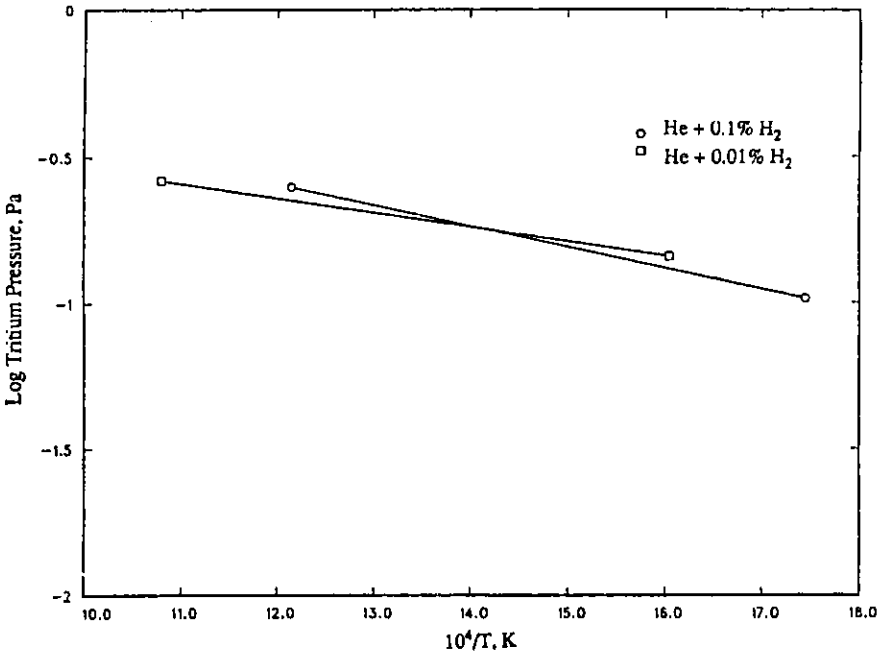

Fig. I-13. Tritium Pressure as Function of Inverse Temperature and Hydrogen in Helium Purge Gas for MOZART Li_2O Experiment

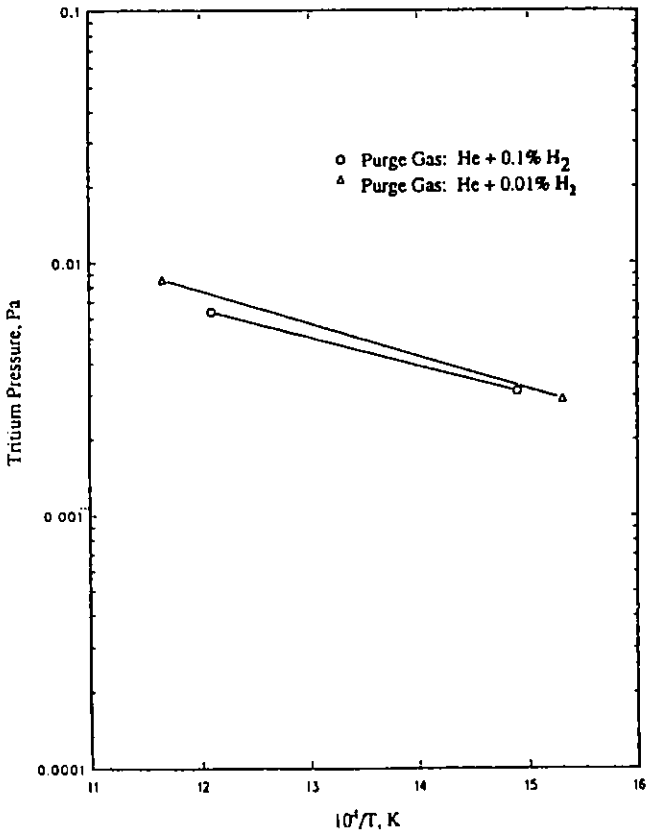

Fig. I-14.

Tritium Pressure as Function of Inverse Temperature and Hydrogen in Helium Purge Gas for CRITIC Li_2O Experiment

Analysis of the MOZART data for other irradiated samples ($LiAlO_2$ and Li_2ZrO_3) also showed a similar temperature dependence of the tritium pressure in the non-steady-state plateau regions. For the two lithium zirconate samples (grain sizes: 1 x 10^{-4} cm and bimodal 2-4 x 10^{-4} cm and 20 x 10^{-4} cm), there was little difference in the tritium pressure. The apparent activation energies were 1.4 and 2.2 kcal/mol (5.9 and 9.2 kJ/mol), respectively. For the three $LiAlO_2$ samples (S1, S2, and S5), there were significant differences in the tritium pressures in the plateau regions. The largest differences were between samples S1 and S2. These samples were made from the same material, with sample S1 being irradiated at higher temperatures than S2. The apparent activation energies were also slightly dependent on the purge gas composition, the activation energy decreasing with increasing hydrogen content. The apparent activation energies were as follows: He + 0.01% H_2 gas, 2.15 kcal/mol (9.01 kJ/mol) for S1 and 15.4 kcal/mol (64.52 kJ/mol) for S2; He + 0.10% H_2 gas, 1.60 kcal/mol (6.70 kJ/mol) for S1 and 12.27 kcal/mol (51.41 kJ/mol) for S2.

Currently, we are unable to explain the reason for the difference in apparent activation energies between these two samples. The third aluminate sample (S5) had a larger grain size and higher density than those for samples S1 and S2. The sample was irradiated in the same upper temperature region as used for S1. The apparent activation energies were 9.7 kcal/mol (41 kJ/mol) for He + 0.01% H_2 purge gas and 4.7 kcal/mol (20 kJ/mol) for He + 0.10% H_2 purge gas. Comparison of sample S1 and S5 data suggests a dependence of the plateau-region tritium pressure on either grain size or porosity.

The above data suggest that a much less activated process is controlling the tritium release in the plateau regions. This process must result in some type of "trapping" of tritium to account for the observed tritium release being below the steady-state release. Possible "trapping" mechanisms are trapping in helium bubbles, trapping in interconnected closed pores, chemical trapping, and dissolution/permeation of tritium into lines of the experimental apparatus. These trapping mechanisms are being investigated as possible causes of the plateau regions.

Determining the effect of hydrogen concentration in the purge gas on tritium behavior may help identify the controlling mechanism in the plateau region. The MOZART data suggest that hydrogen may affect different breeder materials differently. For Li_2O, increasing the hydrogen concentration led to a slight increase in the apparent activation energy of the process controlling the plateau level, while only changing the tritium pressure slightly (see Fig. I-14). For $LiAlO_2$, increasing the hydrogen content decreased the apparent activation energy but increased the corresponding tritium pressure. If the apparent trends observed for changes in the hydrogen concentrations in the purge gas are correct (i.e., an increase in hydrogen content decreases activation energy for Li_2O, but increases activation energy for $LiAlO_2$), then a gas-phase diffusion process cannot be rate controlling. This appears to rule out gas-phase percolation and trapping in interconnected porosity. The other trapping mechanisms are being investigated, with attention being given to the expected dependence on hydrogen in the purge gas.

2. Modeling of Tritium Inventory during Pulsed Operation

To assist the breeder blanket design effort, we calculated the tritium inventory for a lithium oxide blanket operated in the pulsed mode. Pulsed operation is planned for the International Thermonuclear Experimental Reactor (ITER). In this mode, the tritium inventory may build up beyond that for steady-state operation. Our calculations were simplified by focusing on an isothermal region of the blanket. The temperature profile during the burn portion of the pulsed operation is given by the equation:

$$T = T_{min} + (T_{max} - T_{min})\{1 - \exp[-0.01522(t - t_o)]\} \qquad (I\text{-}4)$$

where T = temperature at time t
T_{min} = minimum temperature
T_{max} = maximum temperature
t = time of current pulse
t_o = starting time of the current pulse

After the burn portion of the cycle, a dwell time of 100 s between burns is expected. Thermohydraulic calculations[31] indicated that the minimum temperature was reached very soon after the burn ended, and that the blanket was at the minimum temperature for almost all of the dwell time. Initial calculations have also indicated that at the minimum temperature (119 °C) the tritium transport is so slow that the inventory changes negligibly during the dwell periods. As a result, all additional calculations assumed no release of tritium during the dwell time.

The first set of calculations was performed for a burn time of 1000 s, a dwell time of 200 s, a minimum temperature of 119 °C, and a maximum temperature of 402 °C. A graph of inventory as a function of time for these conditions is shown in Fig. I-15, where the y-axis values represent the fraction of inventory for steady-state operation at 402 °C. The figure indicates that the inventory increases during the first cycle. At the beginning of the second cycle, while the temperature is near the minimum, the inventory increases sharply. As the temperature increases, the inventory decreases until the inventory reaches a minimum at the end of the cycle. At the start of the third cycle, the inventory again increases sharply, then decreases as the temperature increases. For the first several cycles, the inventory at corresponding times increases with each cycle (e.g., the inventory at the end of cycle 3 is greater than it is at the end of cycle 2). After seven cycles, the inventory at the end of the cycle is 103% of the steady-state inventory at 402 °C. The inventory at the beginning of the seventh cycle is about 175% of the steady-state inventory. After about 20 cycles, the inventory at the end of the cycle is equal to the steady-state inventory.

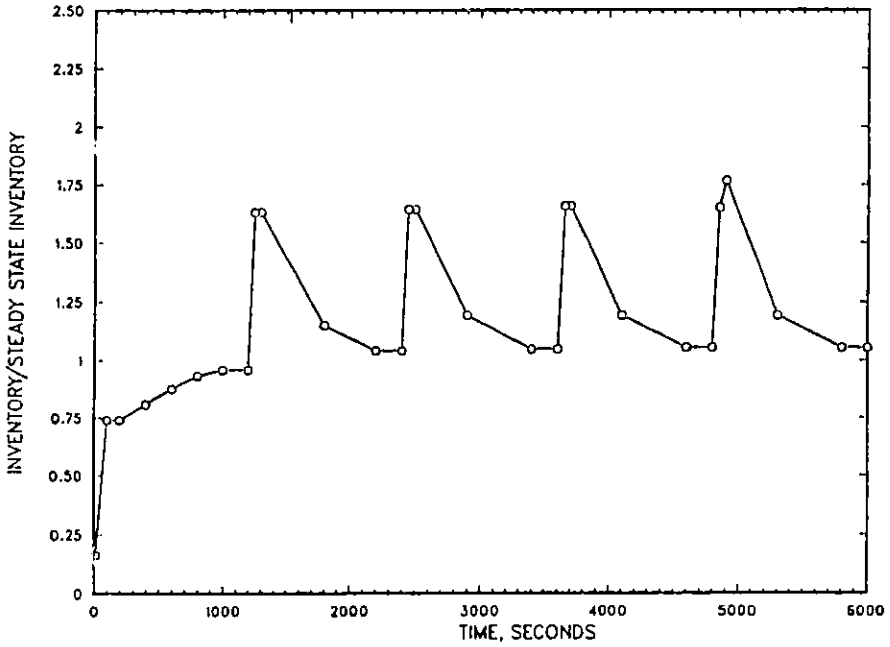

Fig. I-15. Inventory for Steady-State Operation at 402 °C as Function of Time

A second set of calculations was performed for an isothermal section of blanket with a maximum temperature of 452°C and a minimum temperature of 119°C. The burn time was 1000 s. The calculated results are shown in Fig. I-16, which shows that the inventory is within 1% of the steady-state inventory at the end of 5 cycles and reaches the steady-state inventory after only 12 cycles. However, the inventory at the beginning of each cycle is now about 250% of the steady-state inventory. When analyzing these results, one must keep in mind that the steady-state inventory at 450°C is about one-third smaller than that at 400°C. In addition, the absolute inventory at the start of a cycle at 450°C is less than the steady-state inventory at 400°C.

In conclusion, these calculations suggest that, for the proposed ITER thermal cycling and tritium generation rates, the tritium release will reach a periodic cycle, with the release at the end of a pulse being equal to the steady-state release after a reasonable number of pulses (12 pulses for 450°C, about 20 pulses for 400°C).

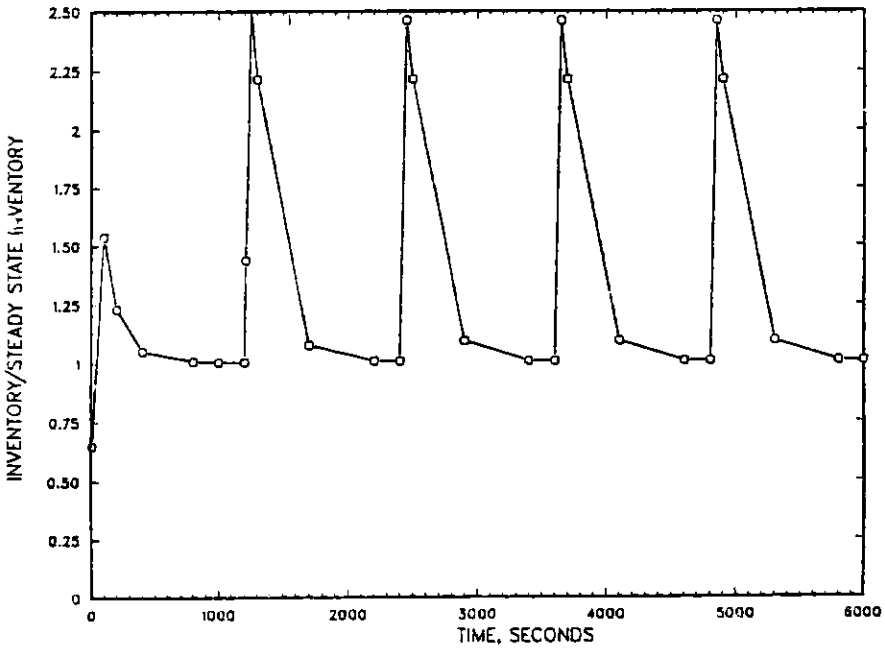

Fig. I-16. Inventory for Steady State at 452°C as Function of Time

3. Methods for Increasing Tritium Release

Modeling of tritium release has led us to the conclusion that tritium diffuses as a triton-lithium vacancy complex in the candidate breeder material Li_2O. It appears likely that a triton-lithium vacancy complex would also be the mobile species in the other candidate oxide ceramic breeder materials. If this is the case, tritium diffusion in these materials might be increased by doping them to increase the lithium vacancy concentration and thereby increase the carrier concentration. Calculations on the effect of doping $LiAlO_2$ to increase the lithium vacancy concentration are underway.

In lithium aluminate, lithium is the most mobile of the three ions. Ionic conductivity data[32] and NMR data[33] indicate an activation energy for lithium diffusion in the extrinsic region of about 18 kcal/mol (75 kJ/mol). Konishi and Ohno interpret their conductivity data as having a break in the conductivity vs. inverse temperature plot at 763°C.[32] The region from 763°C to 1000°C has an

activation energy of 29 kcal/mol (121 kJ/mol). The interpretation is that this represents the intrinsic lithium diffusion activation energy. The intrinsic activation energy is the sum of the lithium migration energy and the energy needed to form a lithium vacancy, i.e.,

$$H_{intrinsic} = H_{migration} + 1/2\ H_{Frenkel} \qquad (I\text{-}5)$$

This expression leads to a calculated enthalpy for formation of a Frenkel defect in $LiAlO_2$ of 21.798 kcal/mol (91.333 kJ/mol). Using this value, we estimated the mole fraction of defects present in $LiAlO_2$ at the melting point to be on the order of 8×10^{-2}. This value is much too high (a reasonable number of defects at the melting point is 1×10^{-4}), suggesting that the Frenkel defect formation energy is too low and that the conductivity observed between 760 and 1000°C is not in the intrinsic regime. Some support for this view is gained by looking at other oxide materials with melting points in the same general range as $LiAlO_2$ (see Table I-7). Of particular interest are Al_2O_3 and Li_2O.

For alumina the energy of formation of a cation Frenkel defect has been reported as 120 kcal/mol[34] (503 kJ/mol). For lithium oxide, a Frenkel defect energy of 69.6 kcal/mol (271 kJ/mol) can be calculated from the lithium diffusion data of Oishi et al.,[35] while Chadwick et al.[36] arrive at an estimate of 58 kcal/mol (243 kJ/mol) based on their ionic conductivity data. [Reports by Konishi and Ohno[32] give an activation energy for lithium conductivity in Li_2O in the intrinsic region of 29.8 kcal/mol (125 kJ/mol) leading to an $H_{Frenkel}$ of 32 kcal/mol (134 kJ/mol) and a molar ratio of 1.6×10^{-2} defects at the melting point.] Owing to the similarity in chemical composition and structure of $LiAlO_2$ to Al_2O_3 and Li_2O, one would expect that the cation defect formation energy for $LiAlO_2$ would be comparable to that for alumina or lithium oxide.

Calculations for tritium diffusion via a triton/lithium vacancy complex in $LiAlO_2$ were performed using a Frenkel defect formation energy of 58.15 kcal/mol (244 kJ/mol), in agreement with literature values for Li_2O,[35,36] and a lithium migration energy of 18.164 kcal/mol (76.107 kJ/mol). The latter was derived from NMR and ionic conductivity data for $LiAlO_2$. For these energies, the diffusion would be in the extrinsic region at the temperatures of interest (300-400°C). Doping the lithium aluminate would increase the diffusivity in this region by increasing the carrier concentration. Our calculations showed that, upon increasing the number of lithium vacancies by doping from 1×10^{-5} to 1×10^{-4} at 300°C, the proportion of tritium in the more mobile form (lithium vacancy-triton complex) increases from 7% to 38%, increasing the effective carrier concentration and diffusivity by a factor of five.

Table I-7. Melting Points and Enthalpy of Formation for a Frenkel Defect in Selected Oxides

Compound	Melting Point, °C	$H_{Frenkel}$ kcal/mol	$H_{Frenkel}$ kJ/mol	Ref.
Li_2O	>1700	58-69.6	243-271	35,36
Al_2O_3	2072	120	503	34
MgO	2852	149.4	626	37
$LiAlO_2$	1900-2000			

E. Tritium Mass Transport in Ceramic Breeder Materials
(P. E. Blackburn)

Lithium ceramics such as Li_2O are being investigated for use as tritium breeding materials, where the lithium in the breeder material is converted to tritium after reacting with a neutron. The tritium is characteristically released from the solid as T_2O and HTO. Within the solid, tritium may also be found as LiOT, which may transport lithium (and tritium) to cooler parts of the blanket. This process may cause loss of lithium from the blanket, blocking of flow paths, and increase of the tritium inventory. Laboratory studies have established the LiOH(g) pressure for reaction of Li_2O(s) with water vapor.[38] The pressure of LiOT and HTO or T_2O above Li_2O is essentially the same as that for reactions involving hydrogen. The purpose of this work is to investigate the transport of LiOH (in place of LiOT) from the blanket material.

Noda[39] has measured the transport of LiOH from Li_2O with 500 vppm water vapor at 970 and 1015 °C and helium purge gas velocities from 6 to 1200 cm/s (flow rates from 0.1 to 20 L/min). In these experiments, the purge gas passed through a bed of 5-mm dia Li_2O spheres packed in a cylinder 2 cm in diameter and 10 cm high. At 1015 °C the concentration of LiOH in the emerging helium varied between 2.6×10^{-4} and 1.3×10^{-4} atm at velocities between 12 and 1200 cm/s. Noda's data show a nearly constant LiOH pressure over a wide variation in purge stream velocity.

We assembled a fixed bed system to obtain high gas velocities and good contact between the gas and the lithium oxide. In this arrangement, a silver tube within a quartz furnace tube was used to hold seven cylindrical Li_2O pellets (8 mm long by 5.3 mm diameter) in a close-packed configuration. A platinum sieve on the downstream end was used to hold the pellets in place. For calculational purposes, the space through which the gas flows was divided into three different regions: (1) a single region bounded by two concentric silver cylinders, (2) six triangular regions bounded by Li_2O on two sides and by a silver cylinder on a third side, and (3) six small triangular regions bounded by Li_2O on all three sides. The quartz-tube assembly was placed in a clam shell furnace with two chromel-alumel thermocouples (one to control the furnace temperature and one to measure temperature). Helium flowed through two rotometers, one through a water saturator and the other directly from the high purity tank helium. The two helium streams were mixed and flowed into the silver-lined quartz tube containing the lithium oxide pellets. Needle valves on the rotometers were adjusted to reduce the water content to 5×10^{-4} atm. The gas flow from each rotometer was measured with bubble-o-meters to assure accuracy in the flow rates. Total flow rates as high as 7000 cm^3/min (STP) allowed us to reach gas velocities as high as 2600 cm/s at 850 °C. The exhaust end of the furnace tube was connected to a flask containing water to trap lithium hydroxide which might have been swept out of the furnace tube.

The experimental measurements consisted of adjusting the gas flow through the furnace, heating to 850 °C, and holding the temperature for times ranging from 40 to 300 min followed by cooling to room temperature. The Li_2O pellets were positioned 3.17 cm (1.25 in.) upstream from the center of the furnace. It was assumed that condensation of LiOH would begin 3.17 cm (1.25 in.) downstream from the center of the furnace on the inside of the silver tube (46-cm long, 2-cm dia). After cooling, the silver tube was removed from the quartz tube and placed in a glass tube which was mounted vertically with the downstream end at the bottom. About 80 mL of water was added through the bottom of the water tube. (The water was added to a 100 mL volumetric flask along with 20 mL of 1N HCl to produce the 0.2N HCl solution required for chemical analysis.) The pellets inside the silver sheet and platinum sieve were wedged in place to fix their position. The silver tube was soaked in water for times varying from one hour to three days.

The pressure of LiOH was calculated from the lithium analysis and the ideal gas law,

$$P(LiOH) = nRT/V \qquad (I-6)$$

where n is the number of moles of lithium transported per minute, R is the gas constant, T is the absolute room temperature, and V is the volume flow of helium per minute (STP) corrected for the fraction of helium gas (55.9%) flowing over the Li_2O. The data are summarized in Table I-8.

The gas velocity was calculated from the total volume (column 4 in Table I-8) and the total effective areas of the three regions. For this calculation, effective diameters were computed from

$$d_{eff} = 4A/P_w \qquad (I-7)$$

where d_{eff} is the effective diameter, A is the geometric area, and P_w is the area perimeter. The effective area is

$$A_{eff} = \pi d_{eff}^2/4 \qquad (I-8)$$

The total effective area was determined to be 0.1655 cm^2. The water pressures (column 6 in Table I-8) were determined from the water saturator temperature and relative concentrations of dry and wet helium and were used to normalize the LiOH pressures to water pressures of 500 ppm. The logarithm of the normalized LiOH pressure is given in column 7, Table I-8.

An attempt was made to correlate a decrease in the pressure of LiOH with an increase of flow velocity (assuming that the process is diffusion controlled). In the case of LiOH gas production from water vapor and lithium oxide, there is a two-step process: water vapor diffuses from the flowing helium to the lithium oxide, then lithium hydroxide gas is formed and diffuses into the flowing helium. Each of these two steps is diffusion controlled. We assumed that the two processes, occurring simultaneously, can be calculated from the product of the fractional saturation of each process.

The fractional saturation of each process may be calculated from tables and equations of Darken.[40] The fractional saturation is given as a function of Dt/L^2, where D is the diffusivity of LiOH or H_2O gas in helium, t is the time in seconds, and L is the half-thickness of the gas volume flowing past the lithium oxide. To estimate L, we used the square root of the product of the diameter of the geometric area and the effective diameter. The diffusivities of LiOH and H_2O gas in helium were estimated from the equation[41]:

$$D_{AB} = \frac{(0.00107 - 0.000246\sqrt{1/M_A + 1/M_B})T^{1.5}\sqrt{1/M_A + 1/M_B}}{P_t(r_{AB})^2[f(kT/e_{AB})]} \qquad (I-9)$$

where D_{AB} is the diffusivity of LiOH (or H_2O) in helium, M_A and M_B are molecular weights of LiOH (or H_2O) and helium, T is absolute temperature, P_t is total pressure, r_{AB} is molecular separation at collision, $f(kT/e_{AB})$ is a collision function given graphically in Ref. 41.

Table I-8. Calculated Results for LiOH Pressure from Transpiration Measurements

Run	Time, min	Weight Lithium, μg	Tot. Vol., cm^3/min (STP)	Velocity, cm/sec	$P(H_2O)$, atm	-log P(LiOH),[a] atm
3	44	45	132	50.2	0.00115	4.49
4	308	112	139	52.7	0.000836	4.89
5	185	226	252	95.7	0.00147	4.79
6	40	109	4728	1794	0.000597	5.47
8	161	137	196	74.4	0.000843	4.68
9	207	95	179	67.9	0.000824	4.90
10	76	64	793	301	0.000469	5.16
11	198	250	1570	596	0.000541	5.31
12	182	208	3509	1332	0.000438	5.66
13	60	79	6900	2618	0.000451	5.90

[a]Water pressure was normalized to 5×10^{-4} atm.

The time for the reaction was calculated from the gas velocity in Table I-8 divided into the length of the Li_2O cylinders (8 mm) for our experiments and the length of Noda's pebble bed (>10 cm) for his experiments. The average length traveled in the pebble bed is assumed to be 20 cm. We were unable to calculate the length without knowing the number of spheres in the cylinder.

Darken gives formulas for calculating the fractional saturation of slabs, cylinders, and spheres for short times and long times.[40] As stated earlier, our experiments have three different regions. The single region bounded by silver cylinders does not involve Li_2O and only concerns the calculation of gas velocity and the volume of gas flowing in the other two regions. This leaves the six large triangular regions (bounded on two sides by Li_2O and by silver on a third side) and six small triangular regions (bounded by Li_2O on all three sides). The small triangular regions, accounting for 15% of the total gas containing LiOH, were grouped together with the large triangular regions, accounting for the rest of the LiOH. We chose to treat the large triangular regions as slabs and assumed that L is twice the half-thickness of the slab with a value of 0.191 cm. Doubling the slab thickness is necessary because the long side of this region is silver. The short-time equation for fractional saturation is

$$F = 1.128 \frac{\sqrt{Dt}}{L} \qquad \text{(I-10)}$$

The fractional saturation equation for long times is

$$F = 1 - \exp^{-\left[\frac{\frac{Dt}{L^2} + 0.0851}{0.933}\right]} \qquad \text{(I-11)}$$

At 850°C (1123 K) the diffusivities (D) calculated with Eq. I-9 are 6.22 and 6.98 cm^2/s for LiOH and H_2O, respectively. The residence times are given in Table I-9. Fractional saturations for LiOH and H_2O are calculated with Eq. I-10 for $t < 5$ ms and Eq. I-11 for $t > 5$ ms. These fractional saturations apply to a single-step process. The two-step process is assumed to be the product

$$F_{prod} = F_{H_2O} \cdot F_{LiOH} \qquad \text{(I-12)}$$

Values for the product are given in column 6 of Table I-9. These calculated fractional saturations may be compared to the measured saturation (P_{LiOH}/P°) in column 5. The measured saturation is plotted against the calculated saturation in Fig. I-17.

Table I-9. Calculation of LiOH Fractional Saturation for Our Experiments[a]

Flow Rate cm^3/min (STP)	Flow Rate cm^3/s (at 850°C)	Velocity, cm/s	Residence Time, s	P_{LiOH}/P°	Fract. Sat.	Log P/P°	Log Fract. Sat.
132	8.3	50.2	0.016	1.90	0.999	0.278	-0.0006
139	8.7	52.7	0.0152	0.75	0.998	-0.123	-0.0009
252	15.8	95.7	0.0084	1.05	0.961	0.020	-0.017
4728	297	1794	0.00045	0.20	0.103	-0.706	-0.987
196	12.3	74.4	0.0107	1.24	0.986	0.092	-0.006
179	11.2	67.9	0.0118	0.74	0.991	-0.131	-0.004
793	49.8	301	0.0027	0.41	0.612	-0.390	-0.213
1570	98.6	596	0.0013	0.29	0.309	-0.542	-0.510
3509	220	1332	0.00060	0.13	0.138	-0.887	-0.859
6900	433	2618	0.00031	0.074	0.070	-1.128	-1.154

[a] T = 850°C, $D_{LiOH} = 6.22\ cm^2/s$, $D_{H_2O} = 6.98\ cm^2/s$, L = 0.19 cm.

Fractional saturated data were derived from Noda's paper[39] to calculate the degree of LiOH gas saturation when helium and 500 ppm water flow through a cylinder packed with 5-mm dia spheres of Li_2O. The cylinder was 2 cm in diameter and 10 cm high. These data are summarized in Table I-10. The pressure of LiOH measured by Noda divided by that calculated from Tetenbaum and Johnson data[38] is plotted against the calculated fractional saturation in Fig. I-17. The residence time, calculated from the height of the reactor cylinder divided by the gas velocity, is a minimum value. Longer times will increase the fractional saturation.

Our measurements covered flow velocities from 50 to 2600 cm/s at 850°C and water pressures of 500 ppm. The data at low velocities produced degrees of saturation in general agreement with the Noda data for comparable residence times for helium gas in the reaction chamber. Noda's chamber was 10 cm high, compared to 8 mm for the present experiments. If the chambers were equal in other respects, the gas velocity in Noda's chamber would need to be 12.5 times that in our chamber for the same residence time. Since short Li_2O cylinders (8 mm in length) were used in our experiments, we were able to achieve short residence times with substantial undersaturation at the highest flow rates. The other dimension, thickness of the slab in which diffusion occurs, was estimated to be similar for these two experiments. There is reasonable agreement between the measured and calculated saturation, as shown in Fig. I-17. Noda's measurements and our calculation of his data, plotted in Fig. I-17, agree that the helium in his experiment was fully saturated with LiOH gas.

This work established conditions for calculating LiOH undersaturation in helium as a function of the dimensions of the Li_2O purge channels and the velocity of the purge gas. We proposed that fractional saturation of two-step reactions which are interdependent can be treated as the product of each fractional saturation in which each process is diffusion controlled. Comparison of our experimentally measured fractional saturation agreed with the calculated fractional saturation within experimental uncertainties. The model for this calculation will allow us to predict the degree of saturation for various flow rates and channel dimensions.

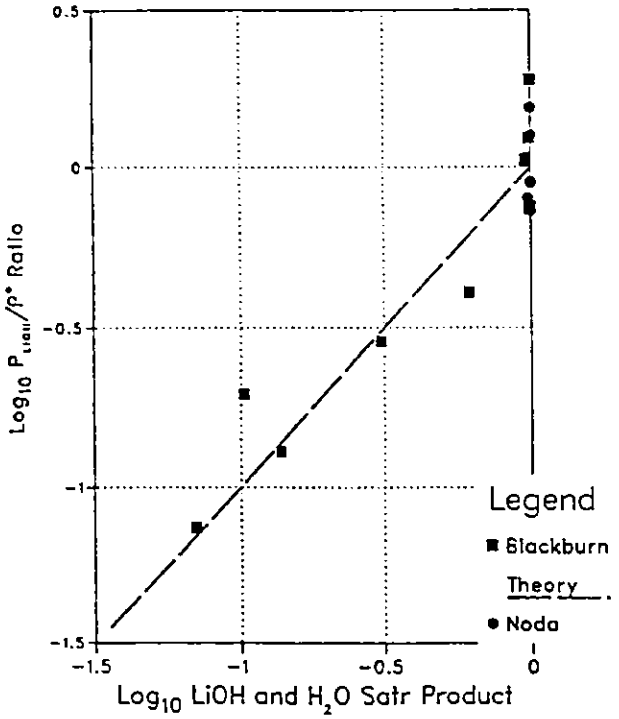

Fig. I-17.

Calculated vs. Measured LiOH Saturation

Table I-10. Calculation of LiOH Fractional Saturation from Noda's Data[a]

Flow Rate							
cm^3/min (STP)	cm^3/s (at 850°C)	Velocity, cm/s	Residence Time, s	P_{LiOH}/P^o	Fract. Sat.	Log P/P^o	Log Fract. Sat.
200	14.4	12	1.567	1.57	1.0	0.196	0.0
1000	72	60	0.333	1.33	1.0	0.124	0.0
2500	180	150	0.133	1.01	1.0	0.004	0.0
5000	360	300	0.0667	1.01	1.0	0.004	0.0
10000	720	600	0.0333	0.80	1.0	-0.097	0.0
20000	1440	1200	0.0167	0.86	0.9994	-0.065	-0.0003

[a] T = 850°C, D_{LiOH} = 7.79 cm^2/s, D_{H_2O} = 8.79 cm^2/s, L = 0.2 cm.

F. Interaction of Hydrogen with Li_2O Surfaces
(S.-W. Tam)

Both in-reactor and out-of-reactor experiments on solid ceramic breeders have indicated that substantial increase of tritium release rates occurs when a small amount of H_2 (~0.1%) is added to a helium purge gas stream. It is expected that surface processes play a major role in this effect. Despite its significant impact on tritium inventory in ceramic breeders, the interaction of hydrogen with lithium ceramic surfaces is still poorly understood. Only from such an understanding can one construct realistic models for the tritium release/inventory which have the reliability and predictive capability that are necessary for use in fusion reactor design. This effort is complementary to both the tritium release modeling effort and the experimental investigation on the $H_2/H_2O/LiAlO_2$ system (Sec. I.C and D).

The interaction of H_2 with lithium ceramic surfaces is expected to involve charge transfer and quasi-chemical bond formation. An accurate description of these processes requires a quantum

mechanical approach. We have utilized the so-called Extended Huckel (EH) method combined with a quantum chemical cluster approach to the analysis of the H_2/Li_2O (110) surface.[42,43] The candidate breeder Li_2O was chosen because it is a prime candidate for ITER and has been ranked highly in various breeder evaluation studies.[44] The tools that we have developed could, of course, be used to analyze other lithium ceramic breeders.

The EH method is based on the following considerations. A cluster of atoms (in our case, Li and O) is arranged in the correct crystalline positions so that it simulates approximately the (110) surface of Li_2O. In actual simulations, the numbers of atoms included are necessarily finite. We have tested the effect of cluster size and found a cluster size of the order of 60-70 atoms to be adequate. This size represents two layers of the (110) surface with a lateral extent, as illustrated in Fig. I-18. This type of cluster approach is extremely useful irrespective of the particular approach (EH in our case) one uses to calculate the electronic structure and properties. The philosophy behind the EH method is similar to that of the tight-binding method (TB) in solid-state problems. The only difference is that, instead of dealing with an infinite or semi-finite system, one is adapting the EH to deal with a finite but large cluster of atoms. One then represents a cluster state $|\Psi\rangle$ for the cluster in terms of atomic-like orbitals $|\phi_i\rangle$ and scalar coefficients a_i as follows:

$$|\Psi\rangle = \sum_i a_i |\phi_i\rangle \qquad \text{(I-13)}$$

A variational calculation leads to the following secular equation:

$$\det | H_{ij} - E S_{ij} | = 0 \qquad \text{(I-14)}$$

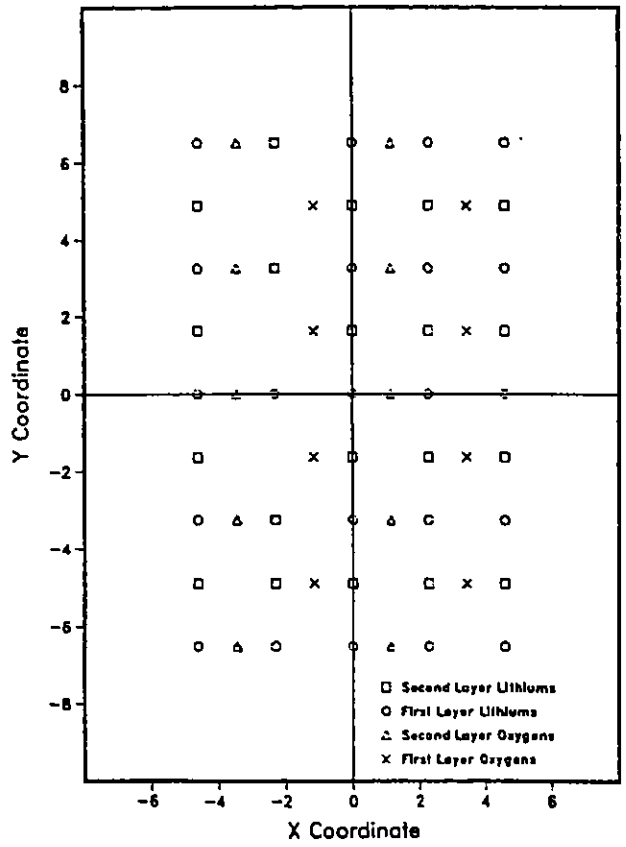

Fig. I-18.

Overhead View of Two Layers on the (110) Surface of Li_2O

Here H_{ij} is the coulomb integral for i=j and the resonance integral for i≠j, E is the energy for the particular cluster state (or molecular orbital), and S_{ij} is the so-called overlap integral. These integrals can be evaluated explicitly within EH for Slater type orbitals (STO) utilized for the ϕ_i; STOs are atomic-like orbitals with parameters adjusted to give the best results for isolated atoms.[45] The total energy of the system is then calculated by filling up the cluster with available electrons in pairs. The semiempirical nature of EH offers a good compromise between accuracy and flexibility. This method provides good estimates of trends in behavior and properties of a system in a wide variety of configurations.

In the present study, we utilized EH to analyze the interaction of H_2 with the (110) surface in several different geometries. The sites of interest include those midway between the nearest neighbor O-O (site A), O-Li (site B), and Li-Li (site C). In each of those configurations, the H_2 was allowed to approach the site from above. The total energy of the system is then calculated within EH as a function of h, the vertical distance between the hydrogen molecule, and the surface site in question. The axis of the hydrogen molecule is maintained parallel to the solid surface. Since the present analysis is concerned with non-dissociative adsorption, the separation between the hydrogen atoms is maintained at the normal interatomic distance of 0.746 Å. The issue of dissociative adsorption will be addressed in the next stage of our work.

Figure I-19 shows the result over site A, the mid-point between two nearest neighbor oxygen atoms. The interaction is practically zero when h is of the order 5-6 Å. It shows a minimum around 1.75-2 Å with a depth of about 0.3 eV. Further decrease in h results in a rapidly rising repulsive barrier. This implies that at site A, H_2 can be adsorbed by a non-dissociative mechanism from the gas phase without a very strong binding energy. Figures I-20 and -21 show the H_2 interaction with respect to Li-O (site B) and Li-Li site (C). Like Fig. I-19, these figures both show similarly shallow wells. The minimum of the potential well at site B occurs at h = 2.2 Å with a depth of about 0.22 eV. The corresponding minimum at site C takes place at h=2 Å with a depth of about 0.21 eV.

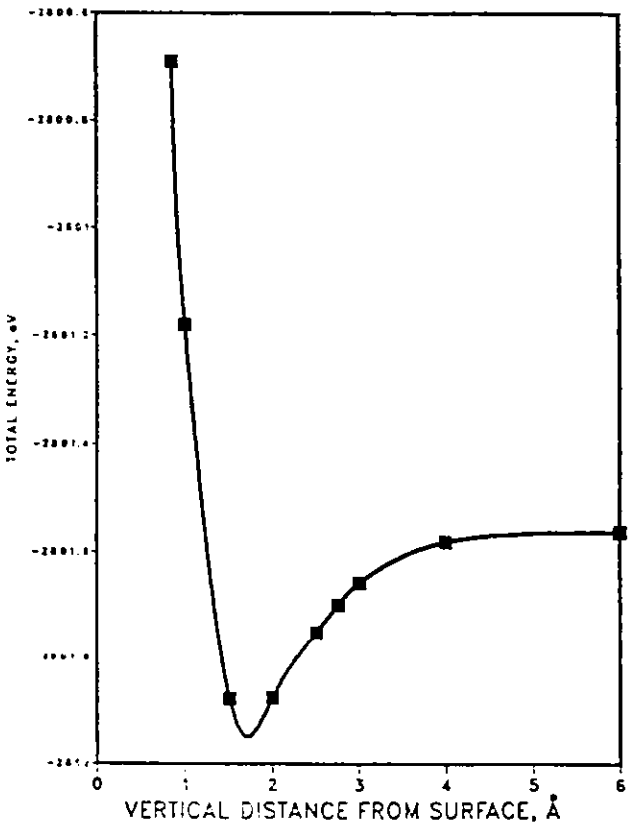

Fig. I-19.

Hydrogen Interaction with Li_2O (110) Surface at Site A (mid-point between two nearest neighbor oxygen atoms)

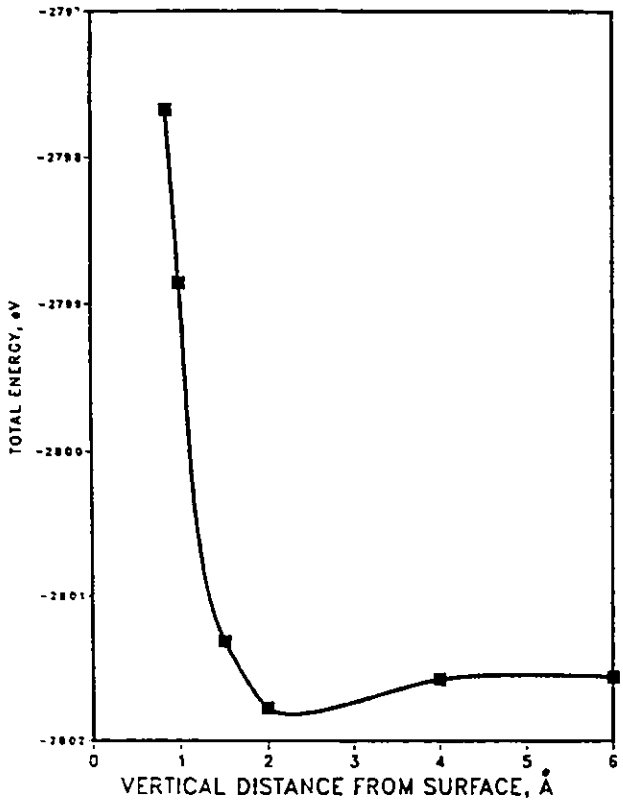

Fig. I-20.

Hydrogen Interaction with Li_2O (110) Surface at Site B (mid-point between nearest neighbor oxygen and lithium atoms)

Fig. I-21.

Hydrogen Interaction with Li_2O (110) Surface at Site C (mid-point between two nearest neighbor lithium atoms)

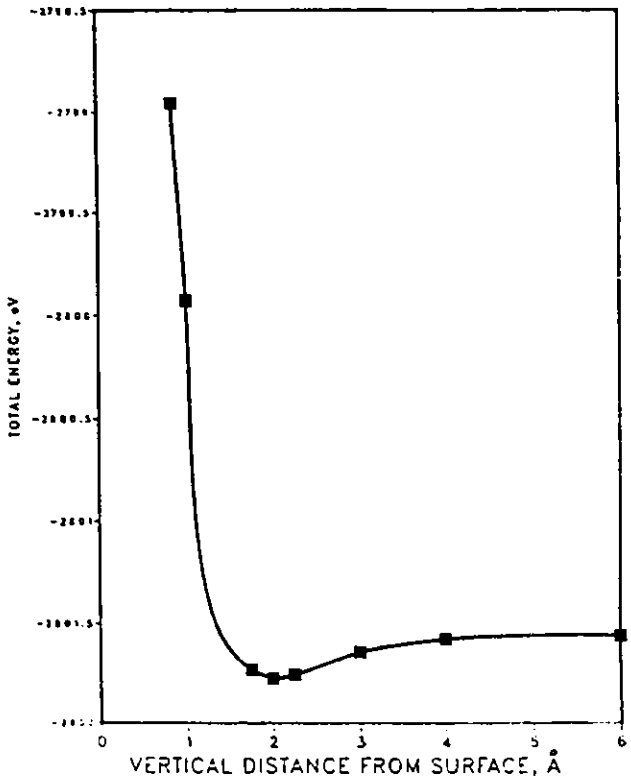

All three sites bind a hydrogen molecule with a binding energy of around 0.2-0.3 eV at a height of around 2 Å. Although the present analysis has concentrated on molecular adsorption, the choice of the adsorption sites reflects an interest in dissociative chemisorption. It is conceivable that these sites may represent precursor sites from which further (and stronger) dissociative chemisorption processes may originate. Confirmation of these hypotheses will require more detailed analysis of dissociative chemisorption and surface migration barriers.

G. Blanket Design Studies

(P. A. Finn and D.-K. Sze)

The International Thermonuclear Experimental Reactor (ITER) is an international project whose purpose is to produce a conceptual design of a tokamak reactor which can be used to test components for a prototype power reactor. Designs of each of the reactor systems are being generated in the U.S., the U.S.S.R., Japan, and the European Community. One of the most important systems for ITER is the blanket in which tritium is bred for fuel. Several different blanket designs, each with a different type of lithium-containing material, have been proposed. One blanket system has to be chosen; therefore, the technical advantages and disadvantages of each of these blankets have to be examined, problems evaluated, and a ranking established. The two candidate breeder blankets being evaluated in the U.S. program are an aqueous lithium salt blanket and a ceramic breeder blanket. Our design work on these two blanket types is summarized below.

1. Aqueous Salt Blanket

For the aqueous salt blanket, we previously quantified the effects of radiolysis, electrolytic decomposition, and steel and/or beryllium corrosion within the salt solution and also generated a conceptual design of the components in the tritium processing system. In the report period, we prepared a design of the processing system for the U.S. ITER aqueous salt blanket design and provided it to the staff at the Tritium Systems Test Assembly (TSTA), the designated coordinator of the U.S. tritium systems design for ITER. This information was incorporated into a total tritium systems design for ITER, i.e., the plasma exhaust processing systems plus the blanket streams.

The salt, water, and molecular hydrogen flow paths for the tritium processing system and the blanket are shown in Fig. I-22. As a point of reference, let us start at the blanket (left-hand side of figure). The salt solution leaves the blanket and is passed to a combination recombiner/depressurizer unit to recombine the radiolysis products and reduce the pressure from 15 atm to 1 atm (1.5 MPa to 0.1 MPa). The salt solution is then passed to a flash evaporator to remove the salt from the water stream from which tritium will be extracted. The liquid phase remaining is a concentrated salt solution, containing radioactive corrosion products. This salt solution is passed through ion exchangers and a filter to remove the corrosion products. The purified solution enters a salt mixer in which nontritiated water is added to dilute the salt solution before it passes to the heat exchanger. After the heat exchanger, the salt solution is again pressurized and reenters the blanket.

The vapor from the flash evaporator is condensed (Condenser No. 1); the water is purified by ion exchange columns which remove ionic species carried from the flash evaporator. The purified water is then passed to a water distillation unit in which the tritium content in the water is increased from 3.7×10^{11} Bq/L to 3.7×10^{13} Bq/L. The concentrated tritiated water is passed to a vapor phase catalytic exchange unit (VPCE) in which the tritium in the water is exchanged with the protium in a hydrogen gas stream. Since this exchange process is not as favorable in this direction, the tritiated hydrogen stream is not as concentrated as was the input tritiated water stream. To remove the tritium from the molecular hydrogen stream, a cryogenic distillation unit is needed. Prior to this unit, the gas is dried to remove

entrained water and passed through molecular sieve beds to remove other impurities. The species leaving the cryogenic distillation unit are molecular tritium and molecular hydrogen. The tritium is transferred to the fueling system; the protium is recycled to the VPCE unit. The entrained water is returned to the water distillation unit.

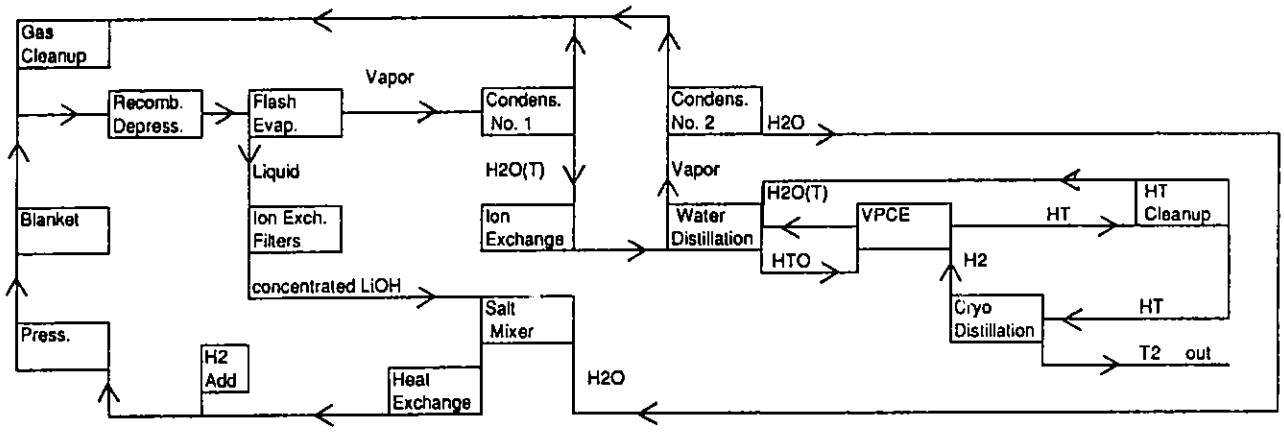

Fig. I-22. Flowsheet for Tritium Recovery System with Aqueous Salt Solution Blanket

The total throughput for this system was calculated to be 45 g/day tritium, 1.5 kg/day deuterium, and 320 kg/day protium (water distillation factor = 100, cryogenic distillation factor = 1000). The tritium bred in a 880 MW fusion reactor in which the breeding ratio is one would be approximately 150 g/day. Only 30% of this tritium would be collected (45 g/day) because the reactor is expected to be operated for less than 30% of the year. Thus, if the tritiated water concentration is allowed to rise while the reactor is operational (i.e., acting as a storage medium for the unprocessed tritium), and if this processing system is operated >95% of the time, then this system is sized correctly. However, if the processing system is required to collect 150 g/day tritium, then the VPCE unit would have to have three times the protium throughput (970 vs. 320 kg/day) since its efficiency is directly proportional to the protium flow. In addition, the cryogenic unit would have to have three times the refrigerant capacity. No further design studies of the aqueous salt blanket are planned.

2. Ceramic Solid Breeder Blanket

For the ceramic breeder blanket, the effects of radiolysis and electrolytic decomposition were examined for the borated water shield and water coolant.

a. Borated Water Shield

The effects of radiolysis and electrolytic decomposition were determined for a solid breeder blanket shield containing a 0.25 M borated water solution. The reaction between a neutron and boron-10 produces alpha recoils with an energy (E) of 2.79 MeV. The reaction rate (RR) is calculated to be 0.1045 of the neutron flux (F). This rate includes a small contribution from the neutron reaction with oxygen in water. The total neutron flux for the shield in the U.S. ITER solid breeder design is 3.54 x 10^{20} n/s. Using this information and $G(H_2)$ of 1.65 for radiolysis of water due to alpha particles [where $G(H_2)$ is the number of molecules of hydrogen produced per 100 eV of energy], we calculated that the

amount of hydrogen gas, $A(H_2)$, generated in the boric acid solution is 2.82 mol/s, from the following equation:

$$A(H_2) = \frac{(RR)\ (F)\ (E)\ G(H_2)}{(6 \times 10^{23})\ (100)} \qquad (I\text{-}15)$$

At the same time, a maximum of 1.41 mol/s oxygen is produced. Although some of this oxygen may be in the form of hydrogen peroxide, we assume that all is gaseous oxygen to obtain an upper estimate on the pressure. The hydrogen and oxygen produced from radiolysis must be recombined each time the boric acid passes out of the reactor. This recombination can be accomplished by passing the solution through a hydrophobic catalyst.

For the ceramic oxide blanket, a non-pressurized boric acid shield is desired. The gas pressure produced from radiolysis was calculated to correspond to a hydrogen pressure [$p(H_2)$] of 0.06 MPa. To maintain this pressure, the mass flow rate (MF) of the boric acid solution has to be set at an appropriate value. We calculated this rate to be 4×10^5 mol/s or 7.2 m^3/s, using the H_2 solubility data [$S(H_2)$] in Table I-11 at 40°C and the equation:

$$MF = S(H_2)\ A(H_2)/[p(H_2) \bullet \text{Solub. Corr.}] \qquad (I\text{-}16)$$

The solubility correction for 0.25 M boric acid is also given in Table I-11. Since the volume of the shield solution is ~0.1 m^3, this flow rate corresponds to a residence time of 0.1 s, which is not unreasonable. The associated temperature rise (ΔT) in the solution was also calculated. Since 10-30 MW of the total reactor power (P) will be deposited in the shield, ΔT for the boric acid solution is only 0.3-1°C, as calculated from

$$\Delta T = P/(MF)\ (HT) \qquad (I\text{-}17)$$

where HT is the specific heat.

A salt solution which is circulated in a magnetic field induces a potential gradient (V), the magnitude of which is determined by the product of the magnitude of the field (B), the coolant velocity (v), and the coolant channel length (l). Since the shield's surface area is ~48 m^2, the linear velocity at a flow rate of 7.2 m^3/s is 0.2 m/s. The coolant channel diameter is 0.008 m, which corresponds to the length, l, through which the magnetic field interacts. The magnetic field is 3 T. Using these values, we calculated the potential gradient to be 0.005 V. Since the resistance losses of a 0.25M $B(OH_3)$ solution result in a potential of 7 V at a current density of 1 mA/m^2, the potential gradient from the magnetic field interaction is expected to have no significant effect on corrosion.

b. Water Coolant

For a water coolant, the total gamma and neutron dose in the ITER design is expected to be 1 W/cm^3 for gamma radiation and 3 W/cm^3 for neutron radiation. The measured $G(H_2)$ range is 0.2-0.43 for gamma irradiation of water and 0.7-1.1 for neutron irradiation of water. To obtain an upper limit on expected radiolysis, the higher G values were used in our calculations, which indicated 0.8 mol/s of hydrogen production from water radiolysis for a water volume of 2×10^6 cm^3. The associated oxygen production is 0.4 mol/s; again, all is assumed to be present as molecular oxygen.

To remove 1200 MW of heat (the amount produced from a 880 MW fusion device), the water flow rate must be 4.75 x 10^5 mol/s for a temperature rise of 35 °C. Using the solubility of hydrogen in Table I-11, we calculated a hydrogen pressure of 0.02 MPa. A recombiner is needed to recombine the gases generated, and a system is also needed to continuously add hydrogen to suppress radiolysis. Suppression of radiolysis is desired for the water coolant to minimize stress-corrosion cracking initiated by the presence of oxygen also generated during radiolysis.

Table I-11. Gas Solubility in Water and Borated Water

	20 °C	40 °C
H_2 Solubility in Water, MPa/mol fraction	6850	7634
O_2 Solubility in Water, MPa/mol fraction	3876	5435
Solubility Correction for 0.25M Boric Acid	0.9	0.9
H_2O Vapor Pressure, MPa	0.0023	0.0073

Due to the effects of radiolysis, water in the neutron field will contain ionic species. The potential gradient generated by this fluid moving in a magnetic field is 0.1-0.3 V for the following solid breeder design conditions with water coolant: a coolant linear velocity of 3-4 m/s, magnetic flux density of 3-8 T, and a coolant channel width of 1 cm. Because the ionic species generated in water radiolysis have a short lifetime (10^{-4} s), the ion conductivity is an order of magnitude less than 3 μS/cm, assuming the expected purity is maintained in the recirculated coolant. The resistance losses at 3 μS/cm (2.86 V) are greater than those for the induced potential (0.1-0.3 V). Thus, corrosion caused by electrolytic effects is not expected to be significant for the water coolant.

H. Design of Breeding Blanket Interface

(R. G. Clemmer, P. A. Finn, L. R. Greenwood, and D. -K. Sze)

The Breeding Blanket Interface (BBI) is that system which performs the necessary processing and recycling of the tritium recovered from a fusion reactor blanket. Although considerable attention has been given to studies of tritium breeding and recovery and also to many aspects of tritium processing, very little work had been done on the BBI. Therefore, a study was initiated to define the necessary components of this BBI system and to plan for testing such an integrated system of components in the TSTA. This possible upgrade is the subject of an ongoing study, begun in July 1987, involving Los Alamos National Laboratory (LANL), the Japan Atomic Energy Research Institute (JAERI), and Argonne National Laboratory (ANL).

The first phase involved determining the conditions of the product tritium output streams for various blankets. Blankets investigated included the three major blanket types (liquid metal, solid breeder, and aqueous salt solution). The conditions determined included temperature, flow rate, chemical composition, and concentrations of impurities and radionuclides. We developed a methodology to systematically evaluate impurity source terms and to follow the transport of impurities and radionuclides through the paths of the system to the blanket output stream. We have performed such analysis for the

three blanket types. Results for the liquid metal blanket analysis were reported previously.[46,47] For the solid breeder blanket, a very detailed study of probable impurity levels was performed, and the data were directly used by the U.S. design team for the ITER to calculate blanket activation and afterheat in the ITER blanket. For the aqueous salt solution blanket, our studies uncovered and/or quantified a number of problems such as radiolysis, electrolysis, and corrosion (see Sec. I.G).

We recently completed phase two, preconceptual design of the BBI for two of the blanket types: aqueous salt solution and solid breeder blanket. A summary of the major design features of the two BBI systems is given in Table I-12.

For the reference designs, we prepared a development schedule and estimated costs. Owing to the current budgetary situation, funds are not available to pursue both reference designs. Therefore, current efforts involve studying the available options to identify the best choice at minimum cost. Various methods of reducing the development costs are being evaluated, including the following: (1) concentrate the BBI effort on the solid breeder blanket alone (Li_2O); (2) evaluate various testing scenarios in an effort to minimize the TSTA/BBI budget requirements, yet maintain the stated programmatic goals; (3) evaluate reducing the scope of the testing and/or the possible range of experimental variables; and (4) select (with input from ANL, LANL, and JAERI) the most attractive option and define an experimental program for that option.

Table I-12. Features of BBI Reference Design for Two Blanket Types

	Blanket Type	
	Aqueous Lithium Salt	Solid Breeder
Breeder material	LiOH (aqueous)	Li_2O
Neutron multiplier	Be	Be
Structural material	Stainless Steel (SS)	SS
Coolant	Aqueous Salt Solution	H_2O
Tritium enrichment method	Water distillation	none
Tritium enrichment factor	100	---
Tritium recovery method	VPCE[a]	He purge
Tritium carrier	Aqueous Salt Solution	He + H_2
Tritium concentration in carrier	10 Ci/L(average)	0.1 %
H/T ratio in blanket	2.0×10^5 (average)	100
H/T ratio in BBI inlet	2000	100
Tritium capacity	45 g/day	150 g/day
Scale factor for TSTA/BBI	0.010	1.0
Tritium flow rate for TSTA/BBI	0.45 g/day	150 g/day
Protium flow rate for TSTA/BBI	3000 g/day	5000 g/day

[a]VPCE = Vapor Phase Catalytic Exchange unit.

I. Dosimetry and Damage Analysis
(L. R. Greenwood)

1. Dosimetry Measurements in the Omega West Reactor

Neutron dosimetry measurements and radiation damage calculations were performed for three short irradiations by Battelle Pacific National Laboratory in the Omega West Reactor (OWR) at Los Alamos National Laboratory. The irradiations occurred during February-April 19[illegible] with a maximum

neutron fluence of 8.3×10^{19} n/cm^2. The samples were irradiated in a furnace at 200°C with helium gas cooling. The irradiation histories are given below, where exposure values are full-power (8 MW) hours.

Experiment	Dates	Exposure, FPH
12	2/26 to 2/29/88	13.50
13	3/1 to 3/11/88	60.28
14	3/14 to 4/20/88	132.10

The dosimetry capsules measured about 6 mm long by 1.2 mm OD and contained small wires of Ni, Fe, Ti, 0.1% Co-Al, and 80.2% Mn-Cu. Each wire was gamma counted at ANL and saturated activities were computed, correcting for gamma absorption and the exact irradiation history. The resultant activities are listed in Table I-13 for the three OWR runs. Uncertainties are typically ±2%, including ±1.5% for calibration and less than ±1% for counting statistics. In several cases, uncertainties were unusually large due to a longer than normal decay before we received the samples. As can be seen, the values are in excellent agreement among the three separate runs. Consequently, we averaged the data for one common spectral analysis.

Table I-13. Activation Rates Measured in the Omega West Reactor at 8 MW

	Activities,[a] atom/atom-sec		
Reaction	Run 12	Run 13	Run 14
$^{58}Fe(n,\gamma)^{59}Fe$ ($\times 10^{-11}$)	6.36 (4.1%)	6.05 (4.5%)	6.04 (6.0%)
$^{59}Co(n,\gamma)^{60}Co$ ($\times 10^{-9}$)	2.15	2.00	2.10
$^{54}Fe(n,p)^{54}Mn$ (10^{-12})	3.10	3.14	3.17
$^{58}Ni(n,p)^{58}Co$ ($\times 10^{-12}$)	4.08	4.03	4.07
$^{46}Ti(n,p)^{46}Sc$ ($\times 10^{-13}$)	4.22 (2.4%)	4.21 (2.2%)	4.29 (2.2%)
$^{55}Mn(n,2n)^{54}Mn$ ($\times 10^{-15}$)	9.04 (2.3%)	9.17 (2.2%)	9.14 (2.2%)

[a]Uncertainty is ±2% unless noted in parentheses.

Neutron spectral adjustments were then done with the STAY'SL computer code using the initial spectrum determined previously.[48] The full power flux values and fluences for each experiment are listed in Table I-14. Radiation damage calculations were performed with the SPECTER computer code,[49] and the results are listed in Table I-15.

Table I-14. Neutron Flux and Fluences[a] for the Omega West Reactor at 8 MW

	Flux,	Fluence,[a] 10^{18}n/cm^2		
	10^{13}n/cm^2•s	Run 12	Run 13	Run 14
Thermal (<0.5 eV)	6.89	3.35	14.96	32.78
0.5 eV-0.1 MeV	4.72	2.29	10.23	22.41
0.1-1 MeV	5.79	2.81	12.55	27.50
>1 MeV	2.93	1.42	6.34	13.89
Total	17.40	8.46	37.78	82.78

[a]Uncertainty is ±10%

Table I-15. Radiation Damage Parameters for the Omega West Reactor (dpa x 10^{-3}, He in atom parts per billion)[a]

	Run 12		Run 13		Run 14	
Element	dpa	He	dpa	He	dpa	He
Al	3.62	1.23	16.2	5.49	35.4	12.0
Ti	2.22	1.15	9.91	5.13	21.7	11.3
V	2.49	0.042	11.1	0.19	24.4	0.41
Cr	2.26	0.324	10.1	1.45	22.1	3.17
Fe	2.00	0.569	8.93	2.54	19.6	5.57
Ni	2.11	8.88	9.42	39.7	20.6	86.9
Cu	1.93	0.473	8.62	2.11	18.9	4.63
Nb	1.94	0.109	8.66	0.49	19.0	1.07

[a]The abbreviation dpa = displacements per atom and He = helium production.

2. Radiation Damage for High-Temperature Superconductors

We calculated the production of atomic displacement damage in the new superconducting material $YBa_2Cu_3O_7$, using our new computer code SPECOMP.[50] New damage cross sections and atomic recoil energy distributions were first calculated for the elements barium and yttrium. The results have been added to the SPECTER computer code for routine calculation of damage in any specified neutron spectrum.

To calculate radiation damage in a compound material, it is first necessary to have calculated damage in each of the pure elements which make up the compound. Since barium and yttrium were not available in SPECTER, we used the DISCS computer code[51] to determine the displacement damage and recoil energy distributions for each element. These calculations use the basic neutron cross-section data given in the evaluated neutron data file ENDF/B-V (from National Neutron Cross Section Center, Brookhaven National Laboratory). Each reaction channel is considered separately, including elastic and inelastic scattering, hydrogen and helium production, and multiple (n,xn) reactions. The relative importance of each reaction channel can be seen in Figs. I-23 and -24. At lower energies (e.g., fission reactors), the damage is dominated by elastic and inelastic scattering. For fusion (e.g., 14 MeV), the damage mainly comes from the (n,2n) reaction, with a 5-10% contribution from (n,p) and (n,n') reactions.

We then used the SPECOMP code to compute damage for the superconductor, assuming a displacement energy threshold for each element in the compound of 20 eV. The resultant damage cross section is shown in Fig. I-25. The dotted line shows the result of a simpler approximation, a weighted sum of elemental damage. As can be seen, the true compound damage is 10-20% lower at neutron energies below 1 MeV. By 20 MeV, the true compound damage is 5-10% higher. These results have been added to SPECTER for routine calculations. Users can thus determine the correct dpa in this superconductor by simply giving a neutron spectrum and length of irradiation time. This compound damage file in SPECTER now contains about a dozen entries for tritium breeder materials, insulators, and alloys.

We plan to add more elements and compounds, such as SiC, and to also begin conversion of our files and programs to the newly released neutron cross-section data in ENDF/B-VI.

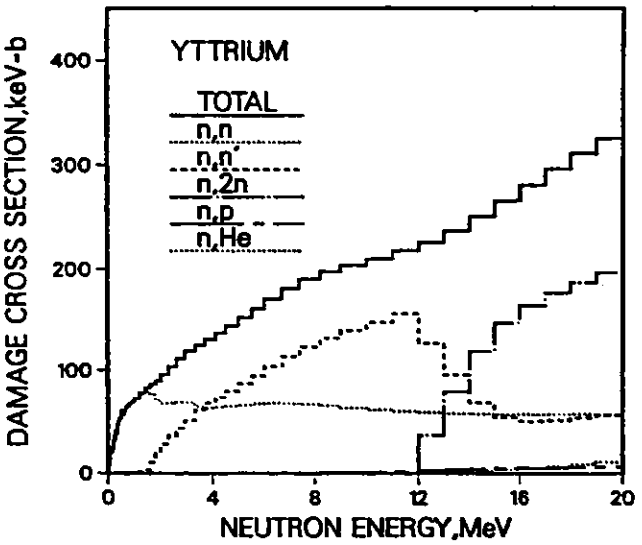

Fig. I-23.

Displacement Damage Cross Section for Yttrium. (The contribution from each reaction channel is shown separately).

Fig. I-24.

Displacement Damage Cross Section for Barium. (The contribution from each reaction channel is shown separately).

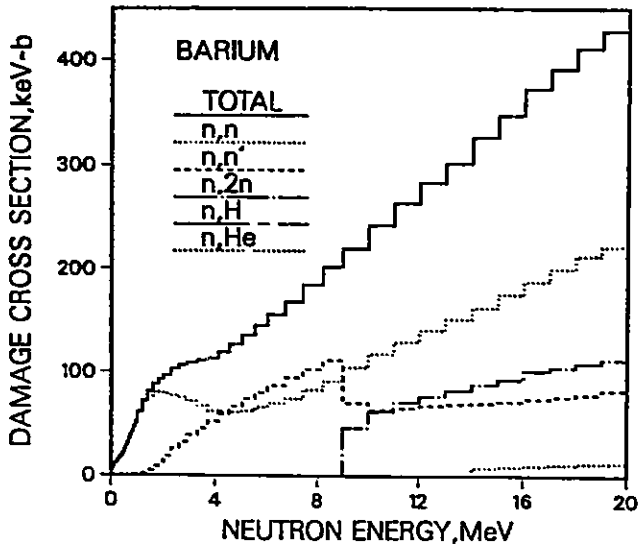

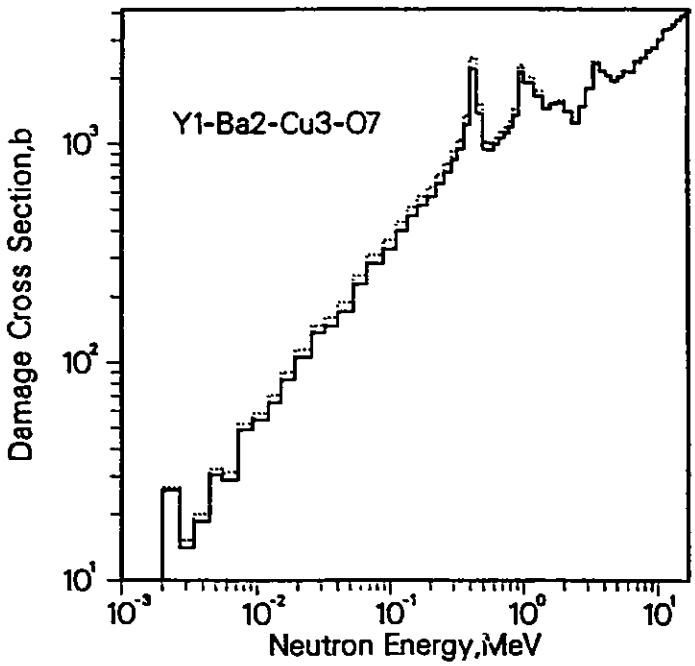

Fig. I-25. Calculated Damage Cross Section for the New Ceramic Superconductor $YBa_2Cu_3O_7$. SPECOMP results (solid line) are compared to the weighed sum of elemental damage (dotted line).

REFERENCES

1. N. C. Rasmussen et al., *Reactor Safety Study*, Nuclear Regulatory Commission Report WASH-1400, NUREG-75/014 (1975).

2. R. Wilson et al., Rev. Mod. Phys. 57, S1 (1985).

3. *Reactor Risk Reference Document (Draft for Comment)*, U. S. Nuclear Regulatory Commission Report NUREG-1150 (1987); *Severe Accident Risks: An Assessment for Five U.S. Nuclear Power Plants (Second Draft for Peer Review)*, U.S. Nuclear Regulatory Commission Report NUREG-1150 (1989).

4. D. A. Powers, J. E. Brockman, and A. W. Shiver, *VANESA: A Mechanistic Model of Radionuclide Release and Aerosol Generation During Core Debris Interactions with Concrete*, U. S. Nuclear Regulatory Commission Report NUREG/CR-4308 (1986).

5. A. T. D. Butland, M. A. Mignanelli, P. E. Potter, and P. N. Smith, "The Vaporization of Chemical Species and the Production of Aerosols during a Core Debris/Concrete Interaction," Proc. Committee on Safety of Nucl. Installations (CSNI) Specialist's Mtg. on Core-Debris Concrete Interactions, Electric Power Research Institute Report EPRI NP-5054-SR pp. 5-33 (1987).

6. D. Cubbiciotti, J. Nucl. Mater. 130, 3 (1985).

7. G. Erikkson, Chemica Scripta. 8, 100 (1975).

8. T. M. Besmann, *SOLGASMIX-PV, A Computer Program to Calculate Equilibrium Relationships in Complex Chemical Systems*, Oak Ridge National Laboratory Report ORNL/TM-5775 (1977).

9. Y. Bottinga and P. Richet, Earth Planet. Sci. Lett. 40, 382 (1978).

10. R. G. Berman and T. H. Brown, "Development of Models for Multicomponent Melts: Analysis of Synthetic Systems," Ch. 11, *Reviews in Minerology*, Vol. 17, *Thermodynamic Modeling of Geological Materials: Minerals, Fluids, and Melts*, Mineralogical Society of America, Washington, DC (1987).

11. Y. Bottinga, D. F. Weill, and P. Richet, "Thermodynamic Modeling of Silicate Melts," Ch. 11, *Advances in Physical Geochemistry*, Vol. 1, *Thermodynamics of Minerals and Melts*, Springer-Verlag, New York (1981).

12. M. F. Roche, J. L. Settle, L. Leibowitz, and C. E. Johnson, *Vaporization of Strontium, Barium, Lanthanum, and Uranium from Mixtures of Urania, Zirconia, Steel, and Concretes at 2150 K and 2400 K*, Electric Power Research Institute Report EPRI NP-6613 (1990).

13. R. S. Roth, T. Negas, and L. P. Cook, *Phase Diagrams for Ceramists*, Vol. IV, American Ceramic Society, Columbus, OH (1981).

14. D. R. O'Boyle and A. E. Dwight "The Uranium-Plutonium-Zirconium Ternary Alloy System," Proc. of Fourth Int. Conf. on Plutonium and Other Actinides, Santa Fe, NM, October 5-9, 1970.

15. L. Leibowitz, R. A. Blomquist, and A. D. Pelton, J. Nucl. Mater. 167, 76 (1989).

16. D. E. Peterson and E. M. Foltyn, Bull. Alloy Phase Diagrams 10, 160 (1989).

17. L. Leibowitz, E. Veleckis, R. A. Blomquist, and A. D. Pelton, J. Nucl. Mater. 154, 145 (1988).

18. F. L. Oetting, M. H. Rand, and R. J. Ackermann, *The Chemical Thermodynamics of Actinide Elements and Compounds*, Part I, *The Actinide Elements*, International Atomic Energy Agency, Vienna (1976).

19. T. B. Massalski, *Binary Alloy Phase Diagrams*, American Society for Metals, Metals Park, Ohio (1986).

20. P. Gordon and A. R. Kaufmann, Trans. AIME 188, 182 (1950).

21. J. D. Grogan, J. Inst. Metals 77, 571 (1950).

22. G. G. Michaud, Can. Metal. Q. 5, 355 (1966).

23. A. K. Fischer and C. E. Johnson, J. Nucl. Mat. 155-157, 466 (1988).

24. J. L. Falconer and J. A. Schwarz, Catal. Rev. Sci. Eng. 25, 141 (1983).

25. H. Kudo, J. Nucl. Mater. 87, 185 (1979).

26. J. M. Miller, R. A. Verrall, D. S. MacDonald and S. R. Bokwa," The CRITIC-1 Irradiation of Li_2O--Tritium Release and Measurement," presented at Third Topical Meeting on Tritium Technology in Fission, Fusion and Isotopic Applications, Toronto, Canada, May 1-6, 1988.

27. M. Tetenbaum, A. K. Fischer, and C. E. Johnson, Fusion Tech. 7, 53 (1985).

28. M. Tetenbaum and C. E. Johnson, J. Nucl. Mater. 126, 25 (1984).

29. M. Briec, J. J. Abassin, C. E. Johnson, M. Masson, N. Roux, and H. Watanabe, "The MOZART Experiment, Ju-Pile Tritium Extraction from Li_2O, $LiAlO_2$, and Li_2ZrO_3", Proceedings, 15th Symposium on Fusion Technology, Utrecht, The Netherlands, Sept. 1988.

30. P. Bertone, J. Nucl. Mater. 151, 281 (1988).

31. M. Billone, Argonne National Laboratory, unpublished results (1988).

32. S. Konishi and H. Ohno, J. Am. Cer. Soc. 67, 4188 (1984).

33. T. Matsuo, H. Ohno, K. Noda, S. Konishi, H. Yoshida, and H. Watanabe, J. Chem. Soc., Faraday Trans. 2, 79 (1983).

34. F. A. Kroger, in *Structure and Properties of MgO and Al_2O_3 Ceramics*, Vol. 10, *Advances in Ceramics*, ed., W. D. Kingery, American Ceramic Society, Columbus, OH, p. 1 (1984).

35. Y. Oishi, Y. Kamei, and M. Akiyama, J. Nucl. Mater. 87, 341 (1979).

36. A. V. Chadwick, K. W. Flack, J. H. Strange, and J. Harding, Solid State Ionics 28-30, 185 (1988).

37. W. C. Mackrodt, in *Structure and Properties of MgO and Al_2O_3 Ceramics*, Vol. 10, *Advances in Ceramics*, American Ceramic Society, Columbus, OH, p. 62 (1984).

38. M. Tetenbaum and C. E. Johnson, J. Nucl. Mater. 120, 213 (1984).

39. K. Noda, "Mass Transfer and Compatibility of Lithium Oxide," presented at ITER Specialist's Meeting on Materials Data Base, August 22-26, 1988, Germany.

40. L. S. Darken and R. W. Gurry, *Physical Chemistry of Metals*, McGraw-Hill, New York p. 447 (1953).

41. R. E. Treybal, *Mass-Transfer Operations*, 2nd Ed., McGraw-Hill, New York, p. 25 (1968).

42. R. Hoffmann, J. Chem. Phys. 39, 1397 (1963).

43. W. A. Harrison, *Electronic Structure of Solids*, W. H. Freeman and Co., New York (1979).

44. D. L. Smith et al., *Blanket Comparison and Selection Study*, Argonne National Laboratory Report ANL/FPP-84-1 (1984).

45. S. P. McGlynn, L. G. Vaquickenborne, M. Kinoshita, and D. G. Carroll, *Introduction to Applied Quantum Chemistry*, Holt, Rinehart, and Winston, New York (1972).

46. R. G. Clemmer, P. A. Finn, L. R. Greenwood, T. L. Grimm, D. K. Sze, J. R. Bartlit, J. L. Anderson, H. Yoshida, and Y. Naruse, *The Requirements for Processing Tritium Recovered from Liquid Lithium Blankets: the Blanket Interface*, Argonne National Laboratory Report ANL/FPP/TM-216 (March 1988).

47. R. G. Clemmer, T. L. Grimm, P. A. Finn, D. K. Sze, L. R. Greenwood, J. R. Bartlit, J. L. Anderson, H. Yoshida, and Y. Naruse, "The Blanket Interface to TSTA: the Requirements for Liquid Lithium Blanket Processing," presented at Third Topical Meeting on Tritium Technology in Fission, Fusion, and Isotopic Applications, May 1-6, 1988, Toronto, Canada.

48. L. R. Greenwood, in *Damage Analysis and Fundamental Studies Quarterly Progress Report*, Department of Energy Report DOE/ER-0046/25, pp. 5-7 (May 1986).

49. L. R. Greenwood and R. K. Smither, *SPECTER: Radiation Damage Calculations for Materials Irradiations*, Argonne National Laboratory Report ANL/FPP-TM-197 (January 1985).

50. L. R. Greenwood, "SPECOMP Calculations of Radiation Damage in Compounds," in *Reactor Dosimetry: Methods, Applications and Standardization*, H. Farrar and E.P. Lippencott, eds., ASTM STP1001, pp. 598-602 (1989).

51. G. R. Odette and D. R. Dorian, Nucl. Technol. 29, 346 (1976).

II. SEPARATION SCIENCE AND TECHNOLOGY
(G. F. Vandegrift)

The Division's work in separation science and technology is mainly concerned with developing a technology base for the TRUEX (TRansUranic EXtraction) solvent extraction process. The TRUEX process extracts, separates, and recovers TRU elements from solutions containing a wide range of nitric acid and nitrate salt concentrations. The extractant found most satisfactory for the TRUEX process is octyl(phenyl)-N,N-diisobutylcarbamoylmethylphosphine oxide, which is abbreviated CMPO. This extractant is combined with tributyl phosphate (TBP) and a diluent to formulate the TRUEX process solvent. The diluent is typically a normal paraffinic hydrocarbon (NPH) or a nonflammable chlorocarbon such as carbon tetrachloride (CCl_4) or tetrachloroethylene (TCE). The TRUEX flowsheet includes a multistage extraction/scrub section that recovers and purifies the TRU elements from the waste stream and multistage strip sections that separate TRU elements from each other and the solvent. Our current work is focused on facilitating the implementation of TRUEX processing of TRU-containing waste and high-level defense waste, where such processing can be of financial and operational advantage to the DOE community.

The major effort in TRUEX technology-base development involves developing a generic data base and modeling capability for the TRUEX process, referred to as the Generic TRUEX Model (GTM). The GTM will be directly useful for site-specific flowsheet development directed to (1) establishing a TRUEX process for specific waste streams, (2) assessing the economic and facility requirements for installing the process, and (3) improving, monitoring, and controlling on-line TRUEX processes. The GTM is composed of three sections that are linked together and executed by HyperCard and Excel software. The heart of the model is the SASSE (Spreadsheet Algorithm for Stagewise Solvent Extraction) code, which calculates multistaged, countercurrent flowsheets based on distribution ratios calculated in the SASPE (Spreadsheet Algorithms for Speciation and Partitioning Equilibria) section. The third section of the GTM, SPACE (Size of Plant and Cost Estimation), estimates the space and cost requirements for installing a specific TRUEX process in a glove box, shielded-cell, or canyon facility. The development of centrifugal contactors for feed- and site-specific applications is also an important part of the effort.

Another project is underway to determine the feasibility of substituting low-enriched uranium for the high-enriched uranium currently used in producing fission-product ^{99}Mo. Technetium-99m, the daughter of ^{99}Mo, is widely used in medical diagnosis.

A. Generic TRUEX Model Development
(J. M. Copple)

1. Model Enhancements

The first-generation GTM for IBM-PC compatibles is complete. Like the already developed GTM for the Macintosh computer, this model has the capability to calculate distribution ratios for the important components of acidic nitrate-based TRU-containing waste and high-level waste streams in TRUEX-process flowsheets for either the TRUEX-TCE or the TRUEX-NPH solvent. All calculations are based on an operating temperature of 25 °C. The GTM also calculates the concentration profile of feed components in flowsheets that are designed by the user and generated by the model.

The Generic TRUEX Model for the IBM-PC consists of the 54 files and one directory listed in Table II-1. Although the model consists of many files, a user only has to open "GTM.XLM", and the rest of the files are automatically opened when needed.

Table II-1. Complete File Listing for the Generic TRUEX Model

GTM_HC.XLM	SASSE_RE.XLM	HELP_C1.XLS
GTM_BANN.XLS	SASSE_FU.XLS	HOLDER.XLS
GTM.XLM	SASSE_PR.XLS	LASTCARD.XLS
GTM_SETU.XLM	SASSE_CO.XLS	OPFOUR.XLS
GTM_DRIV.XLM	SASSE_CH.XLC	OPTION_C.XLS
CARDS.XLW	SASSE_GE.XLM	OX_AC_RE.XLS
RO_CARDS.XLW		OX_TITLE.XLS
	SPACE_TE.XLS	REINIT.XLS
OXAL_DRI.XLM	SPACE_RE.XLM	SASSINFO.XLS
OXAL_MOD.XLM	SPACE_GE.XLM	SCFEMENU.XLS
OXAL_IN.XLS	SPACE_SU.XLS	SEC_CARD.XLS
OXAL_OUT.XLS	HC_EXPOR.XLS	SPACINFO.XLS
OXAL_BAN.XLS		SPSTMENU.XLS
	REPORTS	SP_TITLE.XLS
SSPE_NPH.XLS		SS_T_C.XLS
SSPE_TCE.XLS	ACT_CARD.XLS	STFEMENU.XLS
HET_TCE.XLS	CHRGEBAL.XLS	STREAM_I.XLS
HET_NPH.XLS	DISPFLOW.XLS	S_I_HELP.XLS
C_T_MACR.XLM	FEEDCARD.XLS	TITLE_C.XLS
FITCOEFS.XLM	FULLINFO.XLS	WARNING.XLS

The GTM was created to be used with the IBM-PC and Macintosh computers in a number of different ways. Options that can be accessed through the front end allow one to

- Use all features of the GTM for a specific feed solution.
- Calculate the charge balance, density, ionic strength, and activities (hydrogen, nitrate, and water) of an aqueous feed solution.
- Calculate oxalic acid additions to fission-product-containing waste.
- Calculate TRUEX flowsheets for a specific feed solution.
- Estimate space and costs for user-specified flowsheet.

Using SASSE with user-specified distribution ratios is an option that does not require the front end.

A much improved version of the Generic TRUEX Model is in development. This new version removes some of the limitations found in the first-generation model while also adding new features. One of the major limitations in the first-generation model was its inability to handle solvent loading. The new version will be able to calculate distribution ratios and flowsheets where the concentrations of extractable species are high enough to reduce significantly the concentration of CMPO due to its complexation of these species. Another limitation, the ability to only model centrifugal contactors, will be eliminated with the addition of the ability to handle solvent extraction units of pulsed columns and mixer settlers. With this addition, changes in SPACE will also be made to incorporate the different costs and sizes of the extraction equipment. One important enhancement is that the new versions for both the Macintosh and IBM-PC will consist of nearly identical code.

2. SASSE Development

(R. A. Leonard, J. M. Copple, D. B. Chamberlain, M. C. Regalbuto, and W. B. Seefeldt)

a. Introduction

The electronic worksheet called SASSE has been developed for detailed evaluation of proposed flowsheets in conjunction with information from the generic TRUEX data base. In addition to establishing whether or not each effluent will reach its specified composition, the use of sensitivity analysis with the SASSE worksheet allows one to identify an appropriate strategy for process monitoring and control.

Two Excel macros have been written to support SASSE. The one macro, designated SASSE_generate, generates SASSE worksheets for flowsheet calculations. When used independently of the GTM, the appropriate distribution coefficients or coefficient equations must be supplied by the user. Within the GTM, these coefficients are calculated by SASPE. The other macro, SASSE_report_generator, generates reports from the final SASSE worksheet. The reports include (1) tables for the concentration of the various components in the input and output streams and (2) tabular and graphical reports of the stage-to-stage concentration profile for each component.

The major effort in this report period was to revise the SASSE worksheet so that (1) it will be appropriate when the amount of other-phase carryover is large, that is, greater than 2 to 5%, (2) the residence time of each phase in each stage will be explicit rather than implicit, and (3) the volume of each phase in each stage can be specified. These modifications will be used for modeling pulsed columns and for following time-dependent chemical reactions, interfacial or in either phase. Once the layout for the modified SASSE worksheet is developed and tested, the two SASSE macros will be revised accordingly. It is envisioned that the revised SASSE worksheet can be used for either low or high levels of other-phase carryover. As revised, the worksheet will calculate only steady-state concentration profiles for each component.

b. New SASSE Worksheet

A revised SASSE worksheet has been developed and is being tested. In this worksheet, the user specifies (1) the composition and flow rate of each organic and aqueous feed, (2) the volume of the organic and aqueous phases in each stage, (3) the fraction of aqueous phase in the organic phase (this aqueous fraction applies only to that portion of the organic phase that goes to the next stage), as well as the fraction of organic phase in the aqueous phase (this organic fraction applies only to that portion of the aqueous phase that goes to the next stage) in every stage, and (4) the fraction of organic and aqueous flow leaving a given stage that is taken as an effluent. Based on these user-specified parameters, the revised worksheet calculates the steady-state organic and aqueous flows and residence times in every stage. Using the D values as supplied by the user or as calculated in SASPE, some user-specified information, and the calculated flows, the SASSE worksheet then calculates the organic and aqueous steady-state compositions for every component in every stage.

The advantages of the revised SASSE worksheet are as follows. (1) The user can specify organic and aqueous feeds and effluents at any stage not just at the end stages of each section as was previously the case. This change allows for sampling streams at specific contactor stages in the middle of a section to be included in the model. (2) Large other-phase carryover can be accommodated in any stage. (3) The computer time is greatly reduced because the steady-state flows and the steady-state component concentrations are calculated with a noniterative algorithm.

While testing the revised SASSE worksheet, which allows any amount of other-phase carryover, we found that the number of process stages the worksheet can handle is limited. The limiting factor is the inversion of a 2m matrix (where m is the number of stages) to determine the organic and aqueous flow rates at each stage. Excel 2.2 can invert matrices only if they have no more than 28 rows and columns. Thus, the SASSE worksheet, as currently revised, can be used only if a process has 14 or fewer stages. Since we anticipate processes with up to 30 stages (that is, the worksheet must be able to invert matrices that have 60 rows and columns), we are investigating further revisions to the worksheet. This effort includes (1) writing an Excel macro that will employ a Gauss elimination technique to solve the system of 2m linear equations, (2) developing an algorithm, like the Thomas algorithm, for reducing the 2m linear equations to m linear equations whose coefficients form tridiagonal matrices, (3) developing an iterative solution for flow calculations in the SASSE worksheet, and (4) altering the SASSE worksheet so that the user specifies some additional flow parameters.

The first revision, development of a Gauss elimination macro, has proven to be more complex and cumbersome than anticipated. Thus, work on this method has been set aside. The second revision, the equation reduction, is being explored. If such a reduction is possible, the Thomas algorithm can be used in place of the matrix inversion to solve the equations. This could be done in the SASSE worksheet and should be able to handle 30 process stages easily.

c. Model for Solvent Extraction in Columns

A new model has been developed for analyzing solvent extraction processes carried out in columns.[1] In this model, each column is treated as a series of well-defined equilibrium stages where the backmixing (other-phase carryover) between stages can be large. By including all mass transfer effects between stages in the backmixing value, the same number of stages can be used for all extracted components, no matter what their distribution coefficients. This greatly simplifies the modeling required for multicomponent solvent extraction processes. In particular, the model will allow us to use one SASSE worksheet to model all the components in a solvent extraction process carried out in a column or columns, just as we can now do for staged equipment such as centrifugal contactors and mixer settlers. Results from the new model will be compared with those from two common methods for modeling columns, the Height of an Equivalent Theoretical Stage (HETS) and the Height of a Transfer Unit (HTU).

The current SASSE worksheet, which is limited to 14 process stages, and the data contained in another report[2] are being used to test the pulsed column model. In testing this model, we are looking for a single stage height and a single backmixing (other-phase carryover) fraction that correlates both the cerium extraction and stripping data. These data were obtained in two separate sieve tray columns with different column heights. In the initial model tests, we will use only those data taken at a single pulse intensity in the columns. If a single stage height and a single backmixing (other-phase carryover) fraction can be found, this would give us our first positive indication that the new model for pulsed columns will work. With such a model, the same number of stages can be used for all the components in the SASSE worksheet, even though their distribution ratios differ widely.

B. Density Studies

1. Density Correlation at Elevated Temperatures
(I. R. Tasker)

Densities of aqueous solutions are necessary for the GTM to convert between molar concentration (the scale commonly used to describe feed solutions) and molal composition (the scale upon which most solution physical chemistry is based). One of the improvements required in GTM is an ability to treat changes in density resulting from changes in temperature. A constraint on the method

adopted is that it should be easily formulated into current methods of density calculations. This constraint dictates that we use an equation identical in form to that previously used, now calculating all of the component parts at the new temperature.

In the previous report (ANL-90/16, Sec.II.B), equations and partial data for estimating densities of complex aqueous solutions at elevated temperature were given. The species considered were Ag^+, Am^{3+}, Ba^{2+}, Ca^{2+}, Ce^{3+}, Cm^{3+}, Cs^+, Cu^{2+}, Eu^{3+}, Fe^{3+}, Gd^{3+}, H^+, La^{3+}, Na^+, Nd^{3+}, Ni^{2+}, Pm^{3+}, Pr^{3+}, Rb^+, Sm^{3+}, Sr^+, UO_2^{2+}, Y^{3+}, Cl^-, F^-, HSO_4^-, NO_3^-, and SO_4^{2-}. In the text below, the remaining ions of interest (Al^{3+}, Cr^{3+}, $H_2C_2O_4$, H_3PO_4, Np^{4+}, NpO_2^+, Pd^{2+}, Pu^{3+}, Pu^{4+}, Rh^{3+}, $Ru(NO)^{3+}$, and Zr^{4+}) are considered. As a matter of completeness, the theoretical outline used to treat the data is given below.

For $Cr_{(aq)}^{3+}$, no data are available on volumes as a function of temperature, although a value at 25 °C is available.[3] The temperature dependence was assumed to be the same as that given in the previous report for Fe^{3+}. Hence, the apparent molar volume (V_ϕ°) is estimated as

$$V^\circ_{\phi,Cr^{3+}} = -45.16 + (0.461 \cdot T) - (0.00938 \cdot T^2) \text{ mL/mol} \qquad \text{(II-1)}$$

No volumetric data are available for Al^{3+} as a function of temperature. Good data at 25 °C have recently become available.[4] In the absence of any other information, the temperature behavior of Al^{3+} was assumed to be the same as that given in the previous report for Fe^{3+}. Hence,

$$V^\circ_{\phi,Al^{3+}} = -50.96 + (0.461 \cdot T) - (0.00938 \cdot T^2) \text{ mL/mol} \qquad \text{(II-2)}$$

Millero[3] lists a V_ϕ° value for $H_2C_2O_4$ of 16.0 mL/mol at 25 °C. However, this value was rejected by Chamberlain (CMT Division) since it did not fit experimental data; instead, he calculated a value from experimental data. There are little data available on any oxalate species as a function of temperature. Sohnel[5] lists some data for sodium oxalate. The standard treatment of these data yielded

$$V^\circ_{\phi,C_2O_4^{2-}} = V^\circ_{\phi,H_2C_2O_4} = 23.8 + 0.318 \cdot T - 0.004543 \cdot T^2 \qquad \text{(II-3)}$$

This equation yields a V_ϕ° value of 28.91 mL/mol at 25 °C, in marked disagreement with Chamberlain's value (16.0 mL/mol). In view of the uncertainties involved in the oxalate data, a pragmatic approach was taken: the temperature dependence suggested by the sodium oxalate data was combined with the 25 °C value of Chamberlain to yield

$$V^\circ_{\phi,H_2C_2O_4} = 44.04 + (0.318 \cdot T) - (0.004543 \cdot T^2) \text{ mL/mol} \qquad \text{(II-4)}$$

This equation is not very satisfying, and further work on densities of aqueous oxalate solutions as a function of temperature is recommended.

Apparent molar volumes for H_3PO_4 were calculated from the fit of Sohnel,[5] who used Ref. 6 as a data source. The polynomial used to fit the data is

$$V^{\circ}_{\phi,H_3PO_4} = 42.23 + (0.0579 \cdot T) - (0.0000544 \cdot T^2) \text{ mL/mol} \qquad \text{(II-5)}$$

No data at any temperature are available on aqueous volumes of Np^{4+}. Neptunium IV (Np^{4+}) behaves similarly to U^{4+},[7] yet no data on U^{4+} are available. Numerous correlations were investigated,[8-18] but none was found to apply with any degree of certainty to trivalent ions, let alone quadrivalent ions. Moreover, there is available in the literature only a single estimate, at one temperature, of V°_{ϕ} for a quadrivalent ion (-53.5 mL/mol for Th^{4+}).[3,10] In view of these problems, the following approach was adopted: by examining the variation of V°_{ϕ} with charge, a general trend becomes apparent. For example, the data listed by Millero[3] show that

6 out of 7 M^{+} ions have V°_{ϕ},M^{+} in range -1 to +15 mL/mol
12 out of 14 M^{2+} ions have V°_{ϕ},M^{2+} in range -15 to -25 mL/mol
13 out of 13 M^{3+} ions have V°_{ϕ},M^{3+} in range -39 to -45 mL/mol
1 M^{4+} ion (Th^{4+}) has V°_{ϕ},Th^{4+} of -53.5 mL/mol

Further, examining the coefficients of the temperature variation of metal ions indicates that as the charge increases, the effect of temperature becomes slightly less important. Thus, we decided to entirely ignore the effect of temperature on V°_{ϕ} for aqueous metal species in the 4+ state and use the 25 °C value of Th^{4+} as a representative value. Hence,

$$V^{\circ}_{\phi,Np^{4+}} = -54 + (0 \cdot T) + (0 \cdot T^2) \text{ mL/mol} \qquad \text{(II-6)}$$

The same reasoning for Np^{4+} was applied to Pu^{4+}, yielding

$$V^{\circ}_{\phi,Pu^{4+}} = -54 + (0 \cdot T) + (0 \cdot T^2) \text{ mL/mol} \qquad \text{(II-7)}$$

No volumetric data whatsoever are available on NpO_2^{+}. The closest "analogue," though of different charge, is UO_2^{2+}. If we examine the trends outlined above for Np^{4+}, we would expect the V°_{ϕ} for UO_2^{2+} to be in the range -15 to -25 mL/mol at 25 °C. Its value is, in fact, +6.50 mL/mol, the excess positive volume probably being a result of the greater volume of this larger ion. If similar behavior is assumed for NpO_2^{+}, we estimate its V°_{ϕ} at 25 °C to be about 25 mL/mol larger than "typical" monovalent ions, i.e., 30 mL/mol. In the absence of any other data, we will assume the temperature dependence to be similar to that of UO_2^{2+}; since this is so small compared with the uncertainty in the first term on the right-hand side, we estimated that

$$V^{\circ}_{\phi,NpO_2^{+}} = 30 + (0 \cdot T) + (0 \cdot T^2) \text{ mL/mol} \qquad \text{(II-8)}$$

No volumetric data are available for Pu^{3+}. The trivalent ion of closest ionic radius is Nd^{3+} (reported in ANL-90/16, Sec.II.B). Therefore, we estimated that

$$V^{\circ}_{\phi,Pu^{3+}} = -43.69 - (0.066 \cdot T) + (0.00075 \cdot T^2) \text{ mL/mol} \qquad \text{(II-9)}$$

No volumetric data are available for Pd^{2+}. Since Ni^{2+} (reported in ANL-90/16, Sec.II.B) is its homologue in the periodic table, we estimated that

$$V^{\circ}_{\phi,Pd^{2+}} = -33.2 + (0.0359 \cdot T) - (0.000052 \cdot T^2) \text{ mL/mol} \qquad \text{(II-10)}$$

No data are available on the volumetric properties of Rh^{3+}. The closest analogue for which data are available is Fe^{3+}; therefore, we estimated that

$$V^{\circ}_{\phi,Rh^{3+}} = -39.89 + (0.461 \cdot T) + (0 \cdot T^2) \text{ mL/mol} \qquad \text{(II-11)}$$

No volumetric data are available for $Ru(NO)^{3+}$; the ion was thus approximated as a "generic" ion by using the trends outlined for Np^{4+}. Temperature variation was assumed to be similar to that for UO_2^{2+} and, therefore, negligible. Thus,

$$V^{\circ}_{\phi,Ru(NO)^{3+}} = -42 + (0.0 \cdot T) + (0.0 \cdot T^2) \text{ mL/mol} \qquad \text{(II-12)}$$

No volumetric data are available on ZrO^{2+}. The values used in the GTM were estimated as follows: for the bivalent ions UO_2^{2+}, Mg^{2+}, Ni^{2+}, Co^{2+}, Zn^{2+}, Fe^{2+}, Mn^{2+}, Cu^{2+}, Cd^{2+}, Ca^{2+}, Hg^{2+}, Sr^{2+}, Pb^{2+}, and Ba^{2+}, apparent molar volume data[3] and crystal ionic volumes ($4/3\ \Pi r_c^3$, where r_c is the crystal ionic radius)[19] were plotted and fitted by the simple linear relationship

$$V_{\phi} = -25.6 + 1.4504 \quad V_c \qquad \text{(II-13)}$$

where V_c is the crystal ionic volume. The plot is shown in Fig. II-1. The crystal ionic volume of ZrO^{2+} was assumed to be the sum of the volumes for Zr^{4+} and O^{2-}. The relationship yields at 25 °C

$$V_{\phi,ZrO^{2+}} = -8.6 \text{ mL/mol} \qquad \text{(II-14)}$$

In the absence of any other data, the temperature dependence of ZrO^{2+} was assumed to be that of UO_2^{2+}, yielding

$$V_{\phi,ZrO^{2+}} = -8.6 + (0.00812 \cdot T) - (0.00202 \cdot T^2) \text{ mL/mol} \qquad \text{(II-15)}$$

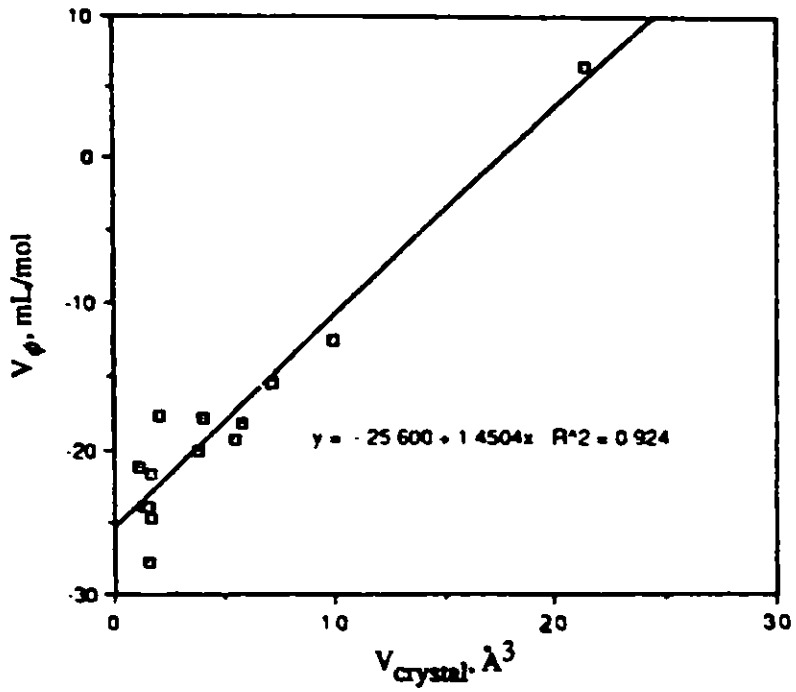

Fig. II-1. Fit of V_ϕ vs. V_c for Bivalent Ions

2. Verification of Density Predictions
(S. M. Smidt and I. R. Tasker)

a. Introduction

A check on the accuracy of the GTM's density predictions is necessary because of the assumptions and approximations that are needed to prevent overcomplicating the model. For instance, the model assumes that the volume (V) of a complex species may be obtained by using the additivity principle, i.e., the volume of a complex species is the sum of the volumes of its component parts. By reference to the work of Millero,[3,20,21] we can see that this assumption is not true. For example, by definition, $V(H^+) = 0.0$ mL/mol; we would thus expect that $V(SO_4^{2-}) = V(HSO_4^-)$, $V(SeO_4^{2-}) = V(HSeO_4^-)$, and $V(CO_3^{2-}) = V(HCO_3^-)$; in fact, the values are, respectively, 13.98/35.67, 21.0/31.1 and -4.3/23.4 mL/mol. A second example of a weakness in the density prediction section of the GTM is that it makes the unlikely assumption that oxalate ($C_2O_4^{2-}$) exists as a major component in solution. Although preliminary work suggested that errors would be small, the concern was that an error in calculating solution composition, when the activities of important species are changing rapidly with composition, could lead to a larger error in the activity estimation. There is thus a need to determine how these assumptions affect the accuracy of the model. To address this need, we prepared test solutions of $Al(NO_3)_3$ and oxalic acid in 0.02M HNO_3, as well as $Al(NO_3)_3$ and H_2SO_4 in 0.02M HNO_3. Complexation of the Al^{3+} by oxalate and sulfate should produce various species, the presence of which will provide a test of the model accuracy.

b. Solution Preparation

First, stock solutions of $Al(NO_3)_3$ in 0.02M HNO_3 were made. The aluminum nitrate crystals used had been recrystallized twice from 0.02M HNO_3 to purify them. However, this purification process leaves the crystals "wet" with an unknown amount of the acid. Due to this acid, the actual composition of the aluminum nitrate crystals weighed into the stock solutions was not known and had to be determined later by analysis. This analysis will be discussed shortly.

For oxalate solutions, one stock solution was approximately 1 molal in $Al(NO_3)_3$, the other was approximately 0.5 molal in $Al(NO_3)_3$. From each stock solution, four solutions containing oxalic acid in varying molalities were made, the density of each solution was then measured, and the measured density compared with a value predicted by GTM.

For the systems with sulfuric acid, a 2 m aluminum nitrate solution in 0.02M HNO_3 was made first (where m indicates molality, and M indicates molarity). From this, 1 and 0.5 m solutions were made by diluting a known amount of stock with 0.02M HNO_3.

From each of the three aluminum nitrate solutions, four solutions containing H_2SO_4 in varying molalities were prepared. The H_2SO_4 was added in the form of 8.53M H_2SO_4. The density of each solution (including the stock aluminum nitrate solutions) was then measured.

c. Aluminum Analysis

An analysis of aluminum is necessary for this work. We decided to attempt to refine a technique in the literature for analytical determination of aluminum.[22] To this end, trial determinations were made on 99.9% pure aluminum metal obtained from Ken Jensen (ANL Analytical Chemistry Laboratory). Unfortunately, the method did not work. The problem centered on the preparing of a 5% 8-hydroxyquinoline solution in 2N acetic acid. According to the procedure, 2.50 g of 8-hydroxyquinoline was to be dissolved in 5.70 mL of the acetic acid. In fact, very little of the 8-hydroxyquinoline dissolved. It was later discovered that this procedure had already been proven unsatisfactory.[23]

Subsequently, a procedure used in the ANL Analytical Chemistry Laboratory (ACL) was tested.[24] There was still some trouble dissolving the 8-hydroxyquinoline, but it was finally dissolved. Three samples of the pure aluminum were analyzed. There was larger-than-acceptable scatter in these results, indicating that the analytical technique needs further refinement. In the light of time pressures, samples were sent to ACL for analysis. The procedure finally adopted is given below for future reference.

a. Cover solid sample with 6M HCl and heat until the sample is dissolved.
b. Evaporate to dryness, being careful not to splatter.
c. Cover residue with ~50 mL H_2O plus ~1 mL concentrated HCl. Heat to dissolve residue. Use sufficient HCl to yield a final HCl concentration of about 0.5M.
d. Dilute to pre-selected volume (100, 500, or 1000 mL, depending on sample size).
e. Transfer an aliquot of the sample solution from step d containing 20-30 mg Al^{3+} into a 250-mL beaker.
f. Add 1 mL of 3.6% (wt/vol) ferric nitrate solution.
g. Dilute to 75 mL with H_2O and heat to boiling.
h. Add 10 mL of 4M NaOH solution.
i. Allow hydrated ferric oxide precipitate to settle, and filter through a 9-cm Whatman #42 (or equivalent) paper into a 600-mL beaker.
j. Transfer the precipitate onto the paper. Wash the beaker five times with 0.01M NaOH wash solution. Discard the filter paper and precipitate.
k. Add three drops methyl red indicator solution
l. Add concentrated HCl drop by drop with stirring until the indicator turns red.
m. Add 2M HCl drop by drop with stirring between additions of acid, until any $Al(OH)_3$ precipitate that may have formed dissolves.
n. Add 0.7 mL of 2.5% (wt/vol) solution of 8-hydroxyquinoline for each milligram of aluminum present, plus 10 mL in excess and sufficient H_2O to bring the volume to about 350 mL. [A 2.5% (wt/vol) solution of 8-hydroxyquinoline is made by dissolving 12.5 g 8-hydroxyquinoline in 14.5 mL of 6M HCl and then diluting to 500 mL with water.]

o. Slowly introduce 20 mL of 20% (wt/vol) ammonium acetate solution with stirring.
p. Heat to boiling, digest on a steam bath for 30 min, and cool to 50°C. If necessary, the solution can stand overnight at room temperature.
q. Filter through a clean, weighed, medium-porosity sintered glass filtering crucible.
r. Wash the precipitate with no more than 100 mL of warm (50-60°C) 8-hydroxyquinoline solution. Finally, wash twice with 5 mL of cold H_2O. The 8-hydroxyquinoline wash solution is prepared as 8 mL of the 2.5% solution (step n) diluted to 500 mL with H_2O. Three drops of bromocresol purple indicator and 2M NH_4OH are added to that solution until purple (pH=6) color appears, then it is diluted to 1000 mL. (The bromocresol purple is prepared as a 0.1% solution, i.e., 100 mg dissolved in 20 mL ethanol, diluted to 100 mL with water.)
s. Dry the crucible and precipitate at 150°C overnight.
t. Cool the crucible and precipitate in a dessicator for 45 min, allow to cool another 15 min in ambient air, and weigh.
u. Calculate the aluminum composition (wt %) as

$$\text{wt \% } Al^{3+} = \frac{A \cdot 5.874}{B \cdot C} \qquad \text{(II-18)}$$

where A = weight of aluminum-8-hydroxyquinoline

$$B = \text{Aliquot fraction} = \frac{\text{sample aliquot (mL)}}{\text{total sample volume (mL)}}$$

C = weight of sample

The following points about the procedure should be noted:

- Steps a-d are necessary only when dealing with aluminum metal or solid samples.
- Steps e-l are necessary only when the sample contains iron impurities which must be removed.
- For measurements performed on our solutions, only steps m-t were necessary.

d. Determination of Solution Composition

Having determined the aluminum composition of the solution, we must now determine the hydrogen ion concentration in order to evaluate the total solution composition. Direct titrimetric analysis of $[H^+]$ in hydrolyzing solutions such as those of aluminum salts is not possible. An indirect method must be sought.

The method employed here was to use the Al^{3+} analysis of the various solutions, all of which had been prepared with great precision, to calculate the amount of $Al(NO_3)_3 \cdot 9H_2O$ that would have been present in the original stock solution. The difference between this calculated amount and the experimental amount is ascribed to HNO_3 wetness on the $Al(NO_3)_3 \cdot 9H_2O$ crystals.

e. Results and Conclusion

The results are shown in Tables II-2 and II-3. For the oxalic acid containing solutions, the difference between the experimental results and the GTM prediction is surprisingly small, with the relative error never exceeding 1%. For solutions containing H_2SO_4, however, the agreement is not as close.

Table II-2. Experimental and Calculated Density for the System $Al(NO_3)_3$-HNO_3-$H_2C_2O_4$-H_2O

	Comp., M				Density, g/mL	
Solution	$[H^+]$	$[Al3^+]$	$[Ox^{2-}]$	$[NO^{3-}]$	Expt.	Calc.
6.2 Ox A/16	0.3037	0.8857	0.1439	2.6730	1.1464	1.1457
6.2 Ox B/17	0.7547	0.8661	0.3696	2.6138	1.1499	1.1439
6.2 Ox C/17	1.0416	0.8542	0.5131	2.5780	1.1529	1.1444
6.2 OX D/18	0.3667	0.8821	0.1755	2.6620	1.1458	1.1453
6.2 Ox E/18	0.3895	0.4973	0.1861	1.5092	1.0867	1.0813
6.2 Ox F/19	0.6736	0.4905	0.3282	1.4887	1.0901	1.0820
6.2 Ox G/19	1.0107	0.4828	0.4969	1.4653	1.0949	1.0854
6.2 Ox H/20	1.4666	0.4725	0.7250	1.4341	1.1017	1.0940
6.1 A/13	0.0160	0.8974	0.0000	2.7082	1.1432	1.1474
6.1 B/13	0.0175	0.5005	0.0000	1.5190	1.0700	1.0812

Table II-3. Experimental and Calculated Density for the System $Al(NO_3)_3$-HNO_3-H_2SO_4-H_2O

	Conc., M				Density, g/mL		Rel.	Error*, % (molal)		
	HNO_3	$Al(NO_3)_3$	H_2SO_4	Total	Expt.	Calc.	Error,%	$[HNO_3]$	$[Al(NO_3)_3]$	$[H_2SO_4]$
133-A	1.2457	1.5199	1.2360	4.5694	1.3051	1.2562	-3.76	-6.00	-6.03	-6.03
133-B	0.8779	1.5857	0.8675	4.7675	1.2959	1.2663	-2.28	-3.48	-3.52	-3.52
133-C	0.2380	1.7263	0.2264	5.1905	1.2789	1.2860	0.56	-0.76	-0.79	0.78
134-A	0.7539	0.8764	0.7400	2.6431	1.1816	1.1471	-2.92	-3.91	-3.89	-3.88
134-B	0.5154	0.9023	0.5009	2.7214	1.1714	1.1497	-1.85	-2.39	-2.39	-2.39
134-C	0.2756	0.9281	0.2605	2.7994	1.1609	1.1531	-0.67	-0.87	-0.84	-0.83
134-D	1.2265	0.8246	1.2137	2.4866	1.2012	1.1487	-4.37	-6.18	-6.16	-6.15
134-E	0.4230	0.4972	0.4064	1.5082	1.1046	1.0824	-2.01	-2.35	-2.37	-2.38
134-F	0.3990	0.4986	0.3824	1.5124	1.1034	1.0824	-1.90	-2.28	-2.25	-2.23
134-G	0.0835	0.5167	0.0661	1.5675	1.0863	1.0840	-0.21	-0.28	-0.24	-0.29
134-H	0.6478	0.4841	0.6318	1.4683	1.1162	1.0842	-2.87	-3.50	-3.49	-3.49

*The errors listed are differences in molality of a solution when the conversion from molarity is made using first the experimental density and then the GTM calculated density.

It is clear from Tables II-2 and II-3 that, over a wide range of molalities, the density predictions of GTM do not hold up. The more complex the solution, the less accurate the prediction. This is as we expected, because GTM predicts densities by using apparent molar volumes according to the additivity principle (at infinite dilution).

To examine the effect of this error, we calculated the molalities of the components of the solution from the molarities, using both the experimental and the GTM predicted densities. The errors in the molarities are shown in the final columns of Table II-3. It is obvious that the errors in density are magnified in calculating concentration. The results are shown graphically in Fig. II-2 (where "error" refers to the average of the errors listed in the last three columns of Table II-3).

In conclusion, the magnitude of the errors produced by the GTM in estimating density, and hence in calculating molalities, can reach significant levels. Work on the implications of this finding is continuing.

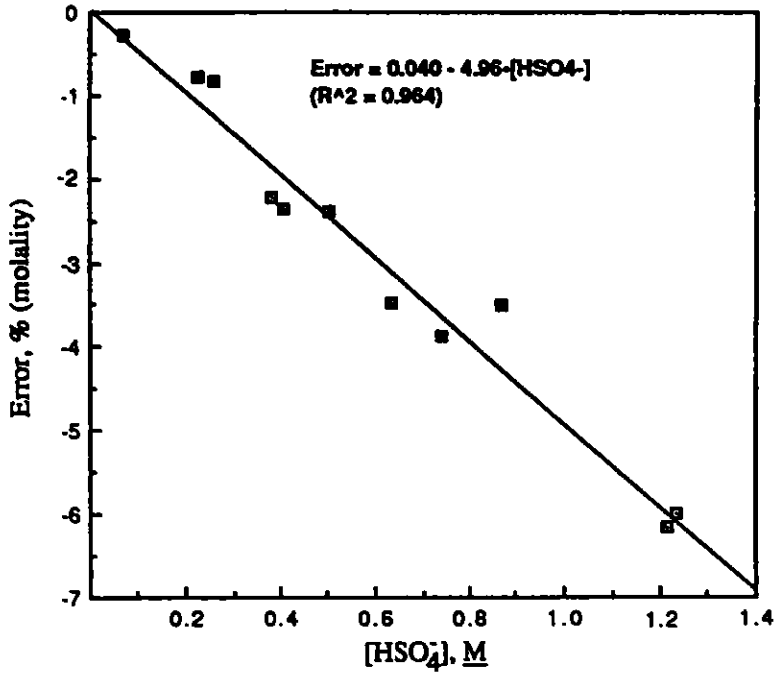

Fig. II-2. Plot of Error in Molarity Calculation Versus $[HSO_4]$

C. Estimation of Aqueous Electrolyte Activities at Elevated Temperatures
(I. R. Tasker)

The SASPE section of the GTM uses the Bromley model[25] of multicomponent electrolyte solutions for estimating activity coefficients of individual ions (ANL-88-28, p. 79). The Bromley equation is

$$\log\gamma_{12} = \frac{-A^{\circ} Z_1 Z_2 \sqrt{I}}{1 + \sqrt{I}} + \frac{\nu_1 F_1 + \nu_2 F_2}{\nu_1 + \nu_2} \qquad \text{(II-17)}$$

In Eq. II-17,

$$F_1 = (Y_{12} \log\gamma^{\circ}_{12} + Y_{14} \log\gamma^{\circ}_{14} + \ldots Y_{1j} \log\gamma^{\circ}_{1j})$$

$$+ \frac{A^{\circ}\sqrt{I}}{1 + \sqrt{I}} \quad (Z_1 Z_2 Y_{12} + Z_1 Z_4 Y_{14} + \ldots Z_1 Z_j Y_{1j}) \qquad \text{(II-18)}$$

$$F_2 = (X_{12} \log\gamma^{\bullet}_{12} + X_{32} \log\gamma^{\bullet}_{32} + \ldots X_{i2} \log\gamma^{\bullet}_{i2})$$

$$+ \frac{A^{\bullet}\sqrt{I}}{1 + \sqrt{I}} \quad (Z_1 Z_2 X_{12} + Z_3 Z_3 X_{32} + \ldots Z_i Z_2 X_{i2}) \qquad \text{(II-19)}$$

where

$$Y_{1j} = \left[\frac{Z_1 + Z_j}{2}\right]^2 \left[\frac{m_j}{I}\right] \qquad \text{(II-20)}$$

$$X_{i2} = \left[\frac{Z_i + Z_2}{2}\right]^2 \left[\frac{m_i}{I}\right] \qquad \text{(II-21)}$$

and $A^{\bullet}$ = Debye-Huckel constant [=f(T)]
I = ionic strength = $0.5 \Sigma m_i z_i^2$
Z_i, Z_j = modulus of ionic charge
ν_i, ν_j = stoichiometric coefficients
m_i, m_j = molal composition
γ_{12} = mean activity coefficient at ionic strength of the solution
$\gamma^{\bullet}_{12}$ = mean activity coefficient of single-component electrolyte at ionic strength of solution

The essential problem, then, is one of determining the various $\gamma^{\bullet}_{12}$. This may be achieved by using literature data or, if such data are absent, by estimation methods.

Thus far, all of our calculations have been performed for 25 °C. To extend GTM to elevated temperatures requires that Eq. II-17 hold as a function of temperature. Examination of Eq. II-17 shows that the Debye-Huckel constant and $\log\gamma^{\bullet}$ in the F terms are the only functions of temperature (provided all calculations are performed on a molal basis). The Debye-Huckel constant is available in the literature as a function of temperature; thus, the problem reduces to obtaining values of the activity coefficients of single-component electrolytes as a function of temperature. A number of approaches are available (though not necessarily all useful).

Very few direct measurements of γ as a function of temperature are available in the literature for species of interest to GTM. A search is underway to collect available data, but this will not be sufficient for GTM needs. The lack of direct measurement of γ is due, in part, to the availability of calorimetric measurements that permit the extrapolation of room-temperature activity coefficients to higher temperatures. The variation of mean activity coefficient with temperature may be written as

$$\left[\frac{\partial \ln\gamma_{\pm}}{\partial T}\right]_P = \frac{-(\bar{H} - \bar{H}_o)}{(\nu_1 + \nu_2)RT^2} = \frac{-\bar{L}}{\nu RT^2} \qquad \text{(II-22)}$$

where H = partial molal enthalpy of electrolyte in solution
H^* = partial molal enthalpy of electrolyte at infinite dilution
L = relative partial molal enthalpy
R = gas constant (8.3147 J mol^{-1} K^{-1})
T = absolute temperature (kelvin)

To obtain γ at an elevated temperature, Eq. II-22 must be integrated, and so the temperature dependence of L must be known.

$$\frac{\partial \bar{L}}{\partial T} = \frac{\partial (\bar{H} - \bar{H}^*)}{\partial T} = \bar{C}_p - \bar{C}_p^* = \bar{J} \qquad \text{(II-23)}$$

where $\bar{C}_p$ = partial molal heat capacity of electrolyte in solution
$\bar{C}^*_p$ = partial molal heat capacity of electrolyte at infinite dilution
$\bar{J}$ = relative molal heat capacity of electrolyte

Conventionally, the temperature dependence of $\bar{J}$ is represented as

$$\bar{J} = B + CT + DT^2 \ldots \qquad \text{(II-24)}$$

where B, C, D, ... are constants; therefore, upon integrating Eq. II-24, we have

$$\bar{L} = A + BT + CT^2 + DT^3 \ldots \qquad \text{(II-25)}$$

where A is a constant evaluated by measuring L.

Substituting Eq. II-25 into Eq. II-22, integrating from a reference temperature of 298.15 K, and rearranging give

$$\ln \gamma_{\pm}^{(T)} = \ln \gamma_{\pm}^{(298)} + \frac{A}{(\nu_1 + \nu_2)R} \cdot \left[\frac{1}{T} - \frac{1}{298.15}\right] - \frac{B}{(\nu_1 + \nu_2)R} \cdot \ln \left[\frac{T}{298.15}\right]$$
$$- \frac{C}{(\nu_1 + \nu_2)R} (T - 298.15) - \frac{D}{2(\nu_1 + \nu_2)R} (T^2 - 298.15^2) \qquad \text{(II-26)}$$

If the temperature range is small and appropriate (e.g., 15-70°C), useful approximations can be made. Since J can be assumed to be independent of temperature, Eq. II-24 becomes $\bar{J} = B$, and Eq. II-25 becomes $\bar{L} = A + BT$. Then, Eq. II-26 reduces to

$$\log_{10} \gamma_{\pm}^{(T)} = \log_{10} \gamma_{\pm}^{(298.15)} + \frac{Y}{(\nu_1 + \nu_2)} \cdot \bar{L}^{(298.15)}$$
$$- \frac{Z}{(\nu_1 + \nu_2)} \bar{J}^{(298.15)} \qquad \text{(II-27)}$$

where

$$Y = \frac{(298.15 - T)}{8.3147 \cdot 298.15 \cdot 2.3026 \cdot T} \qquad \text{(II-28)}$$

and

$$Z = \frac{(298.15 - T)}{8.3147 \cdot 2.3026 \cdot T} - \frac{1}{8.3147} \cdot \log_{10}\left[\frac{298.15}{T}\right] \qquad \text{(II-29)}$$

Equation II-27 shows that if the activity coefficient is known at room temperature, then two other room-temperature calorimetric measurements (L and J) will permit extrapolation of the activities over a small temperature range. Facilities for measuring these properties exist at ANL. The Tronac Isoperibal and LKB Heat of Mixing calorimeters at ANL can be tailored to measure L. Although J is usually determined by heat capacity of solution measurements on equipment such as a Picker calorimeter, the Tronac (and to an extent, the LKB) calorimeter can be operated over a wide enough temperature range that J can be determined. Much of the necessary information is unavailable, but accumulation of L and J data available in the literature is underway.

Bromley has addressed the effect of temperature on activity coefficient and "concluded that either of the following equations will provide a satisfactory expression for the variation of B with temperature although each requires enough data to determine the necessary constants"[25]:

$$B = B^* \ln\left[\frac{T - 243}{T}\right] + \frac{B_1}{T} + B_2 + B_3 \cdot \ln T \qquad \text{(II-30a)}$$

$$B = \left[\frac{B^*}{T - 230}\right] + \frac{B_1}{T} + B_2 + B_3 \cdot \ln T \qquad \text{(II-30b)}$$

where T is the temperature (in kelvin); B^*, B_1, B_2, and B_3 are fitted constants; and B is the Bromley parameter in the equation

$$\log \gamma_{1,2} = \frac{-A^{\circ} Z_1 Z_2 \sqrt{I}}{1 + \rho \sqrt{I}} + \frac{(0.06 + 0.6B)\, Z_1 Z_2 I}{1 + \left[\frac{1.5\, I}{Z_1 Z_2}\right]^2} \cdot BI \qquad \text{(II-30c)}$$

where the terms have their previously given meanings, and ρ is a constant set equal to 1.0 at 25 °C. For our needs, the problem with this approach is the lack of available data.

Meissner has suggested an approach to the effect of temperature on strong electrolytes in aqueous solution.[26,27] Meissner defines the reduced activity coefficient Γ as

$$\Gamma = \gamma_{1,2}^{\frac{1}{Z_1 Z_2}} \qquad \text{(II-31)}$$

where the terms have their previous definitions. He found that in pure solution at 25 °C, plots of Γ versus I show that most strong electrolytes fall fairly well onto a family of curves; thus, determination of a single value of Γ at known I can be used to estimate Γ at any other ionic strength. Regarding the effect of temperature, Meissner states that "As a first approximation, for temperatures from 0 °C to 100 °C, isothermal curves of log Γ versus [I] for 40 typical strong electrolytes were found to remain members of the curve family." Meissner went on to shown that for a given strong electrolyte at a given I, log Γ_T is a unique function of log $\Gamma_{25°C}$. At a constant I of 10, this function becomes linear, and in the range 0-150 °C, the following empirically relationship holds:

$$\log (\Gamma_T)_{I=10} = \{1 - 0.005 (T - 25)\} \log (\Gamma_{25°C})_{I=10} \qquad \text{(II-32)}$$

Thus, from Eq. II-32, the reduced activity of an electrolyte at I = 10 may be estimated at an elevated temperature; then by locating this value on the curve family, one can obtain activities at other compositions at the same temperature. The accuracy of this method is estimated to be generally about 20%, with some values considerably worse.

The preceding methods have a level of applicability to the present problem, yet a more easily tractable and a more experimentally accessible treatment would be preferred. The closest approach to this has been the modification to Bromley's equations used by Rastogi and Tassior,[28] which was found to better suit our purposes. They start from the Bjerrum relationship between the activity coefficient ($\gamma_{1,2}$) and osmotic coefficient (ϕ):

$$\ln \gamma_{1,2} = \phi - 1 + \int_0^m (\phi - 1)\, d\ln m \qquad \text{(II-33)}$$

where m is the solute molality. Rastogi and Tassior make use of the fairly extensive data on vapor pressure depression (ΔP) as a function of composition, where

$$\Delta P = P - P_s \qquad \text{(II-34)}$$

$$a_s = \frac{P_s - \Delta P}{P_s} \qquad \text{(II-35)}$$

$$\phi = \left[\frac{-1000}{(\nu_1 + \nu_2) m M_s}\right] \ln a_s \qquad \text{(II-36)}$$

where P is the vapor pressure of solvent in the solution, P_s is the vapor pressure of pure solvent, a_s is the activity of the solvent, and M_s is the molar mass of the solvent. Using Eq. II-18, for activities of a single-component electrolyte in solution, Bromley obtains

$$1 - \phi = 2.303 \frac{A^{\circ} Z_1 Z_2 \sqrt{I}}{3} \cdot \sigma \cdot (\rho \sqrt{I}) \cdot 2.303 (0.06 + 0.6B) Z_1 Z_2 \frac{I}{2} \psi (aI)$$

$$- 2.303 B \frac{I}{2} \qquad \text{(II-37)}$$

where

$$\sigma\ (\rho\ \sqrt{I}\ ) = \frac{3}{(\rho\sqrt{I})^3} \cdot \left\{1 + \rho\ \sqrt{I} - \frac{1}{1 + \rho\ \sqrt{I}} - 2\ \ln\ \left[1 + \rho\ \sqrt{I}\right]\right\} \qquad \text{(II-38)}$$

$$\Psi\ (aI) = \frac{2}{aI}\ \left[\frac{1 + 2aI}{(1 + aI)^2} - \frac{\ln\ (1 + aI)}{aI}\right] \qquad \text{(II-39)}$$

In Eq. II-39,

$$a = \frac{1.5}{Z_1 Z_2} \qquad \text{(II-40)}$$

Equation II-37 is originally presented by Bromley without derivation. It is reported by Rastogi and Tassior also without derivation and without comment, even though the two equations differ by a coefficient equal to 1/3 in front of the leading term on the right-hand side (the term is absent in the Rastogi and Tassior version; the version here is that of Bromley). At the present time, it is unclear whether the alteration by Rastogi and Tassior is a correction or a typographical error. Rederivation is being attempted.

Secondly, we note for the record that by appropriate thermodynamic manipulation, calorimetric measurements can be used to extend the Bromley equations, i.e.,

$$L_\phi = \frac{(\nu_1 + \nu_2)\ A_H Z_1 Z_2\ \sqrt{I}}{2} \cdot \left\{\frac{1}{1 + \rho\ \sqrt{I}} - \sigma\ (\rho\ \sqrt{I}\ )\right\} - 2.303\ (\nu_1 + \nu_2)\ RT^2\ I$$

$$- 2.303\ (\nu_1 + \nu_2)\ RT^2 I\ \left\{\left[\frac{1}{(1 + aI)^2} - \frac{\Psi\ (aI)}{2}\right](0.6 Z_1 Z_2) + \frac{1}{2}\right\}\ \frac{dB}{dT} \qquad \text{(II-41a)}$$

$$\bar{L}_x = \frac{(\nu_1 + \nu_2)}{2} \cdot \frac{A_H Z_1 Z_2\ \sqrt{I}}{1 + \rho\ \sqrt{I}} - 2.303\ \left[\frac{0.6\ Z_1 Z_2}{(1 + aI)^2} + 1\right]\ (\nu_1 + \nu_2)\ RT^2 I\ \frac{dB}{dT} \qquad \text{(II-41b)}$$

$$C_{p,\phi} - \bar{C}^{\circ}_{p,x} = \frac{(\nu_1 + \nu_2) \cdot A_j \cdot Z_1 Z_2 \cdot \sqrt{I}}{2} \cdot \left\{\frac{1}{1 + \rho\ \sqrt{I}} - \frac{\sigma\ (\rho\ \sqrt{I})}{3}\right\} - 2.303$$

$$\cdot\ (\nu_1 + \nu_2)\ \cdot\ RT^2 I\ \left\{\left[\frac{1}{(1 + aI)^2} - \frac{\Psi(aI)}{2}\right](0.6\ Z_1 Z_2) + \frac{1}{2}\right\}\left[\frac{2}{T}\ \frac{dB}{dT} + \frac{d^2 B}{dT^2}\right] \qquad \text{(II-41c)}$$

where L_ϕ = relative apparent molal enthalpy
$L_x = H_x - H_x^\circ$
H_x = partial molal enthalpy of solute
H_x° = partial molal enthalpy of solute at infinite dilution
A_H = Debye-Huckel limiting coefficient for enthalpy

$C_{p,\phi}$ = relative apparent molal heat capacity
$C_{p,x}$ = partial molal heat capacity of solute at infinite dilution
A_j = Debye-Huckel limiting coefficient for heat capacity

In the Rastogi and Tassior method, the correlation is better demonstrated by writing Eq. II-37 as

$$Y = BX \tag{II-42}$$

where

$$Y = (1 - \phi) - 2.303\, A^{\circ} Z_1 Z_2\, \sigma\, \rho\, \sqrt{I} + 2.303 \left[0.06\, \frac{\Psi(aI)}{2}\right] Z_1 Z_2 I \tag{II-43a}$$

and

$$X = -2.303 \left[0.6\, I\, Z_1 Z_2\, \frac{\Psi(aI)}{2} + \frac{I}{2}\right] \tag{II-43b}$$

Plots of Eq. II-42 as shown in Rastogi and Tassior's work prove to be acceptable straight lines, demonstrating their treatment of Eq. II-37 can be used to calculate ϕ and, hence, γ. Compilations of ΔP against composition are available at 100°C in the Smithsonian Physical Tables[29] and International Critical Tables.[30] Using this data to obtain B at two temperatures, Eqs. II-30a and II-30b may be rewritten as

$$B\,T = B_1 + B^{*} T \ln \left[\frac{T - 243}{T}\right] \tag{II-44}$$

$$B\,T = B_1 + \frac{B^{*}\,T}{T - 230} \tag{II-45}$$

to obtain B, and hence γ, at any temperature in between. An examination of the use of these equations is underway.

D. Activity Measurements on $Al(NO_3)_3$
(I. R. Tasker and A. A. DiFilippo)

Details of activity measurements on $Al(NO_3)_3$ by vapor pressure osmometry were described in the previous report (ANL-90/16, Sec.II.H). Progress continued toward determining the thermodynamic activities of aluminum in solution. Due to aluminum hydrolysis in neutral solution, considerable analysis of solution composition is essential.

To calculate $[H^+]$ in $Al(NO_3)_3/HNO_3$ solutions, we first prepared a series of calibration solutions in which pH was varied as a function of ionic strength I and $[H^+]$. The solutions were prepared by weight and consisted of sodium nitrate in dilute nitric acid solutions of known concentration varying from about 0.2 to 0.001 molal in $[H^+]$. A range of ionic strengths was obtained by varying the concentrations of sodium nitrate in solution, yielding 47 solutions to be analyzed.

The densities of all the solutions were measured on a densimeter, and the molalities were then converted to molarities. Ionic strength was calculated using

$$I = \frac{1}{2} \Sigma \, m \cdot z^2 \qquad \text{(II-46)}$$

where m is molality of the species in solution, and z is the charge of the corresponding ion. Finally, the pH of each solution was measured using a Metrohm model 605 pH meter and a combination electrode.

To begin with, graphs of pH versus ionic strength were plotted for seven different $[H^+]$ concentrations. Figure II-3 is the plot for $[H^+] = 0.019649$ m. Data were fit by an equation of the form

$$pH = a + b\,I + c\,(I^2) \qquad \text{(II-47)}$$

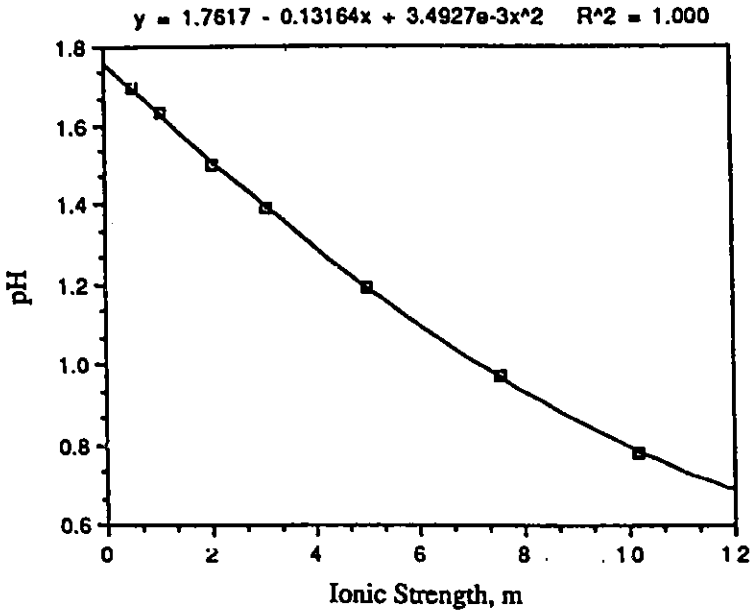

Fig. II-3. Plot of pH vs. Ionic Strength at $[H^+] = 0.019649$ m in Sodium Nitrate Solution

These equations were then used to calculate values of the pH of a solution at rounded values of I (i.e., I = 0.5 and 1, 2, 3...10). Next, at a given ionic strength (e.g., I = 1), a plot of pH versus $[H^+]$ was obtained for ionic strengths ranging from 0.5 to 10, giving 11 different graphs and their corresponding equations. Figure II-4 shows the plot obtained for I = 1.00 m. Data were fitted by an equation of the form

$$pH = X\,([H^+]^Y) \qquad \text{(II-48)}$$

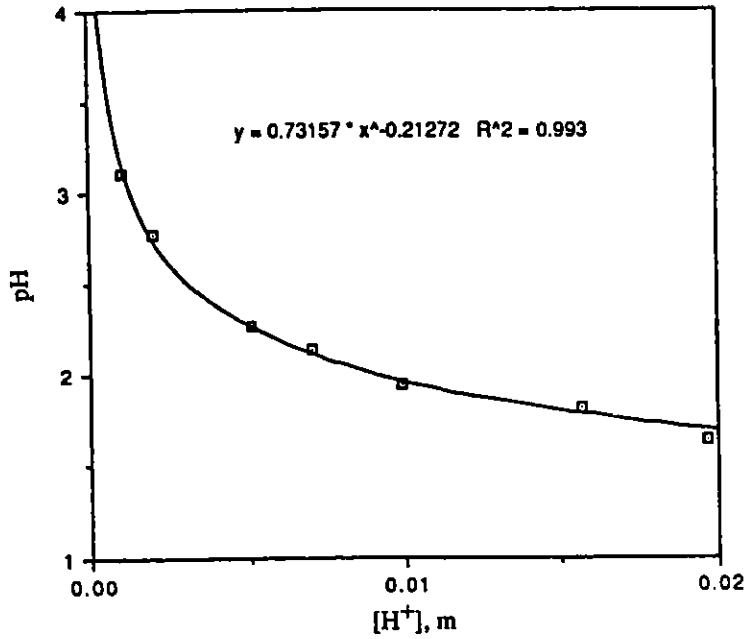

Fig. II-4. Plot of Calculated pH vs. $[H^+]$ at I = 1.000 m for Sodium Nitrate Solution

For the 11 different plots of pH versus $[H^+]$ represented by the above equation, we examined the variation of the parameters X and Y with ionic strength. The parameters X and Y were each plotted against ionic strength, and the data were fitted by functions of the form

$$X = ax + bx \cdot I + cx \cdot (I^2) \qquad \text{(II-49)}$$

$$Y = ay + by \cdot I + cy \cdot (I^2) \qquad \text{(II-50)}$$

The results are shown in Figs. II-5 and 6, respectively. Rearrangement of Eq. II-48 gives

$$[H^+] = (pH/X)^{(1/Y)} \qquad \text{(II-51)}$$

Substitution of Eqs. II-49 and II-50 into Eq. II-51 gives

$$[H^+] = \left[\frac{pH}{ax + bx \cdot I + cx \cdot I^2}\right]^{\left[\frac{1}{ay + by \cdot I + cy \cdot I^2}\right]} \qquad \text{(II-52)}$$

where ax = 0.82490, bx = -0.09744, cx = -0.003801, ay = -0.19799, by = -0.01447, and cy = -0.000036094.

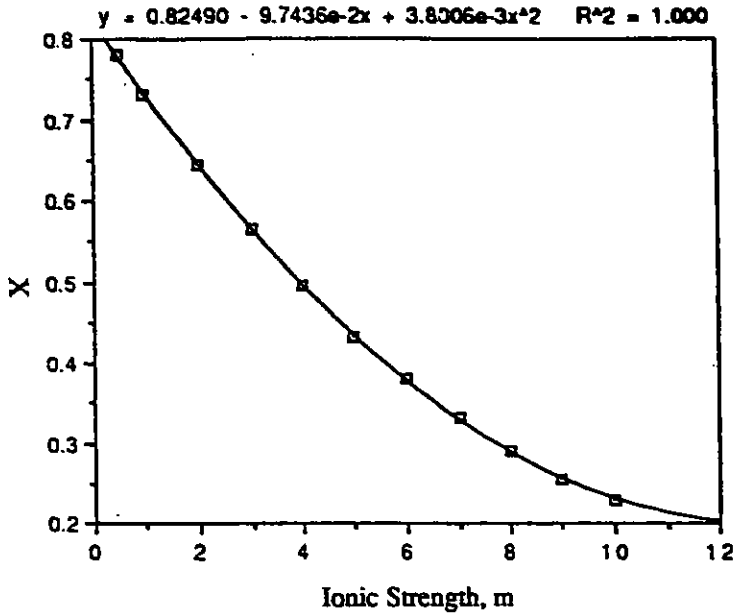

Fig. II-5. Fit of Eq. II-49 to Derived Data as Function of Ionic Strength

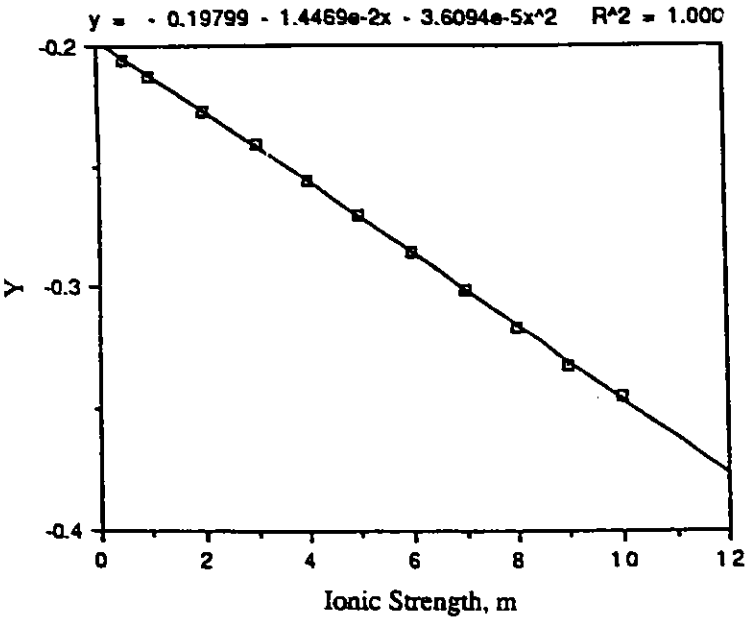

Fig. II-6. Fit of Eq. II-50 to Derived Data as Function of Ionic Strength

If the ionic strength correlation for $NaNO_3$ could be used for $Al(NO_3)_3$, then Eq. II-52 can be used to determine the hydrogen ion concentration in the aluminum nitrate solutions used for activity measurements. These solutions were prepared by using acid of known concentration and purified aluminum nitrate "wet" with dilute nitric acid. The amount of this "wetness" is the source of our uncertainty. By using the known acid concentration and the analytical values for Al^{3+} as a starting point, an initial I can be calculated. This, together with the experimental value of pH, allows a better estimate of $[H^+]$ to be obtained by use of Eq. II-52. This value can be fed back into the ionic strength calculation, and

so an iterative procedure can be set up until a constant value of $[H^+]$ is obtained. Table II-4 and Fig. II-7 show the good agreement between experimental and calculated values of $[H^+]$. At high values of $[H^+]$, the agreement falls off. Reasons for this discrepancy are being investigated. Even so, up to abou 0.02 molal $[H^+]$, the correlation appears to work well enough for present purposes.

Table II-4. Experimental and Calculated $[H^+]$ for Sodium Nitrate Solutions

Meas. Conc., m		Ionic Strength,		Calc. $[H^+]$,	Diff.,
$[H^+]$	$[NaNO_3]$	m	pH	m	m
0.019649	10.144750	10.164400	0.781	0.029003	0.009354
0.019649	7.545267	7.564917	0.972	0.023718	0.004069
0.019649	5.020816	5.040465	1.190	0.023713	0.004064
0.019649	3.033048	3.052697	1.386	0.024331	0.004681
0.019649	2.007271	2.026920	1.501	0.024071	0.004421
0.019649	1.035692	1.055342	1.632	0.022470	0.002821
0.019649	0.502782	0.522431	1.697	0.022091	0.002442
0.015684	7.526248	7.541931	1.161	0.013425	-0.002259
0.015684	5.138256	5.153940	1.362	0.013992	-0.001692
0.015684	2.504432	2.520116	1.620	0.014882	-0.000802
0.015684	1.004363	1.020047	1.822	0.013543	-0.002140
0.015684	0.536933	0.552617	1.858	0.014092	-0.001592
0.009965	9.624280	9.634245	1.130	0.010463	0.000497
0.009965	7.466382	7.476348	1.285	0.009796	-0.000169
0.009965	4.991921	5.001887	1.494	0.010371	0.000405
0.009965	2.992346	3.002311	1.693	0.010807	0.000842
0.009965	2.004762	2.014727	1.808	0.010656	0.000691
0.009965	0.999962	1.009927	1.934	0.010260	0.000294
0.009965	0.501919	0.511885	2.015	0.009606	-0.000360
0.007048	10.064751	10.071800	1.309	0.006622	-0.000427
0.007048	7.571867	7.578915	1.500	0.005824	-0.001224
0.007048	5.024813	5.031861	1.723	0.006089	-0.000959
0.007048	3.031831	3.038879	1.919	0.006380	-0.000668
0.007048	2.010473	2.017521	2.028	0.006426	-0.000623
0.007048	1.100506	1.107555	2.122	0.006482	-0.000566
0.007048	0.506294	0.513343	2.179	0.006560	-0.000488
0.005086	9.495916	9.501002	1.465	0.004926	-0.000160
0.005086	7.564190	7.569276	1.609	0.004651	-0.000435
0.005086	5.016849	5.021935	1.815	0.005039	-0.000047
0.005086	3.021885	3.026971	2.014	0.005241	0.000155
0.005086	2.007739	2.012825	2.143	0.005047	-0.000039
0.005086	1.006415	1.011501	2.261	0.004920	-0.000166
0.005086	0.505935	0.511021	2.327	0.004767	-0.000319
0.002025	9.932347	9.934373	2.004	0.001942	-0.000083
0.002025	7.497594	7.499619	2.170	0.001784	-0.000241
0.002025	5.038911	5.040936	2.371	0.001878	-0.000147
0.002025	3.062375	3.064400	2.536	0.002010	-0.000015
0.002025	2.000634	2.002659	2.822	0.001505	-0.000520
0.002025	0.999785	1.001810	2.791	0.001830	-0.000195
0.002025	0.502364	0.504389	2.660	0.002488	0.000463
0.001023	9.956798	9.957821	2.306	0.001294	0.000271
0.001023	7.594793	7.595816	2.518	0.001092	0.000069
0.001023	4.999134	5.000157	2.676	0.001210	0.000187
0.001023	3.034356	3.035379	2.918	0.001132	0.000109
0.001023	2.008342	2.009365	2.984	0.001176	0.000153
0.001023	1.006301	1.007324	3.099	0.001118	0.000095
0.001023	0.506229	0.507252	3.170	0.001059	0.000035

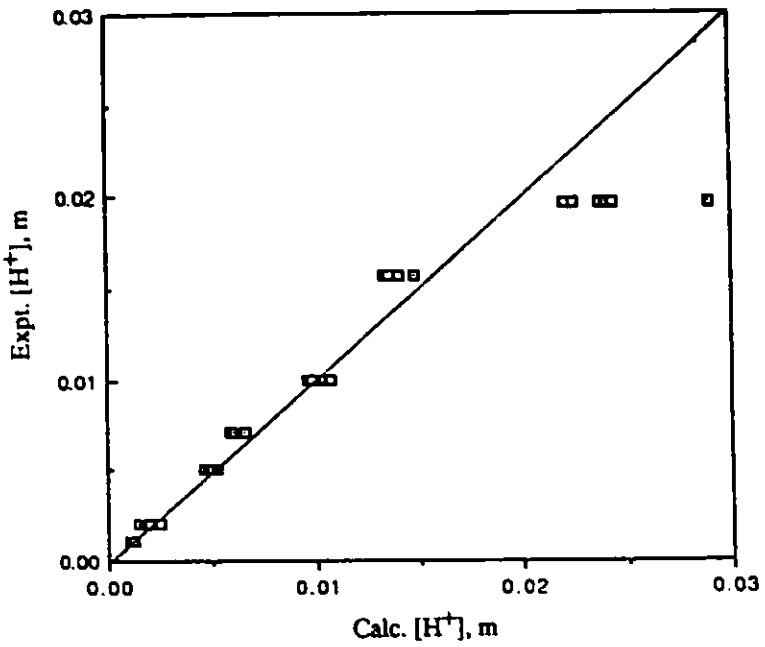

Fig. II-7. Plot of Calculated and Experimental Values of $[H^+]$

E. Extraction Studies

In this report period, laboratory studies were carried out to determine the extraction behavior of oxalic acid, plutonium (IV), rare earths, thorium, neptunium, curium, iron, and americium. These studies provide extraction data which will be used in modeling the TRUEX process.

1. Oxalic Acid
(D. J. Chaiko)

In the TRUEX process, oxalic acid is required as a feed component to reduce the extraction of iron, zirconium, and the noble metals to acceptable levels. However, oxalic acid is itself extracted, and modeling its extraction behavior is an important first step in being able to predict the influence of organic-phase oxalic acid on the partitioning of metal species in the scrub and strip sections. Extraction data for both the TRUEX-TCE and TRUEX-NPH solvents as a function of aqueous nitric acid concentration have been collected and will be used in developing extraction models.

a. Purification of Oxalic Acid

A ^{14}C-labeled formic acid impurity was removed from the oxalic acid stock by anion-exchange chromatography. The purification was carried out with oxalic and formic acid carriers. The acid ionization constants of oxalic acid (1.23) and formic acid (3.75) are such that sufficient separation should be achievable by chromatography. At pH 2.5, approximately 95% of the oxalic acid carries a -1 charge, while only 5% of the formic acid is ionized.

An anion-exchange column was prepared with approximately 1/2 mL of Dowex 1-X8 resin (200-400 mesh anion exchanger in the chloride form). The resin was equilibrated with distilled, deionized water that was titrated to pH 2.5 with hydrochloric acid. After the ^{14}C-labeled oxalic acid was taken to dryness, the material was dissolved with 1 mL of distilled water that had been adjusted to pH 2.5 with HCl. Formic acid (2×10^{-2}M) was added to give a final formate concentration of 0.2 mM.

Oxalate carrier was also added to the ^{14}C-labeled material to give a final oxalate concentration of 0.05 mM. After loading, the ion-exchange column was washed with 14 mL of 0.01 mM formic acid adjusted to pH 2.5 with HCl. The column was then eluted with 15 mL of 1.2M HCl. After washing the eluate several times with 2 mM HNO_3 and taking it to dryness, the sample was diluted with 4 mL of 2 mM HNO_3 and stored frozen.

Forward and reverse distribution ratios were checked at a number of aqueous acid concentrations and they agreed within 5%.

b. Extraction by CMPO-TCE

The reaction order with respect to CMPO concentration during the extraction of oxalic acid was determined for the CMPO-TCE system at 25 °C. Organic-phase CMPO concentrations were varied from 0.033 to 0.25M, while the aqueous nitric acid concentration was fixed at 0.1M. Oxalic acid was present at trace concentrations. The extraction data are shown in Fig. II-8. The slope of the line drawn through the data is 2.0, indicating that oxalic acid extraction is second order with respect to CMPO concentration. This reaction order is the same as that reported by Clarke et al.[31] for the chloride system.

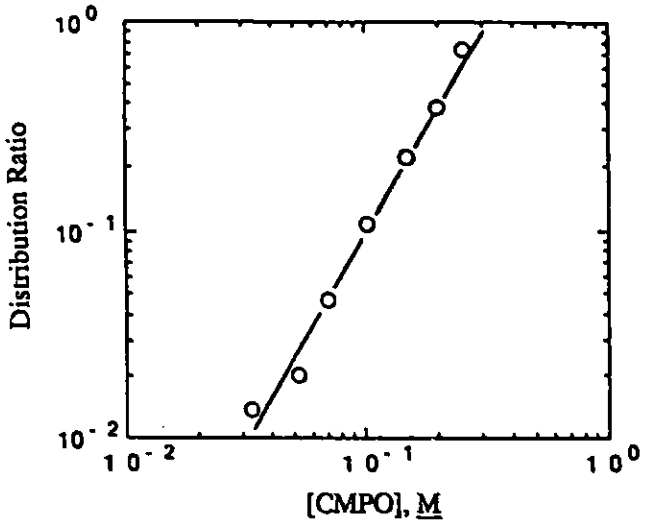

Fig. II-8.

Oxalic Acid Extraction as a Function of the Organic-Phase CMPO Concentration in TCE at 25 °C. The aqueous-phase nitric acid concentration was held constant at 0.1M. The calculated straight-line slope is 2.03.

Extraction of oxalic acid by 0.25M CMPO in TCE as a function of aqueous nitric acid concentration is shown in Fig. II-9. The maximum in the data of Fig. II-9 indicates that oxalic acid is being displaced from the organic phase by nitric acid.

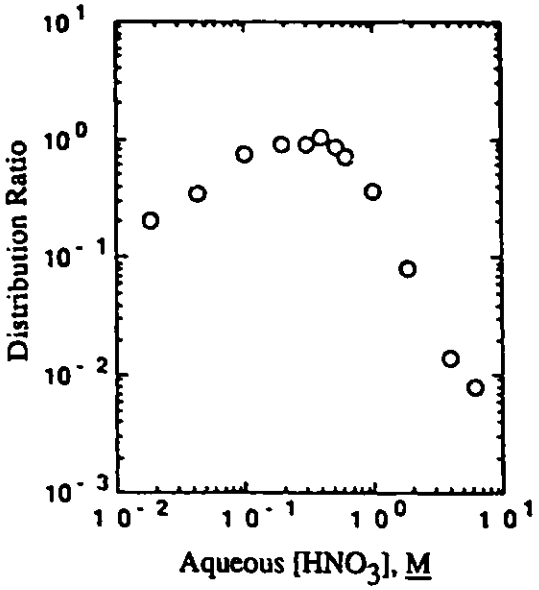

Fig. II-9.

Oxalic Acid Extraction by 0.25M CMPO in TCE as Function of Nitric Acid Concentration at 25 °C

c. Extraction by TBP-TCE

To aid in the modeling of oxalic acid extraction by the TRUEX solvents, extraction data for the TBP-TCE system were also collected. Distribution ratios of oxalic acid present at trace levels as a function of aqueous nitric acid concentration are shown in Fig. II-10 for 0.75M TBP-TCE. The distribution ratios are all lower than the corresponding data obtained for CMPO alone. The reaction order with respect to TBP concentration is two, as indicated by Fig. II-11.

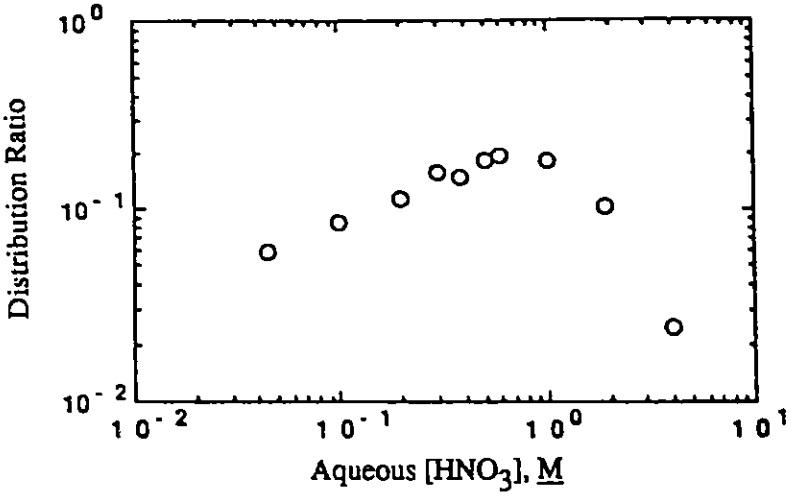

Fig. II-10. Oxalic Acid Extraction by 0.75M TBP-TCE as a Function of Aqueous Nitric Acid Concentration at 25 °C

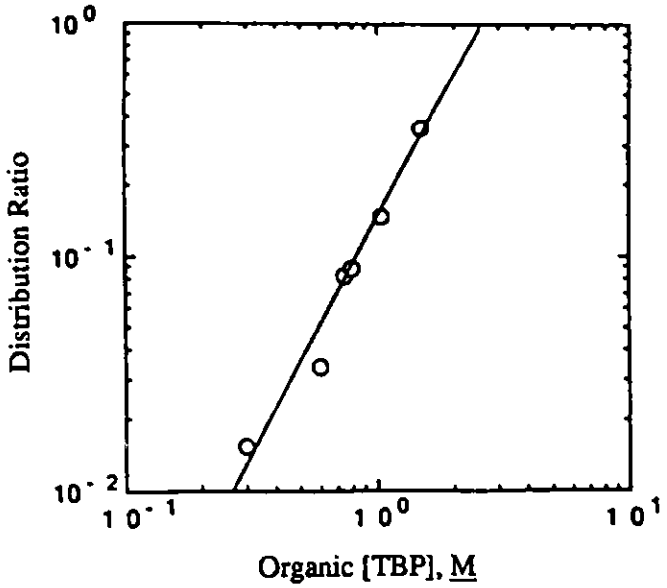

Fig. II-11. Oxalic Acid Extraction at 0.1M Nitric Acid as a Function of Organic Phase TBP Concentration at 25°C. The slope of the straight line is 2.00.

d. Extraction by TRUEX-TCE

Extraction data for oxalic acid were also measured for the TRUEX-TCE solvent (0.25M CMPO and 0.75M TBP in TCE). These data are shown in Fig. II-12.

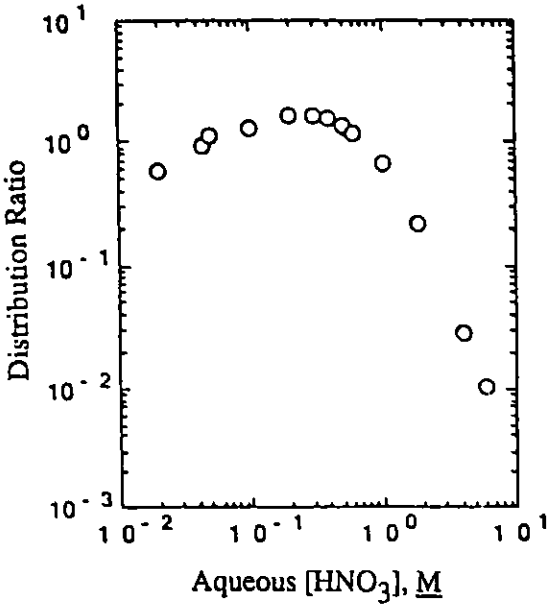

Fig. II-12.

Oxalic Acid Extraction by the TRUEX-TCE Solvent as Function of Aqueous Nitric Acid Concentration at 25°C

Although an extraction synergism is observed with CMPO and TBP mixtures, it is slight. For example, at 0.3M HNO_3, the distribution ratio for the TRUEX-TCE solvent is 1.60, while those for CMPO and TBP alone are 0.90 and 0.16, respectively.

e. Extraction by TRUEX-NPH

Extraction data were collected for the TRUEX-NPH (0.20M CMPO and 1.4M TBP in NPH) solvent as a function of aqueous nitric acid concentration. The data are reported in Fig. II-13. The distribution ratios reach a maximum at about 0.3M HNO_3 and drop off rapidly at higher acid concentrations due to a competition for the extractant molecules from oxalic and nitric acids. Comparison between the TRUEX-TCE and TRUEX-NPH solvents shows that the NPH-based solvent extracts oxalic acid slightly better than the TCE-based solvent. This probably reflects the higher TBP concentration in the NPH-based solvent. Temperature effects on oxalic acid extraction appear to be minimal. The extraction isotherm measured at 25°C (Fig. II-13) is very similar to that reported earlier[32] for the TRUEX-NPH system at 40°C (see Fig. II-14).

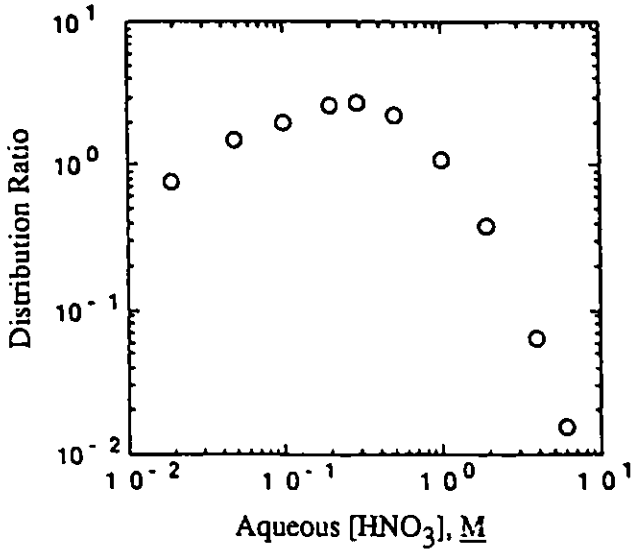

Fig. II-13.

Oxalic Acid Extraction by TRUEX-NPH as a Function of Aqueous Nitric Acid Concentration at 25°C

2. Plutonium (IV) Extraction
(L. Reichley-Yinger)

The focus of this work was to determine the effects of solvent composition and temperature on Pu(IV) extraction by TRUEX-NPH solvent. The effect of [CMPO] was determined by measuring the Pu(IV) distribution ratio for solvents containing 0.0 to 0.4M CMPO and 1.4M TBP in NPH. Temperature effects were determined by measuring the Pu(IV) distribution ratio at 25 and 50°C in the presence and absence of $NaNO_3$ and the complexants $H_2C_2O_4$, H_2SO_4, and H_3PO_4. The effects of $NaNO_2$ and HF on the extraction of Pu(IV) were also determined.

The effect of $NaNO_2$ on Pu(IV) extraction was first noticed while trying to prepare americium-free Pu(IV) for measuring distribution ratios. To determine the oxidation state of the isotopically pure Pu-238 after various amounts of $NaNO_2$ were added, LaF_3 precipitation was done. As the amount of nitrite added increased, the amount of plutonium that precipitated decreased by as much as 30%. Since such a decrease has also been observed for yttrium, which is not known to exist in the IV oxidation state,[33] we concluded that this decrease does not indicate the oxidation of Pu(IV) to Pu(VI) but rather the formation of Pu(IV)-NO_2^- complexes, which may be extracted by TRUEX-NPH. Figure II-15 shows the effect of various amounts of $NaNO_2$ on Pu(IV) extraction by TRUEX-NPH from 0.1 and 1M HNO_3 at 25°C. Increased sodium nitrite appears to enhance the extraction of Pu(IV) at 0.1 and 1M HNO_3 but to different extents. For this reason, Pu(IV) distribution measurements were performed without the addition of sodium nitrite.

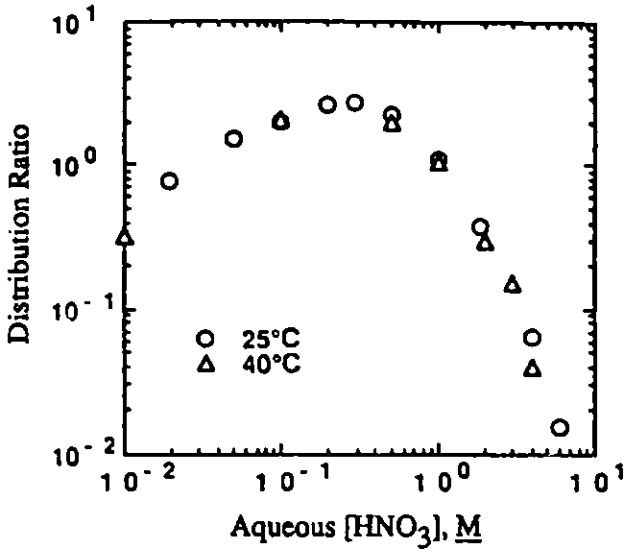

Fig. II-14.

Extraction of Oxalic Acid by TRUEX-NPH at 25 and 40°C. Data at 40°C were reported earlier in Ref. 30.

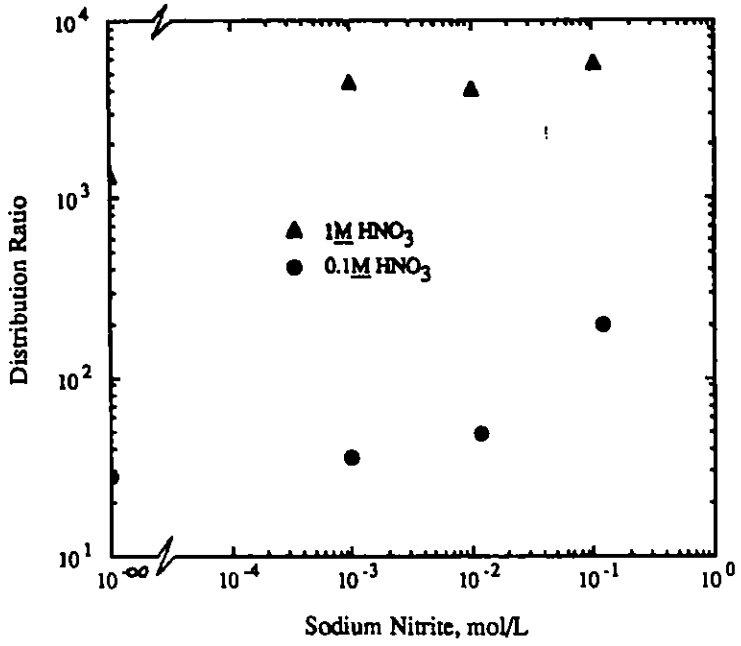

Fig. II-15. Effect of Sodium Nitrite on Pu(IV) Extraction by TRUEX-NPH from Nitric Acid at 25°C

Figure II-16 shows the effect of total [CMPO] in 1.4M TBP-NPH on Pu(IV) extraction from 0.5M HNO_3 at 25°C. The slope of the best-fit line is 1.2. This suggests that, at least at 0.5M HNO_3, Pu(IV) can be treated as extracted by one CMPO. Tri-n-butyl phosphate also extracts Pu(IV) from nitrate media and likely participates with CMPO in the extraction. Since the plutonium distribution ratio has a second-order dependency on [TBP] in the absence of CMPO,[34] the following equilibrium is proposed:

$$Pu(IV) + 4\ NO_3^- + \overline{CMPO} + \overline{TBP} = \overline{Pu(NO_3)_4 \cdot CMPO \cdot TBP} \qquad (II\text{-}53)$$

The effect of temperature on the extraction of Pu(IV) from HNO_3 is shown in Fig. II-17. The increase in temperature from 25 to 50°C decreased the Pu(IV) distribution ratios. Distribution ratios measured at both temperatures have an approximate second-order dependence on NO_3^- concentration between 0.05 and 0.5M HNO_3.

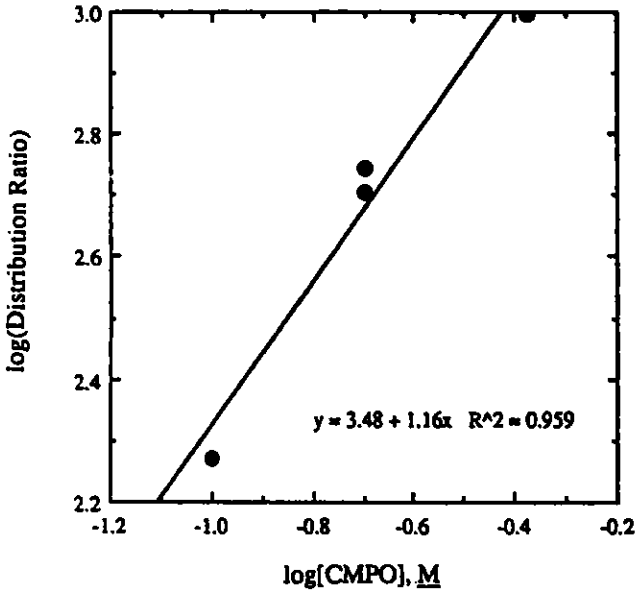

Fig. II-16.

Effect of Total [CMPO] in 1.4M TBP-NPH on Pu(IV) Extraction from 0.5M HNO_3 at 25°C

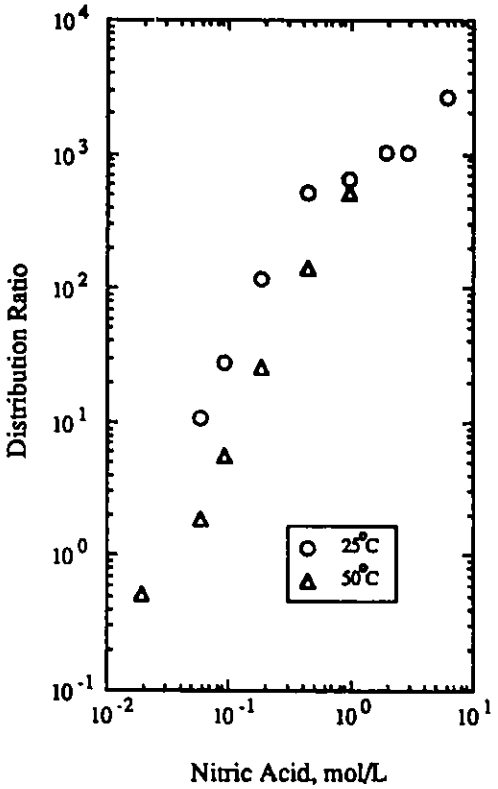

Fig. II-17.

Effect of Temperature on Pu(IV) Extraction by TRUEX-NPH from HNO_3

Figures II-18 to II-21 indicate the effect of HNO_3-$NaNO_3$ solutions ($[NO_3^-]_t$ = 3.2M) containing no complexant, $H_2C_2O_4$, H_2SO_4, and H_3PO_4, respectively, on Pu(IV) extraction by TRUEX-

NPH at 25 and 50°C. The effect of HF on Pu(IV) extraction from 0.1M HNO_3 and 3.1M $NaNO_3$ at 25°C is shown in Fig. II-22. The presence of $NaNO_3$ enhances the extraction of Pu(IV) over that for HNO_3-only solutions (compare Figs. II-17 and -18), while the presence of $H_2C_2O_4$ (Fig. II-19) and H_3PO_4 (Fig. II-21) suppresses Pu(IV) extraction relative to that in the absence of complexants. Hydrofluoric acid also suppresses Pu(IV) extraction. The large differences in the extent of suppression for the forward and back extractions at [HF] > 0.1M can be explained by the presence of Pu(III) in the system. Because it is less complexed by F than the Pu(IV) oxidation state, its D value would be higher than that of Pu(IV) in this system. Sulfuric acid has no observable effect on Pu(IV) extraction. The increase in temperature from 25 to 50°C decreased Pu(IV) extraction in the presence of H_3PO_4. For $NaNO_3$, $H_2C_2O_4$, and H_2SO_4, the increase in temperature had either no effect or an uncertain effect on Pu(IV) extraction.

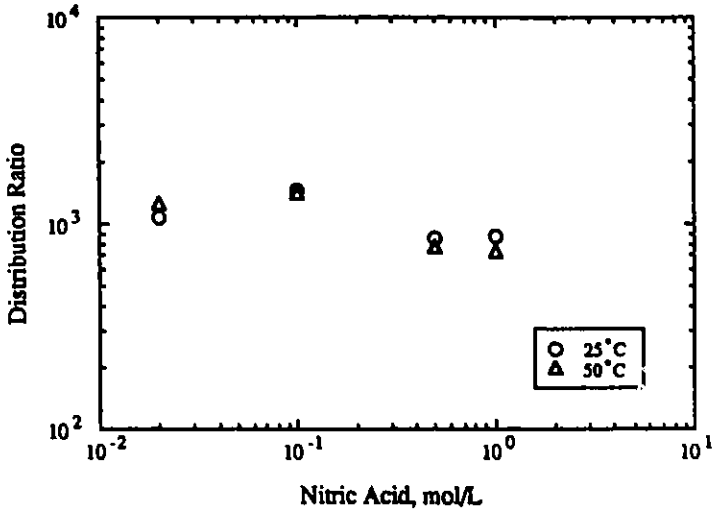

Fig. II-18. Effect of Nitric Acid on Pu(IV) Extraction by TRUEX-NPH from HNO_3-$NaNO_3$ Solutions with $[NO_3^-]_t$ = 3.2M at 25 and 50°C (with no complexant)

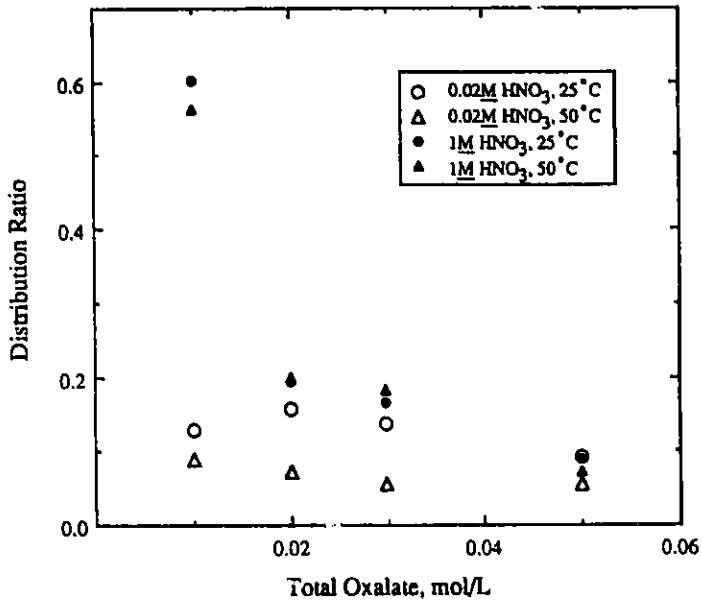

Fig. II-19. Effect of $H_2C_2O_4$ on Pu(IV) Extraction by TRUEX-NPH from 3.2M NO_3^- Solutions at 25 and 50°C

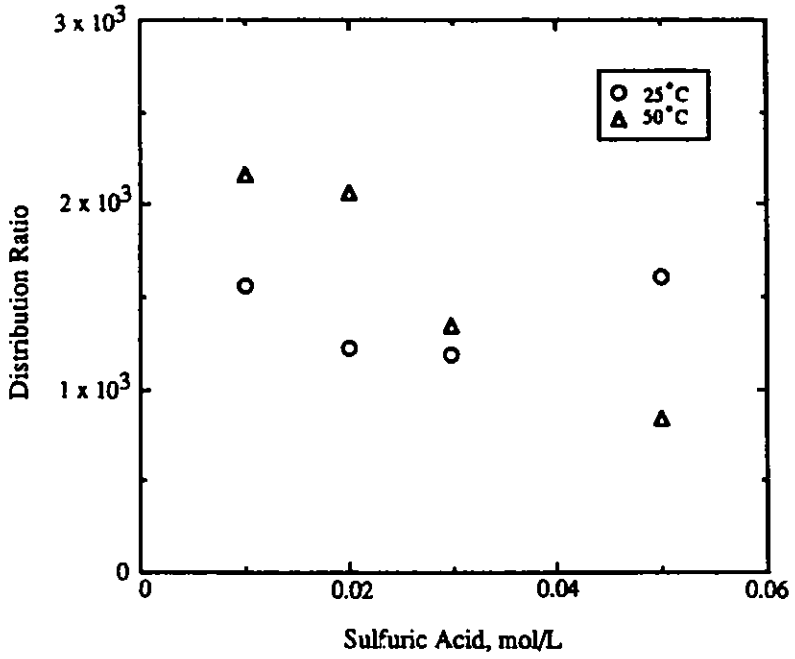

Fig. II-20. Effect of H_2SO_4 on Pu(IV) Extraction by TRUEX-NPH from 0.02M HNO_3 and 3.18M $NaNO_3$ Solutions at 25 and 50°C

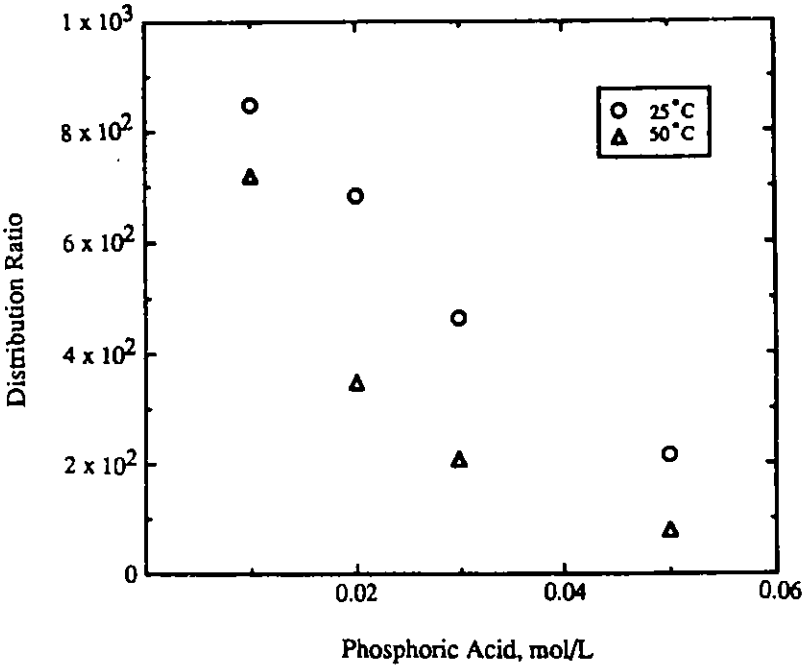

Fig. II-21. Effect of H_3PO_4 on Pu(IV) Extraction by TRUEX-NPH from 0.02M HNO_3 and 3.18M $NaNO_3$

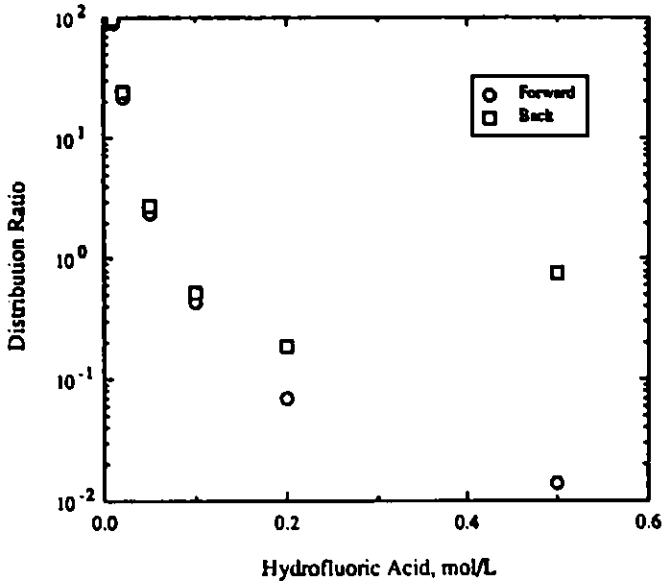

Fig. II-22.

Effect of HF on Pu(IV) Extraction (forward and back) by TRUEX-NPH from 0.1M HNO_3 and 3.1M $NaNO_3$ at 25°C

3. Rare Earth Extraction
(L. Reichley-Yinger)

Distribution ratios for the lanthanides, Ce, Pr, Nd, Sm, Eu, and Gd have been determined between TRUEX-NPH and HNO_3 solutions at 25°C. Since the metal concentrations were measured by inductively coupled plasma/atomic emission spectroscopy (ICP/AES), two metal stock solutions were prepared to prevent interferences. The compositions of the two solutions are listed in Table II-5. Appropriate amounts of these solutions were added to 0.02, 0.1, 0.4, 1, 2, 3, 6, and 8M HNO_3 to permit analysis by ICP/AES. Concentrations of these metal salts are high enough that, if they are extracted significantly (D>1), a significant amount of the CMPO concentration is used in extracting them (solvent loading). Distribution ratios for these metals in 0.02 to 1M HNO_3 are given in Table II-6. For $[HNO_3]$ > 1M, third-phase formation was observed; in this case, distribution ratios between the two organic phases and the aqueous phase were calculated based on the initial and final aqueous-phase metal concentrations. These distribution ratio values are given in Table II-7.

Table II-5. Composition of Rare Earth Stock and Contacting Solutions

		Conc.,[a] mol/L	
Soln.	Metal	Stock[a]	Contacting[b]
A	Ce	1.095	0.0210
	Nd	1.116	0.0223
	Gd	0.553	0.0111
	Y	0.261	0.0052
B	Pr	1.192	0.0238
	Sm	0.565	0.0113
	La	0.580	0.0116
	Eu	0.229	0.0046

[a]Determined by ICP/AES. Errors <5%, in 0.01M HNO_3.
[b]Concentration in original aqueous phase before contact based on diluting stock 100 μL/5 mL solution.

Table II-6. Rare Earth Distribution Ratios[a,b] between TRUEX-NPH and HNO_3 at 25°C

[HNO_3], M	Y	La	Ce	Pr	Nd	Sm	Eu	Gd
0.02	0.0488	0.422	0.506	0.590	0.497	0.546	0.444	0.242
0.09	0.0938	0.768	1.01	1.10	1.03	1.02	0.824	0.489
0.44	0.300	2.63	3.14	4.21	3.20	3.77	3.10	1.52
0.96	0.481	3.88	4.35	6.80	4.55	6.07	5.02	2.24

[a]Errors estimated at <10%.

[b]Determined at O/A phase ratio of one and original aqueous-phase concentrations of metals as shown in Table II-5. Organic phase was pre-equilibrated with nitric acid solution only.

Table II-7. Estimated Rare Earth Distribution Ratios[a,b] between Two Organic Phases and HNO_3 at 25°C

[HNO_3], M	Y	La	Ce	Pr	Nd	Sm	Eu	Gd
1.9	0.698	3.90	5.12	7.71	5.72	7.14	5.74	2.94
3.0	0.943	3.39	4.68	7.32	5.59	7.29	6.00	3.19
6.0	1.60	1.79	2.61	4.76	3.83	6.59	5.88	3.31
8.3	2.62	1.26	2.03	3.92	3.36	6.93	6.64	4.01

[a]Estimated based on the initial and final aqueous-phase metal concentrations.

[b]Determined at O/A phase ratio of one and original aqueous-phase concentrations of metals as shown in Table II-5. Organic phase was pre-equilibrated with nitric acid solution only.

A comparison of the cerium distribution ratio results with radiotracer and ICP/AES results measured earlier (ANL-88-28, pp. 68-70) is shown in Fig. II-23. The present results agree with the radiotracer results at 0.1M HNO_3. Above 0.1M HNO_3, the present results are significantly lower than the radiotracer results. High solvent loading (≤62% based on 3 CMPO/metal ion) causes this deviation from the radiotracer results. The 1986 ICP/AES results follow the radiotracer results up to 1M HNO_3 but then drop toward the present results for 3 and 6M HNO_3, which contained third phases. Third-phase formation was only reported at 10M HNO_3 for the 1986 cerium distribution ratio results.

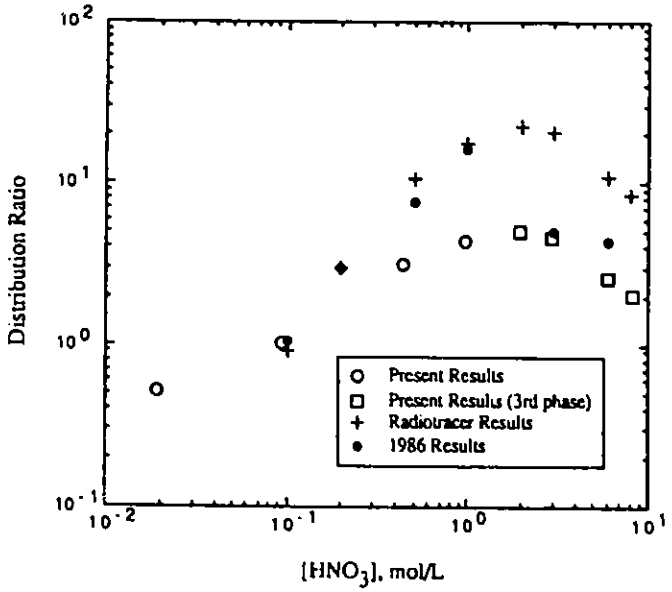

Fig. II-23.

Cerium Distribution Ratios between TRUEX-NPH and HNO_3 at 25°C

Figure II-24 compares the yttrium distribution results to radiotracer and ICP/AES results obtained in 1986. Except for the shape of the curve (there is no maxima for yttrium), the same relative behavior between the results is seen for yttrium as was noted for cerium. High solvent loading is again suggested as the cause of the differences between the radiotracer and ICP/AES results.

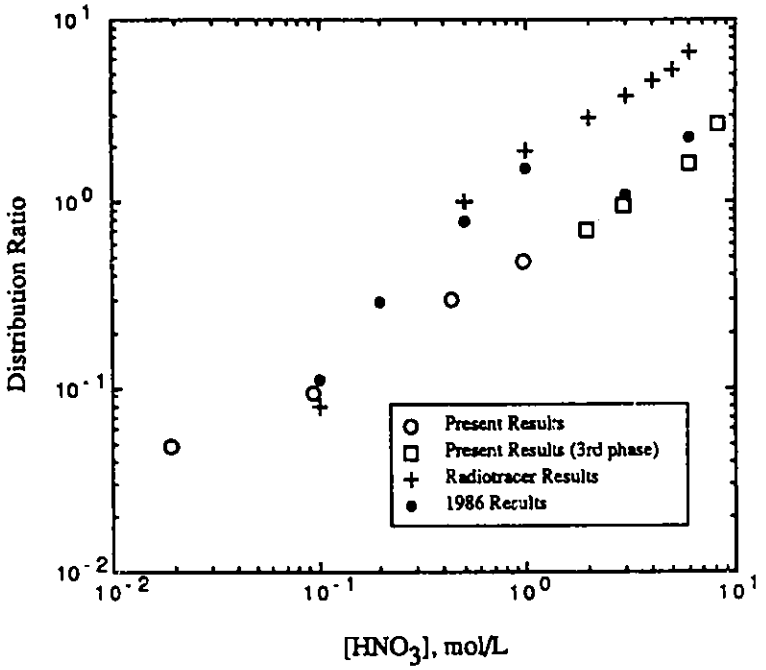

Fig. II-24. Yttrium Distribution Ratios between TRUEX-NPH and HNO_3 at 25 °C

4. Thorium, Neptunium, and Curium Extraction
(J. Sedlet)

a. Introduction

Extraction studies of Th, Np, and Cm were conducted during this reporting period to obtain distribution ratio data for the GTM data base. Distribution ratio measurements for neptunium and plutonium (IV) have given variable results in the past (ANL-90/15, pp. 112-123). It was thought that similar measurements with thorium might provide some insight into this problem since thorium, unlike plutonium and neptunium, has only one oxidation state (IV), while plutonium and neptunium have four oxidation states in acid solution (III, IV, V, and VI). The states of principal interest in the TRUEX process, IV and V for neptunium and III and IV for plutonium, have greatly different distribution ratios. Extraction data for curium were not available, and although it is expected to behave similarly to americium, quantitative information to confirm this was deemed necessary. Curium has several long-lived alpha-emitting isotopes that are produced in nuclear reactors.

b. Experimental

The experimental procedures, reagents, and equipment used to measure distribution ratios have been described in previous semiannual reports and will be reviewed here briefly.

Two TRUEX solvents were used: TRUEX-NPH (0.2M CMPO and 1.4M TBP dissolved in Conoco C_{12}-C_{14}) and TRUEX-TCE (0.25M CMPO and 0.75M TBP in TCE).

Distribution measurements were made by contacting equal volumes (except where noted) of solvent and aqueous solutions in a screw-cap culture tube for three 20-s intervals. The contacting was done with a Vortex mixer. Before the first contact, between the 20-s contacts, and after the final contact, the tubes were placed in a constant-temperature bath for 2 min. The tubes were then centrifuged, the phases separated, and aliquots of each phase measured for radioactive content. All organic phases were pre-equilibrated with aqueous solutions of the same composition as used in the distribution ratio measurements.

The curium isotope used was ^{244}Cm, an alpha emitter with an 18.1 y half-life. The thorium isotope used was ^{230}Th, an alpha emitter with a 7.5×10^4 y half-life. Concentrations of these isotopes were measured by liquid scintillation counting of their alpha particles.

A mixture of ^{239}Np and ^{237}Np was used for neptunium. The former isotope is a beta-gamma emitter with a 56.4 h half-life. In the first extraction, ^{237}Np was added at a concentration of about 10^{-5}M to provide mass. The neptunium concentration was determined by counting the ^{239}Np gamma rays with a sodium iodide crystal.

The reagents used in the extractions for each element are given below.

c. Thorium Extraction Results

The distribution of thorium between nitric acid solutions and TRUEX-NPH was examined to study the behavior of an actinide element with only a IV oxidation state. (For all the work with thorium, the TRUEX-NPH solvent was prepared with the assumption that the CMPO was 98% pure.) It was believed that this study would help clarify the variable results obtained earlier with Pu(IV) and Np(IV) (ANL-90/15, pp. 112-123).

The ^{230}Th obtained from Oak Ridge National Laboratory contained sufficient alpha- and beta-emitting decay products of ^{230}Th and ^{232}Th (present as impurities) to require purification. The thorium was separated from its decay products, principally ^{224}Ra and ^{226}Ra and their daughters, by extracting the thorium from 0.1M HNO_3 into pre-equilibrated TRUEX-NPH at an organic-to-aqueous phase ratio of one. Previous experiments had shown that the distribution ratio of thorium in this system is about 80; thus, about 99% of the thorium should extract and leave divalent radium behind. Analysis of the two phases after contact showed that about 95% extracted. Prior to this purification, three series of extractions were performed with the original ^{230}Th aqueous tracer solution.

The results of the first series are given in Table II-8. The distribution ratios are lower for the forward than the reverse extractions and indicate either that purification from the radium decay products of thorium is necessary, or that more than one thorium species is present. The reverse extraction ratios for thorium are plotted in Fig. II-25, together with those given for neptunium (IV) in a previous semiannual (ANL-90/15, pp. 112-123). The thorium distribution ratio increases up to 3M HNO_3, then drops sharply at 5M. The neptunium ratios also reached a maximum at 3M HNO_3, but decreased only slightly at 5M. The slope for log thorium distribution ratio vs. log [HNO_3] is 1.9 up to about 1M HNO_3. Since radium does not extract at the nitric acid concentrations used, the reverse extractions should represent ratios for pure thorium.

Table II-8. First Series of Distribution Ratios for Thorium between Nitric Acid and TRUEX-NPH at 25°C

	Distribution Ratio		
		Reverse Extractions	
$[HNO_3]$, M	Forward Extraction	1	2
0.05	15.8	25.8	30.4
0.10	25.6	82.5	75.5
0.20	87.3	379	419
0.5	118	2.26×10^3	2.17×10^3
1.0	115	4.88×10^2	6.09×10^3
2.0	117	8.68×10^3	9.1×10^3
3.0	120	9.27×10^3	9.30×10^3
5.0	124	4.72×10^3	4.31×10^3

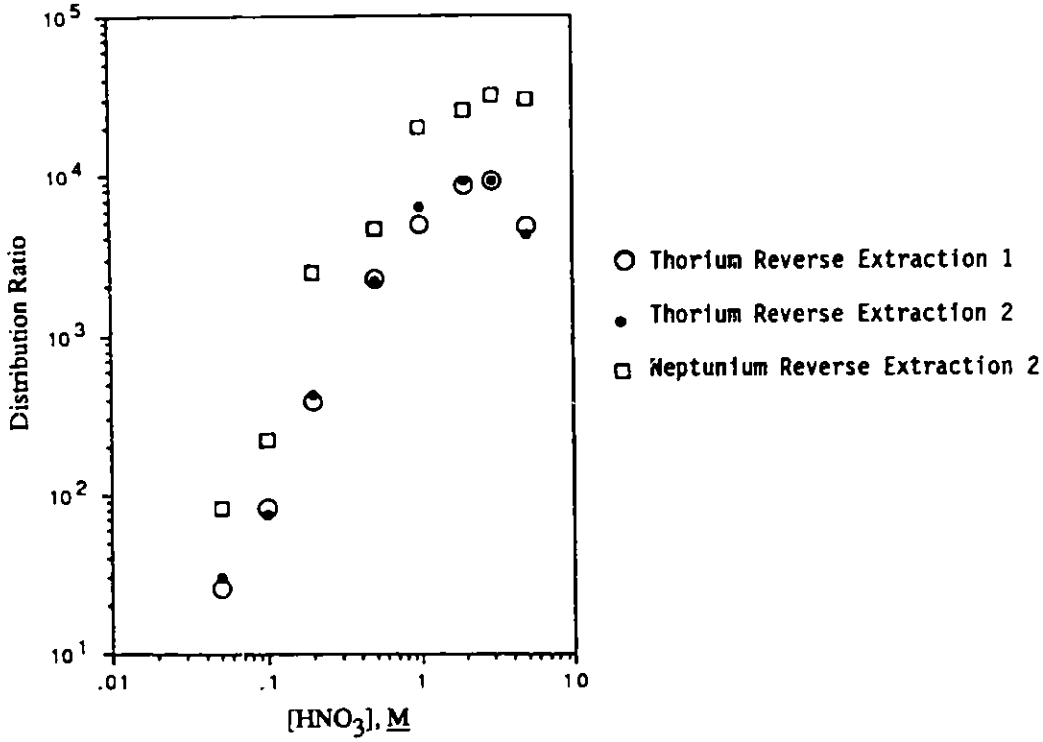

Fig. II-25. Distribution of Thorium and Neptunium(IV) between Nitric Acid and TRUEX-NPH at 25°C

To verify the maximum obtained for thorium, one forward and two reverse extractions were performed at acid concentrations of 1, 2, 3, and 5M HNO_3. In this case, only the solutions from the reverse extractions were analyzed. The results are given in Table II-9 and reflect the same trend as indicated in Fig. II-25, with a maximum at 3M and a sharp drop between 3 and 5M HNO_3. The absolute values, however, differ by 3% (at 3M) to 28% (at 5M).

To extend the acid concentrations to higher values, extractions were performed at 3, 5, 6, and 8M HNO_3 with the purified ^{230}Th, now contained in TRUEX-NPH solution instead of nitric acid. Since small aliquots of this thorium solution were added to the pre-equilibrated organic phase, the measurement is termed a reverse or back extraction. The results are given in Table II-10. In this case, the decrease between 3 and 5M is small, not the factor of two observed previously; the ratios at 3 and 5M are

two to four times greater than measured earlier (Tables II-8 and II-9), but the decrease at higher acidities continues.

Table II-9. Second Series of Distribution Ratios for Thorium between Nitric Acid and TRUEX-NPH at 25°C

	Reverse Extractions	
$[HNO_3]$, M	1	2
1.0	4.70×10^3	5.26×10^3
2.0	9.18×10^3	9.49×10^3
3.0	9.53×10^3	1.00×10^4
5.0	5.19×10^3	5.70×10^3

Table II-10. Third Series of Distribution Ratios for Thorium between Nitric Acid and TRUEX-NPH at 25°C

	Reverse Extractions	
$[HNO_3]$, M	1	2
3.0	2.24×10^4	3.31×10^4
5.0	2.18×10^4	2.72×10^4
6.0	1.38×10^4	1.26×10^4
8.0	1.03×10^4	1.83×10^4

The effect of nitrite ion on thorium extraction was explored because of the reported effect of nitrite on the extraction of Pu(IV), as well as the coprecipitation of Pu(IV), trivalent actinides, and yttrium with lanthanum fluoride.[33] Nitrite ion is usually added to plutonium solutions to stabilize the quadrivalent state. The results obtained by Orlandini[33] could also be interpreted in terms of a Pu(IV)-nitrite complex that is highly extractable and prevents complete coprecipitation. In the case of thorium, any effect of nitrite on the distribution ratios cannot be explained as a redox effect, since thorium has only a single stable oxidation state. We added ^{230}Th in TRUEX-NPH to pre-equilibrated TRUEX-NPH and completed two successive extractions of the organic phase. The results are given in Table II-11. The distribution ratio for 1M HNO_3 in the absence of sodium nitrite was approximately the same as found earlier (Table II-8), but decreased with increasing nitrite concentration. An aqueous thorium-nitrite complex may be formed, but it is much less extractable than the plutonium-nitrite complex. The data in Tables II-9 to II-11 indicate that the extraction mechanisms and thorium speciation are more complex than was expected for a simple ion, and further studies should be performed.

Table II-11. Effect of Nitrite Ion on the Distribution Ratio of Thorium between Nitric Acid and TRUEX-NPH at 25°C

Aqueous Phase Comp., M		Reverse Distribution Ratio	
$[HNO_3]$	$[NaNO_2]$	1	2
1	0	4.31×10^3	5.78×10^3
1	0.01	3.99×10^3	5.78×10^3
1	0.1	2.82×10^3	3.85×10^3
1	1.0	297	599

d. Neptunium Extraction Results

(1) Distribution Ratios for Np(V)

Distribution ratio measurements between nitric acid and TRUEX-NPH solvent were made at 25 °C and 50 °C with a mixture of ^{237}Np and ^{239}Np. The tracer was prepared by extracting ^{239}Np with 5% (v/v) tri-isooctyl amine in xylene solution from its parent, ^{243}Am, in concentrated hydrochloric acid. Sufficient ^{237}Np had been added to give an initial concentration of approximately 10^{-5}M in the first extraction. The extracted neptunium, which is in the IV oxidation state, was converted to the V oxidation state by treating it with 1M HNO_3-0.05M $KMnO_4$ solution to oxidize it to the VI state, then adding an equal volume of 0.25M $NaNO_2$ to reduce the Np(VI) to Np(V). These are fast reactions and were used because the direct oxidation of Np(IV) to Np(V) is slow.

Aliquots of the Np(V) tracer were added to nitric acid solutions in the concentration range of 0.02 to 8M, and four successive extractions were performed, each with fresh TRUEX-NPH solvent previously pre-equilibrated three times with nitric acid of the same concentration. The first three extractions were performed with an organic/aqueous volume ratio of 1 to 4. The fourth extraction was performed with an organic-to-aqueous phase ratio of one. Since it is difficult to convert all of the neptunium to the pentavalent state, and since the distribution ratios for Np(IV) and Np(VI) are much larger than for Np(V), the first three extractions were intended to remove any neptunium, (IV) and (VI), and the fourth extraction was intended to give the ratio for pure Np(V). The aqueous phases for the first and fourth extraction were made 0.01M in sulfamic acid, which reacts with nitrite ion, since low concentrations of nitrite catalyze the oxidation of neptunium to the VI state by nitric acid. The results are given in Table II-12 and plotted for the fourth extraction in Fig. II-26.

Table II-12. Distribution Ratios for Np(V) between Nitric Acid and TRUEX-NPH[a] Solvent at 25 and 50 °C

$[HNO_3]$[b], M		Distribution Ratio[c]							
		25 °C				50 °C			
Actual	Nominal	Extr. 1	Extr. 2	Extr. 3	Extr. 4	Extr. 1	Extr. 2	Extr. 3	Extr. 4
0.01905	0.02	0.00773	0.00698	0.00773	0.00780	0.0074	0.0043	0.0114	0.0038
0.05818	0.05	0.0195	0.0186	0.0194	0.0199	0.0143	0.0120	0.0042	0.0100
0.09275	0.10	0.0288	0.0291	0.0286	0.0305	0.0340	0.0200	0.0207	0.0172
0.1826	0.20	0.0478	0.0497	0.0504	0.0553	0.0589	0.0332	0.0371	0.0302
0.4379	0.50	0.0127	0.0913	0.0990	0.104	0.125	0.0691	0.0802	0.0611
0.9627	1.0	-	0.0208	0.207	0.211	0.205	0.160	0.149	0.133
1.9848	2.0	0.511	0.475	0.458	0.478	0.264	0.269	0.252	0.231
2.959	3.0	0.791	0.964	0.920	0.968	0.411	0.541	0.469	0.400
5.984	6.0	2.87	1.03	1.00	1.30	1.34	1.96	3.87	1.88
8.335	8.0	6.09	9.38	9.09	9.87	3.12	6.33	12.25	5.35

[a]The solvent was prepared with the assumption that the CMPO was 100% pure.

[b]In some cases, the actual (or titrated concentrations) differed from the nominal (or intended) value. Since the results are plotted with the nominal values, both concentrations are given in the table.

[c]Four successive extractions of the aqueous phase were performed, each with fresh solvent.

The distribution ratios for Np(V) were 10^4 to 10^5 times lower than those for Np(IV) and Np(VI), as would be expected for the singly charged Np(V) ion, NpO_2^+. There are some unexpected variations between the four extractions at the same acidity, although in most cases the ratios remained relatively constant from the first or second extraction to the fourth. In general, the ratios are about 40-50% lower at 50 °C than at 25 °C. The large increase in distribution ratio for 8M HNO_3 at 25 °C

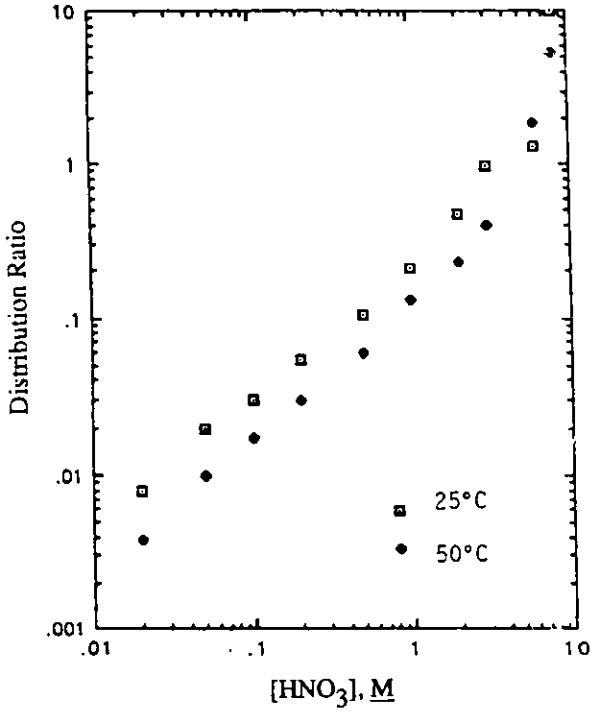

Fig. II-26.

Distribution of Np(V) between Nitric Acid and TRUEX-NPH as a Function of Nitric Acid Concentration at 25°C and 50°C

and for 6 and 8M HNO_3 at 50°C was probably due to partial oxidation of the Np(V) to Np(VI) at these high nitric acid concentrations. The increase in the distribution ratio with increasing acid concentration is nearly linear, with a slope of about 0.85, up to 6M at 25°C and to 3M at 50°C. Figure II-27 compares the distribution ratios at 25°C with those obtained previously at nitric acid concentrations from 0.05 to 5M (ANL-90/15, p. 116). The values agree quite well, except at the highest acidities, where partial oxidation to Np(VI) is possible.

(2) Distribution Ratios for Np (IV)

One set of Np (IV) experiments was performed with TRUEX-TCE solvent before it was decided that the toxic properties of chlorinated hydrocarbons would prohibit its use in the TRUEX process on a large scale. The ^{239}Np-^{237}Np tracer was extracted into TRUEX-TCE from 0.5M HNO_3- 0.02M $Fe(NO_3)_2$ solution to give an initially pure Np(IV) species. The term "initially pure" is used since the neptunium is extracted from a reducing environment; however, partial oxidation of the Np(IV) can occur during or between extractions. The extracted Np(IV) was added to the solvent phase, and two successive extractions were performed at ten nitric acid concentrations ranging from 0.02 to 8M. Thus, each extraction is termed a reverse extraction. Each aqueous phase was made 0.02M in $Fe(NO_3)_2$, 0.04M in hydroxylamine nitrate, and 0.01M in sulfamic acid (to destroy any nitrite ion) before contacting it with the organic phase. Equal volumes of the two phases were used for the acid concentrations from 0.02 to 0.5M. To obtain higher counting rates from the aqueous phase at high distribution ratios, an organic-to-aqueous volume ratio of 1:3 was used for acids in the range of 1 to 8M, and the entire aqueous phase was counted. The results are given in Table II-13 and plotted in Fig. II-28. The two extractions were performed on successive days and the differences (the reasons for which are as yet unexplainable) appear to depend on the acid concentration. The ratios obtained for the first extraction increased approximately linearly with increasing nitric acid concentration (except for a low value at 1M HNO_3) up to 3M HNO_3. The slope of the best-fit curve in this region was about 1.5. The ratios fell below this line at 6 and 8M HNO_3, possibly due to third-phase formation as the Fe(III) concentration increased.

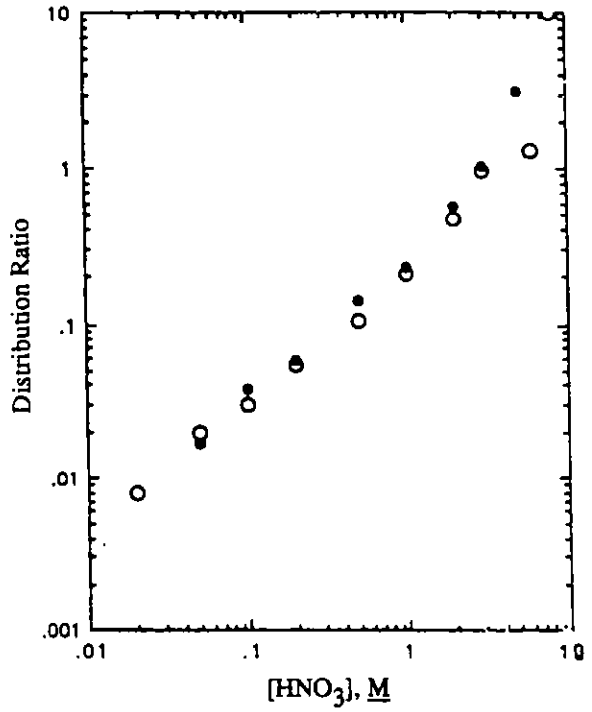

Fig. II-27.

Distribution of Np(V) between Nitric Acid and TRUEX-NPH as a Function of Nitric Acid Concentration at 25 °C. (Open circles from Table II-12, Extr. 4; closed circles from ANL-90/15, p. 116.)

Table II-13. Distribution Ratios for Np(IV) between Nitric Acid and TRUEX-TCE Solvent[a] at 25 °C

	Reverse Extraction	
$[HNO_3]$[b], M	1	2
0.02	12.3	5.9
0.05	46.5	6.5
0.1	104	9.3
0.2	373	66.5
0.5	1.58×10^3	4.92×10^3
1.0	1.51×10^3	7.02×10^3
2.0	1.31×10^4	4.92×10^3
3.0	1.61×10^4	3.63×10^3
6.0	2.51×10^4	2.68×10^4
8.0	1.95×10^4	1.42×10^4

[a]The TRUEX-TCE solvent was prepared with the assumption that the CMPO was 98% pure.
[b]Nominal values. See footnote b in Table II-12.

A series of extractions was performed with ^{239}Np-^{237}Np(IV) tracer after it had been first extracted into TRUEX-NPH to obtain a "solvent-loaded" tracer. The extracted tracer was added to the solvent phase, and the extractions conducted as described above.

In the first series, four successive extractions of the organic phase were performed at 25 °C with nitric acid concentrations ranging from 0.02 to 8.0M. The results are given in Table II-14 and plotted in Fig. II-29, together with distribution ratios obtained earlier for the acid range 0.05-5M HNO_3

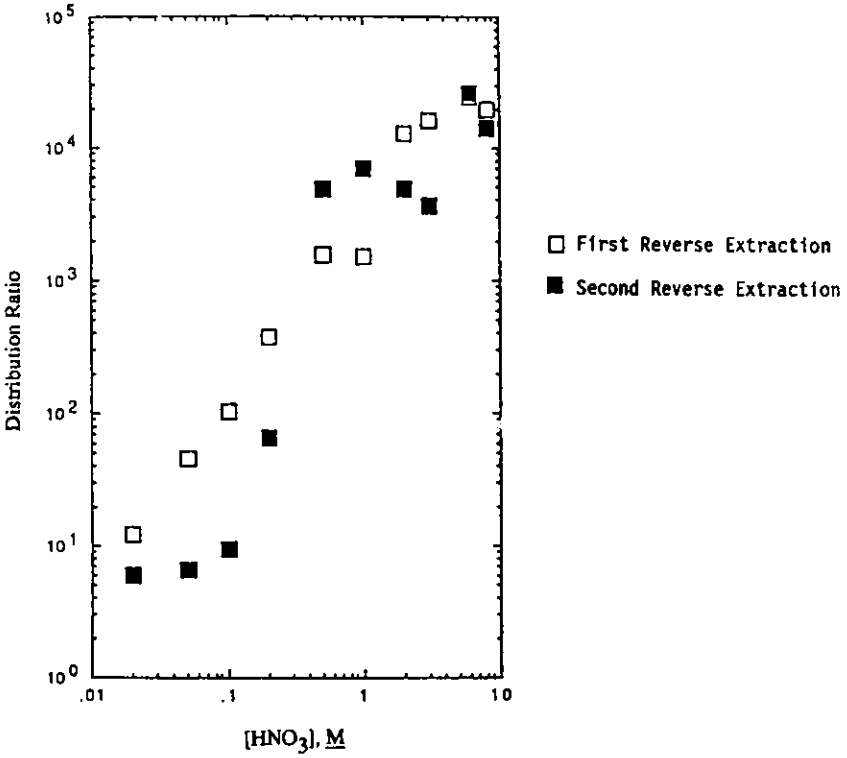

Fig. II-28. Distribution Ratios for Np(IV) in TRUEX-TCE Solvent as a Function of Nitric Acid Concentration at 25 °C

Table II-14. Distribution Ratios for Np(IV) between Nitric Acid and TRUEX-NPH Solvent[a] at 25 °C

	Distribution Ratios				
	Reverse Extr.				Previous Results
$[HNO_3]$,[b] M	1	2	3	4	Reverse Extr. 2[c]
0.02	9.6	10.8	17.9	7.0	
0.05	26.5	36.6	61.8	20.4	83
0.1	50.8	59.3	87.4	27.4	216
0.2	126	172	352	628	2.4×10^3
0.5	1.07×10^3	1.31×10^3	1.40×10^3	1.08×10^3	4.5×10^3
1.0	9.93×10^3	1.06×10^4	7.57×10^3	2.10×10^4	2.0×10^4
2.0	1.21×10^4	2.17×10^4	1.82×10^4	2.06×10^4	2.6×10^4
3.0	3.0×10^4	2.84×10^4	2.18×10^4	3.2×10^4	3.3×10^4
5.0	-	-	-	-	3.0×10^4
6.0	2.37×10^4	3.29×10^4	1.98×10^4	3.6×10^4	
8.0	8.0×10^3	7.6×10^3	4.8×10^3	-	

[a]The TRUEX-NPH solvent was prepared assuming that the CMPO was 98% pure.
[b]Nominal values. See footnote b, Table II-12.
[c]From ANL-90/15, p. 120.

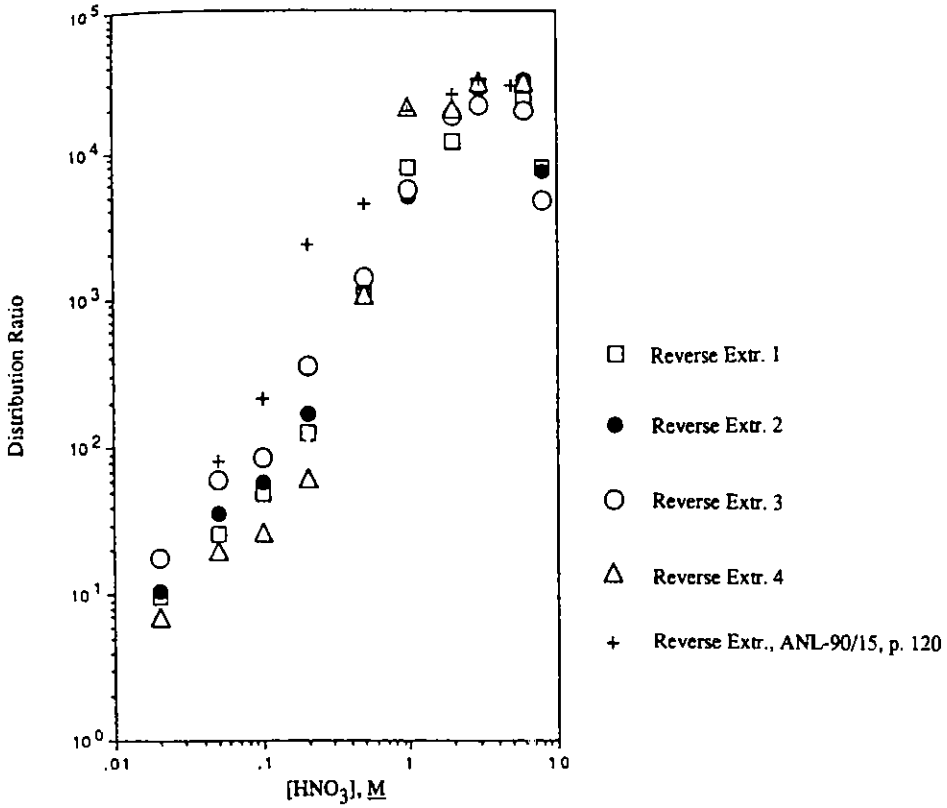

Fig. II-29. Distribution Ratios for Np(IV) in TRUEX-NPH Solvent as a Function of Nitric Acid Concentration at 25 °C

(ANL-90/15, p. 116). As was found earlier, the distributions vary widely, but generally increase to values of 10^3-10^4 at 0.5M HNO_3 and above. The most linear increase with acid concentration was obtained for the first extraction. The slope in this case was about 1.6. The slope of the best-fit line for the 0.05-5M data for all extractions was about the same value. Each aqueous phase was made 0.02M in $Fe(NO_3)_3$, 0.04M in $NH_2OH{\cdot}HNO_3$, and 0.01M in sulfamic acid before extraction. Third-phase formation was observed at 6 and 8M HNO_3, probably due to loading of the organic phase with Fe(III). The decrease in the distribution ratios at these high acidities is believed to be due to this problem. Future experiments will be done with a lower ferrous ion concentration in an attempt to eliminate third-phase formation.

A similar series of extractions was performed at 50 °C, except that the concentrations of $Fe(NO_3)_2$ and $NH_2OH{\cdot}HNO_3$ were half of those used at 25 °C. The results are given in Table II-15 and plotted in Fig. II-30. In this case, three (rather than four) successive extractions of the organic phase were performed. In general, the ratios at 50 °C were 5-10 times lower than those at 25 °C, particularly at low acid concentrations. Third-phase formation was still observed at 6 and 8M HNO_3. At 50 °C, the slope for the best-fit line was about 2.2, significantly greater than the 1.6 slope obtained for 25 °C.

Several series of extractions were performed with aqueous nitric acid/sodium nitrate solutions, with and without complexing agents (oxalic acid, hydrofluoric acid, or phosphoric acid). The aqueous phase compositions are shown in Table II-16 to II-19. In all cases, the sodium nitrate concentration was adjusted to obtain a total nitrate ion concentration of 3.2M. The oxalic, hydrofluoric, and phosphoric acids form complexes with Np(IV). In the absence of complexing agents, each aqueous phase (except as noted in the tables) was made 0.01M in Fe(II) and 0.02M in hydroxylamine nitrate ($NH_2OH{\cdot}HNO_3$) to maintain a reducing environment. Sulfamic acid (0.01M) was also added to destroy nitrite ion. The complexing agents also complex Fe(III), and ferrous ion was not used in such mixtures since some is oxidized to ferric ion. For these experiments, 0.028M $NH_2OH{\cdot}HNO_3$ alone was used as the reducing agent.

Table II-15. Distribution Ratios for Np(IV) between Nitric Acid and TRUEX-NPH[a] Solvent at 50°C

	Reverse Extraction		
$[HNO_3]$,[b] M	1	2	3
0.02	0.178	0.323	0.259
0.05	2.09	2.82	3.10
0.1	13.6	10.0	5.78
0.2	4.1	15.8	260
0.5	152	198	200
1.0	1.84×10^3	3.43×10^3	3.41×10^3
2.0	8.03×10^3	6.79×10^3	2.60×10^3
3.0	6.83×10^3	9.98×10^3	7.57×10^3
6.0	3.51×10^4	3.03×10^4	2.78×10^4
8.0	2.61×10^4	2.22×10^4	1.28×10^4

[a]The TRUEX-NPH solvent was prepared assuming the CMPO was 98% pure.
[b]Nominal values. See footnote b, Table II-12.

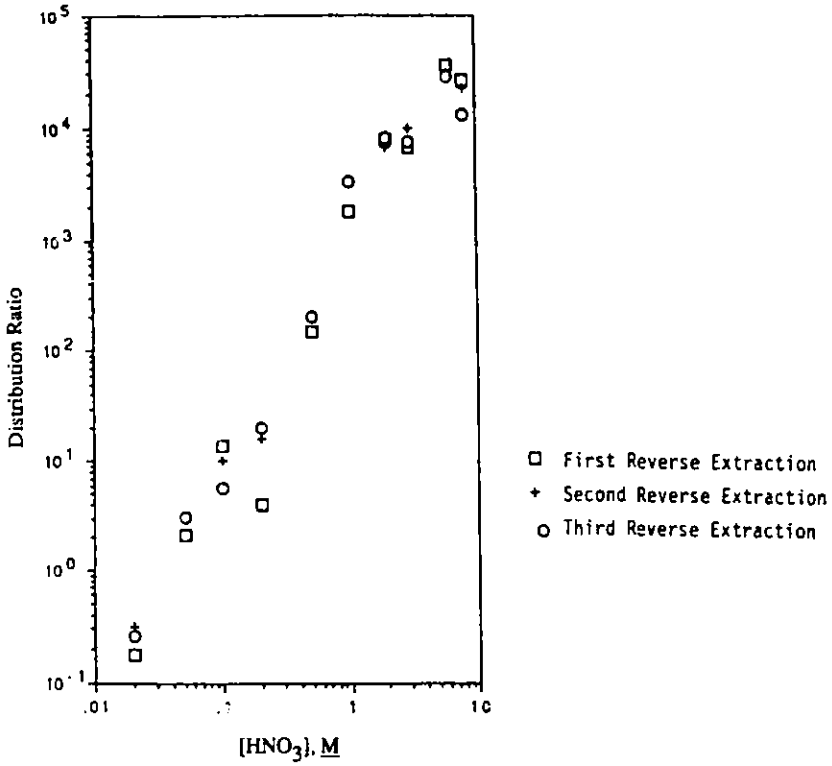

Fig. II-30. Distribution Ratios for Np(IV) in TRUEX-NPH Solvent as a Function of Nitric Acid Concentration at 50°C

The results for nitric acid/sodium nitrate solutions without complexing agent are given in Table II-16. Figures II-31 and II-32 are graphs of the data for Experiment 1 at 25°C and Experiment 1 at 50°C, respectively. The distribution ratios given in Table-II-16 vary considerably between experiments and between successive reverse extractions of the same experiment, as observed for Np(IV) in the absence of strong complexing agents. The total nitrate in concentration was high at all acidities, and thus large distribution ratios might be expected for all the solutions. This was observed at

25 °C, but not at 50 °C. The best data at 25 °C are believed to be from Experiment 2, Reverse Extraction 1, where the ratios ranged from 3.0×10^4 at 0.02M HNO_3 to about 7×10^4 at 0.5 and 1.0M HNO_3. At

Table II-16. Distribution Ratios for Np(IV) between Nitric Acid/Sodium Nitrate Solutions and TRUEX-NPH[a] at 25 and 50 °C

Exp. No.	Conc., M		10^3 x Distribution Ratio[b]					
			25 °C			50 °C		
	$[HNO_3]$	$[NaNO_3]$	RE-1	RE-2	RE-3	RE-1	RE-2	RE-3
1	0.02	3.2	5.33	12.9	15.4	0.083	0.034	0.012
2			30.1	19.8		0.051	0.049	
3						0.200	0.019	
1	0.1	3.1	57.9	7.96	6.81	0.818	0.439	0.163
2			65.1	81.9		0.153	0.113	
3						0.675	0.332	
1	0.5	2.7	77.4	31.1	62.2	13.2	21.2	12.9
2			65.4	81.9		0.290	0.096	
3						12.2	17.3	
1	1.0	2.2	65.3	51.2	37.8	21.2	23.2	20.8
2			65.3	68.2		0.382	0.117	
3						13.0	24.6	

[a]The solvent was prepared with the assumption that the CMPO was 100% pure.
[b]Multiply all results by 10^3. Two separate experiments were performed at 25 °C and three at 50 °C. The values on the corresponding lines at each concentration were obtained from the same experiment. Two or three successive extractions of the solvent were performed for each experiment and are listed in order as RE (Reverse Extraction) -1, -2, or -3. At 25 °C, each aqueous phase was made 0.01M in Fe(II), 0.02M in $NH_2OH \cdot HNO_3$, and 0.01M in sulfamic acid. At 50 °C, the same reagents were added in the first and third experiments. No reducing agents or sulfamic acid were used in the second experiment.

Table II-17. Distribution Ratios for Np(IV) between Oxalic Acid/Nitric Acid/Sodium Nitrate Solutions and TRUEX-NPH[a] Solvent as Function of Oxalic Acid Concentration

$[H_2C_2O_4]$, M	$[NO_3]$, M	Distribution Ratio			
		0.02M HNO_3		0.1M HNO_3	
		25 °C	50 °C	25 °C	50 °C
0.01	3.2	0.0357	0.00787	1.72	0.422
0.02	3.2	0.00616	0.00384	0.242	0.0833
0.03	3.2	0.00171	0.00240	0.0990	0.0404
0.05	3.2	0.00322	0.00297	0.0388	0.0205

[a]The solvent was prepared with the assumption that the CMPO was 100% pure.

Table II-18. Distribution Ratios for Np(IV) between Hydrofluoric Acid/Nitric Acid/Sodium Nitrate Solutions and TRUEX-NPH[a] Solvent at 25 and 50 °C

	Distribution Ratio			
	25 °C		50 °C	
[HF],[b] M	RE-1	RE-2	RE-1	RE-2
0.01	82.6	79.8	62.6	67.4
0.02	20.3	20.3	18.5	18.4
0.05	2.59	2.86	2.70	2.96
0.1	0.514	0.608	0.575	0.699
0.2	0.0818	0.0938	0.105	0.127
0.5	0.0077	-	0.0108	0.0106

[a]The solvent was prepared with the assumption that the CMPO was 100% pure.
[b]The nitric acid and sodium nitrate concentrations were 0.1 and 3.1M in all solutions.

Table II-19. Distribution of Np(IV) between Phosphoric Acid/Nitric Acid/Sodium Nitrate Solutions and TRUEX-NPH[a] at 25 °C

	Distribution Ratios		
$[H_3PO_4]$,[b] M	RE-1	RE-2	RE-1/RE-2
0.01	300	358	1.19
0.02	262	324	1.24
0.03	209	285	1.36
0.05	147	206	1.40

[a]The solvent was prepared with the assumption that the CMPO was 100% pure.
[b]The nitric acid and sodium nitrate concentrations were 0.1 and 3.1M in all solutions.

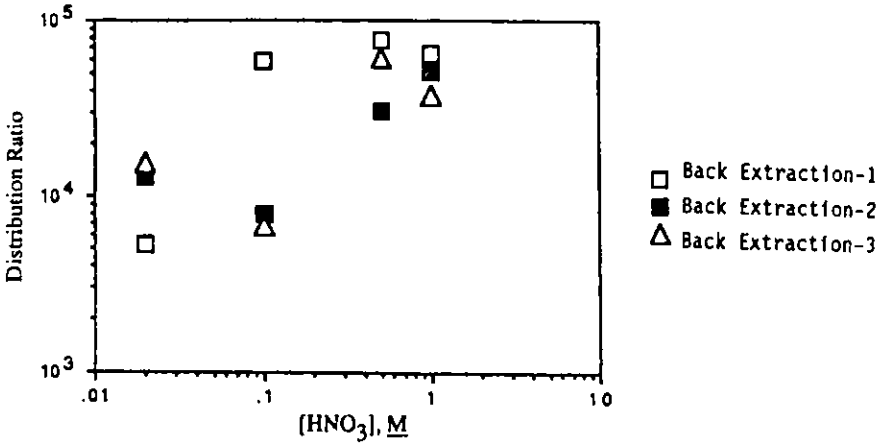

Fig. II-31. Distribution of Np(IV) between HNO_3-$NaNO_3$ Mixtures and TRUEX-NPH as a Function of HNO_3 Concentration at 25 °C. Data from Table II-16, Experiment 1.

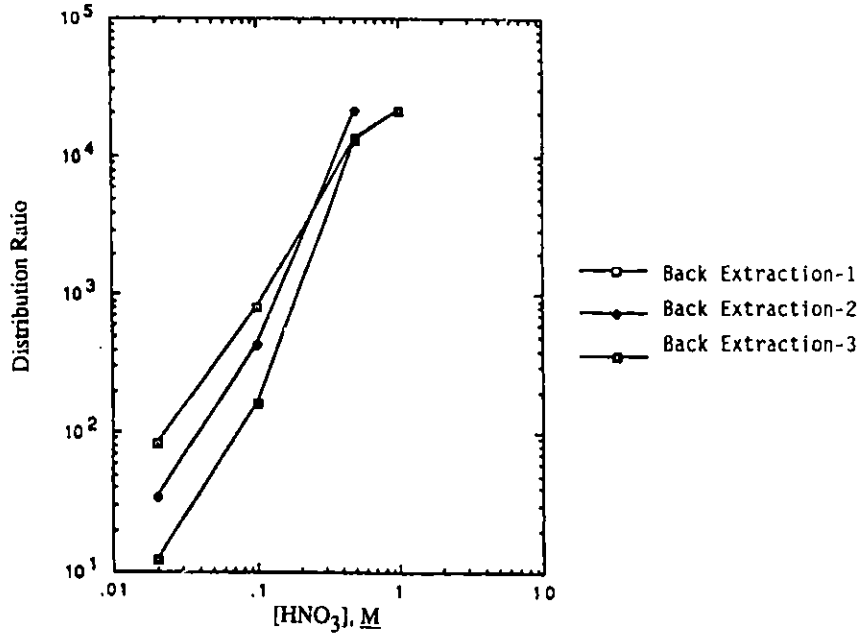

Fig. II-32. Distribution of Np(IV) between HNO_3-$NaNO_3$ Mixtures and TRUEX-NPH as a Function of HNO_3 Concentration at 50°C. Data from Table II-16, Experiment 1.

50°C, the ratios were surprisingly low at 0.02 and 0.1M HNO_3, but increased to at least 1.2×10^4 at 0.5 and 1M HNO_3 in Experiments 1 and 3. The ratios remained low in Experiment 2, but no reducing agents were added. It is likely that Np(IV) is unstable at 50°C and that some is oxidized to Np(V), which has a much lower distribution ratio than Np(IV). At the higher acidities, 0.5 and 1M HNO_3, the Np(IV) may be stabilized as the nitrate complex, so that less oxidation occurs and the distribution ratio is large. The most reliable data for Np(IV) at 50°C are believed to be those obtained from Experiment 1, Reverse Extraction 1. The data from Experiment 2, Reverse Extraction 1, approximately plot as a straight line with a slope of about 0.5.

Distribution ratios for Np(IV) between oxalic acid/nitric acid/sodium nitrate solutions and TRUEX-NPH were measured as described for the nitric acid/sodium nitrate solutions. The nitric acid concentration was kept constant at 0.02M in one series of solutions and at 0.1M in a second series, while the oxalic acid concentration was varied from 0.01 to 0.05M at both nitric acid concentrations. Two successive reverse extractions of the solvent phase were performed. Since the distribution ratios are very low in the presence of oxalic acid, the concentration of neptunium remaining in the solvent phase after its first contact with the aqueous phase was too low to give meaningful results for the second reverse extraction. The results for the first extraction are given in Table II-17 and are plotted in Figs. II-33 and II-34. The following observations are apparent from the data. The presence of oxalic lowers the distribution ratios greatly, from 10^3-10^4 to 1.7 or less. Thus, Np(IV) cannot be extracted from solutions containing oxalate, except perhaps at very high nitric acid concentrations, but can be stripped from TRUEX solvents with dilute oxalic acid. The distribution ratios are usually 2-4 times lower at 50 than at 25°C. Increasing the nitric acid concentration from 0.02 to 0.1M increases the distribution ratio by factors of 10 to 50. While the change in the distribution ratio with increasing oxalic acid concentration is linear in the 0.1M HNO_3 series, it is not orderly in the 0.02M HNO_3 series. In the latter series, the ratio at

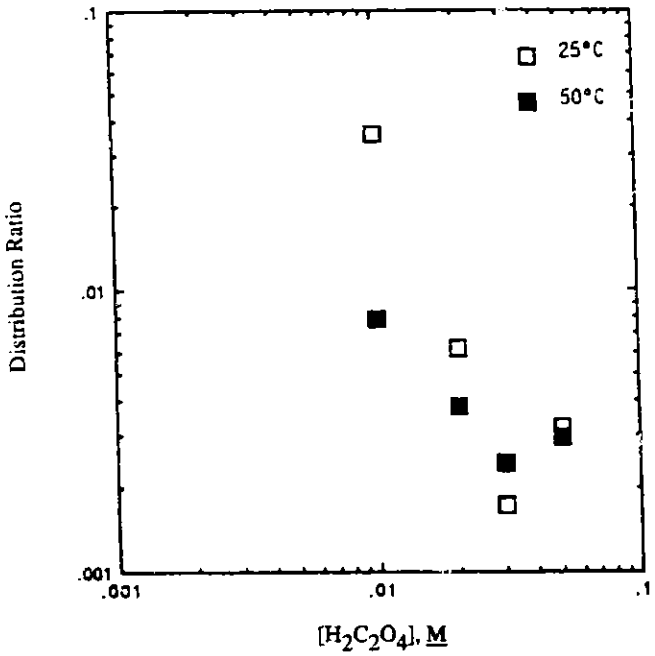

Fig. II-33.

Distribution of Np(IV) between Oxalic Acid/Nitric Acid/Sodium Nitrate Solutions and TRUEX-NPH as a Function of Oxalic Acid Concentration at 25 and 50°C. The nitric acid and sodium nitrate concentrations were kept constant at 0.02 and 3.2M, respectively.

Fig. II-34.

Distribution of Np(IV) between Oxalic Acid/Nitric Acid/Sodium Nitrate Solutions and TRUEX-NPH as a Function of Oxalic Acid Concentration at 25 and 50°C. The nitric acid and sodium nitrate concentrations were kept constant at 0.1 and 3.1M, respectively.

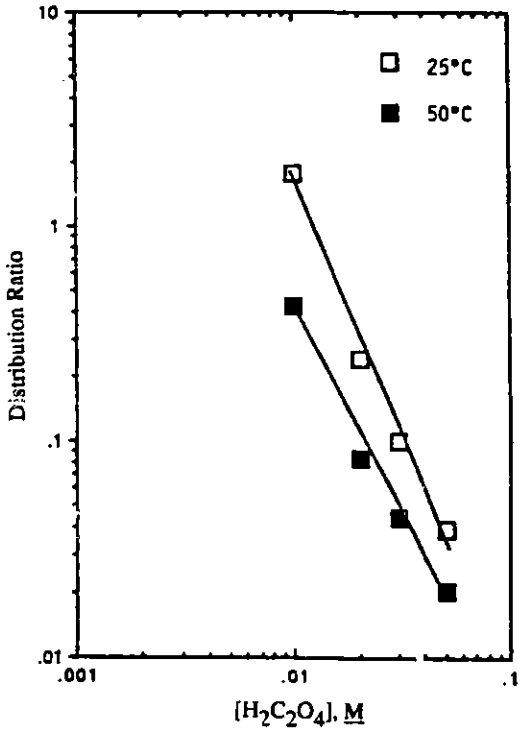

0.05M is greater than that at 0.03M $H_2C_2O_4$, and is greater at 50°C than 25°C in 0.03M $H_2C_2O_4$. These results are very unusual, and the measurements should be repeated to determine if this behavior is correct.

Distribution ratio measurements were also performed with a series of solutions containing 0.1M HNO_3, 3.1M $NaNO_3$, and hydrofluoric acid concentrations in the range of 0.01 to 0.5M. Two successive extractions of the solvent were performed. The results are listed in Table II-18 and plotted, for the first extraction only, in Fig. II-35. The second extraction agreed fairly well with the first, except in 0.5M HF at 25°C, where the neptunium activity remaining in the solvent phase was too low to measure. It is seen that the distribution ratios are markedly lowered by hydrofluoric acid, although not as much as by oxalic acid. This is expected since the oxalate complex of neptunium is stronger than the fluoride complex. The effect of temperature on the ratios is relatively small, and at hydrofluoric acid concentrations of 0.05M and above, the ratio is larger at 50°C than that at 25°C. This is the first such temperature effect encountered for neptunium and should be confirmed by further measurements. The plot (Fig. II-35) of the data shows that one straight line can fit all the data adequately. The slope of this line is about 2.3.

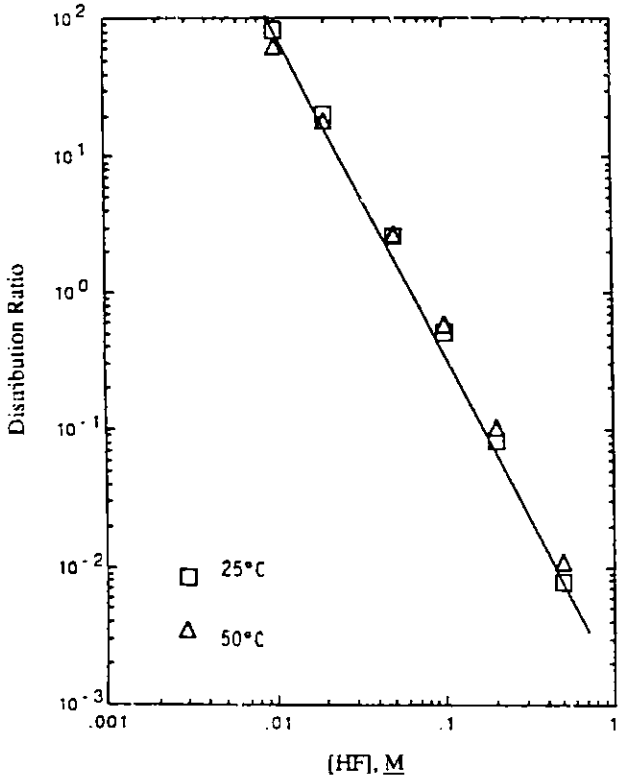

Fig. II-35.

Distribution of Np(IV) between Hydrofluoric Acid/Nitric Acid/Sodium Nitrate Solutions and TRUEX-NPH as a Function of Hydrofluoric Acid Concentration at 25 and 50°C. The nitric acid and sodium nitrate concentrations are 0.1 and 3.1M, respectively.

A series of extractions was also performed with TRUEX-NPH solvent and phosphoric acid/nitric acid/sodium nitrate solutions. In this series, the nitric acid and sodium nitrate concentrations were kept constant at 0.02 and 3.2M, respectively, and the phosphoric acid concentration was varied from 0.01 to 0.05M. The results are given in Table II-19. It is seen that phosphoric acid lowers the distribution ratio, but its effect is much less than that of oxalate and fluoride, and its complex with neptunium is correspondingly weaker. The second reverse extraction gave higher ratios than the first, but not uniformly so over the entire concentration range, as shown by the ratio of the two extractions

(Table II-19). The increase of this ratio for the second over the first extraction may be due to the presence of a small fraction of the less extractable Np(V) in the first extraction. Since the Np(V) would remain in the aqueous phase, the second reverse extraction of the organic phase would result in a higher distribution ratio. A log-log plot of the data shows a nonlinear concave curve. The three highest concentrations vary linearly with phosphoric acid concentration, but at the lowest concentration the ratio is less than required to give a linear plot that includes all four concentrations.

e. Curium Extraction Results

The ^{244}Cm was separated from its first decay product, ^{240}Pu, by extracting the plutonium into TRUEX-NPH from 0.1M HNO_3. Forward and reverse distribution ratios were measured between nitric acid (concentration range 0.05-5M) and TRUEX-NPH at 25 °C. The results are given in Table II-20 and plotted in Fig. II-36, together with the reverse extraction values obtained by Reichley-Yinger for Am(III) (ANL-90/15, pp. 124-125).

Table II-20. Distribution Ratios for Cm(III) and Am(III) between TRUEX-NPH[a] and Nitric Acid Solutions at 25 °C

	Curium Dist. Ratio			Am Dist. Ratio	
$[HNO_3]$, M	Forward	Reverse	% diff.[b]	Reverse[c]	% diff.[d]
0.05	0.160	0.141	12.6	0.221	36
0.10	0.626	0.617	1.5	0.847	27
0.20	2.17	2.10	3.6	2.98	30
0.50	8.74	8.83	1.0	11.4	22
1.0	16.8	16.7	0.6	22.5	26
2.0	23.1	23.1	0	30.4	24
3.0	23.6	21.6	8.9	29.8	28
5.0	20.6	18.4	11.3	20.1	8

[a]The solvent was prepared with the assumption that the CMPO was 98% pure.
[b]Percent difference between forward and reverse ratios for curium.
[c]From ANL-90/15, pp. 124-125.
[d]Percent difference between reverse distribution ratios for curium and americium.

The differences between the ratios for americium and curium averaged about 27% at acidities up to 3M HNO_3. The difference became much smaller after the maximum was reached. At concentrations of 0.2M HNO_3 and below, the change in the ratio with acid concentration is nearly linear, with an initial slope of about 2 for both elements.

Distribution ratios for ^{244}Cm at 50 °C in the acid range of 0.02 to 8.0M HNO_3 are given in Table II-21. At 50 °C the ratios are about a factor of 10 lower than those at 25 °C at acidities up to about 0.1M HNO_3. At 0.2M HNO_3 and above, the results are three to four times lower. The forward and reverse extractions in Table II-21 agree fairly well except at 0.02M HNO_3, the lowest acidity. The shape of the plot for distribution ratio vs. nitric acid concentration is similar to that at 25 °C, except that the linear portion of the curve, up to about 1M HNO_3, has a slope of about 1.6 compared to about 2 at 25 °C. The maximum distribution ratio occurs at about 3M HNO_3 at both temperatures.

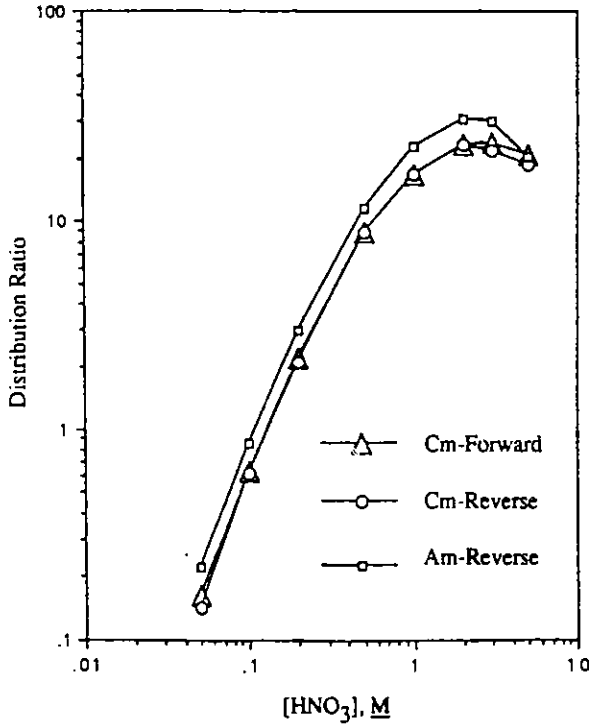

Fig. II-36.

Distribution Ratios for Curium and Americium between TRUEX-NPH and Nitric Acid Solutions at 25 °C

Table II-21. Distribution Ratios for Curium between Nitric Acid and TRUEX-NPH[a] at 50 °C

	Distribution Ratios	
$[HNO_3]$,[b] M	Forward	Reverse
0.02	0.011	0.020
0.05	0.066	0.080
0.1	0.160	0.167
0.2	0.562	0.614
0.5	2.03	2.21
1.0	5.03	5.66
2.0	7.85	7.97
3.0	8.60	8.03
6.0	7.90	7.88
8.0	7.82	8.71

[a]The TRUEX-NPH solvent was prepared with the assumption that the CMPO was 100% pure.
[b]Nominal values. See footnote b in Table II-12.

Distribution ratios between nitric acid and TRUEX-TCE at 25 and 50 °C are given in Table II-22 and plotted in Fig. II-37. The forward and reverse ratios at 0.05M HNO_3 for 25 °C differ by a factor of two, and the plot indicates that the reverse distribution ratio is more in line with a smooth curve through the other distribution ratio values at other nitric acid concentrations. The initial slope of this curve is about 1.8. Compared with the data for TRUEX-NPH, the ratios with TRUEX-TCE are very similar up to about 0.2M HNO_3. As the acidity increases, the ratio with TRUEX-NPH increases to larger values, reaching a maximum of about 23 (Table II-20) at 2-3M HNO_3 before decreasing. With

TRUEX-TCE solvent, the maximum ratio was 9, which was reached at 1M HNO_3. The ratios at 50°C were generally about one-half those at 25°C with TRUEX-TCE. With TRUEX-NPH, the temperature dependence was substantially greater, the ratios decreasing by a factor of 3 to 4 from 25 to 50°C.

Table II-22. Distribution Ratios for Curium between Nitric Acid and TRUEX-TCE at 25 and 50°C

	25°C		50°C	
$[HNO_3]$, M	Forward	Reverse	Forward	Reverse
0.02	0.0313	0.0311	0.0121	0.0155
0.05	0.234	0.125	0.0879	0.102
0.10	0.560	0.563	0.216	0.234
0.20	1.98	1.98	0.766	0.878
0.5	6.10	6.30	3.31	3.50
1.0	9.00	8.63	4.05	4.42
2.0	7.86	7.01	3.50	3.52
3.0	6.17	6.14	2.77	3.04
6.0	4.83	5.02	2.36	2.75
8.0	4.88	5.04	2.60	2.50

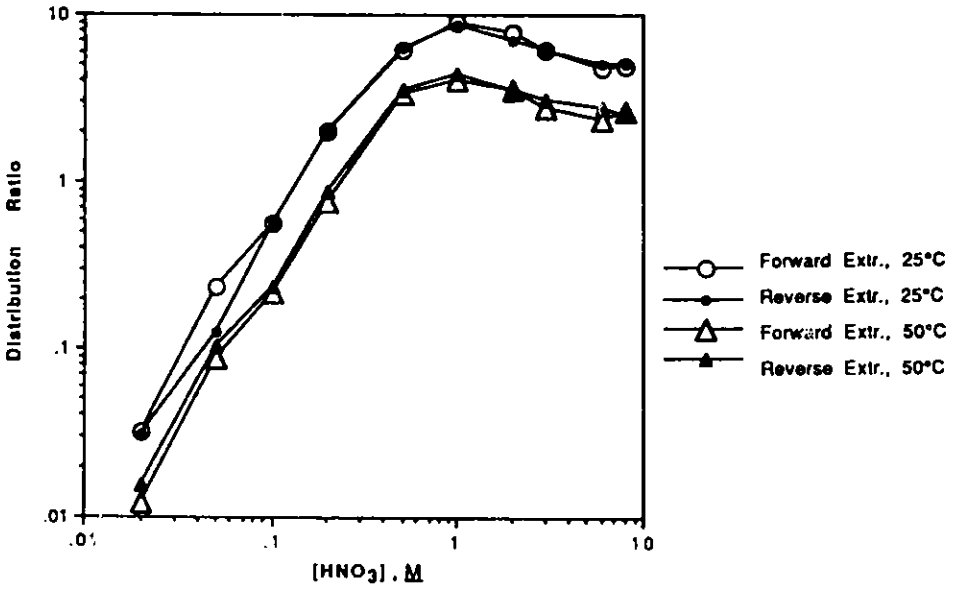

Fig. II-37. Distribution of Curium between Nitric Acid and TRUEX-TCE as a Function of Acid Concentration and Temperature

5. Iron Extraction
(D. R. Fredrickson)

The extraction of iron is very different from all other species treated by the GTM in that it is rate controlled. While other species are equilibrated in seconds (as manifested by their D values being the same if measured at 15, 60, or 600 s whether performed as forward or reverse extraction), D values for Fe(III) extraction by the TRUEX solvents vary with time of contact. Differences in the D values or Fe(III) measured for forward and reverse extractions have been found to not be equivalent even after 600 s for low concentrations of nitric acid. To assist the GTM modeling work, we studied ^{59}Fe forward and reverse extractions to define low nitric acid concentration points. Reported in the last semiannual report (ANL-90/16, Sec. II.G.2) were ^{59}Fe extractions for both TRUEX-TCE and TRUEX-NPH with 0.02 and 0.05M HNO_3 at 25°C. Continuing this work, a series of ^{59}Fe forward and reverse extractions was done using both TRUEX-TCE and TRUEX-NPH with 0.2 and 0.3M nitric acid at 25°C. Since the extraction is dependent on the time that the aqueous and organic phases are mixed, various contact times were used (15, 30, 60, and 300 s). Forward and reverse distribution ratios (D_f and D_{rev}, respectively) between nitric acid and TRUEX-TCE are shown in Table II-23. Similar results with TRUEX-NPH are shown in Table II-24. As has been described earlier for other experiments at low nitric acid concentrations, the D_f and D_{rev} values are far apart, even at 300 s contacts.

Table II-23. Distribution Ratios for ^{59}Fe between Nitric Acid Solutions and TRUEX-TCE for Various Contact Times at 25°C

	15 s		30 s		60 s		300 s	
$[HNO_3]$, M	D_f	D_{rev}	D_f	D_{rev}	D_f	D_{rev}	D_f	D_{rev}
0.2	3.28×10^{-3}	0.109	3.64×10^{-3}	0.064	6.19×10^{-3}	0.024	0.0110	0.0354
0.3	3.62×10^{-3}	0.188	4.82×10^{-3}	0.065	7.18×10^{-3}	0.042	0.0100	0.0274

Table II-24. Distribution Ratios for ^{59}Fe between Nitric Acid Solutions and TRUEX-NPH Solvent for Various Contact Times at 25°C

	15 s		60 s		300 s	
$[HNO_3]$, M	D_f	D_{rev}	D_f	D_{rev}	D_f	D_{rev}
0.2	0.0105	0.144	0.0108	0.0737	0.0116	0.0442
0.3	0.0115	0.233	0.0156	0.0686	0.0174	0.0331

The effect of contact time on the extraction of ^{59}Fe by TRUEX-NPH over a wide range of nitric acid concentrations (0.02-6M) was also determined for 50°C. The tabulated data are given in Table II-25 and plotted in Figs. II-38, -39, and -40 for contact times of 15, 60, and 300 s, respectively. The higher rates at increased nitric acid are shown by the D_f and D_{rev} having moved closer together at $[HNO_3] > 1M$.

Table II-25. Distribution Ratios for ^{59}Fe between Nitric Acid Solutions and TRUEX-NPH for Various Contact Times at 50 °C

	15 s		60 s		300 s	
$[HNO_3]$, M	D_f	D_{rev}	D_f	D_{rev}	D_f	D_{rev}
0.02	0.00827	0.809	0.00700	0.175	0.00931	0.173
0.05	0.00496	0.341	0.00436	0.0827	0.00626	0.118
0.10	0.00607	0.222	0.00474	0.0599	0.00589	0.062
0.20	0.0109	0.168	0.00690	0.0851	0.00672	0.027
0.30	0.0100	0.115	0.00814	0.0182	0.00882	0.0201
0.50	0.0199	0.123	0.0141	0.0244	0.0154	0.0236
1	0.0310	0.534	0.0321	0.0651	0.0331	0.0391
2	0.0702	1.34	0.0895	0.248	0.0963	0.106
3	0.0735	4.61	0.179	0.704	0.236	0.278
4	0.241	7.55	0.359	1.61	0.626	0.782
5	0.505	10.4	0.582	4.21	1.27	1.94
6	0.743	21.1	1.95	9.66	5.49	7.34

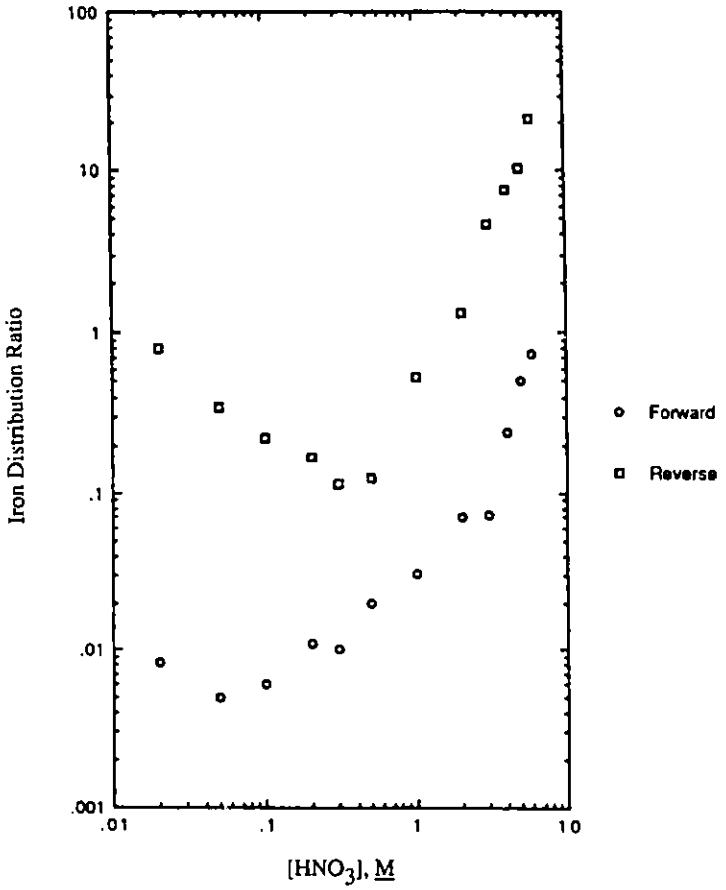

Fig. II-38. Iron Distribution Ratio as Function of Nitric Acid Concentration for TRUEX-NPH at 50 °C and a 15-s Contact Time

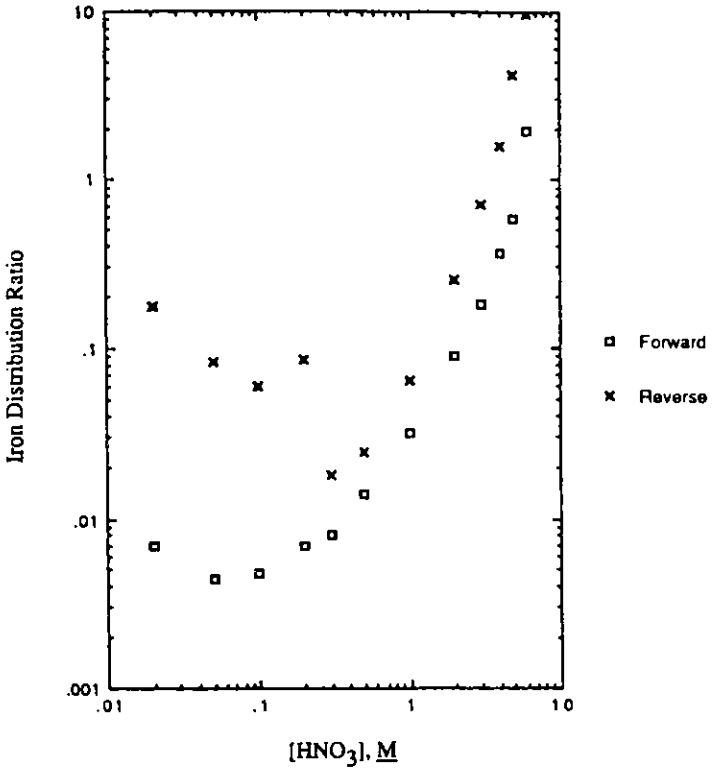

Fig. II-39. Iron Distribution Ratio as Function of Nitric Acid Concentration for TRUEX-NPH at 50°C and a 60-s Contact Time

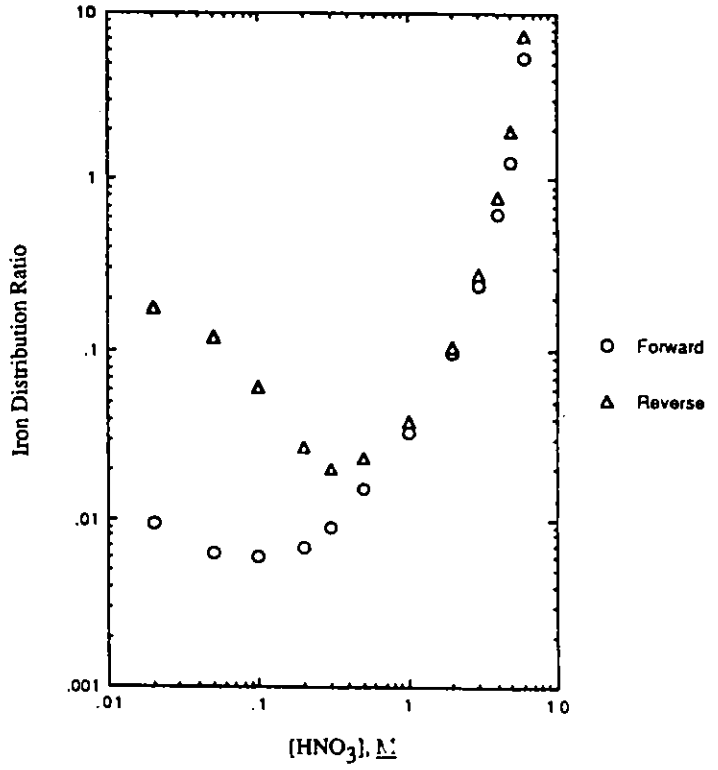

Fig. II-40. Iron Distribution Ratio as Function of Nitric Acid Concentration for TRUEX-NPH at 50°C and a 300-s Contact Time

In the last semiannual report (ANL-90/16, Sec. II.G.2), distribution ratio data were presented for ^{59}Fe between TRUEX-NPH and TRUEX-TCE and three nitric acid concentrations (0.5, 1.0, and 2M) with a constant nitrate concentration of 3.2M at 25°C. To assess the effect of temperature, we repeated the same series of measurements at 50°C. Again, since the extraction is rate dependent, varying contact times (15, 60, and 300 s) were used. The effect of adding 0.1M oxalic acid was also determined. Tables II-26 and II-27 give the distribution ratios for ^{59}Fe extraction with TRUEX-NPH at 50 and 25°C, respectively. Tables II-28 and II-29 give the distribution ratios for ^{59}Fe extraction with TRUEX-TCE at 50 and 25°C, respectively. As expected, increasing the temperature increased the extraction rates, as evidenced by the closeness of the D_f and D_{rev} for 60 s at 50°C when compared to 25°C. Also, oxalic acid dramatically decreased the D value for Fe(III) by complexing it in the aqueous phase.

Table II-26. Distribution Ratios for ^{59}Fe between Nitric Acid/Salt Solutions and TRUEX-NPH at 50°C

Extr. No.	Solution	15 s		60 s		300 s	
		D_f	D_{rev}	D_f	D_{rev}	D_f	D_{rev}
A-1	0.5M HNO_3 2.7M $NaNO_3$	0.124	1.40	0.526	0.783	0.578	0.628
XX-1	1.0M HNO_3 2.2M $NaNO_3$	0.111	1.24	0.356	0.646	0.388	0.400
VV-1	2.0M HNO_3 1.2M $NaNO_3$	0.133	1.64	0.250	0.599	0.306	0.326
A-2	0.5M HNO_3 0.1M Oxalic Acid 2.7M $NaNO_3$	0.0032	--	0.0034	0.0064	0.0036	--

Table II-27. Distribution Ratios for ^{59}Fe between Nitric Acid/Salt Solutions and TRUEX-NPH at 25°C

Extr. No.	Solution	15 s		60 s		300 s	
		D_f	D_{rev}	D_f	D_{rev}	D_f	D_{rev}
A-1	0.5M HNO_3 2.7M $NaNO_3$	0.199	6.60	0.581	1.84	1.10	1.05
XX-1	1.0M HNO_3 2.2M $NaNO_3$	0.100	7.12	0.379	2.05	0.66	0.71
VV-1	2.0M HNO_3	0.043[a]	11.9[a]	0.155[a]	3.16[a]	0.47[a]	0.70[a]
	1.2M $NaNO_3$	0.052[a]	13.5[a]	0.173[a]	2.89[a]	0.46[a]	0.67[a]

[a]Duplicate extractions.

Table II-28. Distribution Ratios for ^{59}Fe between Nitric Acid/Salt and TRUEX-TCE at 50°C

Extr. No.	Solution	15 s		60 s	
		D_f	D_{rev}	D_f	D_{rev}
A-1	0.5M HNO_3 2.7M $NaNO_3$	0.135	0.350	0.161	0.173
XX-1	1.0M HNO_3 2.2M $NaNO_3$	0.078	0.244	0.087	0.097
VV-1	2.0M HNO_3 1.2M $NaNO_3$	0.050	0.170	0.056	0.063
A-2	0.5M HNO_3 0.1M Oxalic Acid 2.7M $NaNO_3$	0.0008	--	0.0009	--

Table II-29. Distribution Ratios for ^{59}Fe between Nitric Acid/Salt and TRUEX-TCE at 25°C

Extr. No.	Solution	15 s		60 s		300 s	
		D_f	D_{rev}	D_f	D_{rev}	D_f	D_{rev}
A-1	0.5M HNO_3 2.7M $NaNO_3$	0.067	1.23	0.159	0.347	0.197	0.214
XX-1	1.0M HNO_3 2.2M $NaNO_3$	0.040	1.17	0.092	0.222	0.113	0.118
VV-1	2.0M HNO_3 1.2M $NaNO_3$	0.027	1.83	0.061	0.247	0.077	0.083
A-2	0.5M HNO_3 0.1M Oxalic Acid 2.7M $NaNO_3$	0.0011	--	0.0010	0.018	0.0010	--

The influence of oxalic acid (0.1-0.3M) on the extraction of ^{59}Fe from TRUEX-NPH solvent was determined for contact times of 15, 60, and 300 s at 50°C. Results are given in Table II-30. An equilibrium condition exists at 300 s where the rates for forward and reverse extraction are nearly the same.

As can be seen in Table II-30, certain distribution ratios at 15 s were higher than those at 60 s. It appears that, with the technique used (the ^{59}Fe spike was added to the top of the organic phase before contacting), as the ^{59}Fe tracer passed through the organic phase, the amount of ^{59}Fe that was extracted in this short pass of the spike solution was greater than that from the aqueous solution containing ^{59}Fe complexed by oxalate during the 15-s contact. To verify this, samples AX and AY were rerun at 15-s contact time with the following technique: (1) the organic phase was pre-equilibrated in the usual manner, three times each with fresh aqueous phase; (2) the aqueous phase (in another centrifuge tube) to be used for the extraction was spiked with ^{59}Fe, mixed, and placed in a 50°C water bath, (3) the treated organic phase was also placed in the 50°C water bath, and (4) the organic was added to the spiked aqueous phase and the contact made. Also, all of the data for the 300-s contact time were obtained by this technique. All future measurements will use this modified technique.

Table II-30. Effect of Oxalic Acid on Distribution Ratio for ^{59}Fe between Nitric Acid/Salt Solutions and TRUEX-NPH at 50 °C

Conc., M				15 s		60 s		300 s[a]	
Oxalic Acid	HNO_3	$NaNO_3$	Solution	D_f	D_{rev}	D_f	D_{rev}	D_f	D_{rev}
0.01	0.5	2.7	AX	0.062	0.245	0.038	0.071	0.040	0.049
0.01	0.5	2.7	AX[a]	0.034	0.428				
0.02	0.5	2.7	AY	0.023	0.125	0.023	0.040	0.023	0.027
0.02	0.5	2.7	AY[a]	0.019	0.453				
0.05	0.5	2.7	AZ	0.012	0.110	0.008	0.013	0.008	0.009
0.1	0.5	2.7	A-2	0.011	0.0052	0.003	0.006	0.004	0.006
0.2	0.5	2.7	A-3	0.002	0.035	0.002	0.005	0.002	0.004
0.3	0.5	2.7	A-4	0.003	0.032	0.002	0.004	0.002	0.004
0.1	1.0	2.2	XX-2	0.015	0.154	0.013	0.016	0.014	0.016
0.2	1.0	2.2	XX-3	0.006	0.069	0.007	0.009	0.007	0.009
0.3	1.0	2.2	XX-4	0.004	0.077	0.004	0.005	0.004	0.005
---	0.2	---		0.0046	0.102	0.006	0.040	0.006	0.017
---	0.2	---		0.0059					
---	0.2	---		0.0066					

[a]With pre-equilibrated organic phase and aqueous phase spiked with ^{59}Fe.

The influence of hydrofluoric acid (0.01-0.05M) on the extraction of ^{59}Fe from TRUEX-NPH was determined at a 60-s contact time and 50 °C. All extractions and transfers were carried out in 15-mL translucent polypropylene centrifuge tubes. Experimental results are given in Table II-31. The addition of HF to the system decreased the D values and increased the rate to equilibrium.

As an extension of this work, experiments were carried out to measure the effects of ^{59}Fe diffusion through a static interface during temperature equilibration. Two experiments were performed with (1) 0.02M HNO_3 where $D_{Fe} = 0.008$ (15 s) and (2) 0.05M HNO_3/2.75M $NaNO_3$ where $D_{Fe} = 0.124$ (15 s). The static test was done as follows. Into an 8-mL centrifuge tube, 3 mL of aqueous phase along with ^{59}Fe was added and equilibrated at 50 °C. Next, in a separate tube, TRUEX-NPH (4 mL) was pre-equilibrated with the aqueous phase, three times at room temperature, and then heated to 50 °C. Finally, this TRUEX-NPH was carefully pipetted into the centrifuge tube (without mixing) containing the ^{59}Fe-aqueous solution (bottom 3 mL aqueous phase, top 4 mL organic phase). A series of 10-100 μL samples was taken from the organic phase (always at a point ~1 mL above the interface) at intervals over a period of 1 h. Between sample takings, the centrifuge tube was thermostated at 50 °C. (See the first 10 points in Figs. II-41 and 42.) At this point, each centrifuge tube was vortexed for 15 s, centrifuged, and reheated to 50 °C. Then, another series of samples was taken over a period of an hour in an identical manner as described above. Figures II-41 and II-42 summarize the data for the increase in organic iron content vs. time at the aqueous phase. Figure II-41 indicates considerable effect on the D value caused by diffusion of ^{59}Fe into the organic phase under static conditions with 0.02M HNO_3 (~2/3 of ^{59}Fe counts). Although much more ^{59}Fe diffused into the organic phase, Fig. II-42 indicates less effect of diffusion of ^{59}Fe into the organic phase with 0.5M HNO_3/2.7M $NaNO_3$.

6. Americium Extraction
(D. R. Fredrickson)

Experiments have been run at 50 °C to study the effect of various nitric acid/nitrate salt combinations on the extraction of ^{241}Am by TRUEX-NPH. We determined the effect of nitric acid alone (0.02 to 8M); nitric acid (0.02, 0.1, 0.5, and 1M) with $NaNO_3$ and a constant NO_3^- concentration of 3.2M; and (3) oxalic acid (0.01, 0.02, 0.03, and 0.05M) with either 0.02 or 0.1M nitric acid and a total NO_3^- concentration of 3.2M. The present study expands previous work done at 25 °C on the extraction of ^{241}Am by TRUEX-NPH.[36]

Table II-31. Effect of HF on Distribution Ratio of ^{59}Fe between Nitric Acid/Salt Solution and TRUEX-NPH at 50 °C

		60 s	
		D_f	D_{rev}
HH-1	0.01M HF 0.5M HNO_3 2.7M $NaNO_3$	0.288[a]	0.324[a]
HH-2	0.03M HF 0.5M HNO_3 2.7M $NaNO_3$	0.163[a]	0.177[a]
H-1	0.1M HF 0.5M HNO_3 2.7M $NaNO_3$	O.058 0.063[a]	0.089 0.076[a]
H-2	0.3M HF 0.5M HNO_3 2.7M $NaNO_3$	0.020 0.021[a]	0.032 0.028[a]
H-3	0.5M HF 0.5M HNO_3 2.7M $NaNO_3$	0.011	0.015
ZZ-2	0.1M HF 1.0M HNO_3 2.2M $NaNO_3$	0.071	0.095
ZZ-3	0.3M HF 1.0M HNO_3 2.2M $NaNO_3$	0.032	0.040
ZZ-4	0.5M HF 1.0M HNO_3 2.2M $NaNO_3$	0.021	0.029

[a] ^{59}Fe added through the organic phase (old technique).

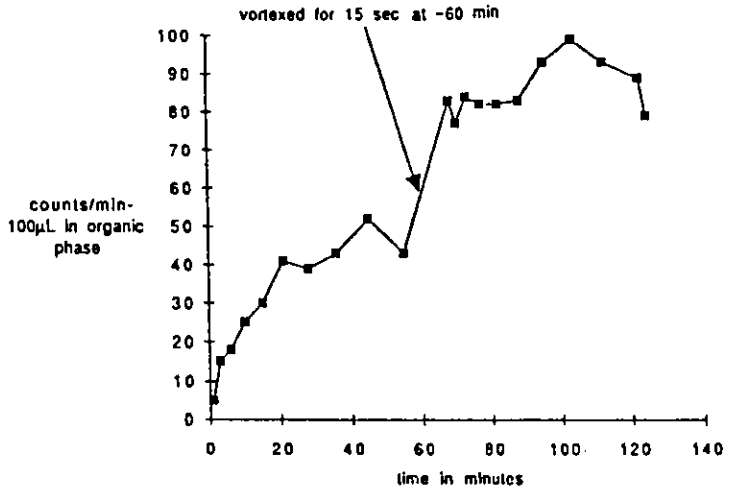

Fig. II-41. Increase in Organic Iron Content vs. Time at Aqueous Phase for 0.02M HNO_3

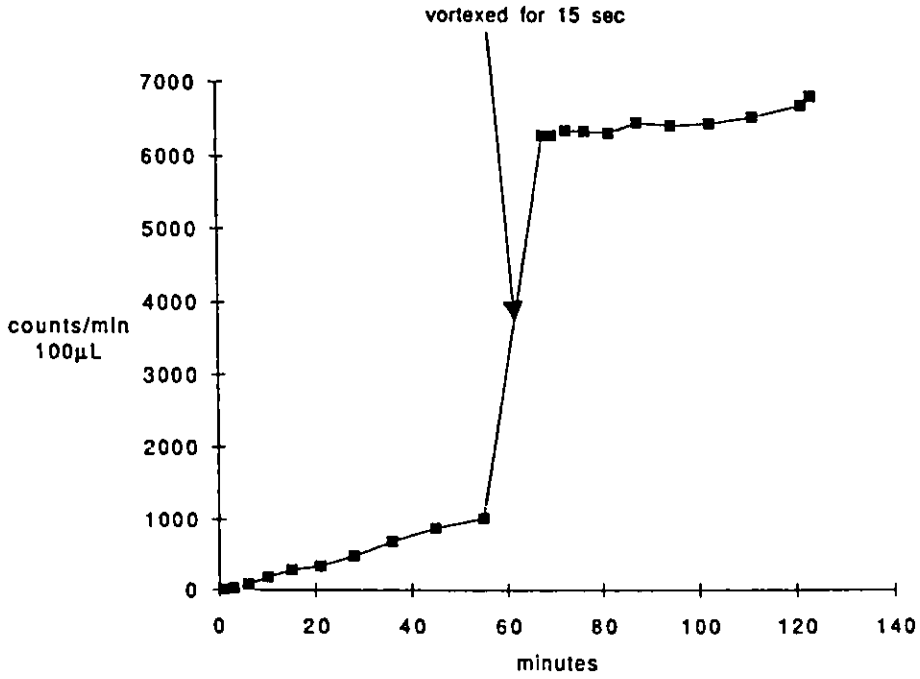

Fig. II-42. Increase in Organic Iron Content vs. Time at Aqueous Phase for 0.05M HNO_3/2.7M $NaNO_2$

The first series was run to determine the effect of nitric acid concentration on the extraction of ^{241}Am by TRUEX-NPH at 52 °C. Standard techniques were used, with 2 mL organic phase and 2 mL aqueous phase. Acid pre-equilibration (3 times, 1:1 aqueous-to-organic ratio) was done at room temperature, followed by spiking the solution with 3µL of ^{241}Am. We found that the temperature is very critical to obtain consistent results. Samples were equilibrated at 52 °C for 15 min followed by three 20-s contacts, with water bath equilibration during the intervals, to ensure the proper temperature. This was followed by centrifugation and separation of the phases. Distribution ratios obtained are tabulated in Table II-32 and plotted in Fig. I-43.

Table II-32. Distribution Ratios for ^{241}Am between Nitric Acid Solutions and TRUEX-NPH at 52 °C

	D_{Am}	
$[HNO_3]$, M	D_f	D_{rev}
0.02	0.014	0.018
0.05	0.085	0.096
0.10	0.336	0.366
0.20	1.09	1.10
0.50	4.30	4.19
1	8.66	9.17
2	11.5	13.4
3	13.0	13.3
6	9.03	10.7
8	9.26	10.2

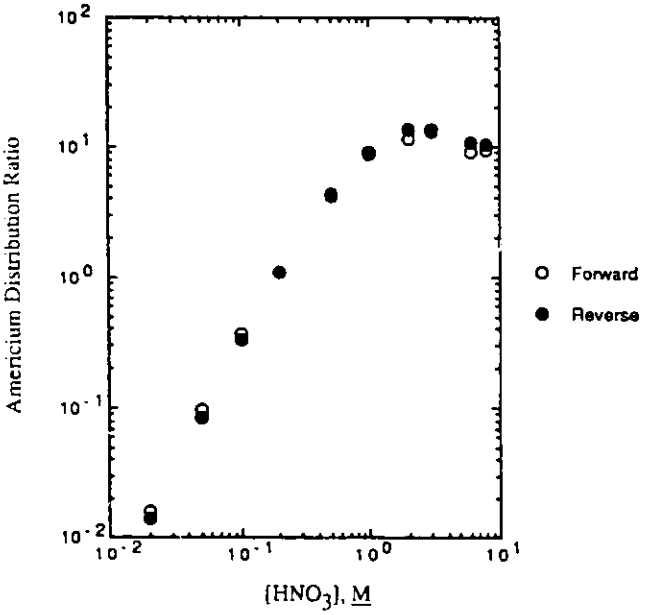

Fig. II-43.

Americium Distribution Ratio as Function of Nitric Acid Concentration with TRUEX-NPH at 25 °C

The next series employed nitric acid with salt ($NaNO_3$) present. Acid pre-equilibration (at 25 °C with 2-mL organic phase and 6-mL aqueous phase) was the first step and was repeated three times with fresh aqueous phase. Finally, the 2-mL treated organic phase was transferred to a 8-mL centrifuge tube, and 2 mL of fresh aqueous phase was added, followed by spiking with 5 μL of ^{241}Am (at either 52 or 50 °C). The procedure already described was then followed. It should be noted that all of the data in this series present a problem (yet unresolved) in that the reverse extraction data are higher than those for forward extraction. We feel that it is likely due to our present technique allowing a lower temperature for reverse extractions than the forward and are pursuing means to test and correct this problem. More will be presented on this problem in the future.

The effect of nitric acid (0.02, 0.1, and 0.5M) with nitrate concentration held constant at 3.2M on the extraction of ^{241}Am by TRUEX-NPH is presented in Tables II-33 and II-34. Table II-33 presents results at 52 °C with a forward and reverse extraction. Table II-34 extends those results to (1) pre-equilibration at 50 °C* and (2) three reverse extractions. The forward distribution ratios obtained for 50 °C at the four acid concentrations did not change significantly using the 50 °C pre-equilibration, and therefore this technique will not be used.

The next series covers the effect of oxalic acid at two concentrations of nitric acid and with the NO_3^- concentration constant at 3.2M. Tables II-35 and II-36 summarize the results for 0.1M HNO_3/3.1M $NaNO_3$ and 0.02M HNO_3/3.18M $NaNO_3$, respectively. As expected from earlier results at 25 °C, oxalic acid addition does drop D_{Am}. These results will all be modeled later. In an effort to establish that the technique used is reproducible, the oxalic acid series was rerun at 25 °C with 0.02M HNO_3/3.18M $NaNO_3$. Table II-37 summarizes the results. Both the forward and reverse distribution ratios agree quite well. The temperature effect decreases the D_{Am} values by a factor of two at 50 °C compared to 25 °C.

---

*Our conventional technique is to pre-equilibrate our organic phase at room temperature. This was done at 50 °C instead, a very time-consuming process.

Table II-33. Distribution Ratios for ^{241}Am between Nitric Acid/Salt Solutions and TRUEX-NPH at 52 °C

Conc., M		D_{Am}	
HNO_3	$NaNO_3$	D_f	D_{rev}
0.02	3.18	304	399
0.1	3.1	176	183
0.5	2.7	56.5	56.7
1	2.2	31.2	35.1

Table II-34. Distribution Ratios for ^{241}Am between Nitric Acid/Salt Solutions and TRUEX-NPH at 50 °C

Conc., M		D_{Am}			
HNO_3	$NaNO_3$	D_f	D_{rev}	D_{rev2}	D_{rev3}
0.02	3.18	302	338	364	481
0.1	3.1	171	238	201	253
0.5	2.7	53.2	62.5	63.1	75.9
1	2.2	29.9	32.7	38.2	46.8

Table II-35. Effect of Oxalic Acid on Distribution Ratio for ^{241}Am between Nitric Acid/Salt Solutions and TRUEX-NPH at 52 °C

	D_{Am}	
Oxalic Acid,[a] M	D_f	D_{rev}
0.01	102	120
0.02	82.3	90.5
0.03	59.3	71.4
0.05	41.4	48.6

[a]With $[NaNO_3]$ = 3.1M and $[HNO_3]$ = 0.1M.

Table II-36. Effect of Oxalic Acid on Distribution Ratio for ^{241}Am between Nitric Acid/Salt Solutions and TRUEX-NPH at 50 °C

	D_{Am}		
Oxalic Acid,[a] M	D_f	D_{rev1}	D_{rev2}
0.01	92.5	99.6	107
0.02	54.7	61.3	66.9
0.03	33.6	45.5	46.7
0.05	44.2	50.7	52.3

[a]With $[NaNO_3]$ = 3.18M and $[HNO_3]$ = 0.02M.

Table II-37. Effect of Oxalic Acid on Distribution Ratio for ^{241}Am between Nitric Acid/Salt Solutions and TRUEX-NPH at 25 °C

	D_{Am}			
Oxalic Acid,[a] M	D_{f1}	D_{f2}	D_{rev1}	D_{rev2}
0.01	194	201	213	213
0.02	115	119	122	123
0.03	78.6	78.6	80.4	78.6
0.05	88.2	89.0	88.1	86.3

[a]With $[NaNO_3]$ = 3.18M and $[HNO_3]$ = 0.02 M.

F. TRUEX-NPH Solvent Degradation

(L. E. Trevorrow and E. H. Van Deventer)

1. Introduction

Because the TRUEX-NPH solvent will be used to treat PUREX raffinates from the reprocessing of irradiated fuel, the solvent will undergo radiolytic and hydrolytic degradation. The purpose of this study is to (1) quantitate the effects of radiolysis and temperature on the degradation of the solvent and (2) develop solvent washing (cleanup) procedures to treat degraded TRUEX-NPH solvents.

2. Analysis of Experimental Results Previously Obtained for TRUEX-NPH Radiolysis and Hydrolysis

This effort involves retrieval, organization, and interpretation of the data obtained in studies of hydrolysis and radiolysis of TRUEX-NPH solvent during 1987-1988 by N. Simonzadeh and A. Crabtree, CMT Division. The goals of this effort are (1) to express the effect of radiolysis and hydrolysis in a mathematical form that could be used in the GTM and (2) to publish the results of the study. The experimental data obtained on hydrolysis and radiolysis were presented in the previous semiannual reports. Interpretation and correlation of the data are presented here.

a. Correlation of Hydrolysis Data

In experiments to determine the effect of hydrolysis on TRUEX-NPH solvent, samples of it were stirred in contact with aqueous solutions of several different compositions at 50, 70, and 95 °C for time periods of about 24 h up to about 800 h. The solutions included 0.25, 2.5, and 6.0M HNO_3, as well as two additional solutions simulating a Hanford waste stream (CAW), containing a mixture of metal ions and 1.4 and 2.4M nitric acid.

The effects of hydrolysis were assessed by measuring the D_{Am} between hydrolyzed solvent and aqueous nitric acid of three concentrations, 0.01, 0.05, and 2.0M. The D_{Am} values at 2.0M decrease with hydrolysis time. From this behavior, it is inferred that the distribution at 2.0M HNO_3 is controlled by an extractant, initially present, whose concentration is decreased by hydrolysis, i.e., CMPO. Therefore, the D_{Am} values for distribution of americium between degraded solvent and 2.0M HNO_3 were assumed to be proportional to the CMPO concentration and were used to derive expressions for its hydrolysis rate.

One of the general characteristics of the variation of D_{Am} with time at 2.0M HNO_3 is a decrease of slope with time, suggesting that the destruction rate is dependent on CMPO concentration.

This characteristic suggests representation of the hydrolysis by a rate law in which the rate is proportional to CMPO concentration, of which the simplest type would be first order with respect to CMPO:

$$-dC/dt = k_{hp}\, C \qquad \text{(II-54)}$$

where C is the CMPO concentration, t is the hydrolysis time, and k_{hp} is the rate constant. In integrated form, Eq. II-54 becomes

$$C = C_0\, e^{(-k_{hp}t)} \qquad \text{(II-55)}$$

where C_o is the initial CMPO concentration. Rearranging gives

$$-\ln C = k_{hp}\, t - \ln C_0 \qquad \text{(II-56)}$$

The americium distribution ratio is proportional to the CMPO concentration raised to the nth power, where n is about 3:

$$D_{Am}/D_{Am_0} = C^n/C_0^{\,n} \qquad \text{(II-57)}$$

or

$$C^n = \left[D_{Am}/D_{Am_0}\right]C_0^{\,n} \qquad \text{(II-58)}$$

whence

$$\ln C = 1/n \ln D_{Am} + \ln C_0 - 1/n \ln D_{Am_0} \qquad \text{(II-59)}$$

Substituting the value for ln C from Eq. II-59 into Eq. II-56 gives

$$-\ln D_{Am} = nk_{hp}\, t - \ln D_{Am\ 0} \qquad \text{(II-60)}$$

Therefore, nk_{hp} can be obtained as the slope of the graph of -ln D_{Am} as a function of t. Figures II-44 to II-58 give data obtained for -ln D_{Am} vs. t along with the line fit to those data. For the data obtained, the relation of -ln D_{Am} with t is not linear over the entire time span of up to 800 h. Since, in centrifugal contactors, solvent will be in contact with aqueous acid only a few hours in an entire operating year, the values of k_{hp} were obtained from the graphs of -ln D_{Am} vs. t by manually fitting a line to the data in the initial portion of the graph, i.e., for times that generally did not exceed 100-200 h.

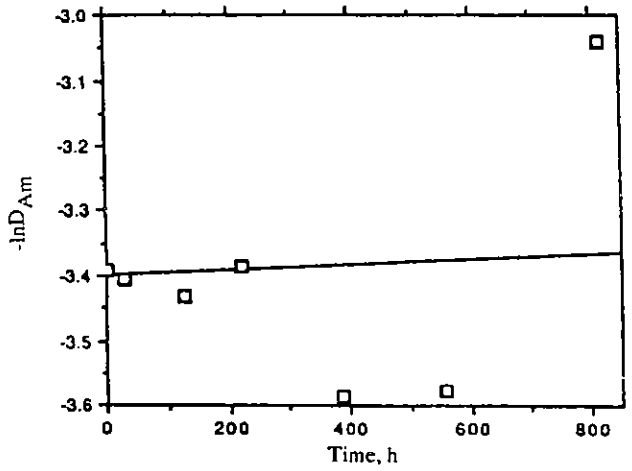

Fig. II-44.

Plot of ln D_{Am} versus Time of Hydrolysis for TRUEX-NPH in Contact with 0.25M HNO_3 at 50°C

Fig. II-45.

Plot of ln D_{Am} versus Time of Hydrolysis for TRUEX in Contact with 2.5M HNO_3 at 50°C

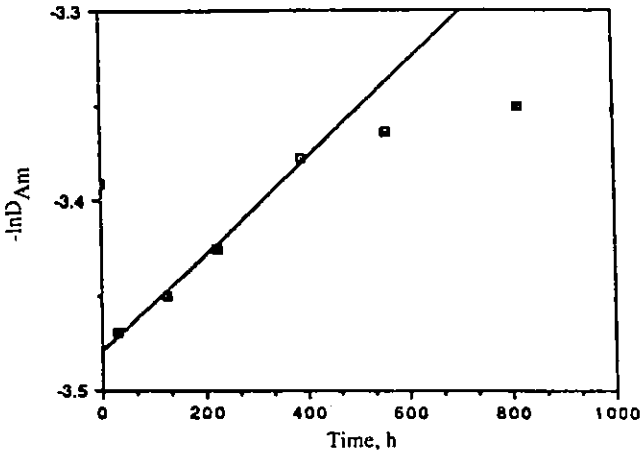

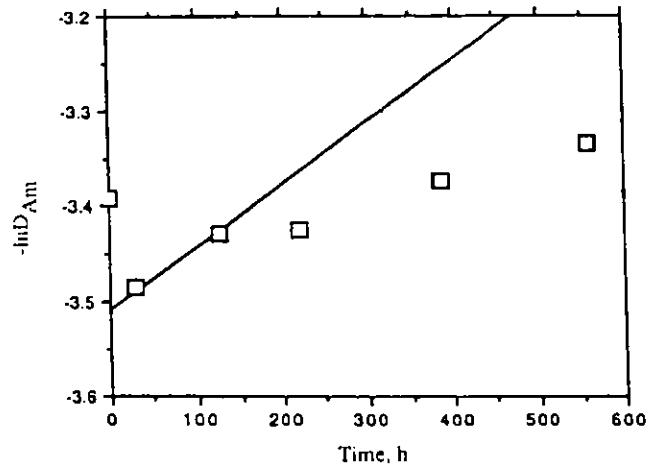

Fig. II-46.

Plot of ln D_{Am} versus Time of Hydrolysis for TRUEX-NPH in Contact with 6M HNO_3 at 50°C

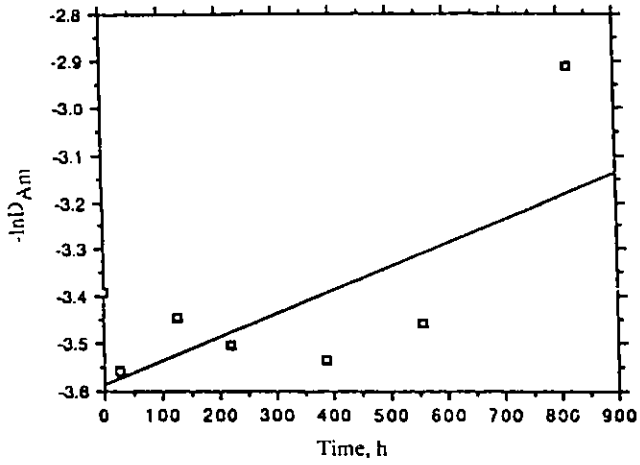

Fig. II-47.

Plot of ln D_{Am} versus Time of Hydrolysis for TRUEX-NPH in Contact with CAW, 1.4M H^+, at 50°C

Fig. II-48.

Plot of ln D_{Am} versus Time of Hydrolysis for TRUEX-NPH in Contact with CAW, 2.4M H^+, at 50°C

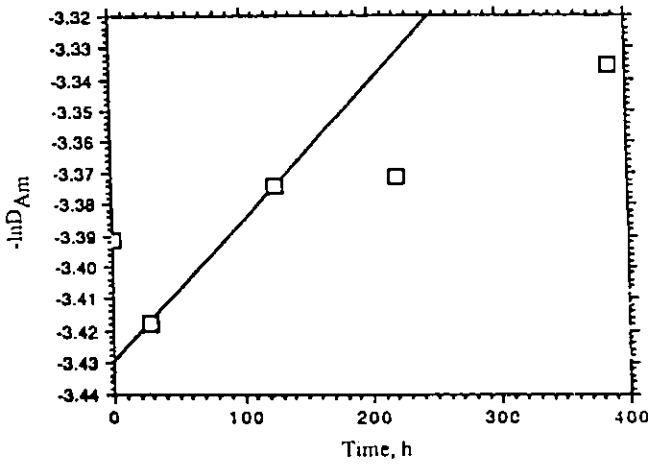

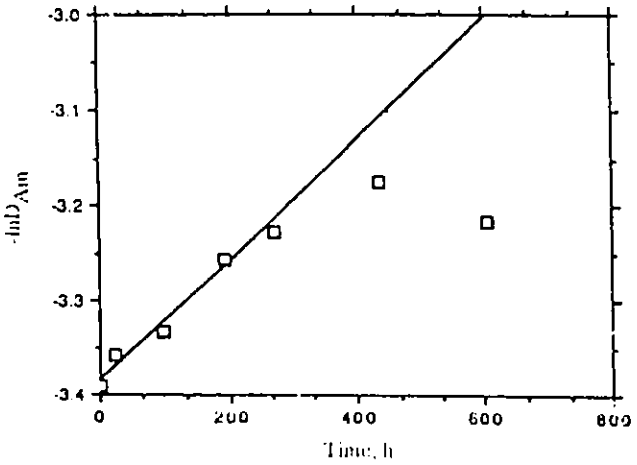

Fig. II-49.

Plot of ln D_{Am} versus Time of Hydrolysis for TRUEX-NPH in Contact with 0.25M HNO_3 at 70°C

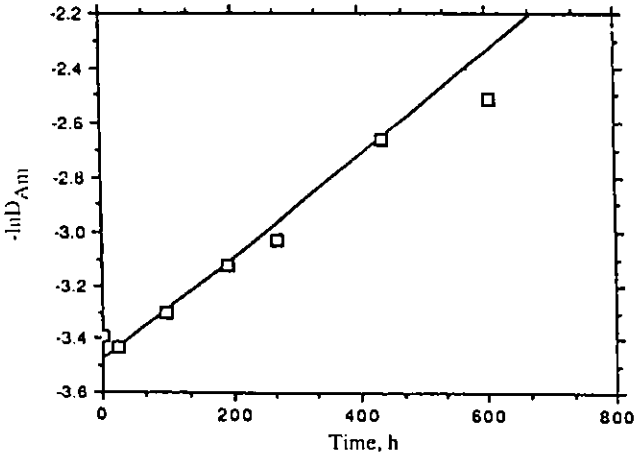

Fig. II-50.

Plot of ln D_{Am} versus Time of Hydrolysis for TRUEX-NPH in Contact with 2.5M HNO_3 at 70°C

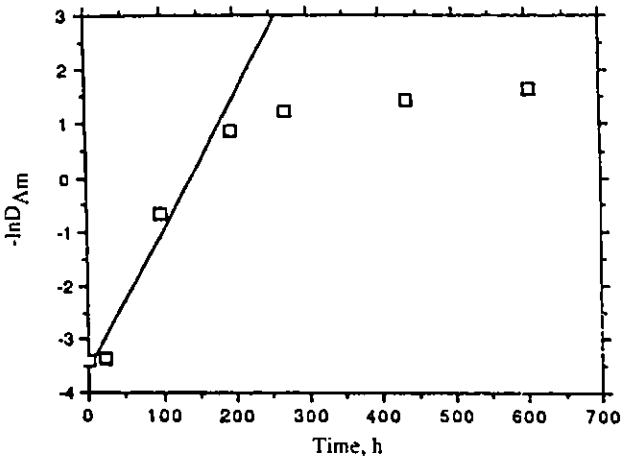

Fig. II-51.
Plot of ln D_{Am} versus Time of Hydrolysis for TRUEX-NPH in Contact with 6M HNO_3 at 70°C

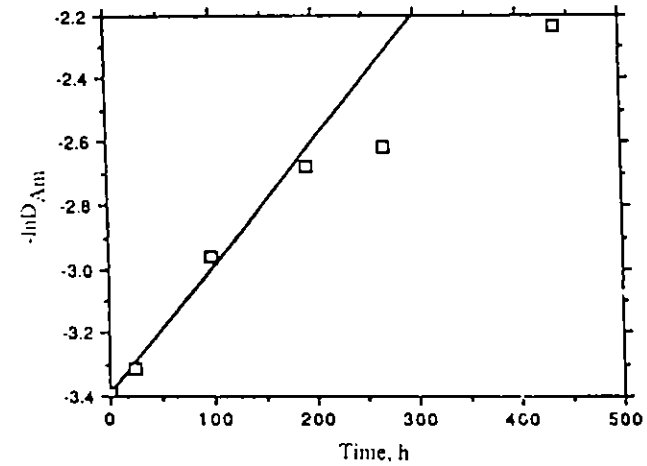

Fig. II-52.

Plot of ln D_{Am} versus Time of Hydrolysis for TRUEX-NPH in Contact with CAW, 1.4M H^+, at 70°C

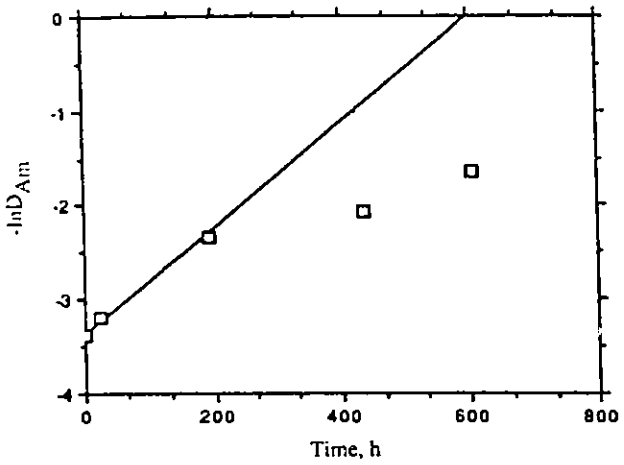

Fig. II-53.

Plot of ln D_{Am} versus Time of Hydrolysis for TRUEX-NPH in Contact with CAW, 2.4M H^+, at 70°C

Fig. II-54.

Plot of ln D_{Am} versus Time of Hydrolysis for TRUEX-NPH in Contact with 0.25M HNO_3 at 95°C

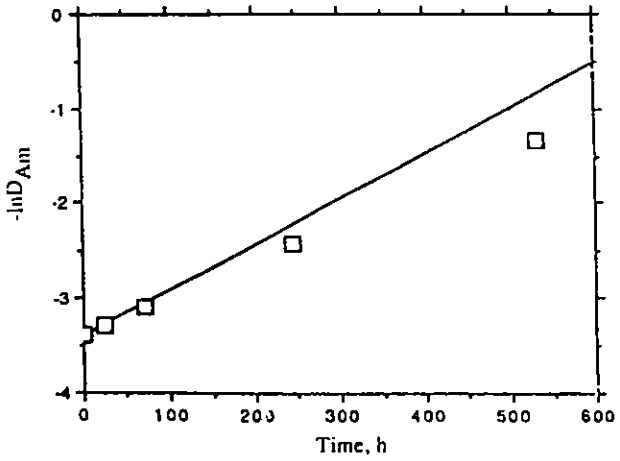

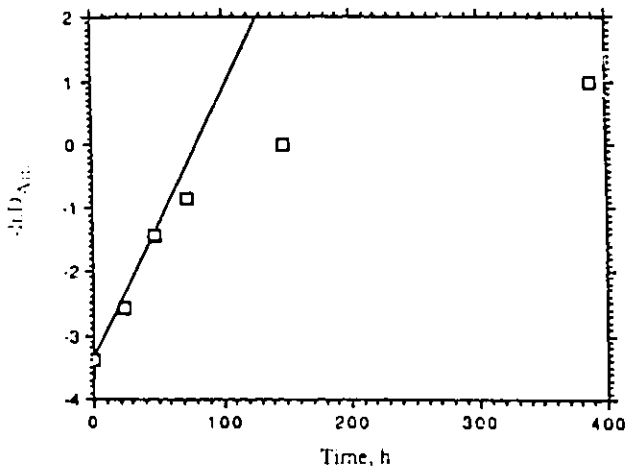

Fig. II-55.

Plot of ln D_{Am} versus Time of Hydrolysis for TRUEX-NPH in Contact with 2.5M HNO_3 at 95°C

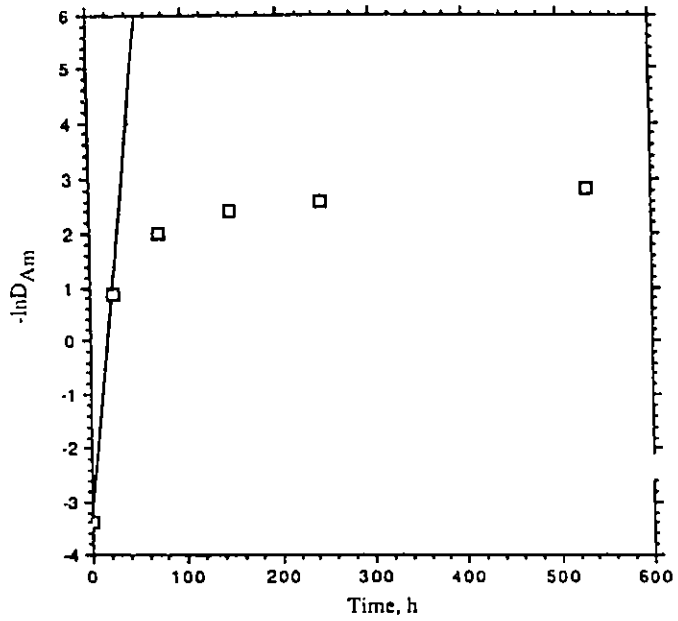

Fig. II-56. Plot of ln D_{Am} versus Time of Hydrolysis for TRUEX-NPH in Contact with 6M HNO_3 at 95°C

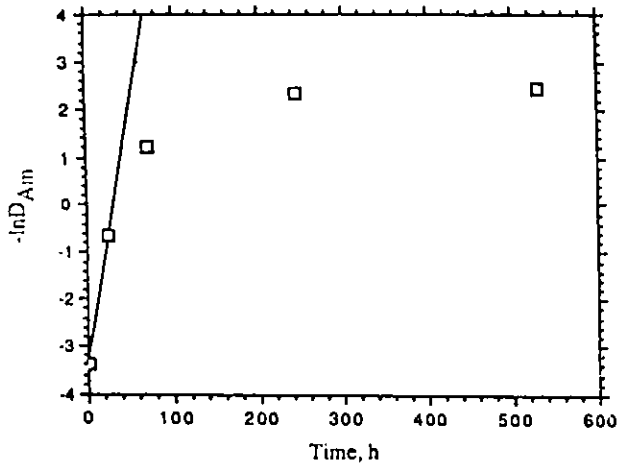

Fig. II-57.

Plot of ln D_{Am} versus Time of Hydrolysis for TRUEX-NPH in Contact with CAW, 1.4M H^+, at 95°C

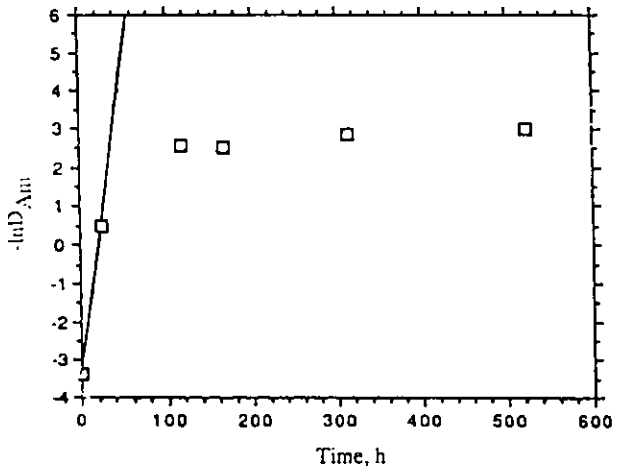

Fig. II-58.

Plot of ln D_{Am} versus Time of Hydrolysis for TRUEX-NPH in contact with CAW, 2.4M H^+, at 95°C

Another general characteristic of the variation of D_{Am} with time is a dependence on acid concentration. This is indicated by the tendency for the data to fall into families of curves, each family corresponding to one of the acid concentrations. Since a representative rate law must express some dependence on acidity, Eq. II-54 is considered to be a pseudo-first-order rate law, and k_{hp} is expressed as a function of acidity. Tests of the data showed that k_{hp} was best correlated with the activity of hydrogen ion in the aqueous phase in equilibrium with solvent {H}:

$$k_{hp} = k_h \{H\} \qquad \text{(II-61)}$$

or

$$nk_{hp} = nk_h \{H\} \qquad \text{(II-62)}$$

Values of nk_h were obtained from the slopes of graphs of nk_{hp} versus {H}, shown in Fig. II-59 through II-61.

Fig. II-59.

Plot of nk_{hp} versus Activity of H^+ in Aqueous Phase in Equilibrium with TRUEX-NPH Solvent for Hydrolysis of CMPO at 50°C

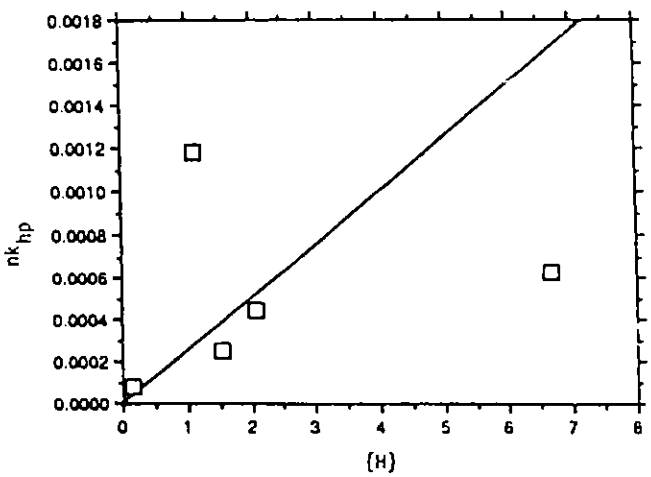

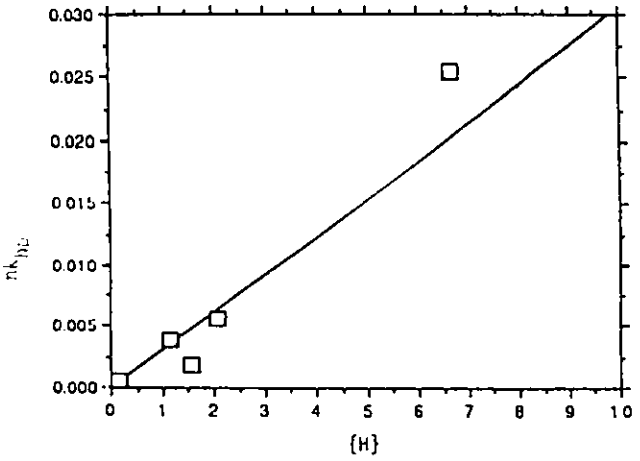

Fig. II-60.

Plot of nk_{hp} versus Activity of H^+ in Aqueous Phase in Equilibrium with TRUEX-NPH Solvent for Hydrolysis of CMPO at 70°C

Fig. II-61.

Plot of nk_{hp} versus Activity of H^+ in Aqueous Phase in Equilibrium with TRUEX-NPH Solvent for Hydrolysis of CMPO at 95°C

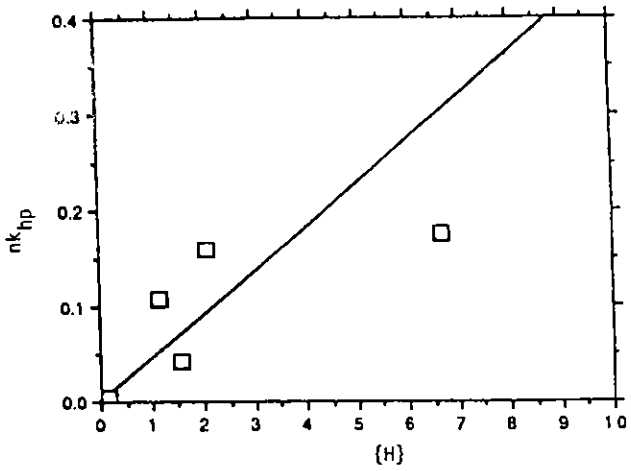

The dependence of k_h on temperature was correlated by an Arrhenius equation:

$$k_h = A\ e^{-E/RT} \qquad \text{(II-63)}$$

where A is the Arrhenius constant, E is the activation energy, R is the gas constant, and T is the temperature. Since

$$nk_h = nA\ e^{-E/RT} \qquad \text{(II-64)}$$

and

$$-\ln nk_n = E/RT - \ln nA \qquad \text{(II-65)}$$

values for nA and E were obtained from the graph of -ln nk_h as a linear function of 1/T, shown in Fig. II-62.

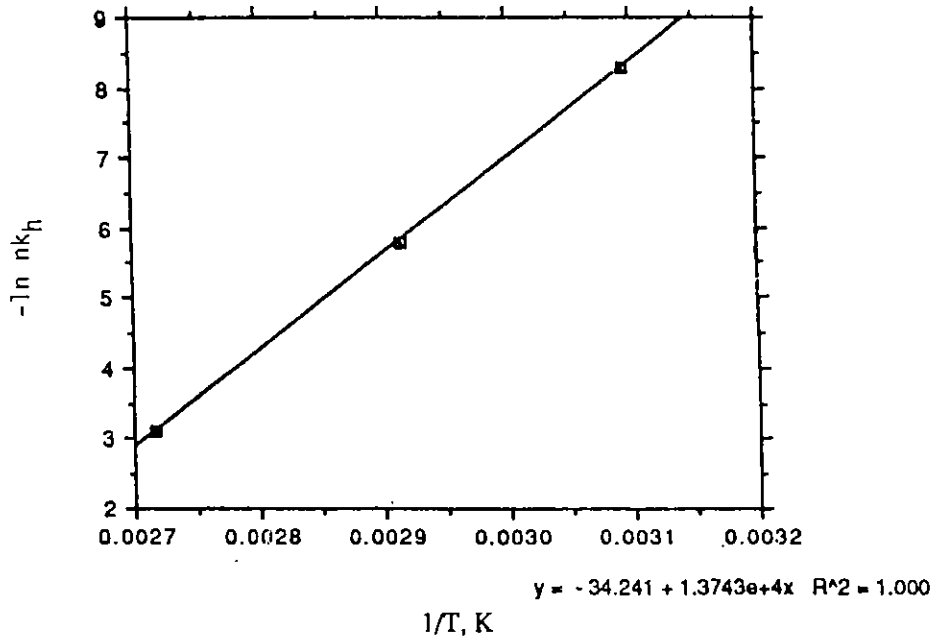

Fig. II-62. Correlation of Rate Constant nk_h for Hydrolysis of CMPO with Temperature

Combining Eqs. II-55, II-61, and II-63, the expression for the concentration of CMPO remaining in NPH solvent after hydrolysis during a time period t is

$$C = C_o e^{-A\{H\}te^{-ERT}} \qquad \text{(II-66)}$$

If D_{Am} varies with the third power of C (i.e., n = 3), A = 2.47 x 10^{14} L mol^{-1} h^{-1}, and E = 27.3 x 10^3 cal mol^{-1}.

b. Correlation of Radiolysis Data

Radiolyzed solvent had been prepared by exposing solvent samples to gamma radiation while in contact with aqueous solutions of the same composition as those used in the hydrolysis studies described above, but at a constant temperature of 50°C. As in the hydrolysis studies, measurements of the americium distribution between degraded solvent and aqueous HNO_3 were used as an analytical tool for determining the concentration of CMPO remaining in the solvent. Distribution of americium between degraded solvent and 2.0M HNO_3 is assumed to be controlled by the concentration of CMPO in solution at the start of radiolysis, whose concentration decreases with dose absorbed. Therefore, distribution ratios of americium at 2.0M acid concentration were used for following the CMPO concentration as a function of dose absorbed by the solvent.

The D_{Am} values obtained at 2.0M acid and for the assumption that D_{Am} is proportional to the third power of the CMPO concentration were used to calculate the molecules of CMPO destroyed per 100 eV absorbed dose (G values). Since the G values showed no regular dependence on the composition of the aqueous solutions in contact with the solvent during irradiation, the

data are combined to yield an average G value. The decrease of CMPO concentration with time as a zero-order rate law can be expressed as

$$-dC/dt = MGP \qquad \text{(II-67)}$$

or

$$-\frac{C}{C_0} = \frac{MG(Pt)}{C_0} - 1 \qquad \text{(II-68)}$$

where C = concentration of CMPO remaining, mol L^{-1}
C_0 = initial concentration of CMPO, mol L^{-1}
G = molecules CMPO destroyed/100 eV absorbed
M = a product of dimensional equivalents, 3.73×10^{-4} (100 eV) W^{-1} h^{-1} mol molecule^{-1}
P = power density of feed solution, W L^{-1}
t = time of irradiation, h

Substituting the relation of D_{Am} to CMPO concentration into Eq. II-68 gives

$$-\left[\frac{D_{Am}}{D_{Am_0}}\right]^{1/3} \frac{C_0}{M} = G(Pt) - \frac{C_0}{M} \qquad \text{(II-69)}$$

The G value is the slope in the graph plotting the term on the left-hand side of Eq. II-69 vs. Pt, as shown in Fig. II-63. The G value thus derived is 0.66 molecule CMPO destroyed per 100 eV absorbed.

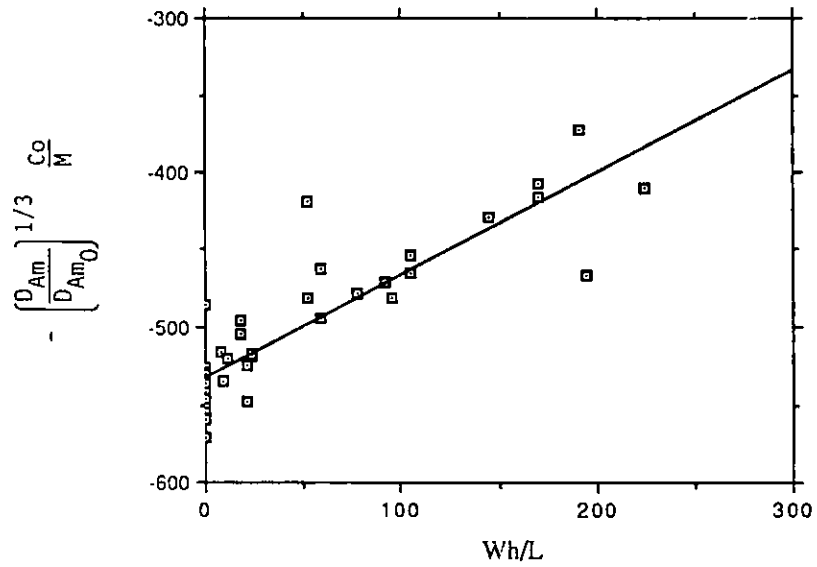

Fig. II-63. Dependence of a Function of D_{Am} (left-hand side of Eq. II-69) on Dose (power density times irradiation time)

3. Solvent Washing
(E. H. Van Deventer)

We have performed four experiments designed to emulate solvent washing in the TRUEX process. The results of these measurements are presented in Table II-38. All measurements were

Table II-38. Distribution Ratios Obtained from Stripping Experiments at 50°C[a]

Expt. No.	Washing Sequence	D value Fe-59	D value Y-88	D value Zr-88	D value Tc-99	D value Ru-103	D value Ce-141	D value Eu-152	D value Th-230	D value U-233	D value Np-239	D value Pu-238	D value Am-241	D value Cm-244
1	.25M Na_2CO_3	1.1E-03	4.6E-03	2.3E-03	7.9E-02	1.1E-01	2.3E-03	1.6E-04	2.1E-03	1.2E-03	1.9E-02	1.2E-03	5.3E-04	4.8E-05
	.25M Na_2CO_3	3.9E-01	1.4E-01	1.5E-01	5.9E-02	6.6E-01	1.1E-01	3.9E-03	3.9E-01	0.24	7.3E-03	1.3E-01	5.6E-02	b
	.25M Na_2CO_3	b	1.4E-01	9.0E-02	6.6E-02	1.9E-01	3.8E+00	b	1.1E+00	b	6.1E-02	2.9E-01	1.1E-01	b
2	.25M Na_2CO_3 + .03M NaF	c	c	c	c	c	2.8E-04	1.6E-04	8.8E-04	c	2.4E-04	c	1.8E-04	1.7E-04
	.25M Na_2CO_3	c	c	c	c	c	b	4.4E-01	7.3E-01	c	1.6E-02	c	7.1E-02	4.7E-02
	.25M Na_2CO_3	c	c	c	c	c	b	b	b	c	b	c	3.3E-01	a
3	.25M HEDPA in .05m HNO_3	c	1.2E-03	1.0E-03	1.9E-00	1.4E-01	1.8E-03	2.0E-04	1.6E-02	8.1E-05	1.5E-03	3.5E-02	8.4E-05	5.2E-05
	.25M HEDPA in .05m HNO_3	c	2.6E-01	2.4E-01	1.9E-00	6.7E+00	b	3.5E-01	9.4E-02	b	1.3E-02	1.6E-01	b	b
	.25M HEDPA in .05m HNO_3	c	b	b	1.8E+00	8.0E+00	b	b	3.6E-02	b	5.8E-02	1.3E-01	b	b
4	.25M HEDPA + .02M HF + .05M HNO_3	1.7E-02	c	c	c	c	4.3E-02	2.6E-04	1.7E-02	c	8.0E-04	c	7.0E-05	7.0E-05
	.25M HEDPA + .05M HNO_3	b	c	c	c	c	1.3E-03	1.4E-01	1.0E-02	c	5.1E-02	c	b	b
	.25M HEDPA + .05M HNO_3	b	c	c	c	c	9.2E-03	b	4.7E-03	c	3.1E-02	c	b	b

[a]For ^{59}Fe, ^{88}Y, ^{88}Zr, ^{99}Tc, ^{103}Ru, and ^{238}Pu, pre-equilibration of the TRUEX-NPH was with 0.04M HNO_3-0.04M HF; for all other isotopes, pre-equilibration was with 0.05M HNO_3.

[b]There was insufficient activity remaining for determination of this distribution ratio.

[c]No determinations of these values were made.

performed with pre-equilibrated, spiked (with the individual isotopes shown in Table II-38) TRUEX-NPH at 50°C with an organic-to-aqueous phase ratio of 5:1. Three successive back extractions were performed for each spike.

As can be seen in the table, in the experiments where TRUEX-NPH was pre-equilibrated with 0.05M HNO_3, all elements stripped with 0.25M Na_2CO_3 (with the exception of neptunium) stripped quite well. When fluoride ions were added, neptunium was also stripped quite well, and the stripping efficiencies (inverse D values) of the other isotopes generally improved.

In the experiments where TRUEX-NPH was pre-equilibrated with 0.04M HNO_3-0.04M HF, the only species not stripped very well by 0.25M Na_2CO_3 were pertechnetate and Ru(III).

For the strips with 0.25M HEDPA (1 hydroxylethane 1-1 di-phosphonic acid) in 0.05M HNO_3, no significant changes in stripping efficiencies were observed with the addition of fluoride ions. In addition, 0.25M HEDPA with 0.05M HNO_3 did not appear to strip iron, technicium, ruthenium, or thorium very efficiently.

G. Determination of Free Acid in Aluminum Nitrate Solutions
(J. L. Reed* and I. R. Tasker)

Aluminum nitrate is an important constituent of many high-level TRU-containing waste streams, and its aqueous chemistry is complex due to hydrolysis and complexation by many anions. Understanding its chemistry is important to our modeling in the GTM.

Under investigation here is the analysis of aqueous aluminum nitrate solutions containing excess nitric acid. Because of the extensive hydrolysis of Al^{3+}, simple potentiometric titration has not been feasible. The feasibility of doing this by the total exchange of cations on a strong acid ion exchange resin (H^+ form) and subsequent titration of the resulting acidic eluents was explored.

In this procedure, 40 mL of the resin in the H^+ form was generated from stock material by soaking in acetone for 45 min, washing with several volumes of water, treating for 45 min with water, filtering, treating for 30 min with 2M NaOH (50 mL), filtering, washing with water, treating with 2M HCl (50 mL) for 10 min, filtering, treating with 2M HCl (50 mL) for 30 min and rinsing with water until neutral. Preliminary experiments involved passing solutions containing Al^{3+} over a Dowex AG 50WX2 cation column until the eluents were neutral, followed by titration of the liberated hydrogen. Although the precision of these experiments was better than 1%, the initial experiments yielded only 67% of the acid expected according to the stoichiometry and solution concentration. We found that the titration curves were symmetrical, and that the amount of hydrogen liberated was independent of the resin volume. This strongly suggests that no aluminum species were present in the eluents (see Table II-39).

To verify the integrity of the procedure, a solution of a "non- hydrolyzing" cation, in this case a $Ba(NO_3)_2$ solution, was subjected to the same procedure (except that the same resin was used for all runs) as that used for the aluminum nitrate solutions. Aliquots (0.9 mL) of 0.21768M $Ba(NO_3)_2$ were passed through 4 mL of resin, and eluents and washings were collected until neutral. The eluents and washings were titrated with 0.05227M NaOH to a phenolphthalein endpoint. The results in Table II-40 show the hydrogen ion liberated (equivalent to the millimoles of NaOH used in the titration). The average is 0.2839 mmol per 0.9 mL aliquot; this yields 0.3154 equivalents/L for the $Ba(NO_3)_2$ solution. We expected 0.43526 equivalents/L (2 x 0.21768); thus, only 72% of the expected hydrogen ion was released.

---

*Chemistry Department, Clark Atlanta University, Atlanta, GA.

Table II-39. Hydrogen Liberated from Ion Exchange of Aluminum Nitrate Solutions

Run[a]	Resin Volume, mL	Hydrogen Ion Liberated, mmol
1	6	4.020
2	12	3.992

[a]For each run a 0.50 mL aliquot of analyte was used, which was 2.0M in aluminum nitrate and 0.020M in nitric acid.

Table II-40. Hydrogen Liberated from Ion Exchange of Barium Nitrate Solutions[a]

Run	Hydrogen Ion Liberated, mmol
1	0.2817
2	0.2869
3	0.2854
4	0.2838
5	0.2817

[a]The $Ba(NO_3)_2$ solutions were 0.2176M, and 0.90 mL aliquots were used.

However, when the resin was regenerated under more stringent conditions (treating with 10M HCl instead of 2M HCl), 96% of the expected acid was released. Results are given in Table II-41. (The barium nitrate was not purified prior to use and produced a slightly cloudy solution.) Nonetheless, treatment of the aluminum nitrate analyte with the regenerated resin yielded only 80% of the expected amount of acid. These results were reproduced within less than 1% when replicate determinations were made (see Table II-42).

Table II-41. Hydrogen Liberated from Ion Exchange of Barium Nitrate Solutions with Regenerated Resin[a]

Run	Hydrogen Ion Liberated, mmol
1	0.3800
2	0.3758
3	0.3727
4	0.3763
5	0.3727

[a]The $Ba(NO_3)_2$ solution was 0.2176M, and 0.90 mL aliquots were used.

Table II-42. Hydrogen Liberated from Ion Exchange of Aluminum Nitrate Solutions with Regenerated Resin[a]

Run	Hydrogen Ion Liberated, mmol
1	2.400
2	2.417
3	2.427
4	2.423

[a]A 0.50 mL aliquot was used which was 2.0M in aluminum nitrate and 0.020M in nitric acid.

The original difficulty is understood to have arisen from two sources. The first was incomplete conversion of the resin to the H^+ form. Although no explanation is offered at this time for the continued difficulty, Higgins and Wymer[35] found that dibasic aluminum nitrate solutions were not absorbed on a very similar resin (NH_4^+ form), even though the pH of dibasic aluminum nitrate solutions is such that the predominant species should have been Al^{3+}.[36] The other source for the difficulty is that, to use this method for determining such low levels of acid compared to aluminum, a much greater analytical precision is needed than is currently available.

An alternative procedure for determining hydrogen is selective absorption of the aluminum species and determination of the eluted acid. The anticipated advantage of such a procedure is that low levels of acid may be determined more accurately in the presence of high concentrations of aluminum. Generally, the binding of cations increases as the charge of the ion increases. The objective was to generate a column which would absorb the tripositive aluminum ions and pass the monopositive hydrogen ions. To this end, an AG 50WX2 resin in the Ba^{2+} form was generated. The difference in selectivity notwithstanding, conditions were not found such that all of the acid placed on the resin (in the Ba^+ form) could be recovered in the eluents. A study was carried out to determine the amount of acid recovered as a function of the resin volume. The relationship was approximately linear (Fig. II-64), with complete recovery only possible in the absence of resin. Each eluent was tested with sulfuric acid to determine if Ba^{2+} was present. All eluents contained barium (see Table II-43). Because this resin will not selectively absorb Al^{3+} and efficiently pass H^+, it is not suitable for this type of analysis.

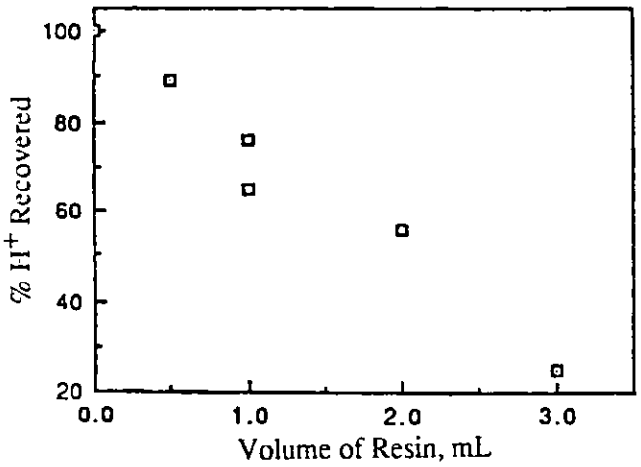

Fig. II-64.

Relationship between Percent H^+ Recovered and Volume of Resin Used

Table II-43. Hydrogen Recovery from Ba^{2+} Resin[a]

Run	Volume of Resin, mL	Fraction of Hydrogen Ion Recovered	Precipitate with H_2SO_4
1	0.5	0.889	yes
2	1.0	0.652	yes
3	3.0	0.251	yes
4	2.0	0.555	yes
5	1.0[b]	0.757	yes

[a]For each run, 1 mL aliquots of 0.2852M HCl were diluted to 10 mL, then passed over the resin.

[b]The aliquot was diluted to 100 mL rather than 10 mL.

H. Use of BAN and DIBAN
(J. L. Reed)

Of interest is the possibility of using BAN or DIBAN solutions as scrub feed solutions in the TRUEX process; BAN and DIBAN are, respectively, basic aluminum nitrate $AlOH(NO_3)_2$ and dibasic aluminum nitrate $Al(OH)_2NO_3$, where the formulas represent the stoichiometries of the solutions and are not representations of speciation. These solutions would make useful feeds for the scrub section of TRUEX processed for several reasons:

- The major function of the scrub section in the TRUEX process is to remove nitric acid from the organic solvent leaving the extraction section. This is necessary to allow effective stripping of americium in the first strip section. (The americium distribution ratio is approximately proportional to $\{NO_3\}^3$; too much nitric acid in the strip section means that D_{Am} values are too high for americium stripping. Both BAN and DIBAN are buffered solutions that have the ability to strip nitric acid very effectively from the organic phase by the acid-base reaction:

  $$nHNO_3 + Al(OH)_n^{(3-n)+} \rightleftarrows Al^{3+} + nNO_3^- + nH_2O$$

- Another important assignment for the scrub-section feed is to maintain high distribution ratios for actinide and lanthanide elements (keeping them in the organic solvent as it passes through the section) while unwanted species are scrubbed back to the extraction section. Even though these solutions effectively strip nitric acid, their nitrate concentration can be kept high enough (>0.5M) to maintain distribution ratios for actinides and lanthanides above one.

- The presence of aluminum ion in the scrub feed solution also effectively scrubs aqueous-phase complexants (oxalic, hydrofluoric, sulfuric, and phosphoric acids) from the solvent before they enter the first strip section and strips plutonium and uranium from the solvent with americium and the rare earths. Aluminum ion in the scrub feed accomplishes this by being itself complexed by these species in the scrub, returning the complexants to the feed section.

A computerized literature survey was conducted by using the Department of Energy Abstracts (1974-1989) and Nuclear Science Abstracts (1948-1976) data bases. We found no citations for BAN, DIBAN, or aluminum nitrate with "solvent extraction," "basic," etc., in the Department of Energy Abstracts and five citations for DIBAN in the Nuclear Science Abstracts. In addition, Chemical Abstracts for the past several years was surveyed for relevant reports relating to aqueous aluminum(III) chemistry.

In one of the citations, Higgins and Wymer[35] proposed that transuranic wastes containing relatively large amounts of aluminum be treated by one of several methods to yield solutions having a DIBAN composition. The aluminum species in such a solution would not be competitively absorbed on a strong-acid cation exchange resin, thus allowing separation of the aluminum from the transuranic wastes. They determined that a strong-base anion exchange resin was best for generating the DIBAN solutions, and the solutions used were 1.6M in DIBAN and had a pH range of 3.0-3.59.

Codding[37] proposed that DIBAN solutions be used as an aqueous phase in the solvent-solvent extraction of UO_2^{2+} into organic-tributylphosphate solutions. The solvent-solvent extraction of UO_2^{2+} was studied with the objective of thermodynamically modeling the extraction process. The speciation and activity of the uranium were studied, but no similar studies were carried out for the aluminum (although an activity coefficient was assigned to the DIBAN). Surak and Thomason[38] have studied and evaluated several methods for analyzing DIBAN solutions to determine aluminum, basicity, nitrogen, ammonia, and nitrate content. According to Gresky,[39] DIBAN solutions are best prepared by the reaction of aqueous

aluminum nitrate with metallic aluminum under reflux with a Hg(II) catalyst. Edding et al.[40] have also observed the formation of a DIBAN phase in the preparation of alumina at 400°C.

It was mentioned earlier that the formulation of DIBAN as $Al(OH)_2(NO_3)$ represents only the stoichiometry of DIBAN solutions. In most studies the compositions used were $Al(OH)_x(NO_3)_{3-x}$ where $1 < x < 2$, with fractional values being very common. The hydrolysis data found in Baes[36] suggest that at the DIBAN solution pH range (2-3.6), $Al(O_4)_2^+$ is not the dominant species. Rather, at these pH values, Al^{3+} would be the dominant species. If BAN or DIBAN is to be used in TRUEX processing, much work will be needed in the preparation, use, and modeling of these solutions.

I. Concentration of TRUEX Waste and Product Streams

(I. R. Tasker)

Associated with GTM development is the need to consider the management of TRUEX process waste and product streams. Problems here could be greatly reduced if the volumes involved in disposal were lessened. One technology being investigated is the FRIDGEVAP evaporator-concentrator produced by LICON, Inc. (Pensacola, FL). Proposals have been made to investigate the incorporation of an evaporator-concentrator into the TRUEX process. The result desired is to be able to reduce total volume of product and waste streams and to recycle nitric acid used in the extraction. The benefit of this is that in, for example, the nonTRU raffinate, the nitric acid need not be neutralized before the stream is immobilized in grout, and the total volume of grout to be finally disposed of is considerably reduced.

In the evaporation and concentration of TRUEX process waste and product streams, two physical processes of interest occur: (1) the production of a distillate, the composition of which will tend to vary, and (2) the concentration of the bottoms, with the potential for a variety of materials precipitating. Both processes must be subject to prediction.

1. Distillation

According to Ellis and Thwaites,[41] at atmospheric pressure the azeotropic composition of the nitric acid/water system is 38.65 mol% HNO_3 (boiling temperature, 120.1°C). This translates into a composition of 34.97 molal HNO_3. Using the density data of Sohnel and Novotny[5] and noting that the azeotropic composition corresponds to 68.8 wt % HNO_3, we estimated a density at 25°C of 1.401 g/mL. The concentration is given by the relationship[42]

$$c = \frac{m\ d}{1 + (0.001\ m\ M)} \qquad \text{(II-70)}$$

where c = concentration (mol/L)
d = density (g/mL)
m = composition (mol/1000 g H_2O)
M = solute molar mass (g/mol)

We calculated that the 38.65 mol% HNO_3 composition corresponds to a concentration, at 25°C, of 15.3 M. A distillate at this concentration is potentially useful for recycling in a TRUEX plant. Data on the vapor-liquid equilibria of the water/nitric acid system are available in the literature.[43-46] We have not yet used these data for our calculations due to present uncertainties in operating conditions.

The next question to address is, what is the effect of dissolved salt on the vapor-liquid equilibrium? The most convenient bibliography of data sources is Ref. 47, from which numerous references were obtained. Wichterle et al. list references for about 40 water/nitric acid/salt systems; from a survey of this work, we made the following generalizations.

The presence of salts in the solution tends to salt out nitric acid, i.e., the vapor phase is enriched in nitric acid. Polovnikova et al.[48] investigated the vapor-liquid equilibria at atmospheric pressure of 16 ternary systems (water + nitric acid + sulfates of Li, Na, K, Zn, Cd, Hg, Cu, Mn, Co, Ni, La, Y, Sc, In, Ga, Al). In every case except K_2SO_4, vapor-phase/nitric acid enrichment occurs. It is noteworthy that $Al_2(SO_4)_3$ [and presumably $Al(NO_3)_3$] exhibits the greatest salting-out capacity. Polovnikova et al.[48] also point out that an estimate of the salting-out capacity of an ion in a ternary system can be made based upon knowledge of its electrostatic characteristics, free energy of hydration, and the absolute entropy of the hydrated cation. (Polovnikova et al. do not report temperature.)

The temperature at which the equilibrium takes place can profoundly alter the effect of the salt on the equilibrium. Yakimov et al.[49] measured the solubility isotherms and vapor pressures in the water/nitric acid/sodium nitrate system at 25, 35, and 50°C. By constructing the isopotentials of water (loci of constant water activity as HNO_3 and $NaNO_3$ vary), interesting behavior was observed. At 25°C nitric acid can be salted in or out, depending upon solution composition. This behavior changed at 50°C, when the nitric acid was salted out under all circumstances. Thus, the temperatures of operation could be of great importance.

Few predictive models have been discovered so far in the literature search. Here, two systems (nitric acid/water/lithium nitrate and nitric acid/water/magnesium nitrate) can be well represented by functions of the mean mole fractions of the electrolytes, mole fraction of water, and separation functions for the electrolytes (functions in terms of the analytical mole fractions of the constituents, the modified ionic strength, and various constants). Though good at representation, the methods have no predictive use. A common thermodynamic framework used is to equate the fugacities of the components in the vapor and liquid phases when at equilibrium. At normal pressures, the vapor phase can be treated by the ideal gas law or one of the simpler equations of state. Since the liquid must be treated as a nonideal solution, various methods have been used. However, most of these are referenced to systems of organic components. Little of a definitive nature has been discovered for systems such as water/nitric acid/salt, though further literature search is needed. On a more empirical line, the work of Shneerson et al.[50] is of interest. Vapor-liquid equilibria in three systems (water/nitric acid/magnesium nitrate, water/nitric acid/calcium nitrate, and water/nitric acid/magnesium nitrate/calcium nitrate) were studied, and the effect of the nitrate salts on the azeotropic point and the vapor compositions was seen to be approximately additive. This suggests that multicomponent system behavior can be predicted from ternary system data.

Finally, it should be noted that the literature search performed has been exploratory and not exhaustive. For example, an interesting approach to the need for activity coefficient models in predicting vapor-liquid equilibrium in electrolyte systems has been taken by Chen et al.[51]; the water/hydrochloric acid system at 298.15 K was well represented up to 18 molal. However, the approach is based upon Pitzer's[7] model of solution activities and would thus, in our case, require measurement of many unknown parameters.

In summary, the literature examined so far indicates that the distillate from a concentrator working on TRUEX waste and product streams would be useful and amenable to recycling. The effect of salts on the distillate composition will increase the nitric acid content. A basis for modeling the behavior should be available with the application of sufficient effort.

2. Precipitation Behavior

An understanding of precipitation behavior makes use of the tools derived from the study of solid-liquid equilibria. For a saturated solution (MX) of an electrolyte dissociating as

$$M_aX_b = aM^{i+} + bX^{j-} \qquad \text{(II-71)}$$

we have

$$K_{sp} = \frac{\{M^{i+}\}^a \quad \{X^{j-}\}^b}{\{M_aX_b\}} = \{M^{i+}\}^a \quad \{X^{j-}\}^b \qquad \text{(II-72)}$$

where K_{sp} is the thermodynamic solubility product, the braces indicate the activity for the identified species, and the solid activity has been assumed to be equal to 1. Replacing the activities by molalities and activity coefficients (γ), we obtain

$$K_{sp} = [M^{i+}]^a \quad [X^{j-}]^b \quad (\gamma^{i+})^a \quad (\gamma^{j-})^b \qquad \text{(II-73)}$$

$$= S \quad (\gamma^{i+})^a \quad (\gamma^{j-})^b \qquad \text{(II-74)}$$

where S is the analytical solubility product. Modeling precipitation behavior is thus an instance of modeling activities and activity coefficients. Numerous models, of varying quality, exist for estimating activities; Zemaitis et al.[52] outline, with examples, the methods of Guggenheim. Davies, Bromley, Meissner, Pitzer and Chen. Incorporation of these methods into estimation procedures is common practice. However, few of these procedures are useful. Zemaitis et al.[52] have addressed the lack of good data and suitable thermodynamic framework in their development of ECES computer software (Equilibrium Composition of Electrolyte Solutions) that claims to predict vapor-liquid-solid equilibria in multicomponent aqueous systems as a function of temperature and concentration. Further investigations are being made into this software. It remains generally true that such predictions are limited by the activity model. Horvath[53] lists a number of references for solubility estimation in simple systems but points out that, at present, one can not estimate whether a salt forms a hydrate and, further, that hydrate melting point estimations are unreliable.

In summary, though numerous models for precipitation/solubility behavior have been presented, most are recognized as poor and of limited application. This has largely been due to a comparative lack of demand for such models. Recent developments in modeling aqueous solutions should provide a framework for modeling precipitation behavior in TRUEX process effluents. Further literature work is planned.

J. Verification Studies

(D. B. Chamberlain, K. A. Barnthouse,* C. J. Conner,* M. A. Internoscia,* A. B. La'O,** R. A. Leonard, F. C. Mrazek, J. E. Stangel,* E. H. Van Deventer, and M. O. Wasserman**)

1. Introduction

Laboratory verification tests of the TRUEX process are being completed to (1) develop a better understanding of the TRUEX process chemistry, (2) test and verify process modifications and enhancements, and (3) verify the results of the GTM computer model. This model is being developed for predicting species extraction behavior and calculating flowsheets for the TRUEX process. Two

---

*Co-op student from University of Cincinnati.

**Co-op student from University of Illinois at Chicago.

centrifugal contactor units are used for these tests: a 16-stage 4-cm centrifugal contactor for non-radioactive tests and a 16-stage 4-cm unit located in a glovebox for radioactive tests. Five verification tests were completed during this report period: three with the TRUEX-TCE solvent and two with TRUEX-NPH solvent. The purpose of these tests is not to demonstrate flowsheets for specific waste streams, but to collect data in order to verify that the TRUEX model predicts actual extraction behavior. Therefore, flowsheets have not been optimized to produce a nonTRU waste stream or to produce a "clean" rare earth (Am) or Pu stream, but to evaluate the extraction behavior in all stages.

2. Test Description

a. Flowsheet

The basic flowsheet used in all five verification tests is shown in Fig. II-65. This flowsheet included two extraction stages, three scrub stages, four strip #1 stages, four strip #2 stages, two carbonate wash stages, and one acid rinse stage. All of the aqueous feed streams except for the extraction feed (DF) remained constant for all of these tests and are shown in Fig. II-65. The extraction section feed, however, was changed for each run. The compositions of these solutions are reported in Tables II-44 and II-45. Runs 5, 6, and 9 contained uranium or radiotracers and were therefore completed in the glovebox.

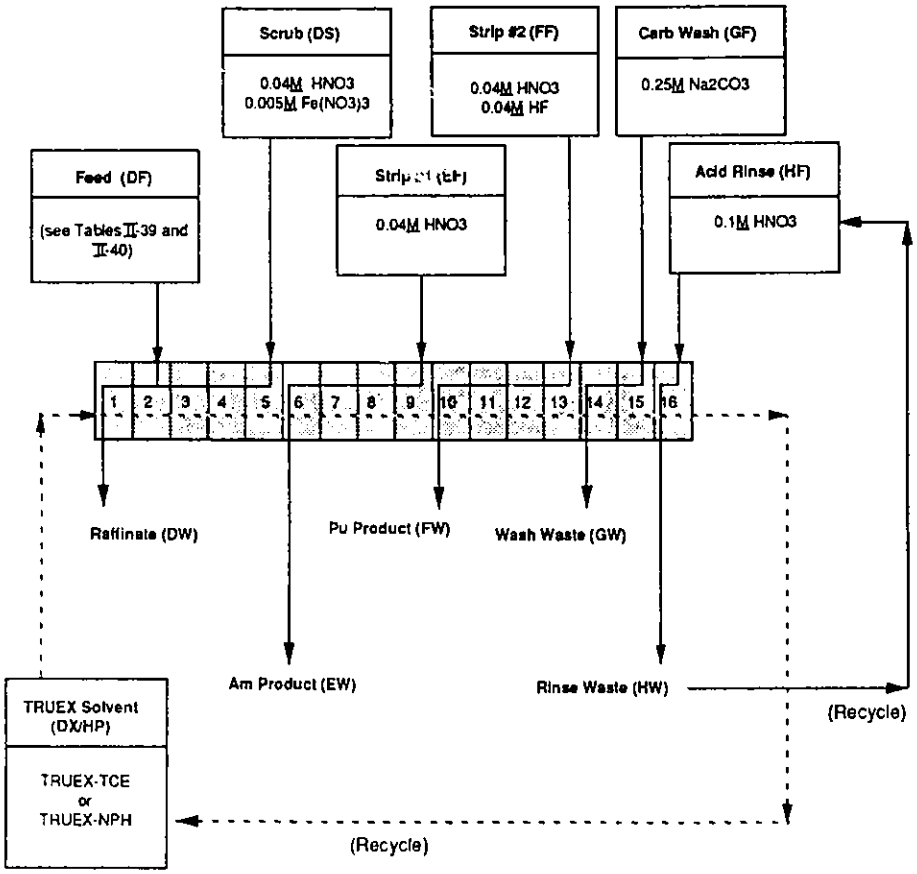

Fig. II-65. Typical Flowsheet for Verification Runs

Table II-44. Extraction Feed Composition (DF) for Verification Runs 5, 6, 8, and 9

Component	Concentrations, M			
	Run 5	Run 6	Run 8	Run 9
H	1.19	1.5	1.26	1.5
Nd	0.008	0.008	0.008	0.008
Al	0.72	0.72	0.72	0.72
Fe	0.13	0.13	0.13	0.13
Na	0.18	0.18	--	0.18
Ca	0.02	0.02	--	0.02
Zr	0.006	0.006	0.006	0.006
$HC_2O_4^-$	0.12	0.12	--	0.12
HSO_4^-	0.27	0.27	0.23	0.27
HF	0.15	0.15	0.17	0.15
NO_3^-	3.23	3.62	3.44	3.62
Pu	--	3.0E-5	--	
TcO_4 (Tc-99m)	--	3E-10	--	3E-10
K	--	--	0.18	--
Rb	--	--	0.00011	--
Cs	--	--	0.006	--
Rh	--	--	0.00014	--
Pd	--	--	0.006	--
Ru	--	--	0.006	--
Sr	--	--	0.006	--
Zr-88	--	--	--	tracer
Y-88	--	--	--	tracer
Ru-103	--	--	--	tracer
Ce-141	--	--	--	tracer
Gd-153	--	--	--	tracer
Np-239	--	--	--	tracer
Am-241	--	--	--	tracer

One scrub section was included in this flowsheet; the feed composition was 0.04M HNO_3 and 0.005M $Fe(NO_3)_3$. The purpose of the scrub section is twofold. First, some of the nitric acid that was extracted in the extraction section is stripped from the organic phase. By removing this nitric acid, the first strip section is better at removing III-oxidation-state elements from the organic phase. Second, the 0.005M Fe added to the feed solution is used to strip oxalic, hydrofluoric, and sulfuric acids from the organic solvent.

The purpose of the first strip section in the TRUEX process is to strip and recover americium from the organic phase. This stream is labeled EW in Fig. II-65. For most of these tests, americium was not added to the DF feed solution, but neodymium and other rare earths that behave like americium were present. By measuring the concentration of neodymium and the other rare earths in these tests, the americium behavior can be inferred. The composition of the first strip solution was the same as in previous verification tests, 0.04M HNO_3.

The purpose of the second strip section in the TRUEX process is to remove and recover plutonium from the organic phase. In most of these tests, we did not have a metal present that behaves similarly to plutonium. The composition of the second strip solution was 0.04M HNO_3 and 0.04M HF.

Table II-45. Extraction Feed Composition (DF) for Verification Run 7

	Concentration, M	
	As-Prepared	As-Measured
Non-Fission-Product Cations		
Total H	2.08	2.54
H^+	2.01[a]	
Total Fe	0.13	conc. not available
Total Al	0.72	0.372
Na^+	0.18	0.198
Cr^{3+}	0.013	0.0131
Ni^{2+}	0.0069	0.0071
Cu^{2+}	0.0014	0.0015
Mg^{2+}	0.0243	0.0014
Ca^{2+}	0.02	0.00095
Mn^{2+}	0.0014	0.00153
Si^{4+}	0.0092	not detected
Fission Products		
Total Zr	0.006	0.0033
Rb^+	0.00565	0.00016
Cd^{2+}	0.00052	0.000055
Cs^+	0.0023	0.0059
Sr^{2+}	0.0014	0.00072
Y^{3+}	0.00074	0.000751
Rh^{3+}	0.00057	0.00047
Pd^{2+}	0.00057	0.00027
Ag^+	0.000036	0.000034
Ba^{2+}	0.0011	0.000032
Non-Fission-Product Cations		
La^{3+}	0.001	0.00049
Ce^{3+}	0.0024	0.00097
Pr^{3+}	0.00362	0.0014
Nd^{3+}	0.0027	0.0029
Sm^{3+}	0.00068	0.00034
Eu^{3+}	0.00005	0.000035
Gd^{3+}	0.00001	not detected
Anions		
Total C_2O_4	0.18	not measured
Total F	0.15	0.138
Total SO_4	0.275	not measured
NO_3^-	3.0	not measured

[a]Calculated using version 1.1c of the Generic TRUEX Model, dated 4/19/89.

Three solvent cleanup stages were included in these tests: two stages of carbonate wash (0.25M Na_2CO_3) and one stage of acid rinse (0.1M HNO_3). The purpose of the two sodium carbonate contacts was to remove acid degradation products from the organic phase and to strip any metals that were not recovered in the strip sections. The last stage, the acid rinse section, was used to neutralize any sodium carbonate that is carried over with the organic, which was then recycled back into the extraction section (stage 1).

In Verification Run 5, uranium was added to the extraction feed (DF) to measure its concentration throughout the flowsheet. In Verification Run 6, three radioactive isotopes were added to the DF feed: ^{59}Fe, ^{241}Pu, and ^{99m}Tc. Both of these tests were completed in a glovebox with the TRUEX-TCE solvent. In Verification Run 7, a complex DF solution was evaluated whose composition was similar to that of a Hanford Current Acid Waste (CAW) solution. In Verification Run 8, the DF solution was simplified from Verification Run 7 and the test repeated. Both of these tests used the TRUEX-NPH solvent. In Verification Run 9, eight radioactive isotopes were added to the DF solution: ^{99m}Tc, ^{88}Zr, ^{88}Y, ^{103}Ru, ^{141}Ce, ^{153}Gd, ^{239}Np, and ^{241}Am.

b. Sampling and Sample Analysis

Two types of samples were collected during each test. The first set of samples was collected from the raffinate and product streams. Approximately 16 min into the test, samples from each raffinate stream were collected on an 8-min cycle. These samples were collected to measure the various component concentrations during steady-state operation. About 55 of these samples were collected during each test. Stage samples, the second type of sample, were collected at the end of the test. These samples consisted of both the organic and aqueous phases that were contained in the contactor rotors. By measuring the concentrations in these samples, we determined the concentration profile (both the organic and aqueous phase) for nitric acid and the metals in solution.

To collect stage samples, the solutions in the rotor (which was presumed at steady state*) and in the mixing zone (which may not be at steady state) were separated. This was accomplished by placing beakers underneath each stage drain valve, turning off all of the feed pumps, then quickly opening each drain valve. The rotors were left on during this operation to prevent solutions inside the rotors from draining. After the solution was drained from the annular region, sample bottles were placed beneath each stage, then the contactor motors were shut down. As the rotors spun down, the solution drained from the rotor and into the sample bottles.

Samples were then analyzed by various techniques, depending upon the analysis desired. These techniques included aqueous titration, organic titration, analysis by inductively coupled plasma (ICP) with atomic emission spectroscopy, nitrate analysis, scintillation counting, and gamma counting. Results from these analyses were evaluated by completing material balance calculations, a flow-rate analysis, and a comparison with the GTM predictions.

3. Results and Discussion

Because of space limitations in this report, only a small fraction of the data collected during these runs will be reported here. These data are representative of the data collected.

a. Verification Run 5

Verification Run 5 was the first test completed in a glovebox. The main reason for completing this run was to test the equipment that we had installed in the glovebox and to verify that our sample collection and handling procedures were adequate. Data were also collected on the extraction of UO_2^{2+} by the TRUEX solvent and were compared with concentrations calculated by the GTM.

---

*Because effluent and stage samples from the same stage in general do not have the same compositions (as they should at steady state), there is concern that about stage samples being representative of the steady-state compositions in the stage. Other means of collecting stage samples are being developed.

This test was completed without any major upsets, but because the sample analysis results for uranium (by laser fluorescence) were inconsistent, additional samples are undergoing analysis to clarify these results.

b. Verification Run 6

Verification Run 6 was the second verification test completed in the glovebox. For this test, ^{59}Fe, ^{239}Pu, and ^{99m}Tc were added at tracer levels to the simplified feed solution (DF). In addition, ^{59}Fe was added to the scrub feed (DS) so that the specific activity of iron was the same as the feed solution.

Aliquots from samples collected during Run 6 were analyzed on a gamma counter to measure the ^{99m}Tc concentration, which has a 6.01-h half-life. Several days later, after the ^{99m}Tc had decayed to lower levels, these same samples were recounted to measure the ^{59}Fe concentrations more accurately. Samples were also analyzed on a scintillation counter to measure plutonium concentrations.

The ^{99m}Tc stage concentrations (after correcting for decay) are plotted in Fig. II-66. For this plot, the GTM concentrations were adjusted to reflect the ^{99m}Tc concentration measured in the DF feed stream. As shown in Fig. II-66, the GTM predictions do not agree with the measured values, although the trends are similar. The measured concentrations are nearly always greater than the GTM predictions. This discrepancy could be accounted for if the TcO_4^- has built up in the recycled organic solvent. This buildup can be clearly seen in Fig. II-67, which shows the ^{99m}Tc concentrations in the DX samples during the run. Because the current GTM does not include the solvent wash stages, the recycle of TCO_4^- could not be accurately modeled. The revised GTM now being developed will incorporate the solvent wash stages, whereupon this analysis will be repeated.

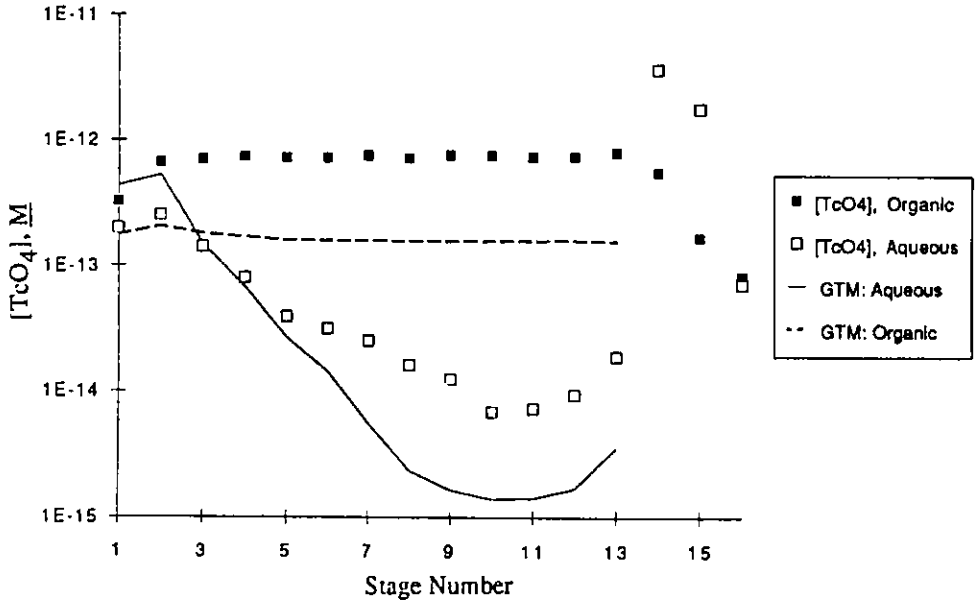

Fig. II-66. Comparison of the Experimental TcO_4 Data with the GTM Predictions for Verification Run 6

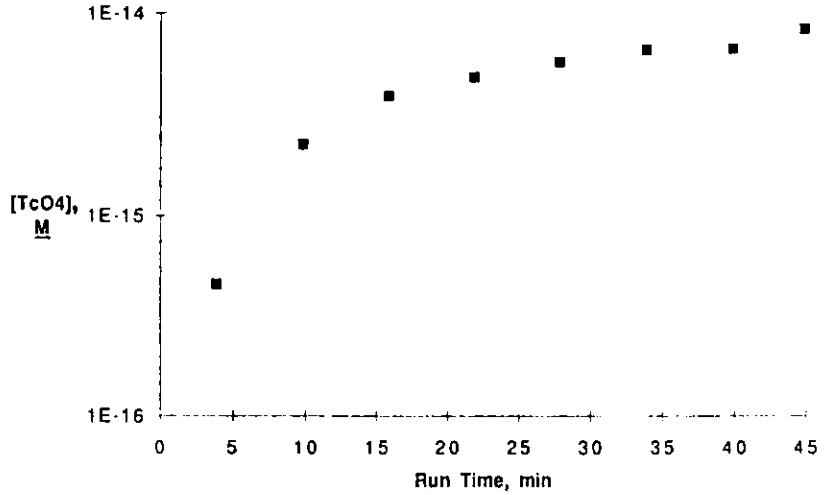

Fig. II-67. Plot of the TcO_4 Concentration in the DX Stream from Verification Run 6

Distribution coefficients (D) measured in the extraction section are also different from the GTM predictions. Where the model predicts a D value less than one, the experimental D value is greater than one (for the extraction section). Otherwise, the trends for the rest of the process are similar in that the organic ^{99m}Tc concentration remains constant until the solvent wash stages (very little of the ^{99m}Tc is stripped from the organic solvent). In the two carbonate wash stages, the ^{99m}Tc was partially stripped from the organic (D values of 0.15 and 0.09). Because the ^{99m}Tc is only partially stripped from the organic and the organic was recycled for this test, the ^{99m}Tc continued to build up in the DX feed.

In Fig. II-68, the technetium concentration in the organic product (HP) is plotted versus the run time. In this figure, the ^{99m}Tc concentration in the organic phase of stage 16 does not agree with that in the raffinate samples. The agreement between the concentration data for a given stage with the corresponding raffinate concentrations gets worse with increasing stage number. For example, in the extraction section raffinate (DW), the stage concentration agrees fairly well with the raffinate concentrations; but at the other end of the contactor for the solvent wash raffinate (HW), the samples differ by an order of magnitude. This difference appears to be because we have not been completely successful in isolating the stages from each other during shutdown. Further tests are needed to see how we can correct this problem and improve the stage sample analysis.

Iron-59 was added to the feed and scrub solutions to measure the movement of iron through the contactor system. Although iron concentrations based upon all five gamma energies can be calculated, only those concentrations based upon the two highest abundance peaks, 1099.3 keV (56.5% abundance) and 1291.6 keV (43.2% abundance), will be reported here.

The iron concentration data are plotted in Fig. II-69. As shown in this figure, there is fairly good agreement for concentrations calculated from both energies. Iron was not detected past stage 12 in the aqueous phase and after stage 9 in the organic phase. Iron-59 was not detected in the carbonate wash (GW) or the acid rinse (HW) raffinate streams. The GTM predictions are also shown in this figure. The differences between the predicted and the experimental data may be due to an inaccurate model and/or to inaccurate data because iron (III) extraction is rate dependent, and stage samples were in contact for long periods before the phases were separated. The aqueous-phase data in the extraction section fit the GTM predictions reasonably well, but not the organic phase.

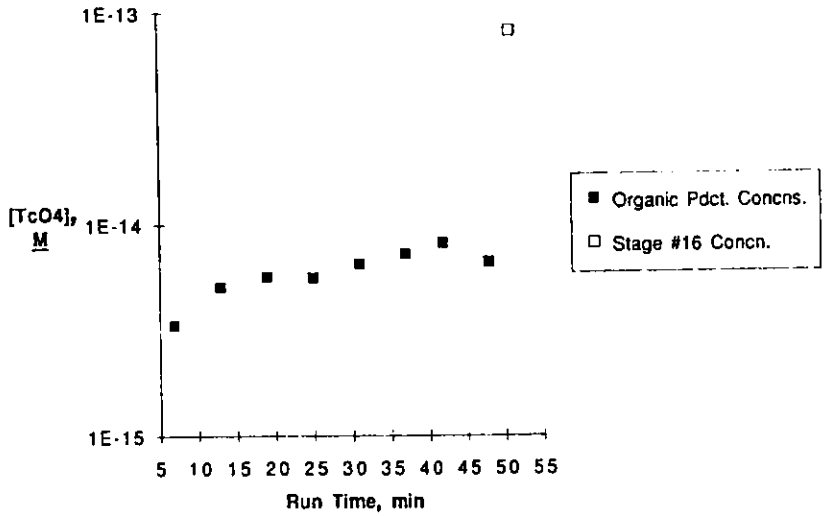

Fig. II-68. Plot of the TcO_4 Concentration in the HP Stream for Verification Run 6

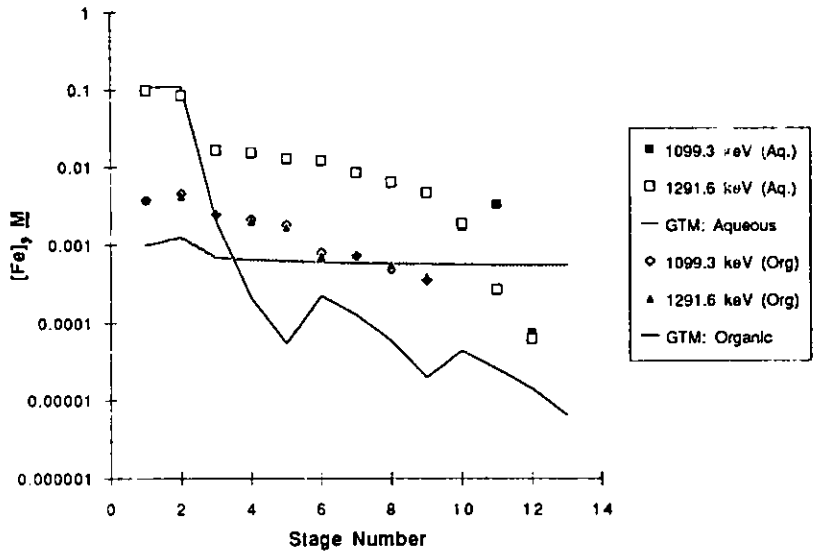

Fig. II-69. Plot of the Aqueous and Organic Phase Stage Concentrations Based upon Various Iron-59 Peaks for Verification Run 6

A typical plot of the iron concentrations in a raffinate stream (in this case, for the second strip) is shown in Fig. II-70. The experimentally measured FW raffinate concentrations were higher than the GTM predictions. In addition, the iron concentration starts out at 10^{-3}M, then increases to a steady-state concentration of nearly 10^{-2}M after about 15 min. As was the case for the technetium data, the measured stage concentrations and the raffinate concentrations agree in the extraction section but not in the strip sections. The iron concentrations in the raffinate also do not agree with the GTM predictions.

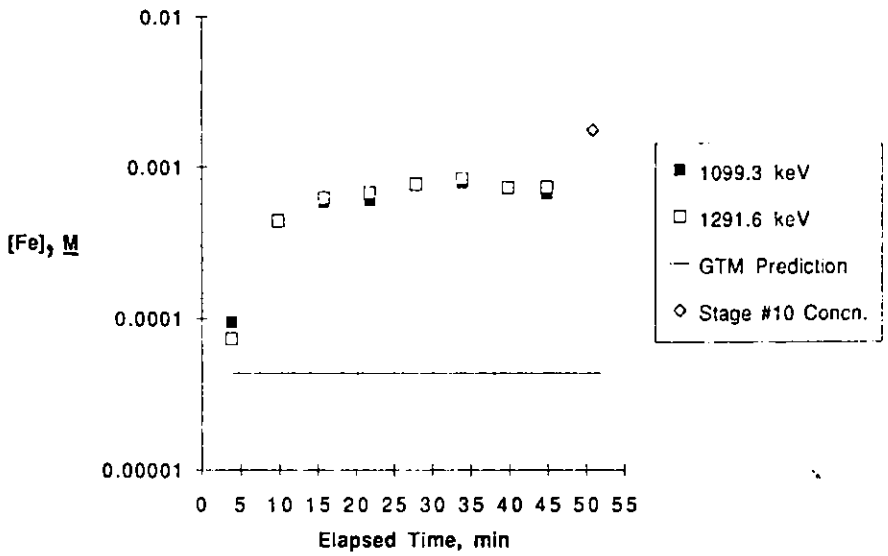

Fig. II-70. Plot of Iron Concentrations Based Upon Various Iron-59 Peaks in the FW Raffinate Stream as a Function of Sample Time for Verification Run 6

To measure the ^{239}Pu concentrations (an alpha emitter), we collected aliquots from each sample and counted them on the scintillation counter after the ^{99m}Tc had decayed. The data collected from this analysis had to be corrected because of the beta interference from the ^{59}Fe. This interference is shown graphically in Fig. II-71, where the ^{59}Fe beta peak (which includes signals from its γ emissions) is superimposed on the ^{239}Pu peak. One can see that the "tail" of the iron peak interferes with the counting window for the plutonium peak. A method was developed to correct the plutonium counts by deleting the effect that the ^{59}Fe has in this spectrum.

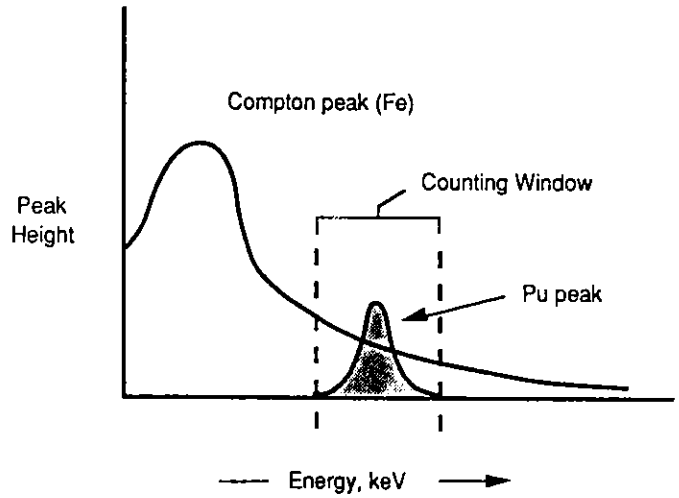

Fig. II-71. Plot of the ^{59}Fe Interference with the ^{239}Pu Analysis

To develop this method, various-sized aliquots of ^{59}Fe solution were counted on both gamma and scintillation counters. Then a relationship was developed between the ^{59}Fe counts measured on the gamma counter and those measured by the scintillation counter. From this relationship, we can predict the effect of ^{59}Fe on the plutonium peak

Using this correction, we calculated the plutonium concentrations, which are plotted in Fig. II-72. These data agree reasonably well with the GTM predictions for the first ten stages. Agreement would have been better if the GTM were able to account for solvent loading by neodymium; the next version of the GTM will have this capability. The data and the model do not agree at all following stage 10. In this run, the first-strip flow rate had been set to 50 mL/min instead of 200 mL/min; thus, all of the neodymium was not stripped from the organic phase. This neodymium carried over into the second strip and complexed the fluoride, resulting in decreased stripping efficiency for plutonium in these stages. One problem with the current version of the GTM is that it cannot correct for the neodymium complexing the fluoride, which reduces the free fluoride concentration. This effect will be part of the upgrade in the next version of the GTM. The solvent wash section of the flowsheet, stages 14-16, did strip the plutonium from the organic phase.

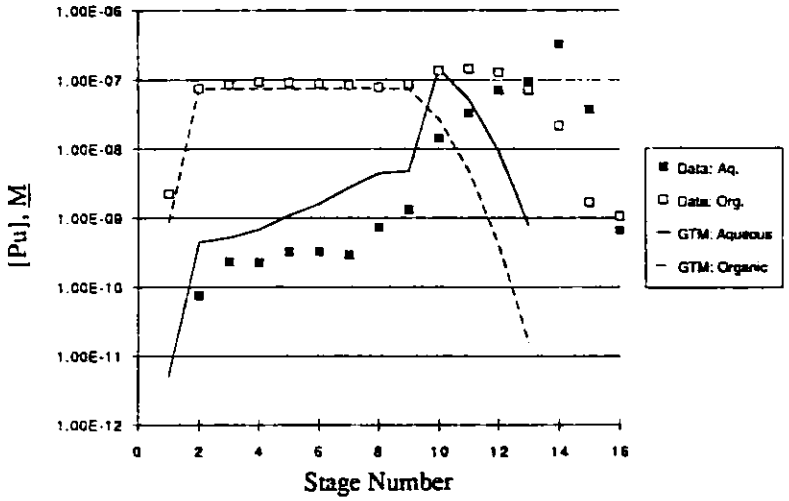

Fig. II-72. Plot of ^{239}Pu Stage Concentrations for Verification Run 6

c. Verification Run 7

Run 7 was the first verification test completed at 50°C using the TRUEX-NPH solvent. For this test, the extraction feed solution (DF) contained many components and was originally prepared in FY 1988. The composition of this solution is given in Table II-45.

An accurate value for the various flow rates in verification runs is important because small changes in one flow can dramatically affect the concentrations in another section. For a typical nonradioactive verification test, flow rates are measured in several different ways. One method is to measure the amount of feed solutions used over a certain time period during the entire run and to also measure the amount of raffinate solution collected. Results of these measurements for Run 7 are reported in Table II-46 (under "calculated flow rate"). The measured flow rates in this table are the values that were measured before the beginning of the run (during pump calibration). The expected flow rates in this table are based upon the pump settings and, therefore, the flowsheet. As shown in this table, the calculated, measured, and expected flow rates for this test agree reasonably well.

Table II-46. Flow Rate in Verification Run 7

	Flow Rate, mL/min		
	Calcd.[a]	Measd.[b]	Expected[c]
		Basis: Feed Solutions	
DX		180	180
DF	284	272	270
DS	49.4	45	45
EF	183	178	180
FF	99.1	90.2	90
GF	56.3	44.7	45
HF	d	17.8	18
		Basis: Raffinate Solutions	
DW	317		315
EW	173		180
FW	88.5		90
GW	50.3		45
HW	d		

[a]Based upon tank depletion or filling.
[b]Based upon initial flow rate check before run.
[c]Based upon pump setting (and flowsheet).
[d]This stream was recycled, so flow rates cannot be calculated.

After the test, samples were stored in an oven at 50°C to prevent the formation of a second organic phase. Unfortunately, precipitates developed in most of the stage samples, though all of the feed and raffinate samples remained free from precipitates. However, aliquots were collected from the stage samples for metals analysis before the formation of these precipitates.

Aliquots from the stage samples were collected for titration analysis, even though some of the samples contained precipitates. Results from the aqueous and organic titrations are shown in Figs. II-73 and II-74. Several aliquots were collected from each sample and titrated several times, and these multiple results are shown in both figures. For the aqueous phase, there is a fairly good fit between the GTM predictions and the experimental data after stage 4, but not in the first three stages. The data show sample variability, probably due to the high metals concentrations in these stages. Differences may also be due to the precipitate formation, which may have changed the acid concentrations. The agreement between the GTM and the experimental data for the organic phase is very good.

Based upon the ICP results, plots were generated of the metal concentrations vs. stage number and time in each raffinate stream. Plots for two rare earths, Nd and La, are shown in Figs. II-75 and II-76. Both are typical of the other rare earths in this test, where the measured concentrations in the strip sections are lower than the GTM predictions. Again, accounting for solvent loading and tying up of the fluoride concentration by complexation of rare earth ions would have increased the accuracy of the GTM predictions.

Figure II-77 shows a plot of three metal concentrations in the first strip raffinate (stage 6). This plot shows the difference between the raffinate and stage concentrations and the difference between the GTM predictions and the experimental data.

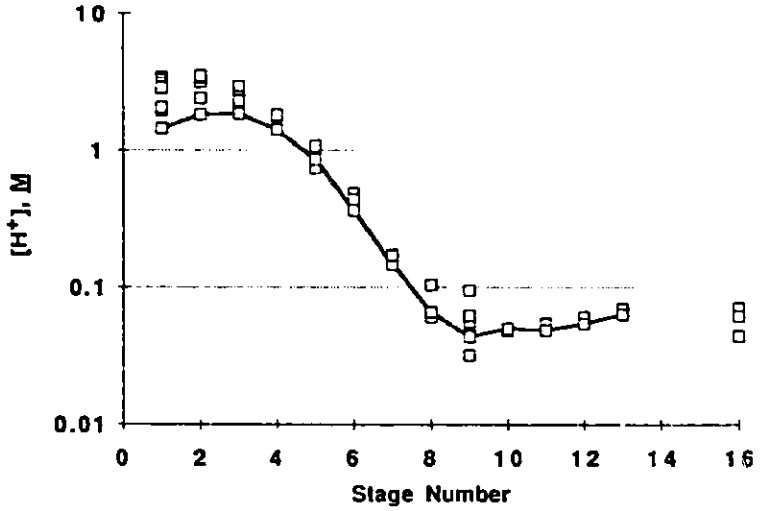

Fig. II-73. Aqueous Acid Stage Profile for Verification Run 7 (GTM predictions shown by curve).

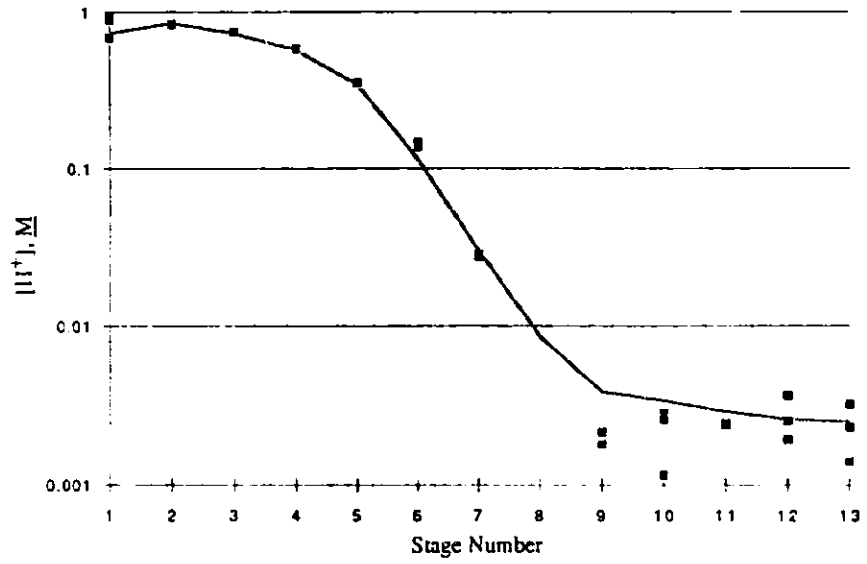

Fig. II-74. Organic Acid Stage Profile for Verification Run 7

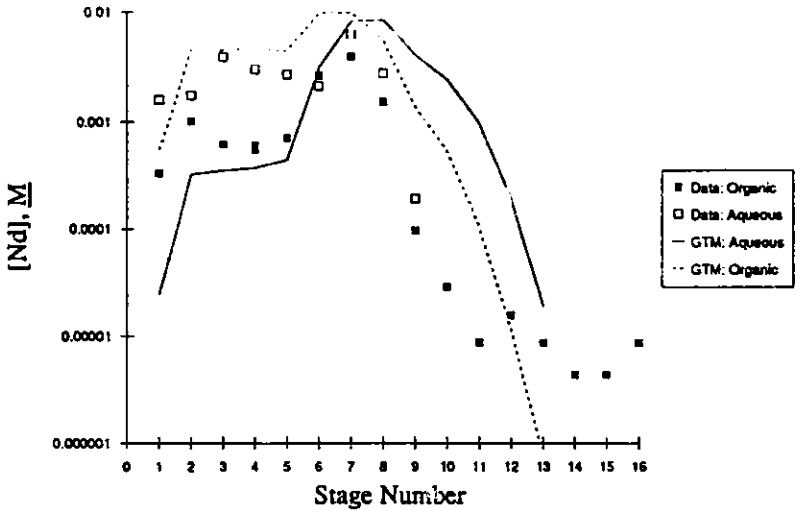

Fig. II-75. Concentration Results for Neodymium in Verification Run 7

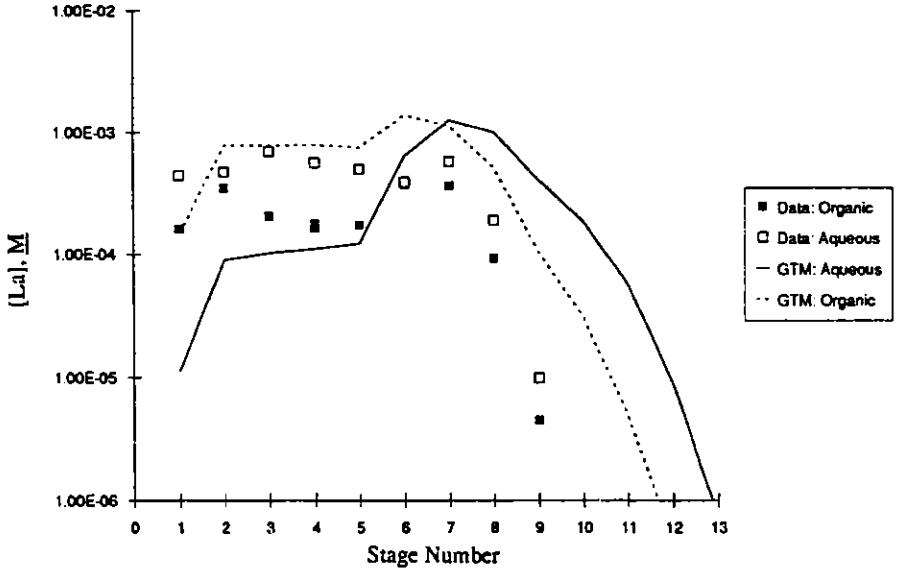

Fig. II-76. Concentration Results for Lanthanum in Verification Run 7

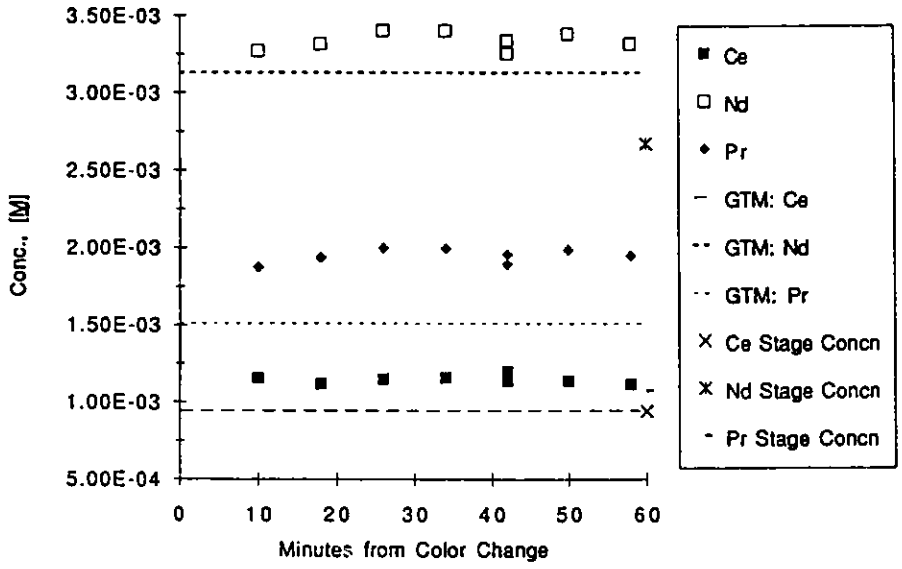

Fig. II-77. Raffinate Concentrations (EW) for Ce, Nd, and Pr in Verification Run 7

d. Verification Run 8

Verification Run 8 was the second test completed at 50 °C using the TRUEX-NPH solvent and was the smoothest-running verification run to date. Stage samples were stored in an oven at 52 °C to prevent the formation of a third phase. When sample aliquots were removed from the stage samples for acid titrations, precipitates were observed in some of the stage samples. All the HP samples were clear except for a small amount of transparent brown precipitate at the bottom of each sample bottle. All the DX samples and the aqueous samples, except for the DF feed sample, were clear of precipitate. In spite of these precipitates, aliquots of both phases were collected and analyzed for the H^+ concentration. Results of these stage-sample analysis are shown in Figs. II-78 and II-79. Aqueous-phase acid concentrations agree with the GTM predictions very well (unlike Run 7, where the concentrations in the extraction and scrub sections did not agree), while there is some discrepancy in the measured and calculated concentrations for the organic phase.

The aqueous-phase acid concentrations in the first-strip raffinate (EW) are plotted in Fig II-80, which indicates that it took about 30 min to reach steady-state operation. The concentration in stage 6 is also plotted in this figure, and it agrees with the raffinate concentrations, though there is significant scatter in the data. For run 8, stage samples were not submitted for ICP analysis because of precipitate formation. Also, raffinate stream data for other components are not reported because they are similar to those from Run 7.

e. Verification Run 9

For this verification test, several radioactive isotopes were added to the DF feed solution. Spectra of the feed sample (after decay of the ^{99m}Tc) are shown in Figs. II-81 and II-82. These spectra were collected on a Ge/Li detector. The possible energies seen during the gamma analysis of these samples are given in Table II-47.

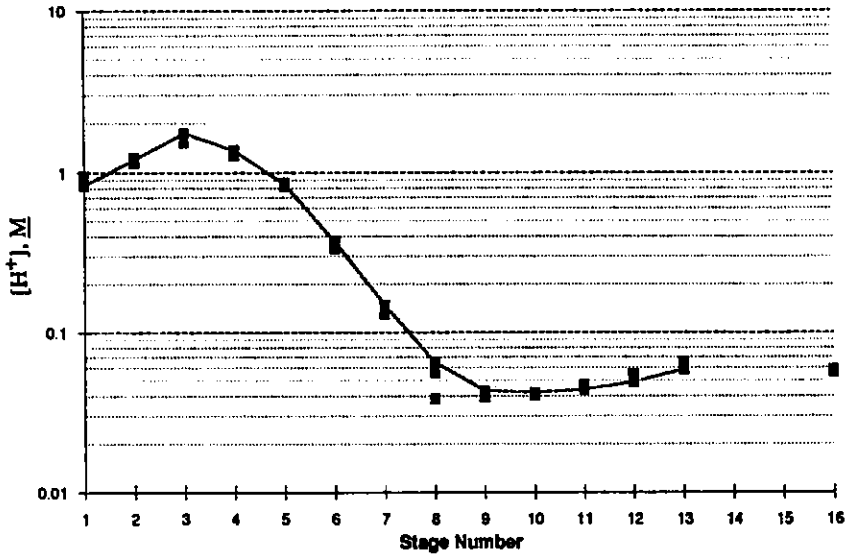

Fig. II-78. Aqueous H^+ Stage Concentrations for Verification Run 8

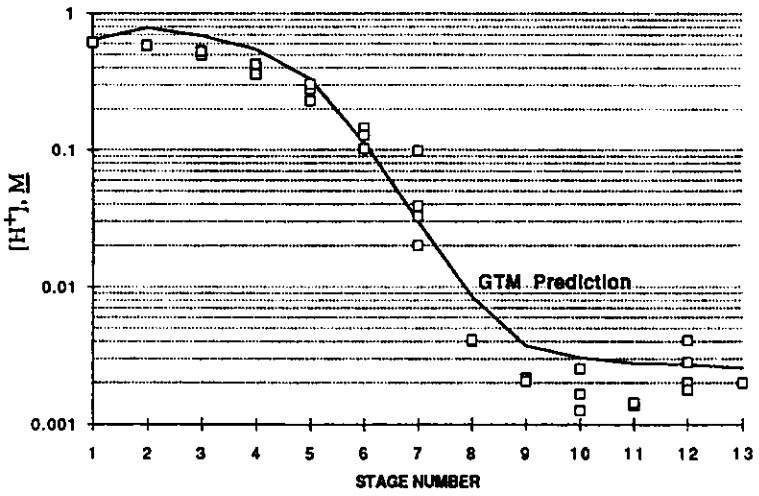

Fig. II-79. Organic H^+ Stage Concentrations for Verification Run 8

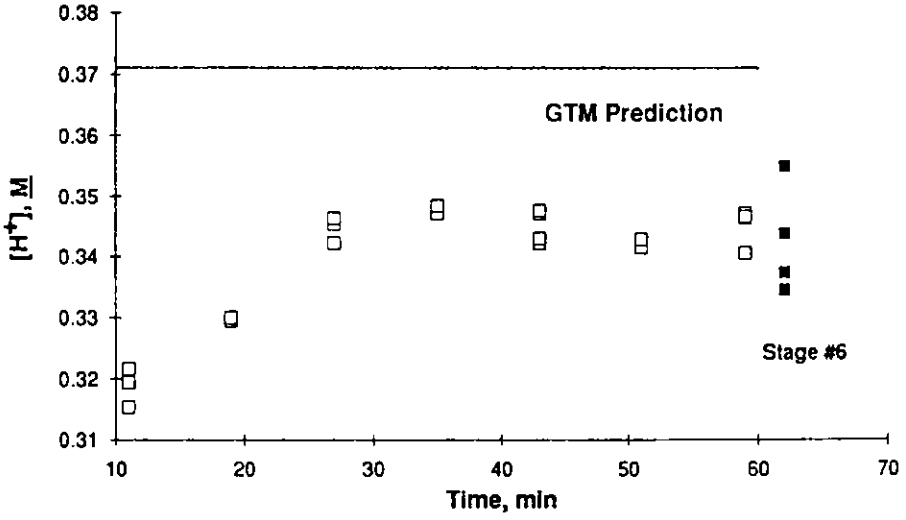

Fig. II-80. First Strip Raffinate Concentrations from Verification Run 8

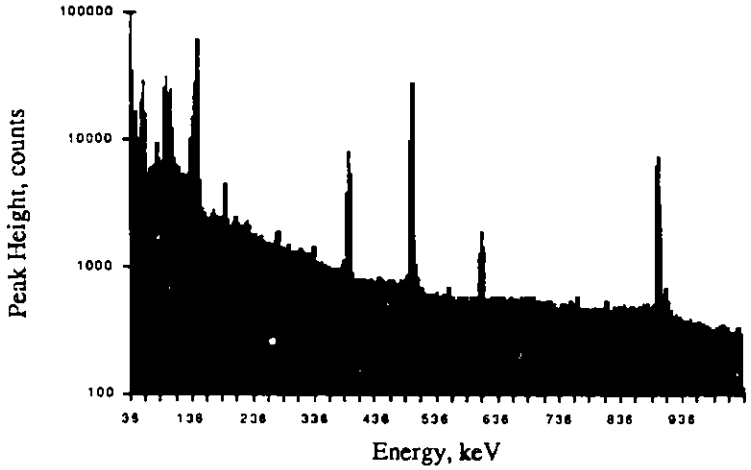

Fig. II-81. Gamma Spectrum A of the DF Feed Solution after ^{99m}Tc Decay in Verification Run 9

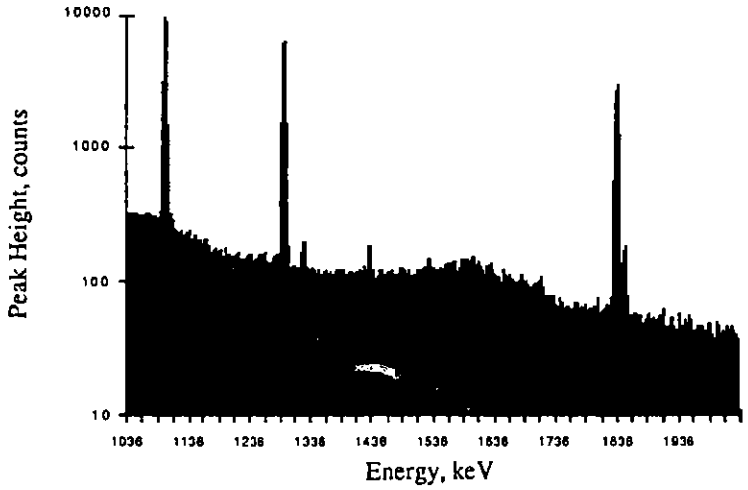

Fig. 82. Gamma Spectrum B of the DF Feed Solution after ^{99m}Tc Decay in Verification Run 9

Table II-47. Possible Energy Peaks by Gamma Energy Analysis from Verification Run 9

Component	Number of Peaks	Energy, keV	Abundance, %	Component	Number of Peaks	Energy, keV	Abundance, %
Fe-59	5	142.5	1.03	Np-239	16	44.7	0.13
Fe-59	5	192.2	3.11	Np-239	16	49.4	0.11
Fe-59	5	334.8	0.26	Np-239	16	57.3	0.14
Fe-59	5	1099.3	56.5	Np-239	16	61.5	1.29
Fe-59	5	1291.6	43.2	Np-239	16	99.6	12.8
				Np-239	16	103.8	20.4
Ru-103	8	20.1	7.11	Np-239	16	106.1	26.4
Ru-103	8	22.8	1.47	Np-239	16	116.9	7.61
Ru-103	8	53.3	0.38	Np-239	16	120.5	2.63
Ru-103	8	295	0.25	Np-239	16	209.7	3.30
Ru-103	8	443.8	0.32	Np-239	16	226.4	0.29
Ru-103	8	497.1	89.5	Np-239	16	228.2	11.20
Ru-103	8	557	0.832	Np-239	16	254.4	0.11
Ru-103	8	610.3	5.64	Np-239	16	277.6	14.50
				Np-239	16	285.4	0.79
Ce-141	5	35.5	4.88	Np-239	16	315.9	1.60
Ce-141	5	36	8.91				
Ce-141	5	40.7	2.66	Am-241	4	20.8	4.85
Ce-141	5	41.8	0.7	Am-241	4	26.3	2.4
Ce-141	5	145.4	48.4	Am-241	4	33.2	0.12
				Am-241	4	59.5	35.9
Gd-153	8	40.9	34				
Gd-153	8	41.5	61.5	Tc-99m	3	20.7	1.35
Gd-153	8	47	18.7	Tc-99m	3	140.5	87.7
Gd-153	8	48.3	5.4	Tc-99m	3	142.6	0.041
Gd-153	8	69.7	2.34				
Gd-153	8	83.4	0.21	Y-88	3	898	94
Gd-153	8	97.4	30.1	Y-88	3	1836	99.4
Gd-153	8	103.2	21.8	Y-88	3	2734	0.6
				Zr-88	1	392.9	97.3

To reduce the number of peaks that must be evaluated, peaks were omitted based upon the following criteria:

1. During the initial screening of the data, no peaks were detected below 39 keV; therefore, all peaks with standard energies below 39 keV were eliminated.

2. Peaks with an abundance less than 5% are not likely to be detected or have greater errors associated with them. For these isotopes, other peaks of higher abundance can be used to evaluate the concentration of that particular isotope. Therefore, these peaks were also eliminated.

3. Two peaks with energies within approximately 1 keV of each other were eliminated, since the detector cannot separate these two peaks. The experimentally determined peak may or may not be a combination of the two energies. Therefore, these peaks were eliminated.

Based upon these criteria, the final peak energies that were be evaluated are listed in Table II-48.

Table II-48. Expected Energy Peaks by Gamma Energy Analysis from Verification Run 9

Component	Energy, keV	Abundance, %
Fe-59	1099.3	56.5
Fe-59	1291.6	43.2
Ru-103	497.1	89.5
Ru-103	610.3	5.64
Ce-141	145.4	48.4
Gd-153	97.4	30.1
Np-239	99.6	12.8
Np-239	106.1	26.4
Np-239	116.9	7.61
Np-239	228.2	11.20
Np-239	277.6	14.50
Am-241	59.5	35.9
Tc-99m	140.5	87.7
Y-88	898	94
Y-88	1836	99.4
Zr-88	392.9	97.3

Figure II-83 gives the calculated and measured americium concentration as a function of the stage number. The fit is fairly good until the strip section is reached (stage 8), where the measured concentrations are higher than the GTM predictions. (Flow rates used for the GTM predictions were those measured during the test). Figures II-84 and II-85 show where we tried to make the GTM predictions fit the data better by varying the flow rate. We first varied the scrub flow rate in the GTM (Fig. II-84) and then the organic solvent flow rate (Fig. II-85); both changes improve the fit of the GTM with the data. This indicates how important it is to accurately measure the flow rates in these verification tests. Figure II-86 gives the measured and calculated gadolinium concentrations at an elevated organic solvent flow rate (220 mL/min instead of the expected 200 mL/min). The fit is excellent between the data and the model calculations.

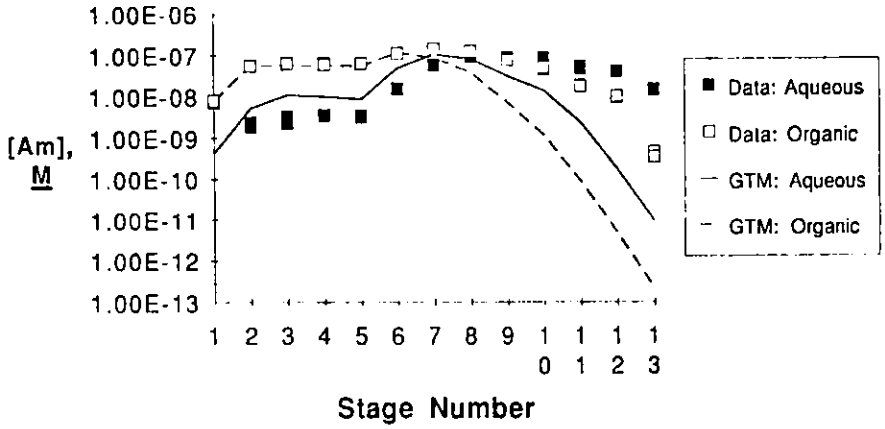

Fig. II-83. Plot of the Americium Concentrations in Verification Run 9

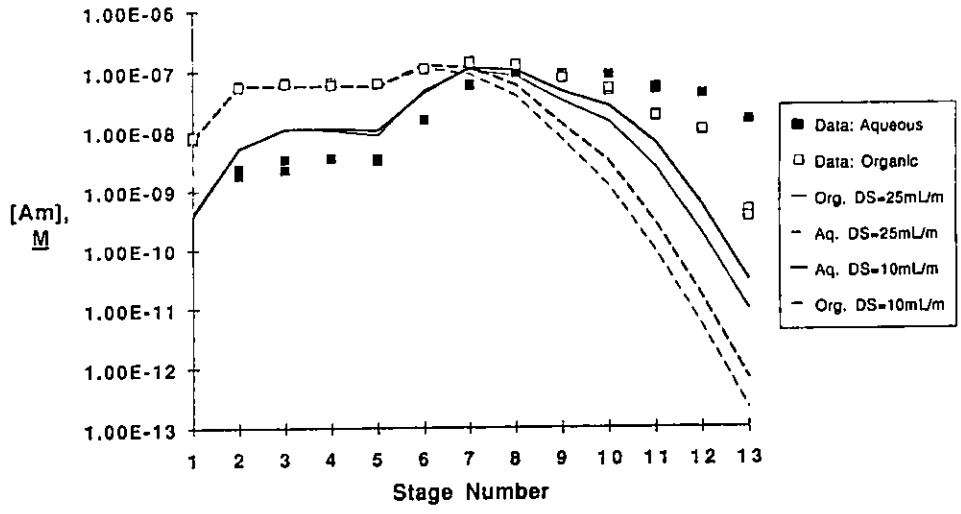

Fig. II-84. Effect of the Scrub Flow Rate (DS) on Americium Concentrations

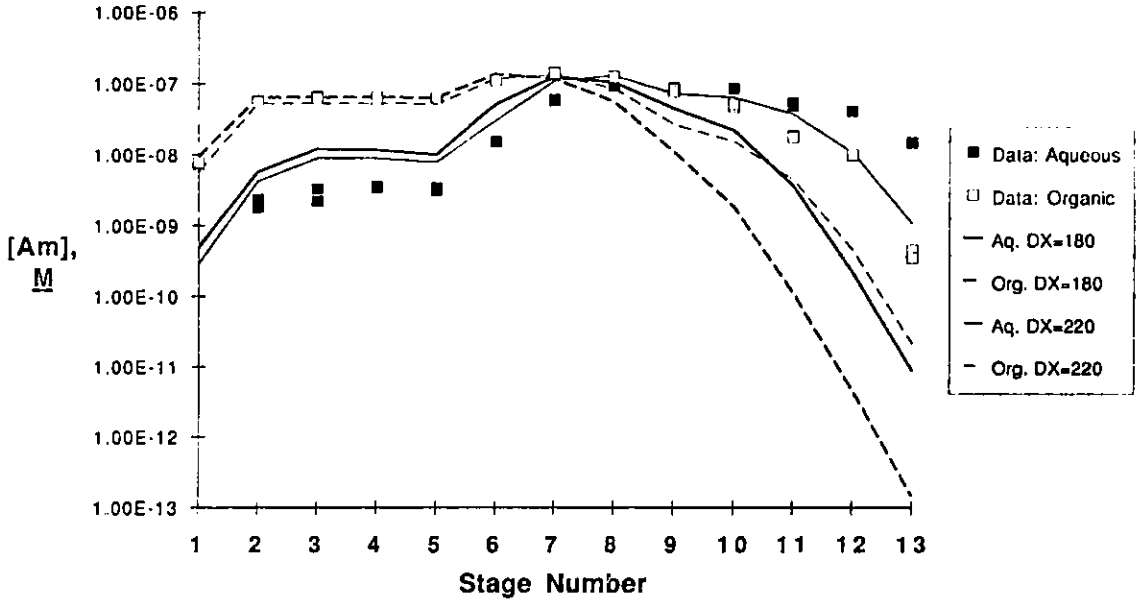

Fig. II-85. Effect of the Organic Flow Rate (DX) on Americium Concentrations

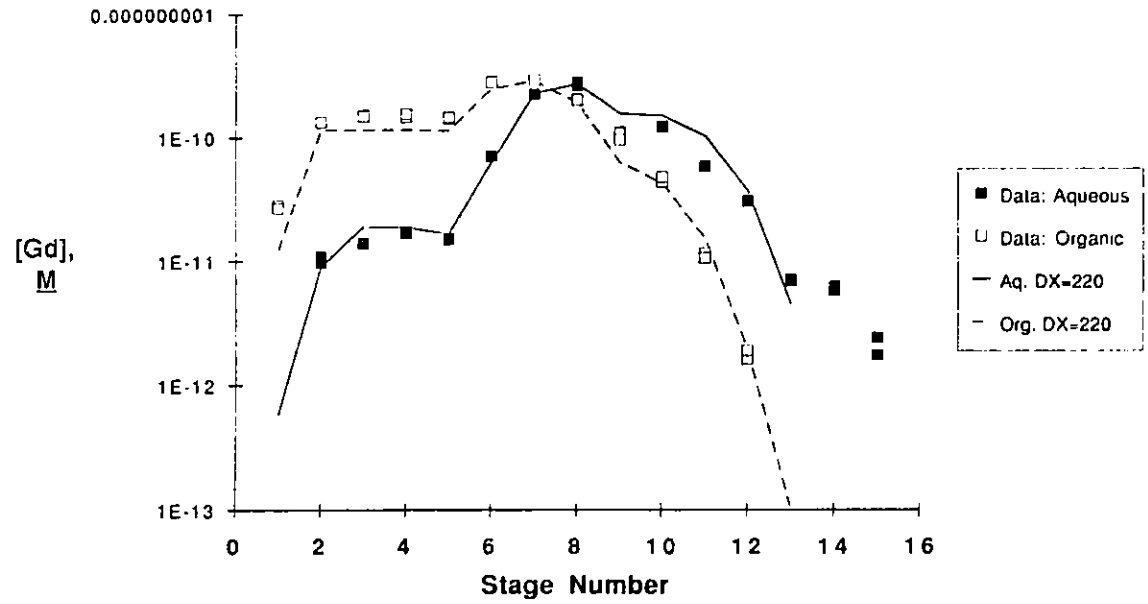

Fig. II-86. Effect of Increased Organic Flow Rate (DX) on Gadolinium Stage Concentrations

4. Contactor Heating Systems

In the first verification test completed using the TRUEX-NPH solvent at room temperature, a second organic phase formed in the extraction and scrub stage samples, where the solvent was heavily loaded. Other studies have shown that a second organic phase forms at 25 °C as the solvent loading increases. Since a second organic phase does not occur at elevated temperatures, Runs 7 and 8 were completed at 50 °C. Accomplishing this required that the feed solutions and the contactor housings be heated.

The housing for each contactor stage was wrapped with an electric mica band heater (Watlow 240 V, 250 W). These band heaters were clamped onto the housings and wired in parallel to an electronic controller. A thermocouple placed on the housing of stage 6 provided a reference temperature for the controller.

Several different systems were evaluated for heating the feed solutions, including hot plates, immersion heaters, recirculating baths, and heat exchangers. The method that we chose to pursue was to install one water bath in the system and recirculate hot water from the bath through the feed tanks (Fig. II-87). For Run 7, coils of PVC tubing were immersed in each carboy. For Run 8, 3/8-in.-O.D. stainless steel tubing replaced the PVC tubing in each tank.

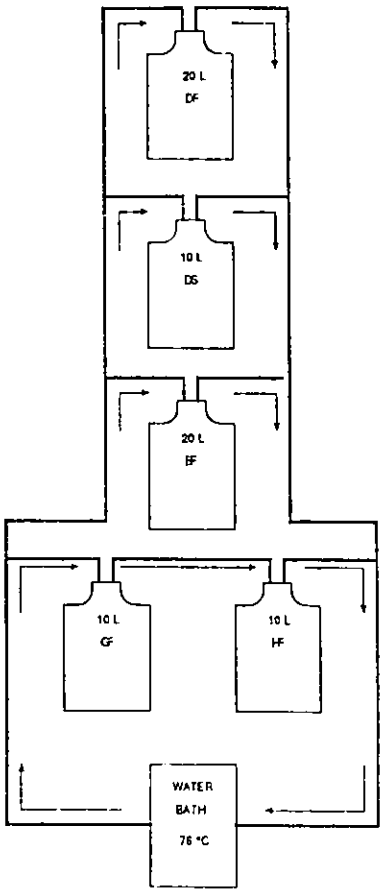

Fig. II-87.

Parallel Heater Configuration used in Verification 8

In Run 7, the tanks were connected in series with the Brinkman water bath. In Run 8 control of the system was improved by piping the tanks in parallel with the Brinkman water bath (Fig. II-87). A hose pinch clamp was attached on the hot water feed line to each carboy, permitting some control of the hot water flow. The solution temperature in each feed tank was regulated by adjusting the water flow. General flow adjustments were made during water tests of the system.

Prior to starting both verification tests at 50°C, the Brinkman water bath was set at a temperature of 76°C to accelerate heating. This was reduced to a set point of 65°C when the feed tank temperatures reached 57°C. Results from the tests with water and from Run 7 show that feed tank temperatures of 57-60°C are good for operating temperatures in the contactors of 50°C. The water bath's 65°C set point maintained the feed tanks at a fairly steady 57-58°C temperature throughout Run 8.

5. Contactor Cleaning/Decontamination

Decontamination of the stainless steel centrifugal contactors proved to be a problem this year. Analysis by ICP of stages downstream from the extraction section showed high levels of Na, Ca, and other metals, and samples collected from the contactor in the glovebox were contaminated with radioactive tracers used in tests several years ago. Based upon discussions with Steve Zoner at Westinghouse Idaho Nuclear Co. (WINCO), two decontamination procedures were recommended:

1. Contact stainless steel with 0.15M tartaric acid in a 1.5M NaOH solution for 4 h at a temperature of 75-80°C. Corrosion rates measured at WINCO were low (0.001 mil after 4 h at boiling). Ethylenediaminetetraacetic acid (EDTA) could be used instead of tartaric acid, but the EDTA did not seem to work as well (based upon WINCO experience). After the contact with the tartaric acid, flush the equipment with 2-4M nitric acid solution to repassivate the stainless steel.

2. A more aggressive cleaning solution is TURCO-4502, an alkaline permanganate solution manufactured by TURCO Products (Division of PUREX Corp., Carson, CA). TURCO Products recommends using an 8-24 wt % solution, though WINCO suggested that a 10-12 wt % solution is adequate. TURCO-4502 contains surfactants and wetting agents to increase its effectiveness. To be most effective, contact should be for several hours at an elevated temperature. After the TURCO-4502 wash, run 0.9M oxalic acid through the equipment to remove the surface contamination (and the discolorization due to manganese dioxide), then repassivate the steel with 2-4M HNO_3. The TURCO-4502 solution has been used successfully to clean up the contactor bank in the glovebox.

K. Centrifugal Contactor Development
(R. A. Leonard, D. B. Chamberlain, L. Chow, K. A. Barnthouse,* and M. O. Wasserman**)

1. Introduction

The Argonne centrifugal contactor is modified as necessary to work with specific solvent extraction processes. To evaluate processes involving high alpha/beta activity levels (in a glovebox) and/or high gamma radiation (in a shielded cell facility), contactors for remote handling have been designed and built. To minimize the feed needed for testing solvent extraction flowsheets, a new 2-cm

*Co-op student from University of Cincinnati.
**Co-op student from University of Illinois at Chicago.

contactor (minicontactor) was designed and built. For each new process system, the solution densities and O/A flow ratios are reviewed, and if necessary, the rotor weirs are modified. To operate the contactor at slightly elevated temperatures (30 to 50°C) with organic and aqueous solutions, a heating system was designed, tested, and used. To operate the contactor at high temperatures (500 to 800°C) with liquid metals and molten salts, a completely new system is being designed and tested.

In support of these development efforts, vibrational measurements are being made using proximity probes and real-time spectrum analyzers. The results are related to rotor design through the BEAM IV program, which models vibrations in rotating systems.

2. Vibration Criteria
(R. A. Leonard, M. O. Wasserman, and R. J. Jaskot)

In this effort, we are developing relatively simple vibration criteria that can be used for the design of rotating equipment, such as the motor/rotor system in the centrifugal contactor. The vibration criteria have been made easy to use by incorporating the model in an Excel worksheet called Beam. We obtained information needed to develop these criteria from experimental testing of motors and motor/rotor systems, using the Zonic 6088 Real Time Spectrum Analyzer (RTSA).

The experimental results and the Beam worksheet were analyzed using the BEAM Analysis IV program[54] on the VAX computer in the CMT Division. Both the BEAM IV program and the Beam worksheet are based on the method of transfer matrices.[54-56] In this method, a beam is divided into short sections, which can be represented easily using transfer matrices. The transfer matrices for the various sections are combined into an overall transfer matrix for the whole beam. With the application of appropriate boundary conditions at the ends of the beam, the overall transfer matrix can be used to calculate the natural frequencies of the beam for both stationary and rotating modes. In the BEAM IV implementation, one is also given the deflection, slope, moment, and shear forces on the beam at various points along its length.

a. Bearing Stiffness

A key parameter in determining the vibration criteria using either the Beam worksheet or the BEAM IV program is the bearing stiffness of the motor. Three motors were evaluated to determine a typical range of stiffnesses for motor bearings. A two-step procedure was used to measure the bearing stiffness of each motor. In the first step, vibration data were obtained for the motor, typically using the RTSA made by Zonic Corp. (Milford, Ohio). In the second step, the data were analyzed using the BEAM IV program. When using the RTSA, the first three natural frequencies were typically measured. In some cases, three resonant frequencies were not found. The highest frequency that the Zonic RTSA can measure is about 40,000 Hz. The motors whose natural frequencies were measured are listed in Table II-49. The natural frequencies obtained are listed in Table II-50. In making these measurements, we used different media for mounting the accelerometer on the motor shaft and different means of isolating the motor from its surroundings. There is some variation in the measurements for a given motor, depending on the setup. Suspending the motor and using quick-drying cement to attach the accelerometer produce displays that are more easily read on the analyzer screen. Thus, these methods are favored.

Three motors were analyzed in detail. To do this detailed analysis on a motor, it was disassembled and measurements were taken of its shaft and armature. The materials which comprise these parts were noted as well. These data were then used to calculate the input for the BEAM IV program. With the basic model for the motor created, the first three natural frequencies were calculated over a wide range of bearing stiffnesses. One value for the bearing stiffness produced natural frequencies close to the measured values for all three frequencies. This value became our calculated bearing stiffness. Analyses were done for 2-, 4-, and 10-cm contactors.

Table II-49. Description of Ten Motors Tested

Motor Reference Number	Mfgr.	Type	Power, hp	Number of Phases	Nominal Speed, rpm	Serial Number	Notes
1	Bodine	710	1/930	1	3600	NH4153[a]	
2						NH4154	
3						NH4185	
4						NJ4006[b]	
5	Bodine	M0052 (NSI-13)	1/60	1	3450	M0052027	c
6	Bodine	254	1/6	1	1700	MG9026	
7	Bodine	284	1/3	1	1700	KF5050	
8	Baldor	VL3501	1/3	1	1725	WO787	
9	Baldor	VL3510T	1	1	1725	F686	
10	Baldor	VM3546T	1	3	1725	F587	

[a]Used at stage 16 of the first 16-stage minicontactor.
[b]Used at stage 15 of the first 16-stage minicontactor.
[c]This is a special-order motor available only in quantities of 25 or more.

Table II-50. Natural Frequencies Measured for Ten Motors

Motor Reference Number	Natural Frequency,[a] Hz			Support Method	Accelerometer Mounting Method[b]	Notes
	1st	2nd	3rd			
1	2,490	-	-	c	d	e
	2,630	-	6,000	c	d	
	2,550	-	7,110	f	d	
	-	2,985	4,260	f	g	
	-	2,865	4,050	c	d	
2	2,430	3,888	-	-	d	h
3	-	-	5,200	-	g	h,i
	-	-	5,260	-	g	h
			5,380			
	2,300	3,472	5,264	-	g	h,j
			5,360			
4	2,280	3,090	4,410	c	d	
	-	2,865	4,200	c	d	
	2,550	-	5,295	c	d	
5	869	2,310	3,195	c	d	
	863	2,295	3,075	c	d	e,k
	863	2,310	3,170	c	d	
	863	2,280	2,985	c	d	e
	855	2,295	3,030	f	d	
	868	2,325	3,300	f	g	
6	1,065	2,490	-	f	d	
	1,095	2,790	16,200	f	g	

(contd)

Table II-50. (contd)

Motor Reference Number	Natural Frequency,[a] Hz 1st	2nd	3rd	Support Method	Accelerometer Mounting Method[b]	Notes
7	-	2,370 2,527	-	c	d	
	653	2,250	9,780	f	d	
	328	2,280	10,800	f	g	l
8	710 940	13,050	36,100	f	d	m
	665 950	-	-	f	g	l
9	483 555	-	-	c	g	l
10	686	1,200 1,600	3,086	c	d	
	330	-	-	c	g	l

[a]Unless otherwise noted, all natural frequencies were measured using the Zonic 6088 RTSA. A dashed line indicates that, although a value was expected based on other tests with the same motor, no peak for the natural frequency was found in the same range. All measurements with the Zonic RTSA were made using the impulse force hammer by PCB, Model 086B01, with aluminum extender and red rubber tip installed. This unit has a sensitivity of 10.2 mV/N and a mass of about 90 g. The accelerometer attached to the motors is PCB model 303A, having a sensitivity of 10.31 mV/(9.81 m/s^2) and a mass of about 2 g. The test setup also includes two power units, set to a gain of x1. Most of the measurements were made by averaging three or five hammer hits; some measurements were made with only one hit.

[b]Accelerometer mounted on flat of motor shaft unless otherwise noted.

[c]Padded surface.

[d]"Petro-wax" or beeswax.

[e]Accelerometer mounted 180° from flat on motor shaft.

[f]Suspended using bungee cords.

[g]Quick-drying cement.

[h]These data are from ANL-89/29, pp. 100-103.

[i]These data were measured using an oscilloscope.

[j]These data were measured by T. M. Mulcahey (ANL Materials and Components Technology Division) using a Hewlett-Packard Multichannel Analyzer.

[k]Data beyond this point for this motor were obtained after the motor was disassembled and re-assembled.

[l]Accelerometer mounted on tip of shaft, perpendicular to the shaft axis.

[m]Accelerometer mounted on coupling nut which is attached to the motor shaft.

(1) 2-cm Contactor

(a) Motor

An existing BEAM IV vibration model for the Bodine 710 motor, the motor currently being used with our 2-cm contactors, was improved by adding the accelerometer mass near the end of the motor shaft. With this change, actual motor-rotor dimensions could be used. Previously, the first three natural frequencies could only be fitted with a single bearing stiffness if slight deviations from actual motor-rotor dimensions were allowed. After these changes had been made, the first three natural frequencies of the Bodine 710 motor, obtained from ANL-89/29 and listed here in Table II-50, gave close to the same value for the bearing stiffness of the motor. Figure II-88 displays the

parameters used for this model for a motor divided into 15 sections. The BEAM IV curves resulting from this model are shown in Fig. II-89 along with three horizontal lines showing where the measured natural frequencies intercept their respective model curves. The average bearing stiffness obtained from this figure, 2.4 x 10^5 lb_f/in. (4.2 x 10^7 N/m), is the same as that for the original model. This analysis indicates that, especially for small motors, the mass of the accelerometer has a significant effect on the vibration characteristics of the motor and should be included in the BEAM IV model.

Section Number		1[a,b]	2[a]	3[c]	4[d,e]	5[f,g]	6[e,f]	7[d]	8[c]
Length	in	9.35E-02	9.35E-02	6.00E-02	1.66E-01	5.12E-01	5.12E-01	1.66E-01	6.00E-02
Modulus of Elasticity	psi	2.90E+07	2.90E+07	2.90E+07	2.90E+07	2.90E+07	2.90E+07	2.90E+07	2.90E+07
Area Moment of Inertia	$in.^4$	1.52E-04	1.52E-04	1.22E-04	4.65E-04	9.45E-02	9.45E-02	4.65E-04	1.22E-04
Linear Density	lb_m/in.	1.22E-02	1.22E-02	1.10E-02	2.14E-02	3.23E-01	3.23E-01	2.14E-02	1.10E-02
Magnitude of Concentrated Weight	lbf	7.00E-03	N/A	N/A	2.18E-02	N/A	2.18E-02	N/A	N/A
Weight Moment of Inertia	lb_f-$in.^2$	1.00E-04	N/A	N/A	2.20E-03	5.59E-02	2.40E-03	N/A	N/A

Section Number		9[a,b]	10[a]	11[h]	12[h,i,j]	13[h,i]	14[h]	15[h]
Length	in	7.60E-02	7.60E-02	2.84E-01	2.50E-01	2.50E-01	1.00E-03	1.00E-03
Modulus of Elasticity	psi	2.90E+07	2.90E+07	2.90E+07	2.90E+07	2.90E+07	2.90E+07	2.90E+07
Area Moment of Inertia	$in.^4$	1.52E-04	1.52E-04	6.00E-05	5.20E-05	5.20E-05	6.00E-05	6.00E-05
Linear Density	lb_m/in.	1.22E-02	1.22E-02	7.70E-03	7.40E-03	7.40E-03	7.70E-03	7.70E-03
Magnitude of Concentrated Weight	lbf	7.00E-03	N/A	N/A	7.90E-03	N/A	N/A	N/A
Weight Moment of Inertia	lb_f-$in.^2$	1.00E-04	N/A	N/A	N/A	N/A	N/A	N/A

Bearings located at sections 1 and 9. Stiffness: 2.4E5 lbf/in
ANLCMT File Name: MINI_69.002A (See M. O. Wasserman, D. G. Wygmans, or R. A. Leonard)

[a] Outer Diameter (O.D.) of the section is 0.236 in.
[b] Includes bearing.
[c] O.D. = 0.312 in.
[d] O.D. = 0.312 in.
[e] Includes copper end plate from armature.
[f] O.D. = 1.178 in.
[g] Includes armature.
[h] O.D. = 0.187 in.
[i] Area moment of inertia calculated using allowance for flat on motor shaft.
[j] Includes accelerometer mass.

Fig. II-88. Parameters Used in Modeling Bodine 710 Motor for 2-cm Contactor

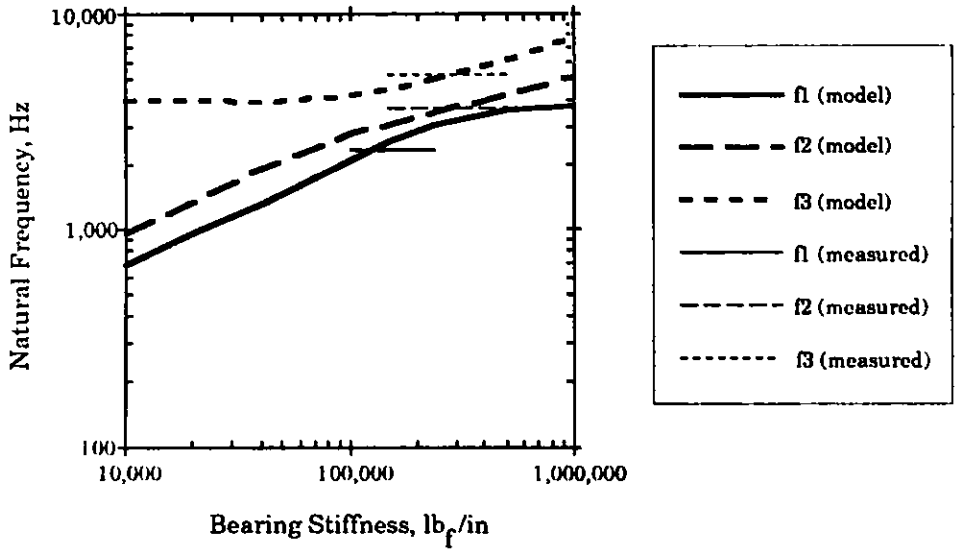

Fig. II-89. Effect of Bearing Stiffness on the First Three Natural Frequencies of the Bodine 710 Motor

The average bearing stiffness for the Bodine 710 motor was then used to obtain the motor deflection curve from BEAM IV for the first three natural frequencies (see Fig. II-90). Note that the second and third natural frequencies correspond to ringing of the motor shaft at the end of the motor. Because of this, these two natural frequencies are reduced sharply when the contactor rotor is added to the motor shaft. The results of adding a contactor rotor to the motor are discussed next.

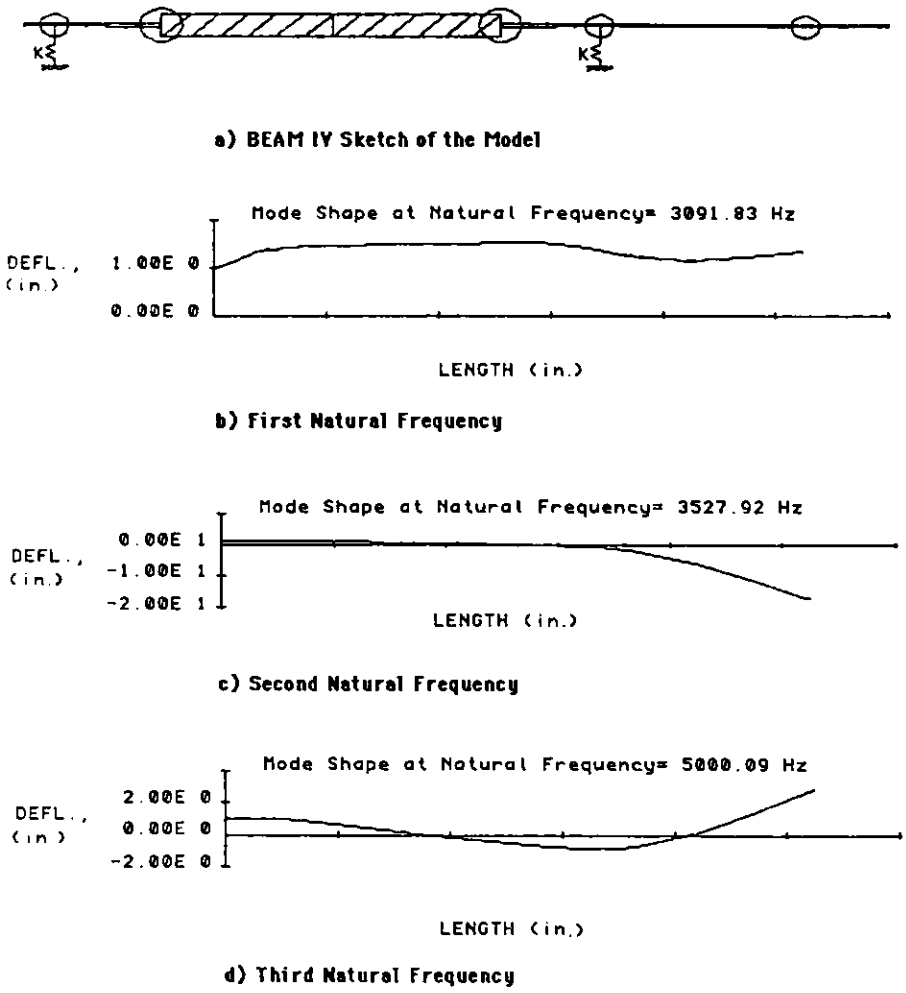

Fig. II-90. Deflection Curves for the Bodine 710 Motor at the First Three Natural Frequencies

(b) Motor and Rotor

The latest version of the BEAM IV model for the Bodine 710 motor was extended to include a 2.5-in. (6.4-cm) long solid rotor attached to the motor shaft through a coupling shaft. The parameters for the 15 sections in this motor/rotor model are listed in Fig. II-91. This system, which was set up and tested in the laboratory, provides a conservative test of actual contactor performance because the solid rotor has more mass than an actual rotor. The actual rotor would be hollow with liquid flowing through it. Measurements for the first three natural frequencies of the motor/solid rotor system using the Zonic RTSA are listed in Table II-51. From the BEAM IV model results shown in Fig. II-92, a bearing stiffness could not be determined using the first two natural frequencies, as the experimental data do not intersect their respective model curves. The third frequency gives a range for the bearing stiffness

between 2.4 x 10^5 and 3.4 x 10^5 lb_f/in. (4.2 x 10^7 and 6.0 x 10^7 N/m). In this case the third natural frequency is the most useful because it increases steadily as bearing stiffness is increased.

Section Number		1[a,b]	2[a]	3[c]	4[d,e]	5[f,g]	6[e,f]	7[d]	8[c]
Length	in	9.35E-02	9.35E-02	6.00E-02	1.66E-01	5.12E-01	5.12E-01	1.66E-01	6.00E-02
Modulus of Elasticity	psi	2.90E+07	2.90E+07	2.90E+07	2.90E+07	2.90E+07	2.90E+07	2.90E+07	2.90E+07
Area Moment of Inertia	in^4	1.52E-04	1.52E-04	1.22E-04	4.85E-04	9.45E-02	9.45E-02	4.85E-04	1.22E-04
Linear Density	lb_m/in	1.22E-02	1.22E-02	1.10E-02	2.14E-02	3.23E-01	3.23E-01	2.14E-02	1.10E-02
Magnitude of Concentrated Weight	lb_f	7.00E-03	N/A	N/A	2.18E-02	N/A	2.18E-02	N/A	N/A
Weight Moment of Inertia	lb_f-$in.^2$	1.00E-04	N/A	N/A	2.20E-03	5.59E-02	2.40E-03	N/A	N/A

Section Number		9[a,b]	10[a]	11[h]	12[h]	13[i,j]	14[j,k]	15[l]
Length	in.	7.60E-02	7.60E-02	2.94E-01	3.13E-02	1.57E+00	3.13E-01	2.50E+00
Modulus of Elasticity	psi	2.90E+07	2.90E+07	2.90E+07	2.90E+07	2.90E+07	2.90E+07	2.90E+07
Area Moment of Inertia	in^4	1.52E-04	1.52E-04	6.00E-05	6.00E-05	1.81E-03	9.35E-04	4.91E-02
Linear Density	lb_m/in	1.22E-02	1.22E-02	7.70E-03	7.40E-03	4.22E-02	3.49E-02	2.20E-01
Magnitude of Concentrated Weight	lb_f	7.00E-03	N/A	N/A	N/A	N/A	N/A	7.90E-03
Weight Moment of Inertia	lb_f-$in.^2$	1.00E-04	N/A	N/A	N/A	1.44E-02	N/A	3.21E-01

Bearings located at sections 1 and 9. Stiffness: 2.4E5 lb/in.
ANLGMT File Name: MINI_89 003 (See M. O. Wasserman, D. G. Wygmans, or R. A. Leonard)

[a] Outer Diameter (O.D.) of this section is 0.236 in.
[b] Includes bearing.
[c] O.D. = 0.2235 in.
[d] O.D. = 0.312 in.
[e] Includes copper end plate from armature.
[f] O.D. = 1.178 in.
[g] Includes armature.
[h] O.D. = 0.1872 in.
[i] O.D. = 0.436 in.
[j] Includes rotor shaft.
[k] Area moment of inertia calculated using allowance for flats on rotor shaft.
[l] O.D. = 1 in. Includes rotor mass and accelerometer mass.

Fig. II-91. Parameters Used in Modeling Bodine 710 Motor with Solid Rotor for 2-cm Contactor

Table II-51. Natural Frequency Measurements for the Bodine 710 Motor with the Solid Rotor

Trial Number[a]	Natural Frequency, Hz 1st	2nd	3rd	Notes
1	175	1582	3540	b
2	180	1575	3270	
3	180	1560	3165	
4	180	1575	3330	
		1710		
5	180	1590	-	
		1740		

[a]Motor 15 of the 16-stage minicontactor, S/N 710NJ4006, was used. This is motor 4 listed in Table II-49.
[b]The third natural frequency was obtained on a separate hammer strike.

Since the BEAM IV model performed rather well when the solid rotor was not attached, it is not clear whether the error is in the experimental measurements or the model. For the second natural frequency (f_2), the BEAM IV model gives 1315 Hz at a bearing stiffness of 2.9 x 10^5 lb_f/in. (5.1 x 10^7 N/m), while the measured value for f_2 is 20% (1.2x) higher. For the first natural frequency (f_1), this difference is much greater. The model gives 72 Hz at a bearing stiffness of 2.9 x 10^5 lb_f/in. (note that f_1 is essentially independent of bearing stiffness), while the measured value for f_1 is 140% (2.4x) higher. In earlier work on the solid rotors with lengths of 2.5 in. (6.4 cm) and longer, we found that f_1 for an operating unit in a secured (clamped down) housing is only slightly greater than

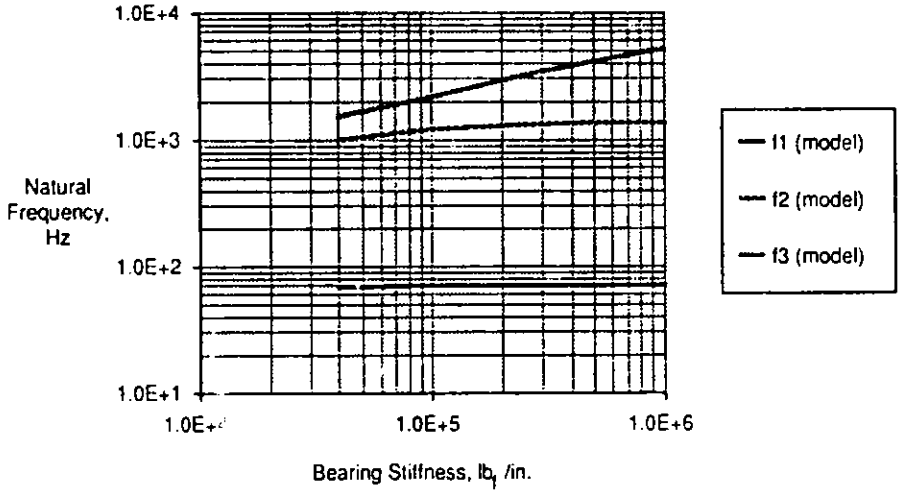

Fig. II-92. Effect of Bearing Stiffness on the First Three Natural Frequencies of the Bodine 710 Motor with a Solid Rotor

60 Hz; for example, f_1 is probably no more than 20% higher than 60 Hz if the solid rotor length is 2.5 in. (6.4-cm) long (ANL-89/29, p. 101). Thus, the earlier data agree quite well with the value of 72 Hz for f_1 from the BEAM IV model.

A bearing stiffness of 2.4×10^5 lb$_f$/in. (4.2×10^7 N/m) for the Bodine 710 motor yielded the BEAM IV deflection curves shown in Fig. II-93 for the motor with the solid rotor that is 2.5-in. (6.4-cm) long. Note that the simple ringing of the shaft and the rotor beyond the motor bearings is now the first natural frequency. This was the second natural frequency for the motor alone (see Fig. II-90). The second natural frequency here, which shows the rotor bending near its neck-down portion while the motor rocks about its midsection, corresponds to the third natural frequency for the motor only. Finally, the third natural frequency for the motor with the rotor, depicting a simple motor displacement between the two bearings, is the first natural frequency for the motor alone. For this last case, the two natural frequencies are very close, 3105 and 3091 Hz, respectively. For contactor design the most important consideration is that the rotor ringing on the motor shaft, f_1 in Fig. II-93, is not much affected by the value for the bearing stiffness (see Fig. II-92). Thus, for most cases, a rough estimate of bearing stiffness should be sufficient for a simple motor/rotor model to calculate the first natural frequency of the contactor rotor.

A final consideration is the effect of the accelerometer position on the natural frequency. Experiments were done in which the accelerometer position along the motor shaft was varied from 1/16 to 5/16 in. (0.2 to 0.8 cm) from the end of the motor shaft. In addition, the BEAM IV model was used to generate curves of natural frequency as a function of bearing stiffness for each accelerometer position. Using these curves with the experimental values for the first three natural frequencies, we determined the bearing stiffness to be $1.6 \times 10^5 \pm 0.6 \times 10^5$ lb$_f$/in. ($2.8 \times 10^7 \pm 1.0 \times 10^7$ N/m). This value is not far from that found above when the position of the accelerometer was not known and was assumed to be at the center of the flat on the motor shaft. Thus, as noted above, accelerometer position affects the frequency response, especially with a small motor such as the Bodine 710 motor. Nevertheless, if the position of the accelerometer is noted, it can be used in an appropriate BEAM IV model to get reasonable predictions for the bearing stiffness of the motor. In these tests, it is most important that the accelerometer be completely and firmly seated on the surface of the object being analyzed.

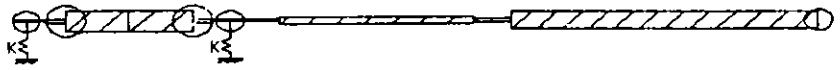

a) BEAM IV Sketch of the Model

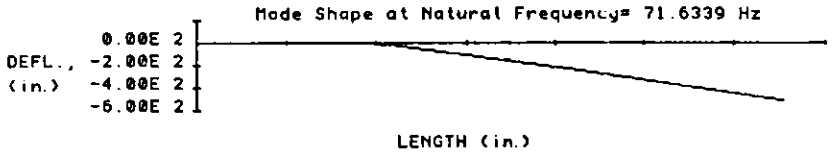

b) First Natural Frequency

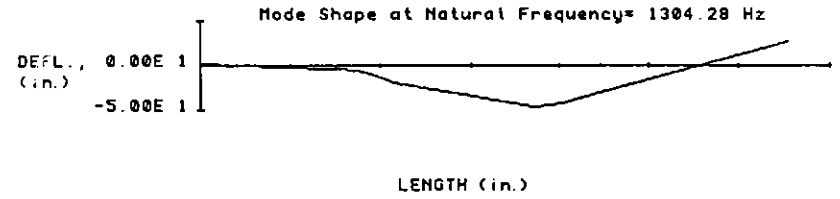

c) Second Natural Frequency

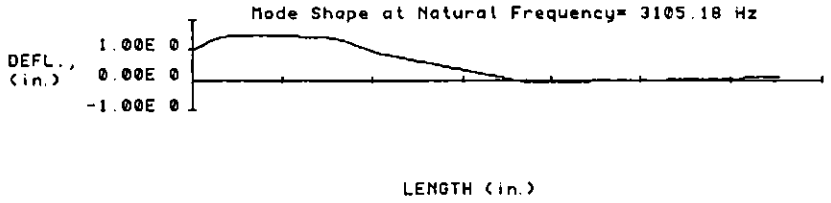

d) Third Natural Frequency

Fig. II-93. Deflection Curves for the Bodine 710 Motor with a Solid Rotor at the First Three Natural Frequencies

(2) 4-cm Contactor

A BEAM IV model was developed for the Bodine M0052027 motor (see Fig. II-94), the face-mounted motor currently being used for the 4-cm contactors. The average bearing stiffness calculated for this motor based on the natural frequencies given in Table II-50 is 9.8×10^4 $lb_f/in.$ (1.7×10^7 N/m). The mass of the accelerometer mounted on the motor shaft for these experiments was included in the BEAM IV model. This mass, although only 3.59 g, significantly affected the analysis of the data.

(3) 10-cm Contactor

A BEAM IV model was developed by Mitchell and Young[57] for the Bodine 254 motor, the face-mounted motor initially used for the 10-cm contactors. Figure II-95 gives the model parameters for 10 sections in this motor. Working with this model and the values of 1000 and 1250 Hz

that they determined for the first natural frequency, Mitchell and Young found the bearing stiffness to be 2.6 x 10^5 and 8.0 x 10^5 lb_f/in. (4.6 x 10^7 and 1.40 x 10^8 N/m). Our values for the first natural frequency of the Bodine 254 motor, 1065 and 1095 Hz based on repeat tests (see Table II-50), are within the range reported earlier by Mitchell and Young and correspond to bearing stiffnesses of 3.1 x 10^5 and 3.8 x 10^5 lb_f/in. (3.7 x 10^7 and 4.6 x 10^7 N/m), respectively. Overall, there is reasonable agreement between these two sets of first natural frequencies. These results give an average value for the bearing stiffness of 4.4 x 10^5 lb_f/in. (7.7x 10^7 N/m), with a standard deviation of 2.5 x 10^5 lb_f/in. (4.4 x 10^7 N/m).

Section Number		1[a,b,i]	2[a,b]	3[a]	4[c]	5[d]	6[e]	7[f]	8[g]	9[h]
Length	in.	1.41E-01	3.10E-02	1.09E-01	3.75E-01	2.12E-01	3.20E-02	1.56E-01	3.20E-02	1.56E-01
Modulus of Elasticity	psi	2.90E+07	2.90E+07	2.90E+07	2.90E+07	2.20E+07	2.90E+07	2.90E+07	2.90E+07	2.90E+07
Area Moment of Inertia	in^4	4.73E-04	4.73E-04	4.77E-04	8.71E-04	9.66E-03	7.49E-03	1.27E-03	3.00E-02	1.33E-03
Linear Density	lb_m/in.	1.97E-02	1.97E-02	2.17E-02	2.93E-02	1.04E-01	8.59E-02	3.47E-02	1.45E-01	3.62E-02
Magnitude of Concentrated Weight	lb_f	6.80E-03	N/A	N/A	N/A	N/A	N/A	N/A	N/A	N/A
Weight Moment of Inertia	lb_f-$in.^2$	2.00E-04	N/A	N/A	N/A	N/A	N/A	N/A	N/A	N/A

Section Number		10[c]	11[j]	12[l]	13[j]	14[k]	15[a,l]	16[a]	17[m]	18[m,n]
Length	in.	9.40E-02	1.41E-01	1.75E+00	1.41E-01	9.22E-01	1.38E-01	1.38E-01	3.12E-01	3.75E-01
Modulus of Elasticity	psi	2.90E+07	2.90E+07	2.90E+07	2.90E+07	2.90E+07	2.90E+07	2.90E+07	2.90E+07	2.90E+07
Area Moment of Inertia	in^4	8.71E-04	2.71E-01	3.38E-01	2.71E-01	9.71E-04	4.77E-04	4.77E-04	4.65E-04	4.17E-04
Linear Density	lb_m/in	2.93E-02	1.41E-01	5.39E-01	1.41E-01	3.09E-02	2.17E-02	2.17E-02	2.14E-02	2.14E-02
Magnitude of Concentrated Weight	lb_f	N/A	N/A	N/A	N/A	N/A	6.80E-03	N/A	N/A	7.90E-03
Weight Moment of Inertia	lb_f-$in.^2$	N/A	N/A	N/A	N/A	N/A	2.00E-04	N/A	N/A	N/A

Section Number		19[m,n]	20[m,n,o]	21[m,n,o]	22[m,n,o]	23[m,n,o]	24[m,n,o]	25[m,n,o]
Length	in	2.03E-01	1.72E-01	1.00E-06	1.00E-06	1.00E-06	1.00E-06	1.00E-06
Modulus of Elasticity	psi	2.90E+07	2.90E+07	2.90E+07	2.90E+07	2.90E+07	2.90E+07	2.90E+07
Area Moment of Inertia	in^4	4.17E-04	4.13E-04	4.13E-04	4.13E-04	4.13E-04	4.13E-04	4.13E-04
Linear Density	lb_m/in.	2.14E-02	1.95E-02	1.95E-02	1.95E-02	1.95E-02	1.95E-02	1.95E-02
Magnitude of Concentrated Weight	lb_f	N/A	N/A	N/A	N/A	N/A	N/A	N/A
Weight Moment of Inertia	lb_f-$in.^2$	N/A	N/A	N/A	N/A	N/A	N/A	N/A

Bearings located at sections 1 and 15. Stiffness: 9.8E+4 lb/in.
ANLCMT File Name: M0052.1 (See M. O. Wasserman, D. G. Wygmans, or R. A. Leonard)

[a] Outer diameter (O.D.) of this section is 0.314 in.
[b] Inner diameter (I.D.) of this section is 0.094 in.
[c] O.D. = 0.365 in.
[d] Includes brass ring from centrifugal switch, O.D. 0.666 in., I.D. = 0.365 in. and steel shaft, O.D. = 0.365 in.
[e] Includes steel plate, O.D. = 0.625 in., I.D. = 0.365 in. and steel shaft, O.D. = 0.365 in.
[f] Includes spring, O.D. = 0.422 in., I.D. = 0.392 in., and steel shaft, O.D. = 0.365 in.
[g] O.D. = 0.891 in., I.D. = 0.365 in.
[h] O.D. = 0.406 in.
[i] Aluminum armature end cap, O.D. = 1.556 in., I.D. = 0.765 in.
[j] Includes nylon sheath over armature, O.D. = 1.62 in., I.D. = 1.556 in., and steel armature, O.D. = 1.556 in.
[k] O.D. = 0.375 in.
[l] Concentrated weight and weight moment of inertia are present due to bearings on motor shaft.
[m] O.D. = 0.312 in.
[n] Area moment of inertia calculation accounts for flat on shaft with respect to a parallel axis.
[o] I.D. = 0.094 in.

Fig. II-94. Parameter Used for Modeling M0052027 Motor for 4-cm Contactor

The results of the bearing stiffness measurements for the three motors discussed here are summarized in Table II-52. These values agree well with the information that bearings of this type are expected to have a stiffness in the range from 10^5 to 10^6 lb_f/in. (2 x 10^7 to 2 x 10^8 N/m).[58]

Starting with the model for the Bodine 254 motor and adding the 10-cm contactor rotor, we made various changes to the dimensions of the rotating system using the model. These changes were continued until the first natural frequency was calculated to be 20% above the operating speed of 1800 rpm (30 Hz). These changes included (1) increasing the coupling shaft diameter, (2) increasing the spacing between the bearings, and (3) increasing the size of the coupling nut. The most significant changes in the first natural frequency occurred when the coupling nut diameter was increased. This analysis indicated that a 1/3-hp Baldor motor could be used without modification for a 10-cm

contactor operating at 1800 rpm if the new coupling nut discussed in Sec.II.K.4.a was also used. If 10-cm contactor operation at 3600 rpm (60 Hz) is required to allow operation at the same throughput with NPH as the diluent, further design modifications will be required. One such design using external bearings is discussed in Sec.II.K.4.a.

Section Number		1[a]	2[b]	3[c]	4[d]	5[e]
Length	in.	6.90E-01	5.60E-01	1.80E-01	3.80E-01	8.60E-01
Modulus of Elasticity	psi	3.00E+07	3.00E+07	3.00E+07	3.00E+07	3.00E+07
Area Moment of Inertia	$in.^4$	9.66E-04	9.71E-04	1.18E-03	6.62E-03	7.49E-03
Linear Density	$lb_m/in.$	3.11E-02	3.11E-02	3.43E-02	8.13E-02	8.35E-02
Magnitude of Concentrated Weight	lb_f	5.61E-02	N/A	N/A	6.95E-02	1.30E-01
Weight Moment of Inertia	$lb_f \cdot in.^2$	6.22E-02	N/A	N/A	8.83E-02	2.14E-01

Section Number		6[f]	7[f]	8[e]	9[g]	10[h]
Length	in.	1.19E+00	1.19E+00	1.04E+00	1.80E-01	1.67E+00
Modulus of Elasticity	psi	3.00E+07	3.00E+07	3.00E+07	3.00E+07	3.00E+07
Area Moment of Inertia	$in.^4$	1.01E+00	1.01E+00	7.49E-03	1.18E-03	9.60E-04
Linear Density	$lb_m/in.$	8.12E-01	8.12E-01	8.65E-02	3.43E-02	3.10E-02
Magnitude of Concentrated Weight	lb_f	N/A	1.30E-01	N/A	N/A	N/A
Weight Moment of Inertia	$lb_f \cdot in.^2$	3.44E-01	2.14E-01	N/A	N/A	N/A

Bearings located at sections 2 and 9. Stiffness: 4.4E+5 $lb_f/in.$

[a] Outer diameter (O.D.) of this section is 0.3746 in.
[b] O.D. = 0.375 in.
[c] O.D. = 0.3939 in.
[d] O.D. = 0.606 in.
[e] O.D. = 0.625 in.
[f] O.D. = 2.133 in., I.D. = 0.625 in.
[g] O.D. = 0.394 in.
[h] O.D. = 0.374 in.

Fig. II-95. Parameters used in Modeling Bodine 254 Motor for 10-cm Contactor

Table II-52. Bearing Stiffness for Several Motors.

Motor Reference Number[a]	Bearing Stiffness,[b] $lb_f/in.$	Notes
2,3	$2.4 \times 10^5 \pm 1.0 \times 10^5$	c
5	$9.8 \times 10^4 \pm 1.6 \times 10^4$	
6	$4.4 \times 10^5 \pm 2.5 \times 10^5$	d

[a] See Table II-49.
[b] Based on natural frequency measurements analyzed using the BEAM IV program for vibrational analysis.
[c] This bearing stiffness was calculated using measurements reported earlier (ANL-89/29, pp. 100-103).
[d] This average bearing stiffness includes measurements made by L. D. Mitchell and K. J. Young.[57]

b. Simple Motor/Rotor Model

Using the bearing stiffnesses determined above for various off-the-shelf motors that could be used in a centrifugal contactor, we developed a simple model for calculating the first natural frequency of the motor/rotor system in a centrifugal contactor. The model employs the same transfer matrix method that is used in the BEAM IV program. However, as it is implemented in an Excel worksheet, this method is made much simpler to use.

Details of the Beam worksheet are as follows. The motor and attached contactor rotor are broken up into 11 massless beam sections, as shown in Fig. II-96. To each section, we assigned an area moment of inertia and a weight moment of inertia. At the right end of each massless section, we assigned a concentrated mass and, when appropriate, a bearing stiffness. Because the weight moment of inertia is included, we are able to model rotating beams with both forward whirl and backward whirl. This Beam worksheet was developed and checked with the BEAM IV program.

An Excel macro called "Beam_driver" facilitates the calculation of the natural frequency. The macro searches for a natural frequency in a user-specified interval on the Beam worksheet. This calculation takes 55 s on a Mac II computer. The Beam worksheet is set up so that it can be used easily. This is done by entering the appropriate motor and rotor dimensions at the top of the worksheet. The concentrated weights, the moments of inertia, and the bearing stiffness are then calculated by the worksheet. A user's manual for the Beam worksheet is being prepared.

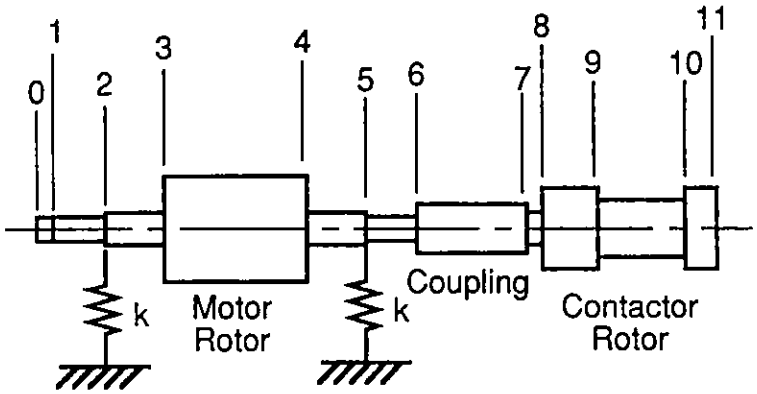

Fig. II-96. Sections for the Motor/Rotor Model in the Beam Worksheet

3. Tests with 4-cm Contactors
(R. A. Leonard, M. O. Wasserman, and K. A. Barnthouse)

A 4-cm contactor was designed, built, and tested for Y-12 plant at Oak Ridge, TN, so that various flowsheets can be evaluated for the recovery of uranium scrap. The design, which builds on earlier 4-cm contactor designs, allows hands-on use of the contactor in the Y-12 pilot plant and permits many solvents to be evaluated over a wide range of O/A flow ratios. The existing rotors for this remote-handled 4-cm contactor were tested extensively. The results of these tests were used to finalize the design for the 4-cm contactors for Y-12.

a. Evaluation of Remote-Handled Units

The sixteen 4-cm rotors for the 8-stage remote-handled contactor consist of (1) eight rotors which have a more-dense-phase weir diameter of 0.750 in. (19.05 mm) and left-handed threads for the motor coupling (the "750" rotors) and (2) eight rotors with a more-dense-phase weir diameter of 0.693 in. (17.60 mm) and right-handed threads (the "693" rotors). Before the initial checkout of the rotors, numbers from 1 to 8 and the upper weir diameter were scribed on each set of rotors. The eight wells of the contactor housing which accommodate these rotors were also numbered from 1 to 8. For the initial checkout, the speed of each motor was measured and found to be 3570 ± 12 rpm. The rotor volume measurements, done outside the contactor as described in the previous report in this series, gave average volumes of 70.7 ± 0.5 mL for the 693-type rotors and 68.3 ± 0.4 mL for the 750-type rotors. Because the 750-type rotors have the larger diameter for the more-dense-phase weir, the smaller volume of liquid held by these rotors is expected.

Because of the new one-piece design for the coupling nut that connects the rotor to the motor (Sec.II.K.4.a), the rotors with left-handed threads should no longer be self-tightening. Instead, they should now require a lock washer. Conversely, the rotors with right-handed threads should be self-tightening. During these tests, we observed that this was the case.

Single-phase flow tests were performed on each of the 16 rotors. The results, given in Figs. II-97 and II-98, are shown with the curve calculated using the WEIR model (described in previous report), which models one-phase flow through contactor rotors. For both sets of rotors, there is a significant discrepancy between the measured and calculated results, with slightly better results for the "693" rotors. Note that the results indicate nearly identical dimensions from rotor to rotor. This consistency can be seen in the small value for the standard deviation of the apparent weir diameter for each rotor type (Table II-53). These weir diameters were calculated using the one-phase flow results and the WEIR worksheet. The calculated weir diameters show that, for the type-693 rotors, the average apparent diameter is 0.665 ± 0.003 in. (the corresponding radius is 8.44 ± 0.04 mm). For the type-750 rotors, the average apparent diameter is 0.706 ± 0.010 in. (the corresponding radius is 8.96 ± 0.12 mm).

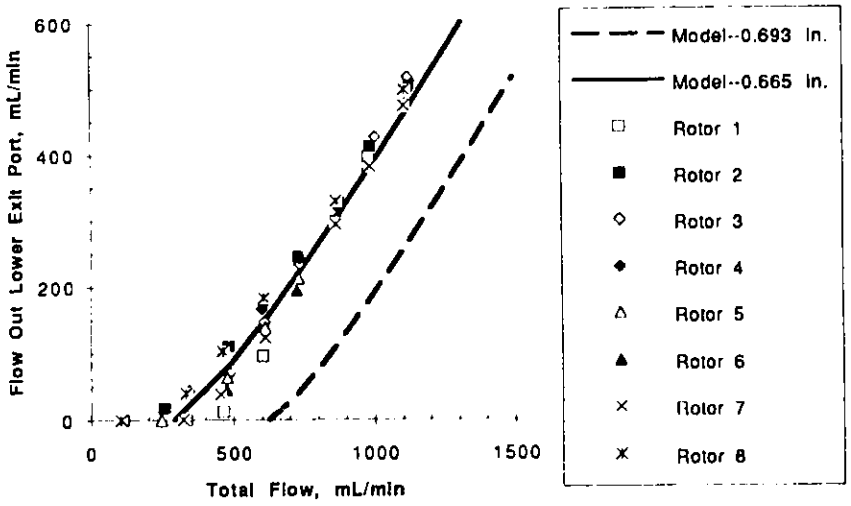

Fig. II-97. Single-Phase Flow Results for 693-Type Rotors. Also shown are the WEIR model curves for the actual (dashed line) and apparent (solid line) upper weir diameters.

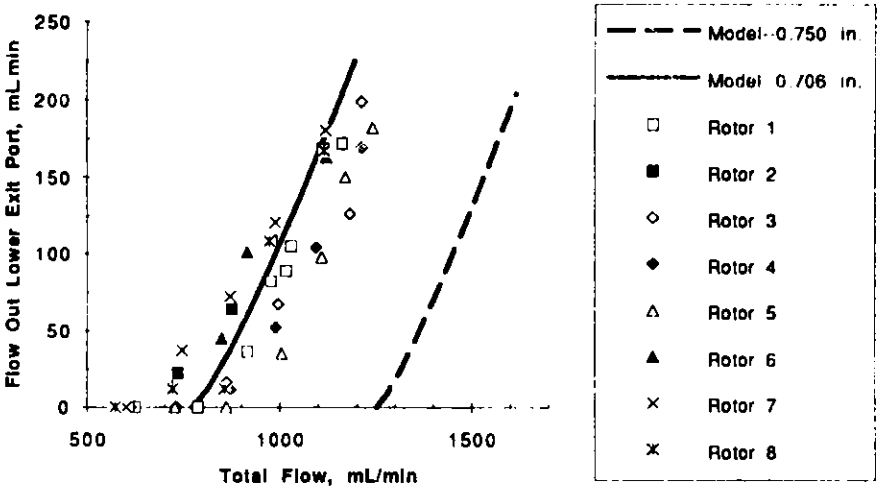

Fig. II-98. Single-Phase Flow Results for 750-Type Rotors. Also shown are the WEIR model curves for the actual (dashed line) and apparent (solid line) upper weir diameters.

Table II-53. Apparent Upper Weir Radii Calculated from Single-Phase Flow Tests with 693- and 750-Type Rotors

Rotor Type	Rotor No.	Apparent Upper (More-Dense-Phase) Weir Size	
		Diameter, in.	Radius, mm
693	1	0.670	8.51
	2	0.661	8.39
	3	0.664	8.43
	4	0.663	8.42
	5	0.665	8.45
	6	0.667	8.47
	7	0.667	8.47
	8	0.661	8.39
	Average:	0.665	8.44
Standard Deviation:		0.003	0.04
750	1	0.710	9.02
	2	0.685	8.70
	3	0.711	9.03
	4	0.715	9.08
	5	0.717	9.11
	6	0.701	8.90
	7	0.701	8.90
	8	0.705	8.95
	Average:	0.706	8.96
Standard Deviation:		0.010	0.12

Three of the rotors, nos. 2 and 7 from the "750" group and no. 8 from the "693" group, vibrated more than the others. The increased vibration could be seen and felt in the contactor housing. It could also be heard. The vibrations increased as throughput was increased. Tightening the nuts holding the rotor down helped somewhat. For rotor 2, switching its motor for another motor produced greatly reduced vibration. Thus, the motors are suspected as the vibration source in each of these cases of higher-than-normal vibration.

Following the completion of the single-phase tests, we did some two-phase tests. These more elaborate tests (1) allowed a better assessment of the contactor capabilities under actual operating conditions and (2) permitted comparison of the apparent weir radii calculated using single- and two-phase flow results. A typical rotor from each group, no. 5 from the "693" group and no. 1 from the "750" group, was selected for the two-phase flow tests. For the tests, the more-dense phase was 0.01M HNO_3 with a density of 997 g/L. The less-dense phase was either TRUEX-NPH with a density of 857 g/L or PUREX-NPH with a density of 819 g/L. Using two different solutions for the less-dense phase allowed a more-thorough analysis of the rotors since two sets of values were obtained for the apparent diameter of the more-dense-phase weir.

Before performing the flow tests, we completed batch tests to determine the dispersion number at O/A ratios of 0.2, 1.0, and 5.0. The resulting dispersion numbers are included in Tables II-54 and II-55. The dispersion numbers listed for TRUEX-NPH and 0.01M HNO_3 were obtained from work done in the previous report period (ANL-90/16, Sec. II.J). The two-phase flow tests were also performed at O/A ratios of 0.2, 1.0, and 5.0. The results, also listed in Tables II-54 and II-55, show how, as the total flow rate is increased for a given O/A flow ratio and a given solution pair, the amount of other-phase carryover increases until it is greater than 1%. The point at which this occurs is the maximum throughput.

Table II-54. Results of Two-Phase Tests with 4-cm Rotor No. 5 (693 Type)

Organic Solution[a]	O/A Ratio	Batch Dispersion Number	Total Flow Rate, mL/min	Other-Phase Carryover, %		Effluent Appearance	
				O in A	A in O	Aqueous	Organic
PUREX-NPH	0.2	5.8×10^{-4}	419	<0.04	0.18	cloudy	cloudy
			440	<0.04	1.2	cloudy	cloudy
			510	0.07	12.5	cloudy	very cloudy
	1.0	11.7×10^{-4}	732	<0.04	0.25	cloudy	cloudy
			771	0.04	1.7	cloudy	very cloudy
	5.0	12.2×10^{-4}	1660	<0.04	0.34	cloudy	cloudy
			1716	<0.04	1.2	slightly cloudy	very cloudy
TRUEX-NPH	0.2	$<1.2 \times 10^{-4}$	457	<0.04	0.21	cloudy	very cloudy
			490	<0.03	3.8	cloudy	very cloudy
	1.0	6.7×10^{-4}	600	<0.09	0.3	slightly cloudy	very cloudy
			664	<0.08	1.2	slightly cloudy	very cloudy
			808	<0.1	13.5	slightly cloudy	very cloudy
	5.0	6.5×10^{-4}	1414	0.03	0.66	cloudy	very cloudy
			1481	0.06	1.03	cloudy	very cloudy

[a]Aqueous solution is 0.01M HNO_3 in all cases.

Table II-55. Results of Two-Phase Tests with 4-cm Rotor No. 1 (750 Type)

Organic Solution[a]	O/A Ratio	Total Flow Rate, mL/min	Other-Phase Carryover, %		Effluent Appearance	
			O in A	A in O	Aqueous	Organic
PUREX-NPH	0.2	807	0.06	<0.05	cloudy	slightly cloudy
		843	0.40	2.3	cloudy	cloudy
	1.0	1341	0.06	0.28	cloudy	very cloudy
		1408	0.12	2.4	cloudy	very cloudy
	5.0	1967	0.77	0.37	cloudy	very cloudy
		2194	1.9	0.44	cloudy	very cloudy
		2314	2.2	1.5	cloudy	very cloudy
TRUEX-NPH	0.2	1063	0.10	0.20	cloudy	very cloudy
		1119	0.06	1.36	cloudy	very cloudy
		1261	0.06	18.3	cloudy	very cloudy
	1.0	484	0.8	<0.04	cloudy	slightly cloudy
		543	1.1	<0.04	cloudy	slightly cloudy
	5.0	33	6.2	<0.07	cloudy	slightly cloudy
		289	18.7	0.23	cloudy	cloudy
		448	16.8	0.33	slightly cloudy	cloudy
		700	27.8	0.15	cloudy	cloudy

[a]Aqueous solution is 0.01M HNO_3 in all cases.

For the 750-type rotor at an O/A flow ratio of 5.0 using TRUEX-NPH as the less-dense phase, the other-phase carryover (O in A) is still 6.2% at the low flow rate of 33 mL/min. The ROTOR worksheet models two-phase flow through the contactor rotor (see ANL-90/16, Sec. II.J). Using the ROTOR model with this result, one can show that the apparent radius for the more-dense-phase weir must be greater than 9.53 mm (Table II-56). The maximum weir radius could not be determined because no experimental points fall within the good operating envelope. For the other test conditions, the data all cross over from good operation (≤1% other-phase carryover) to unsatisfactory operation (>1% other-phase carryover). Using this information along with the type of failure (that is, "A in O" or "O in A") and the dispersion number, the ROTOR model was used to determine the apparent radius for the more-dense-phase weir. In one case, only an upper bound could be determined.

The results in Table II-56 show that the apparent radius for the more-dense-phase weir calculated from the two-phase tests is not far from the actual radius, about 0.1 to 0.2 mm less. The values for the 693-type rotor are especially close, about 0.03 mm less. Since the standard deviations are fairly large, on the order of 0.2 to 0.3 mm, these differences may not be significant. However, for the single-phase flow tests, the radius for the more-dense-phase weir is 0.4 mm less than the actual radius. Since the standard deviations for these tests are smaller, on the order of 0.1 mm, these differences between the actual and apparent radii are significant.

Because of the results of the single-phase flow tests and the benefits seen earlier (ANL-90/16, Sec. II.J) from electrical discharge machining (EDM) of the 2-cm contactors, we decided to increase the radius of both more-dense-phase (upper) weirs by electrical discharge machining. The EDM process was used to enlarge the upper weir diameters of both rotors by 0.016 in., that is, the radii were enlarged by 0.2 mm. Plug gauge measurements indicated that the actual weir diameters are 0.714 in. (18.14 mm, now 714-type, previously 693-type) and 0.766 in. (19.46 mm, now 766-type, previously 750-type). These diameters correspond to weir radii of 9.07 and 9.73 mm, respectively. The results of single-phase flow tests performed on these rotors are given in Table II-57. They show that the increase in the apparent radius for the more-dense-phase weirs of these rotors is about equal to the amount of machining

done. These results show how EDM can be used to fine-tune contactor performance. Based on these results, the actual diameter for the more-dense-phase weirs of the Y-12 contactors was specified to be 0.709 in. (18.01 mm) so that one would get contactor performance characteristic of a 0.693-in. (17.60-mm) weir diameter in the WEIR and ROTOR models. Actual tests of the Y-12 contactor are discussed next.

Table II-56. Apparent Radius for the More-Dense-Phase Weir of Two 4-cm Rotors

		"693" Rotor No. 5[b]			"750" Rotor No. 1[b]		
Organic Solution[a]	O/A Ratio	Dispersion Number for ROTOR Model	Apparent Radius, mm	Apparent Diameter, in.	Dispersion Number for ROTOR Model	Apparent Radius, mm	Apparent Diameter, in.
PUREX-NPH	0.2	5.8×10^{-4}	8.56-8.60	0.674-0.677	7.0×10^{-4}	9.00-9.04	0.709-0.712
	1.0	11.7×10^{-4}	8.63-8.67	0.680-0.683	11.7×10^{-4}	9.28-9.33	0.731-0.735
	5.0	14.2×10^{-4}	9.24-9.26	0.728-0.729	17.5×10^{-4}	9.23-9.29	0.727-0.731
TRUEX-NPH	0.2	8.0×10^{-4}	8.51-8.55	0.670-0.673	9.3×10^{-4}	9.10-9.16	0.717-0.721
	1.0	8.0×10^{-4}	8.60-8.66	0.677-0.682	8.0×10^{-4}	9.41-9.45	0.741-0.744
	5.0	12.0×10^{-4}	<8.96	<0.706	8.0×10^{-4}	>9.53	>0.750
Average for Two-Phase Tests:			8.77	0.691		9.28	0.731
Standard Deviation:			0.26	0.020		0.17	0.013
Value from Single-Phase Tests[c]:			8.45	0.665		9.02	0.710
Actual Value:			8.80	0.693		9.53	0.750

[a]Aqueous solution is 0.01 M HNO_3 in all cases.
[b]Both the upper and lower limits, as calculated from ROTOR Model, are shown. In some cases, only one limit could be determined.
[c]From Table II-53.

Table II-57. Effect of EDM on the Apparent Radius of the More-Dense-Phase Weir

	Rotor No. 5[a]				Rotor No. 1[b]			
	Radius, mm		Diameter, in.		Radius, mm		Diameter, in.	
Measurement Relative to EDM	Actual	Apparent	Actual	Apparent	Actual	Apparent	Actual	Apparent
Before	8.80	8.45	0.693	0.665	9.53	9.02	0.750	0.710
After	9.07	8.67	0.714	0.683	9.73	9.12	0.766	0.718

[a]This 714-type rotor was a 693-type rotor before EDM.
[b]This 766-type rotor was a 750-type rotor before EDM.

b. Tests of 4-cm Contactor for Y-12

After the 16-stage 4-cm contactor for Y-12 was assembled, it was put through a series of tests before shipping to Y-12. These tests included measuring the rotor volumes and performing single- and two-phase flow tests.

Rotor volumes were measured outside the contactor housing using a beaker of water to fill the rotor. This method was discussed in more detail in ANL-90/16, Sec. II.J. Three or more trials were done for each of the 17 rotors (one is a spare rotor). The overall average volume for the 17 rotors was 70.3 ± 0.2 mL. The average volumes for the individual rotors were all within ±0.4 mL of the overall average.

As before, the single-phase flow test involved running one contactor stage while pumping water into the stage. The single-phase flow results are plotted in Figs. II-99 and II-100 along with the curve determined from the WEIR model. The WEIR model curve is based on the actual radius of the more-dense-phase (upper) weir, 9.00 mm (diameter = 0.709 in.). The WEIR model was then used to determine the radius that gives the best fit for each rotor. These apparent weir radii are listed in Table II-58. Their average value, 8.65 mm ± 0.04 mm, is 0.35 mm below the actual radius value of 9.00 mm. In the tests of the 4-cm remote-handled contactors discussed above, a similar difference was observed between the measured and apparent radii. The standard deviation for the Y-12 rotors is much lower than the standard deviation for the other 4-cm rotors. This difference is attributed to the use of a more skilled welder in fabricating the rotors. The use of EDM to machine the final diameter for the upper weir may also be a factor.

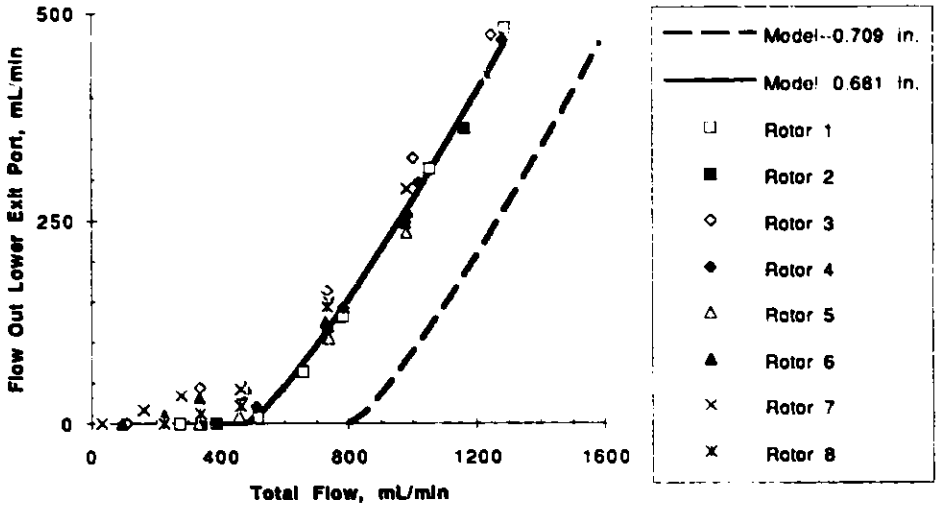

Fig. II-99. Single-Phase Flow Results for Y-12 Rotors 1-8. Also shown are the WEIR model curves for the actual (dashed line) and apparent (solid line) upper weir diameters.

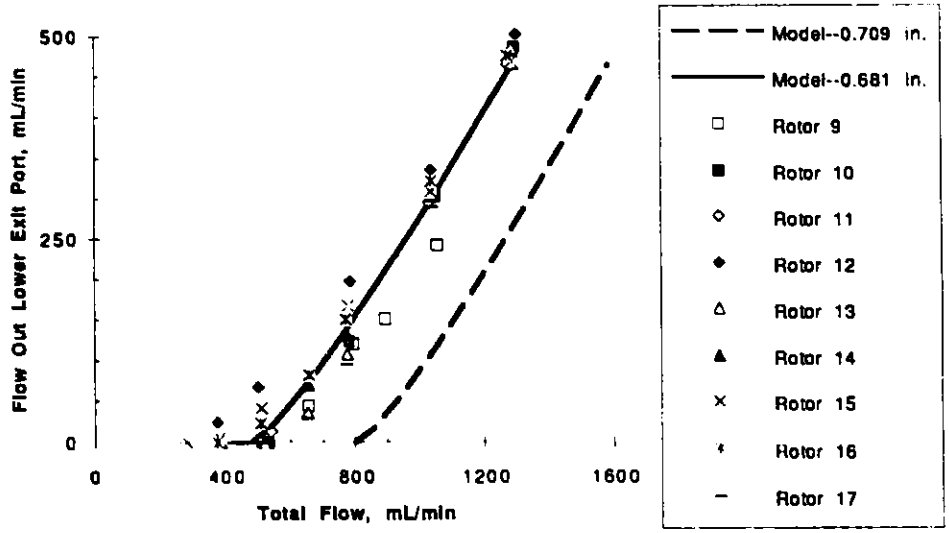

Fig. II-100. Single-Phase Flow Results for Y-12 Rotors 9-17. Also shown are the WEIR model curves for the actual (dashed line) and apparent (solid line) upper weir diameters.

Table II-58. Apparent Upper Weir Radii Calculated from Single-Phase Flow Tests with the Y-12 Rotors

	Apparent Upper (More-Dense-Phase) Weir Size	
Rotor No.	Diameter, in.	Radius, mm
1	0.682	8.66
2	0.682	8.66
3	0.675	8.57
4	0.681	8.65
5	0.683	8.67
6	0.680	8.64
7	0.678	8.61
8	0.680	8.64
9	0.688	8.74
10	0.682	8.66
11	0.682	8.66
12	0.676	8.59
13	0.682	8.66
14	0.682	8.66
15	0.679	8.62
16	0.679	8.62
17	0.683	8.67
Average:	0.681	8.65
Standard Deviation:	0.003	0.04

As the final test of rotor performance, a typical rotor, rotor 1, was tested under two-phase flow conditions. These tests were performed at O/A ratios of 0.33, 1.0, and 3 using TRUEX-NPH and 0.01M HNO_3. The results, listed in Table II-59, show that the contactor can be operated at throughputs up to 600 mL/min at any O/A flow ratio between 0.33 and 3.0. Unsatisfactory performance, defined as >1% other-phase carryover in either effluent, always occurs with aqueous phase in the organic effluent.

In order to model the test results, the batch dispersion number is needed. It was measured using the same solutions (TRUEX-NPH and 0.01 M HNO_3) at O/A ratios of 1/3, 1, and 3. The results, listed in Table II-59, show that the average dispersion number is 9.9×10^{-4} with a standard deviation of $\pm 1.4 \times 10^{-4}$. This value is consistent with past results. The two-phase flow results are indicated by vertical lines in Figs. II-101 to II-103, along with the design curves from the ROTOR model and horizontal lines indicating the design (actual) radius. From these figures, three values for the apparent radius of the more-dense-phase weir were determined and are listed in Table II-60. The average value for the apparent radius of the upper weir is 8.60 ± 0.11 mm (0.677 ± 0.008 in. for the diameter). This apparent radius, determined from the two-phase flow tests, is only 0.05 mm lower than that determined from single-phase flow tests (see Table II-58). Based on the standard deviations for these two values, this difference is not significant. As with the remote-handled 4-cm rotors, the apparent radius of the upper weir (8.60 to 8.66 mm) for the Y-12 contactors is about 0.4 mm less than the actual radius (9.00 mm).

Since the difference between the apparent and actual radius is as anticipated, the contactors should work as well (that is, less than 1% other-phase carryover) at O/A flow ratios from 0.1 to 10, for solvent densities ranging from 819 to 870 g/L, and for flow rates up to 400 mL/min. These operating specifications assume that NPH is the diluent for the solvent. With solvent densities above 870 g/L, the contactors will be operable, but at total flow rates below 400 mL/min. Above a solvent density of 890 g/L, the contactors will become completely inoperable (that is, there will be >1% other-phase carryover in at least one effluent stream). With solvent densities below 819 g/L, the contactors will

again be operable, but at total flow rates below 400 mL/min. At 755 g/L, the density of pure NPH, the contactors will give good operation up to total throughputs of 250 mL/min. In all cases, to achieve these throughputs, there must be some nitric acid, e.g., 0.01M HNO_3 in the aqueous phase.

With the testing completed, the contactors were shipped to Y-12 along with six spare motors, one spare rotor, and a set of contactor drawings entitled "4-cm Contactor (Bench Top)" with ANL drawing number "CMT-E1177". The 16-stage 4-cm contactor was set up at Y-12 and is now fully operational.

Table II-59. Results of Two-Phase Tests with 4-cm Rotor No. 1 of the Y-12 Type

O/A[a] Ratio	Batch Dispersion Number	Total Flow Rate, mL/min	Other-Phase Carryover, %		Effluent Appearance	
			O in A	A in O	Aqueous	Organic
0.33	9.0×10^{-4}	640	<0.04	0.6	cloudy	cloudy
		742	<0.2	1.0	cloudy	very cloudy
1.0	9.1×10^{-4}	711	<0.3	0.6	cloudy	cloudy
		766	<0.3	1.2	slightly cloudy	very cloudy
3.0	11.6×10^{-4}	582	<0.2	0.7	cloudy	cloudy
		791	<0.2	1.1	cloudy	very cloudy

[a]The aqueous phase (A) is 0.01M HNO_3 with a density of 997 g/L at 25°C.
The organic phase (O) is TRUEX-NPH with a density of 857 g/L at 25°C.

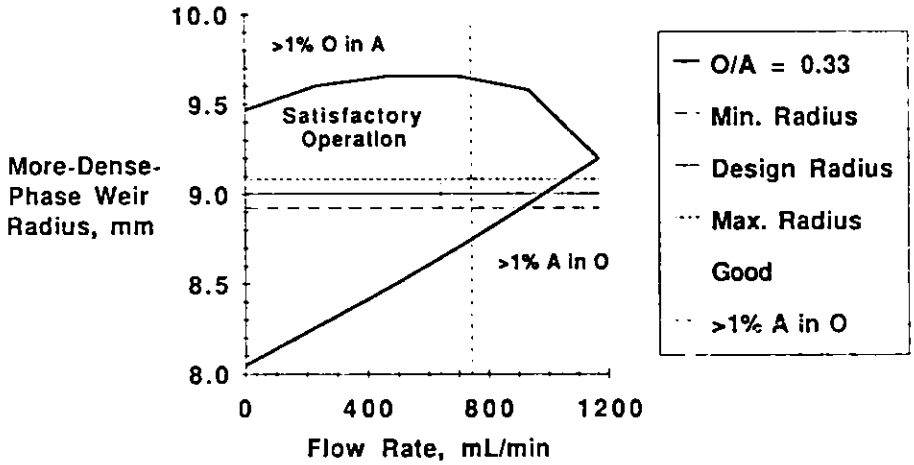

Fig. II-101. Results of the Two-Phase Flow Test for the Y-12 Rotor No. 1 Using TRUEX-NPH and 0.01M HNO_3 at an O/A Ratio of 0.33

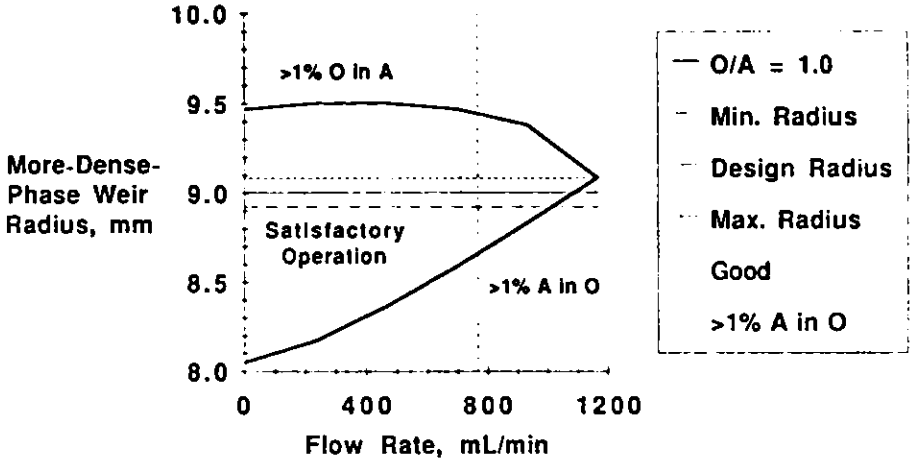

Fig. II-102. Results of the Two-Phase Flow Test for the Y-12 Rotor No. 1 Using TRUEX-NPH and 0.01M HNO_3 at an O/A Ratio of 1.0

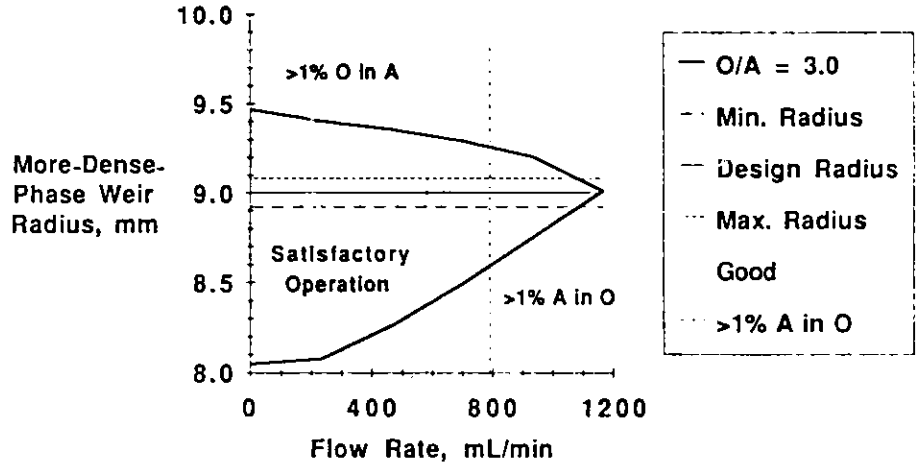

Fig. II-103. Results of the Two-Phase Flow Test for the Y-12 Rotor No. 1 Using TRUEX-NPH and 0.01M HNO_3 at an O/A Ratio of 3.0

Table II-60. Apparent Radius of the More-Dense-Phase Weir for Rotor No. 1 in Y-12 Contactor

O/A Ratio	Apparent Radius,[a] mm	Apparent Diameter,[a] in.
0.33	8.69	0.684
1.0	8.63	0.680
3.0	8.48	0.668
Average:	8.60	0.677
Standard Deviation:	0.11	0.008
Actual Value:	9.00	0.709

[a]Calculated using the ROTOR model with the two-phase flow results given in Table II-59.

4. Consultation with Westinghouse Hanford
(R. A. Leonard and M. O. Wasserman)

We are consulting with Westinghouse Hanford on the final design of the 10-cm centrifugal contactor for TRUEX processing of Plutonium Finishing Plant (PFP) wastes to remove the transuranic elements. The current 10-cm contactor design was reviewed in light of ongoing Hanford tests and plant needs. Special attention was given to (1) modifying the contactor so that a 1/6- to 1/3-hp motor can replace the present 1-hp motor and (2) specifying a new motor/rotor coupling which is self-tightening yet has good coupling stiffness. A second consulting task was working with Westinghouse Hanford on selecting an appropriate Argonne centrifugal contactor to use in a remote pilot plant at Westinghouse Hanford.

a. Design of 10-cm Contactor

The key recommendation on modifications to the 10-cm contactor is to have the clamp nut and the coupling sleeve replaced by a single part, the coupling nut (see Fig. II-104). When this new coupling nut is used with the existing rotor, the coupling will be self-tightening. In addition, because of the greater stiffness of the coupling nut (see the BEAM IV analysis discussed in Sec. II.K.2), it may be possible to use smaller motors that draw less power, that is, motors with a rating of 248 W (1/3 hp) in place of the existing 745 W (1 hp) motors.

Since this work on the final design of the 10-cm contactor, it has been found that, for environmental reasons, NPH will probably be used as the diluent for the TRUEX solvent in place of TCE. This change in diluent lowers the dispersion number by a factor of two, and thereby cuts the throughput of the 10-cm contactor in half. Options to adapt the contactor for use with the TRUEX-NPH solvent were reviewed. The recommended option, to increase the motor speed from 1800 to 3600 rpm, would require a change in the radius of the upper (more-dense-phase) weir of the 10-cm rotor while other contactor dimensions would remain the same. A much stiffer motor and motor/rotor coupling (the coupling nut) would also be required.

Based on the above effort, the design for the motor/rotor coupling was refined by Dave Clem, a mechanical engineer at Westinghouse Hanford. It adds a heavy spindle (as the coupling nut) held in place by two bearings below the motor. The vibrations in the motor are isolated from those in the spindle and the contactor rotor by the use of a torsionally flexible coupling. The two halves of the coupling slip together so that it is easy to disengage the motor from the spindle when changing the motor.

Because the rotor is now supported by the spindle rather than the motor, the motor need be only as large as required to provide power to the rotor, that is, only 124 W (1/6 hp). Also, because greater stiffness can be built into the spindle design, it should be possible to operate the motor/rotor system at 3600 rpm. With the high rotational speed of this new design, we should be able to use the existing contactor to handle 10 L/min of total throughput even though the solvent is TRUEX-NPH. The design, construction, and testing of this modification to the 10-cm contactor are planned for FY 1990 as a joint venture between ANL and Westinghouse Hanford.

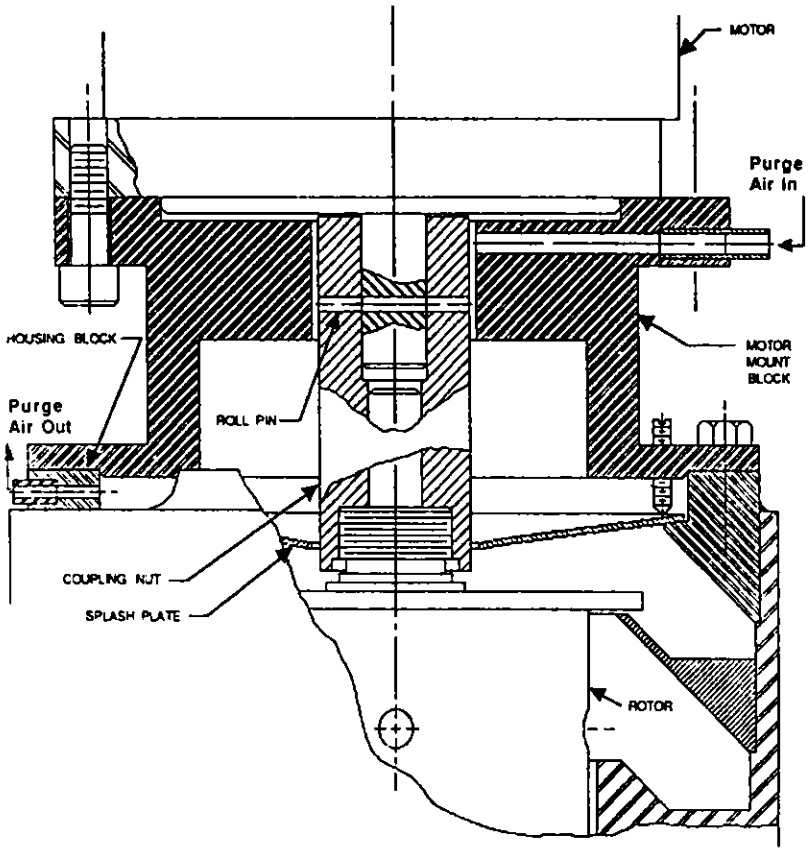

Fig. II-104. Proposed Coupling Nut for the 10-cm Contactor

b. Remote-Handled Laboratory Contactor

The 4-cm contactor was selected for use in the planned Hanford pilot-plant facilities. Based on calculated curves for the 4-cm contactor showing the effect of solvent density and O/A flow ratio on the contactor design, the best radius for the more-dense-phase weir appeared to be 8.80 mm. However, the tests of the 4-cm contactor reported in Sec. II.K.3 suggest that the best radius is 9.00 mm.

L. Separation Processes to Treat Red Water

(L. Reichley-Yinger, D. J. Chaiko, and E. H. Van Deventer)

This work is the first phase of a research project directed toward developing a new and cost-effective process for converting the hazardous red-water waste stream from TNT manufacture to forms that are readily disposable or acceptable for recycling. The process initially separates the red water into its inorganic and organic water-soluble components. The stream containing the water-soluble organic constituents is treated biologically, while the inorganic stream is further processed to recover the sodium sulfite, which can be recycled back into the TNT manufacturing process. Our work focuses on developing the two separations in the process: the separation of the inorganic and organic components of red water by foam fractionation or solvent extraction and the recovery of sodium sulfite from the inorganic stream by solvent extraction. The development of the biotreatment for the organic stream will be done in other ANL divisions.

1. Analyses of Red Water

(L. Reichley-Yinger)

Table II-61 summarizes the results of analyses done to determine the weight percent of organics, sodium nitrate, sodium nitrite, sodium sulfate, sodium sulfite, and solids present in a red water sample obtained from Canadian Industries LTD., Inc. (CIL). Literature values are also given for comparison. The weight percent of organics, the sodium sulfonates and carboxylates, was determined in two ways: titration with 15.9M HNO_3 and ion chromatography. For the ion chromatographic analysis, a sample of red water was contacted with trioctyl(methyl)ammonium chloride until the color of the aqueous phase changed from a deep red to a pale yellow. It was assumed that the organic salts, the sulfonates and carboxylates, were exchanged on a one-for-one basis with chloride. This pale yellow solution was then analyzed for chloride, which resulted from the ion exchange with the organic salts and the hydroxide ion used to maintain the basic conditions needed for the extraction. The weight percent of the organics was calculated from the chloride analysis after correction for the addition of sodium hydroxide.

Table II-61. Composition of Red Water Sample from Continuous Lines at Canadian Industries Ltd.

	Weight %		
	Literature Values		
Component	Eckenrode[67]	Pal[68]	Experimental[a] Results
Organics[b]	9-14	17.3	16[c]
$NaNO_3$	0.3-0.5	1.7	<0.03
$NaNO_2$	3-4	3.5	<0.03
Na_2SO_4	8-12	0.6	3
Na_2SO_3	d	2.3	0.08
Solids	30-32	e	<32[f]

[a]Based on ion chromatographic analysis of aqueous phase after contact with trioctyl(methyl)ammonium chloride, unless noted otherwise.
[b]Sodium salts of sulfonic and carboxylic acids.
[c]Based on titration and on ion chromatographic results assuming a one-for-one exchange with chloride and an average formula weight of 284 g/mol for the organic sodium salts.
[d]Combined with result for sodium sulfate.
[e]Not given.
[f]Determined by air drying of red water.

Along with the analysis of the weight percent of chloride, weight percent of sodium nitrate, sodium nitrite, sodium sulfate, and sodium sulfite was determined by the results of ion chromatographic analyses of the red water after extraction of the organics. The weight percent of solids was determined separately by allowing aliquots of red water to air dry until they came to a constant mass. While the experimental results for the organics and the solids agree with the literature values, those for sodium nitrate, sodium nitrite, sodium sulfate, and sodium sulfite are significantly lower than the literature values. These discrepancies suggest several possibilities: (1) the sample obtained from CIL was not representative of the red water stream, (2) CIL had modified the sellite wash procedure, resulting in slightly different red water composition, or (3) the literature values for the red water composition were measured after ashing of the red-water sample, which would convert the organics to gases and mineral sodium salts.

2. Organic/Inorganic Separation
(D. J. Chaiko)

The majority of the organic compounds in red water are aromatic sulfonate salts, and as such are extremely hygroscopic and therefore insoluble in nonpolar organic solvents. Separation by conventional solvent extraction requires a very powerful extractant in order to favorably partition the organics into an organic diluent. A quaternary amine (aliquot 336) was used successfully to separate the acidic organics from acidified red water; however, the organic phase complex is so stable that stripping the loaded organic phase would be extremely difficult.

Desulfonation of the organics would vastly reduce their aqueous-phase solubility and permit their physical separation from the red water. Although desulfonation of aromatic compounds can be practical in some applications, it is not considered so for red water treatment. Deactivation of the benzene ring by the nitro groups makes the sulfur-carbon bond highly resistant to cleavage.

Three processes for organic/inorganic separation appear to offer enough potential to warrant laboratory investigation: (1) foam fractionation, (2) flocculation, and (3) aqueous biphasic solvent extraction. These three methods and initial results are discussed below.

a. Foam Fractionation
(L. Reichley-Yinger and E. H. Van Deventer)

Table II-62 summarizes the results of the foam fractionation experiments. All experiments were done at pH < 4 since red water, initially at a pH of 8, only forms stable foams below a pH of 4. The percent enrichment of organics in the foamate, calculated from the absorbances of the foamate and raffinate between wavelengths of 300 and 400 nm, is given under various conditions. The first two experiments were done in jacketed beakers, which were open to the environment and subject to evaporation. All later experiments were done in the closed apparatus shown in Fig. II-105. The feed solutions used in these experiments varied from undiluted red water to 1:100 dilutions of red water. The "foam condition" is a qualitative assessment of the amount of water associated with foam that was collected. Dry foam is achieved by allowing the foamate to drain before collection.

Two factors controlling the enrichment of organics in the foamate are the dryness of the foam collected and the dilution of red water used as the feed. For undiluted red water, an enrichment of 0.57% was obtained when a wet foam was collected. This compares to an average enrichment of 3.5% when dry foams were collected. A dry foam collected from a feed that contained the raffinate and foamate from a previous experiment gave an enrichment of 9.8%. An enrichment of 13% was obtained for a dry foam when the feed consisted of a 1:10 dilution of red water, while a 1:100 dilution of red water did not produce a collectable foam.

Table II-62. Percent Enrichment of Organics in Foamate Obtained Under Various Conditions

System	Dilution	Foam Condition	% Enrichment
Open[a]	none	wet	7.5
Open	none	dry	28
Closed[b]	1:100	-	[c]
Closed	none	wet	0.57
Closed	none	dry	3.2
Closed	none	dry	3.8
Closed	none[d]	dry	9.8
Closed	1:10	dry	13

[a]Jacketed beaker used as titration vessel.
[b]Foam fractionation apparatus shown in Fig. II-105.
[c]No collectable foam formed.
[d]Feed consisted of raffinate and foamate from the previous experiment, which gave a 3.8% enrichment.

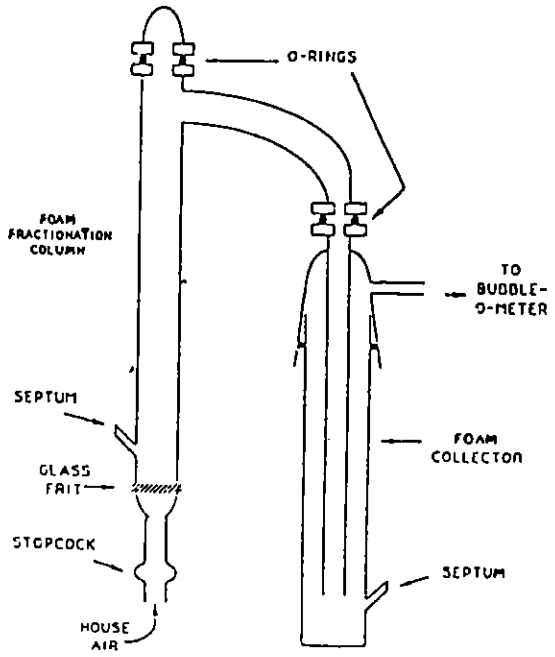

Fig. II-105. Diagram of Foam Fractionation Apparatus

b. Flocculation
(D. J. Chaiko)

Coagulation and flocculation are commonly used methods for industrial wastewater treatment. Inorganic polymers, such as the hydroxocomplexes of Fe^{3+} and Al^{3+}, and organic polymers, such as polyacrylamide or polyethylenimine, are very effective at bringing about the destabilization of

colloidal particles, leading to their aggregation. These particles can then be removed by sedimentation or filtration.

As a separation technique for red water treatment, flocculation involves polymer interactions between particles ranging in size from single molecules to colloidal-size particulates. As these particle-polymer units grow, this material becomes easily filtered from solution. With the formation of a "sweep floc," rapid bridging between particles takes place, and colloidal particles can be trapped in rapidly forming precipitates. This allows small amounts of flocculant to remove ionic species from solution in large excess of the stoichiometric amounts.

Initial experiments have shown that high molecular weight flocculants can be used to selectively precipitate the nitroaromatic sulfonates from the red water samples received from CIL. Two different types of flocculants were studied: a high molecular weight (>4 x 10^6 dalton) cationic polymer (magnafloc 1596C-SP) and a neutral polyethylenimine having an average molecular weight of 10,000. With red water samples diluted 1:50 with deionized water, the cationic flocculant, at a dose level of 250 ppm, produced an easily filtered precipitate, which resulted in a 50% reduction in absorbance at 400 nm. Under similar conditions, the polyethylenimine was much less effective. However, when used in conjunction with hydrous iron colloid at an iron concentration of 5 mM, a clear yellow supernatant was obtained with a polyethylenimine concentration of 200 ppm.

The results of these studies indicate that, in the absence of any particulate material in the red water stream, treatment by flocculation may not offer the best possibility as a primary treatment process. However, when used in conjunction with other treatment approaches, such as aqueous biphasic extraction, flocculation could be effective as a final polishing step in producing a "delistable" inorganic stream.

c. Aqueous Biphasic Separation
(D. J. Chaiko)

Aqueous biphasic systems were originally developed by Albertsson in the mid-1950s for the separation of microbial cells, cell organelles, and viruses.[59] Biphasic separation involves solute partitioning between two immiscible aqueous phases--a polymer-rich layer and an inorganic-salt layer. Biphase formation may also be achieved in the absence of any dissolved salts by using a combination of water soluble polymers. These combinations typically involve a straight chain polymer such as polyethylene glycol (PEG) and a highly branched polymer such as dextran. In recent years, interest in aqueous biphasic systems for application in biotechnology[60,61] and separations of metal ions,[62] ultrafine particles,[63] and organics[64] has increased dramatically.

With regard to wastewater treatment, aqueous biphasic systems have similarities with conventional solvent extraction but do not utilize an organic diluent, which itself may become a source of pollution. In addition, the water-soluble polymers that have been used in biphase formation are inexpensive, nontoxic, and biodegradable. They can also be removed from the process effluents for recycle by ultrafiltration or electrodialysis.

With regard to red water treatment, research using aqueous biphasic systems has concentrated on the PEG system. The PEG system is of interest because of the expected high level of sulfate and other anionic salts in red water (8-12% Na_2SO_4/Na_2SO_3, 3-4% $NaNO_3$, 0.3-0.5% $NaNO_2$).[63] At room temperature, concentrations of approximately 7.5% PEG and 6% Na_2SO_4 by weight easily form an aqueous two-phase system. And, as the phase diagram in Fig. II-106 indicates, increasing temperature promotes biphase formation at much lower salt and PEG concentrations. Since TNT is in the molten state

(> 80°C) when sent to the sellite scrubbers, any recovery of this residual heat would make biphase formation that much easier.

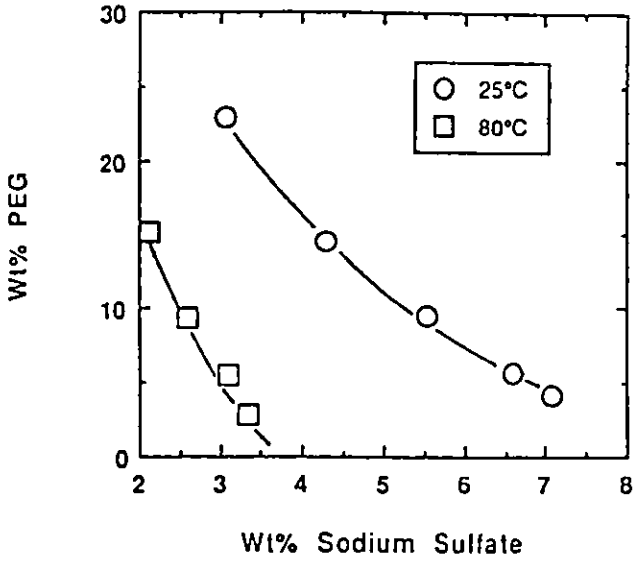

Fig. II-106. Binodial Curves for the PEG/Sulfate System. System compositions above the binodial are biphasic.

When red water is introduced into such a system, the organic components concentrate in the top (PEG) phase, with a distribution ratio of about 10. Through successive batch contacts of undiluted red water with a 7.5% PEG solution (PEG previously equilibrated with 6% Na_2SO_4), a 1000-fold reduction in color of the red water was achieved by the fourth stage. Based on literature data for the PEG system, the distribution ratios of the inorganic salts should be less than one.[65] If this enrichment factor were maintained and not affected by the changing organic and salt concentrations throughout the extraction process, an extremely effective, countercurrent solvent extraction process could be designed. It is highly likely that as the organic material is removed from the residual salt solution, the distribution ratio will remain high or continue to increase, thus providing a highly organic-free salt stream.

Biphasic solvent extraction is thought to be the technology with the greatest promise for successfully separating the inorganic and organic constituents of red water. This process would be run in a continuous, countercurrent mode using a multistage contactor (e.g., mixer-settler, pulsed column, or centrifugal contactor). The choice of contactor technology would be determined by economics and process requirements. As the red water stream flows countercurrent to the flow of the polymer phase, the organic content of the red water will steadily decrease, providing an organic-free salt solution that exits the process. Conversely, as the polymer phase moves through the extraction section, its organic concentration increases. Before exiting the process, the organic-rich polymer phase would be scrubbed with an aqueous acid solution to convert the sodium salts of the organic sulfonates to their acidic forms. If necessary, an additional scrub section can be added to further reduce the inorganic salt concentration in the polymer phase. Because of the phase behavior of the PEG system (see Fig. II-105), sulfate or sulfite is required to maintain the biphase. Scrubbing inorganic salts from the PEG phase, therefore, would require the use of a second polymer, such as dextran, which is immiscible with the PEG phase. Ultimately, the degree of salt removal from the red water organics would be dictated by the combination of economics and the capabilities of any biotreatment process utilized as a final step in degrading the organics to innocuous materials.

REFERENCES

1. R. A. Leonard, M. C. Regalbuto, D. B. Chamberlain, and G. F. Vandegrift, "A New Model for Solvent Extraction in Columns," presented at the Sixth Symp. on Separation Science and Technology for Energy Applications, Knoxville, TN, October 22-27, 1989.

2. H. R. Maxey, D. B. Chamberlain, G. J. McManus, E. L. Colton, and R. L. Nebeker, *Removal of Actinides from ICPP Fuel Reprocessing Wastes: Engineering Studies Terminal Report*, Exxon Nuclear Idaho Co. Report ENICO-1057 (1980).

3. F. J. Millero, *Water and Aqueous Solutions: Structure, Thermodynamic and Transport Processes*, ed., R. A. Horne, Vol 13, Interscience, New York (1972).

4. J. K. Hovey, *Thermodynamics of Aqueous Solutions*, Ph. D. Thesis, University of Alberta (1988).

5. O. Sohnel and P. Novotny, *Densities of Aqueous Solutions of Inorganic Substances*, Elsevier, Amsterdam, Netherlands (1985).

6. Cited in Ref. 5 as *Gmelin's Handbuch der Anorganischem Chemie*, Springer-Verlag, Berlin.

7. J. J. Katz, G. T. Seaborg, and L. R. Moss, *The Chemistry of the Actinide Elements*, Chapman Hall, London (1986).

8. J. W. Akitt, "Limiting Single-ion Molar Volumes," J. Chem. Soc. Farad. I, 76, 2259 (1980).

9. B. E. Conway, R. E. Verall, and J. E. Desnoyers, "Partial Molal Volumes of Tetraalkylammonium Halides and Assignment of Individual Ionic Contributions," Trans. Farad. Soc. 62, 2738 (1965).

10. A. M. Couture and K. J. Laidler, "The Partial Molal Volumes of Ions in Aqueous Solution," Can. J. Chem. 34, 1209 (1956).

11. G. Curthoys and J. G. Mathieson, "Partial Molal Volumes of Ions," Trans. Farad. Soc. 66, 43 (1970).

12. K. Fajans and O. Johnson, "Apparent Volumes of Individual Ions in Aqueous Solution," J. Am. Chem. Soc. 64, 668 (1942).

13. E. Glueckauf, "Molar Volumes of Ions," Trans. Farad. Soc. 61, 914 (1965).

14. L. G. Hepler, "Partial Molal Volumes of Aqueous Ions," J. Phys. Chem. 61, 1426 (1957).

15. J. V. Leyendekkers, "Ion-Water Geometry and the Tammann-Tait-Gibson Effective Pressure and Radius," J. Chem. Soc. Farad. 1, 78, 3383 (1982).

16. P. Mukerjee, "On Ion-Solvent Interaction. Part I. Partial Molal Volumes of Ions in Aqueous Solution," J. Phys. Chem. 65, 740 (1961).

17. V. A. Vasilev, "Theory of Heat Capacities and Volumes of Polyatomic Ions in Aqueous Solutions," Russ. J. Phys. Chem. 55, 544 (1981)

18. R. Zana and E. Yeager, "Ultrasonic Vibration Potentials in Tetraalkylammonium Halide Solutions," J. Phys. Chem. 71, 4241 (1967).

19. R. C. Weast, *C.R.C. Handbook of Chemistry and Physics*, 69th Ed., CRC Press, Boca Raton, FL (1989).

20. F. J. Millero, "The Molal Volumes of Electrolytes," Chem. Reviews 71, 147 (1971).

21. F. J. Millero, *Activity Coefficients in Aqueous Solutions: Structure, Thermodynamics and Transport Processes*, ed., R. A. Horne, Vol. 13, Interscience, New York (1972).

22. L. C. Howick and J. L. Jones, Talanta 9, 1037 (1962).

23. V. N. Tikhonov, *Analytical Chemistry of Aluminum*, Wiley, New York (1973).

24. K. J. Jensen and W. E. Streets, *Methods of Chemical Analysis Used to Characterize Battery Materials*, Argonne National Laboratory Report ANL-80-41 (1981).

25. L. A. Bromley, "Thermodynamic Properties of Strong Electrolytes in Aqueous Solutions," AIChE J. 19, 313 (1973).

26. H. P. Meissner and J. W. Tester, "Activity Coefficients of Strong Electrolytes in Aqueous Solutions," IEC Proc. Des. Dev. 11, 128 (1972).

27. H. P. Meissner, C. L. Kusik, and J. W. Tester, "Activity Coefficients of Strong Electrolytes in Aqueous Solution--Effect of Temperature," AIChE J. 18, 661 (1972).

28. A. Rastogi and D. Tassios, "Estimation of Thermodynamic Properties of Binary Aqueous Electrolyte," IEC Proc. Des. Dev. 19, 477 (1980).

29. *Smithsonian Physical Tables*, Smithsonian Inst. Publ. 374, 9th ed., Washington, DC (1954).

30. *International Critical Tables*, Vol. 3, McGraw-Hill, New York, p. 361 (1926).

31. G. A. Clarke, R. C. Gatrone, and E. P. Horwitz, "The Extraction of Carboxylic Acids by 0ϕ(iB)CMPO," Solvent Extr. Ion Exch. 5, 471 (1987).

32. G. F. Vandegrift et al., *Transuranic Decontamination of Nitric Acid Solutions by the TRUEX Solvent Extraction Process--Preliminary Development Studies*, Argonne National Laboratory Report ANL-84-45 (1984).

33. Kent Orlandini, ANL Environmental Research Division, private communication (1989).

34. J. M. Cleveland, *The Chemistry of Plutonium*, American Nuclear Society, La Grange Park, IL, p. 162 (1979).

35. I. R. Higgins and R. G. Wymer, *DIBAN--Ion Exchange Waste Disposal Scheme*, Oak Ridge National Laboratory Report ORNL-1984 (1955).

36. C. F. Baes, *The Hydrolysis of Cations*, Robert E. Krieger Publ., Malabar, FL, pp. 112-122 (1986).

37. J. W. Codding, *The Partition of Uranium (VI) between Tributyl Phosphate and Basic Aluminum Nitrate Solutions*, IDO-14454 (1958).

38. J. G. Surak and P. F. Thomason, *Statistical Evaluation Methods for the Analysis of Dibasic Aluminum Nitrate (DIBAN)*, Oak Ridge National Laboratory Report ORNL-1931 (1955).

39. J. W. Gresky, *Recovery of Nitrogen Oxides and Rare Gas Fission Products from the Nitric Acid Dissolution of Irradiated Uranium*, Oak Ridge National Laboratory Report ORNL-1208 (1952).

40. H. J. Edding, M. L. Huggins, and A. G. Brown, *Phase Transformations in Alumina*, IDO-14580 (1961).

41. S. R. M. Ellis and J. M. Thwaites, "Vapor-Liquid Equilibria of Nitric Acid-Water-Sulphuric Acid Mixtures," J. App. Chem. 7, 152 (1957).

42. R. A. Robinson and R. H. Stokes, *Electrolyte Solutions*, Butterworths, London (1959).

43. G. L. Wilson and F. D. Miles, "The Partial Pressures of Nitric Acid-Water Mixtures from 0-20°C," Trans. Farad. Soc. 36, 356 (1940).

44. M. R. Vandoni and M. Landy, "Mesure des Tensions de Vapeur Partielles des Melanges NO_3H-H_2O," J. Chim. Phys. 49, 99 (1952).

45. M. A. Yakimov and V. Ya. Mishin, "Investigation of Heterogeneous Equilibria in the Tertiary System UO_2-HNO_3-H_2O," Radiokhimya 6, 545 (1964).

46. E. Hala, I. Wichterle, J. Polak, and T. Boublik, *Vapour-Liquid Equilibrium Data at Normal Pressures*, Pergamon, Oxford (1968).

47. I. Wichterle, J. Linek, and E. Hala, *Vapor-Liquid Equilibrium Data Bibliography*, Elsevier, Amsterdam (1973).

48. G. T. Polovnikova, L. I. Chentsova, and L. N. Nosova, "Liquid-Vapour Equilibrium in Systems Comprising Aqueous Solutions of Nitric Acid and Water," Russian J. Inorg. Chem. 16, 1759 (1971).

49. M. A. Yakimov, V. Ya. Mishin, and E. V. Zalkind, "The Sodium Nitrate-Nitric Acid-Water System at 25°, 35°, and 50°," Russian J. Inorg. Chem. 11, 1032 (1966).

50. A. L. Shneerson, M. A. Miniovich, Zh. M. Filippova, S. N. Soroka, and P. A. Platonov, "Liquid-Vapor Equilibria in the Systems Nitric Acid-Water-Magnesium Nitrate, Nitric Acid-Water-Calcium Nitrate, and Nitric Acid-Water-Magnesium Nitrate-Calcium Nitrate," Russian J. Inorg. Chem. 39, 744 (1965).

51. C.-C. Chen, H. I. Britt, J. F. Boston, and L. E. Evans, in *Thermodynamics of Aqueous Systems with Industrial Applications*, ed., S. A. Newman, ACS Symposium Series 133, Washington, DC (1980).

52. J. F. Zemaitis, D. M. Clark, M. Rafal, and N. C. Scrivner, *Handbook of Aqueous Electrolyte Thermodynamics*, DIPPR/AIChE, New York (1986).

53. A. L. Horvath, *Handbook of Aqueous Electrolyte Solutions*, Ellis Horwood, Chichester (1985).

54. L. D. Mitchell et al., *User's Guide--Beam Analysis II*, Mechanical Engineering Dept., Virginia Polytechnic Institute and State University, Blacksburg, Virginia, Edition 2.2 (1984).

55. E. C. Pestel and F. A. Leckie, *Matrix Methods in Elastomechanics*, McGraw-Hill, New York (1963).

56. W. D. Pilkey and P. Y. Chang, *Modern Formulas for Statics and Dynamics*, McGraw-Hill, New York (1978).

57. L. D. Mitchell and K. D. Young, "Redesign of Contactor Rotor Assembly to Increase Operational Rotor Stability," Mechanical Engineering Dept., Virginia Polytechnic Institute and State University, Blacksburg, Virginia, unpublished report (September 1987).

58. L. D. Mitchell, Mechanical Engineering Dept., Virginia Polytechnic Institute and State University, Blacksburg, Virginia, private communication (September 1987).

59. P.-Å. Albertsson, *Partition of Cell Particles and Macromolecules*, 3rd ed., John Wiley, New York (1986).

60. M. R. Kula, "Extraction and Purification of Enzymes Using Aqueous Two-Phase Systems," in *Applied Biochemistry and Bioengineering*, ed., L. B. Wingard, Jr., Academic Press, New York, pp. 74-79 (1979).

61. H. Walter, D. E. Brooks, and D. Fisher, eds., *Partitioning in Aqueous Two-Phase Systems*, Academic Press, New York (1985).

62. T. I. Zvarova et al., "Liquid-Liquid Extraction in the Absence of Usual Organic Solvents: Application of Two-Phase Aqueous Systems Based on a Water-Soluble Polymer," Mikrochimica Acta [Wien] 3, 449 (1984).

63. A. P. Ananthapodmanabhan and E. D. Goddard, "Process for the Separation of Solid Particulate Matter," U.S. Patent No. 4,7225,358 (1987).

64. N. D. Gullickson, J. F. Scamehorn, and J. H. Harwell, "Liquid-Coacervate Extraction," in *Surfactant-Based Separation Processes*, eds., J. F. Scamehorn and J. H. Harwell, Surfactant Science Series Vol. 33, Marcel Dekker, New York, pp. 139-152 (1989).

65. J. E. Eckenrode, C. G. Denzler, and J. Klein, *Evaluation of TNT Red Water Pollution Abatement Technologies*, U.S. Army Armament Research and Development Command, Chemical Systems Laboratory, ARCSL-TR-80023 (1980).

III. HIGH-LEVEL WASTE/REPOSITORY INTERACTIONS
(J. K. Bates)

A. Glass Studies for Yucca Mountain Project
(J. K. Bates, B. M. Biwer, W. L. Ebert, T. J. Gerding, J. J. Mazer, and A. B. Woodland)

The Yucca Mountain Project (YMP) is investigating the tuff beds of Yucca Mountain, Nevada, as a potential location for a high-level radioactive waste repository. As part of the waste package development portion of this project, which is directed by Lawrence Livermore National Laboratory (LLNL), work is being performed at CMT to study the behavior of the waste form under anticipated repository conditions. Work includes (1) development and performance of a test to measure waste form behavior in unsaturated conditions, (2) performance of experiments to study the behavior of waste package components in an irradiated environment, (3) development of test methods to study the reaction of glass in water vapor and, subsequently, in liquid water, (4) development of static leaching tests to provide long-term release data to the glass modeling effort, and (5) detailed characterization of reacted glass surfaces.

1. Unsaturated Test Method
(J. K. Bates and T. J. Gerding)

The Unsaturated Test Method was developed[1,2] to monitor the reaction of high-level nuclear waste with water under conditions that are relevant to the proposed repository site at Yucca Mountain, Nevada. The repository horizon is located in welded tuff, and the anticipated hydrology is unsaturated. This unsaturated environment adds a new dimension to waste form testing in that the amount of water expected to contact the waste is minimal, and the sequence of water/waste interaction will be from humid air to small volumes of dripping water. The emphasis of the Unsaturated Test is to investigate interactive effects between waste package components, to identify processes that are accentuated due to the small water contact volume, and to provide a measurement of waste form reaction as a function of time. Data obtained from the Unsaturated Test may be used to validate models of glass reaction that have been developed independently from site-specific considerations.

A schematic diagram of the test apparatus is shown in Fig. III-1. The components are the test vessel, which provides for collection and containment of liquid and support of the waste package; the waste package assemblage (WPA), which consists of the glass waste form and presensitized metallic components representing the canister; and a solution feed system to inject test water.

In the Unsaturated Test, the WPA is contacted by drops of reference J-13 groundwater that had been preequilibrated with tuff at 90°C. The experiments are conducted at 90°C. The nature and degree of reaction are determined from analysis of the water that has contacted the WPA and by surface analysis of the WPA components. The test schedule incorporates batch and continuous testing. In the batch mode, tests are terminated at 13-week intervals through 52 weeks. In the batch mode, the test apparatus is disassembled and analyses of both the solution and assembly components are performed. In the continuous mode, the WPA (including liquid associated with the WPA) is transferred to a new test vessel, and the test is continued. Generally, both batch and continuous tests are replicated. In addition, investigation of the test components is possible at each sampling point, and yet the test can continue for an unspecified number of test periods or until information most useful to repository evaluation is obtained.

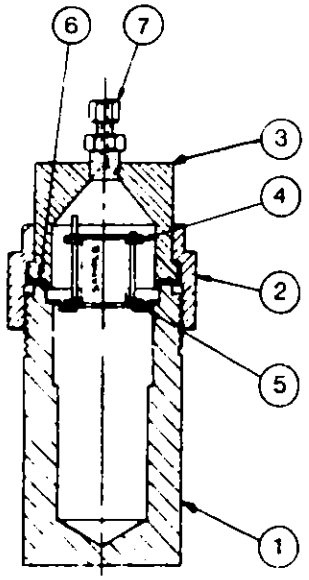

1. Body
2. Nut
3. Cap
4. Retainer Top
5. Retainer Bottom
6. Ethylene Propylene Gasket
7. Swagelok Fitting

Fig. III-1. Schematic Drawing of the Unsaturated Test Apparatus

The YMP Unsaturated Test Method is being used in the N2 and N3 test series. Each test series has now passed the 52-week period, where the batch tests have all been terminated, and where changes in solution compositions for the ongoing continuous tests are less pronounced than in earlier periods. Thus, the interval between sampling periods in the continuous tests has been extended from 13 to 26 weeks. This allows more solution to accumulate in the test vessel, therefore enabling a more complete set of solution analyses to be performed. With the increased solution volumes, analyses are performed for pH (0.1 mL); anions (0.1 mL); organic and total carbon (0.5 mL); filtered and unfiltered transuranic elements ^{237}Np, ^{239}Pu, and ^{241}Am (0.3 mL); and glass-forming cations (remaining solution, which is generally ~1 mL). Procedures to perform analyses on small solution volumes are being written to control the operations.

a. N2 Unsaturated Test

The N2 Unsaturated Tests with SRL 165 glass (simulation of glass to be produced by the Defense Waste Processing Facility at the Savannah River Plant) have been completed through the 182-week sampling period. All the batch tests have been completed, and three continuous tests and one blank are ongoing with samplings at 26-week intervals. The continued release of actinide elements and selected cations over a 120-week period of the N2 tests is shown in Figs. III-2 and -3.

b. N3 Unsaturated Test

The N3 Unsaturated Test is in progress using ATM-10 glass (simulated West Valley glass containing actinides plus ^{99}Tc) that was received from the Materials Characterization Center and remelted to obtain the required form of the glass. The test was started July 6, 1987, according to the Unsaturated Test matrix[3] and has been completed through the 117-week sampling period. The release of actinide elements and selected cations oven an 80-week period of N3 tests is shown in Figs. III-4 and -5. The components from this test must be analyzed using surface analytical techniques to provide a more detailed description of the glass reaction over the first one-year period.

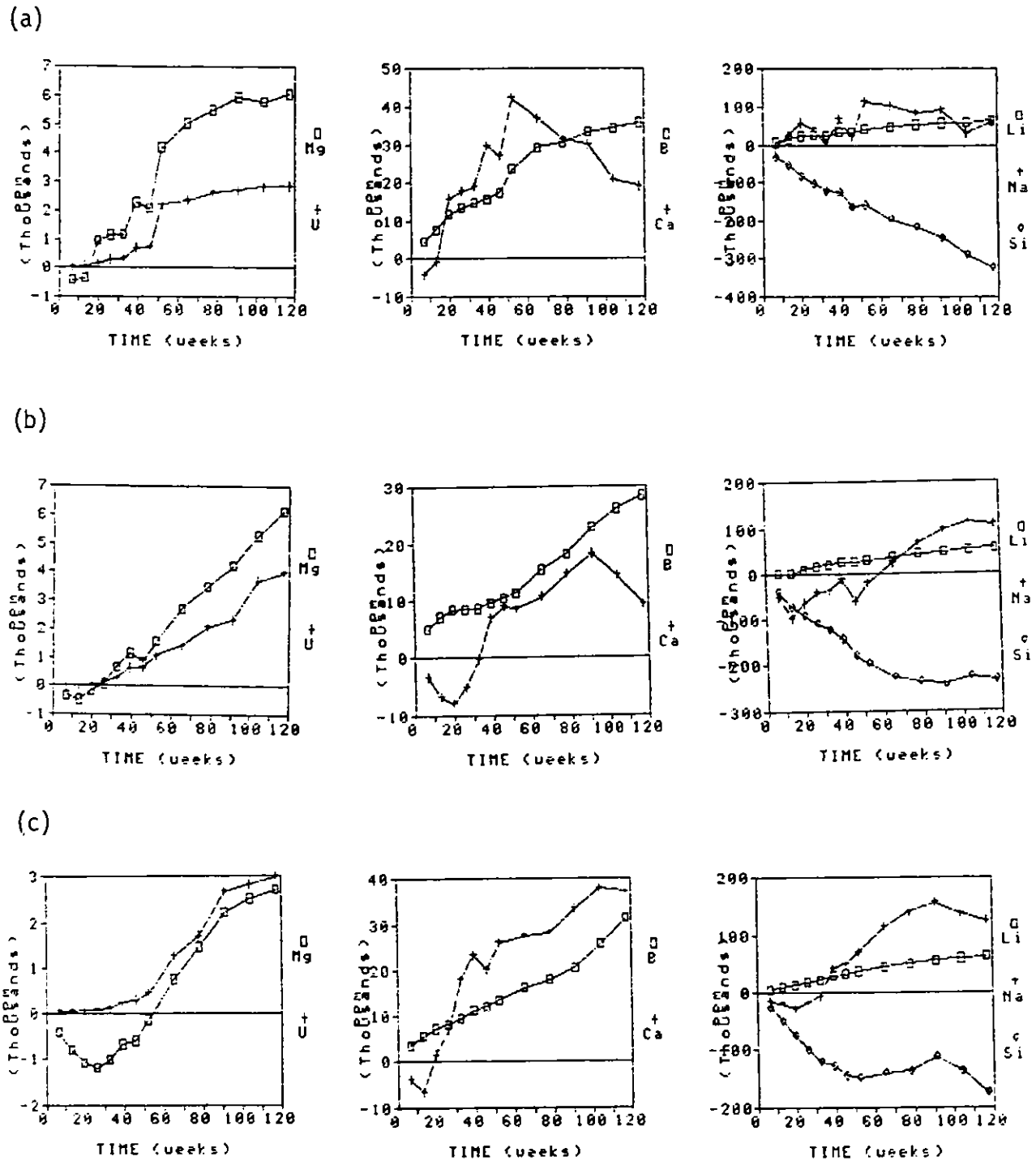

Fig. III-2. Cation Release from N2 Test Series: (a) N2-9, (b) N2-10, and (c) N2-12

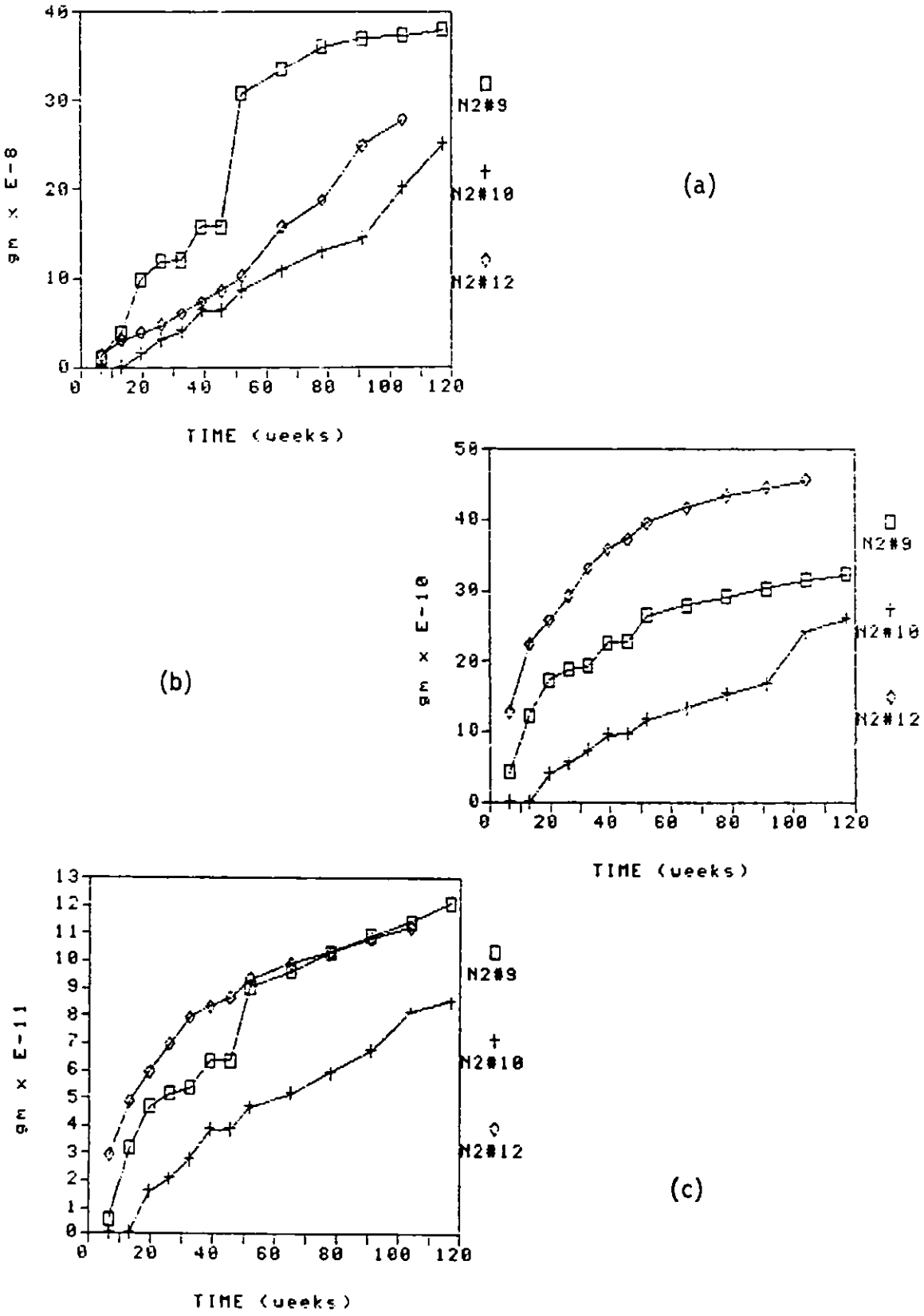

Fig. III-3. Transuranic Release from N2 Test Series (N2-9, -10, -12): (a) Np, (b) Pu, and (c) Am

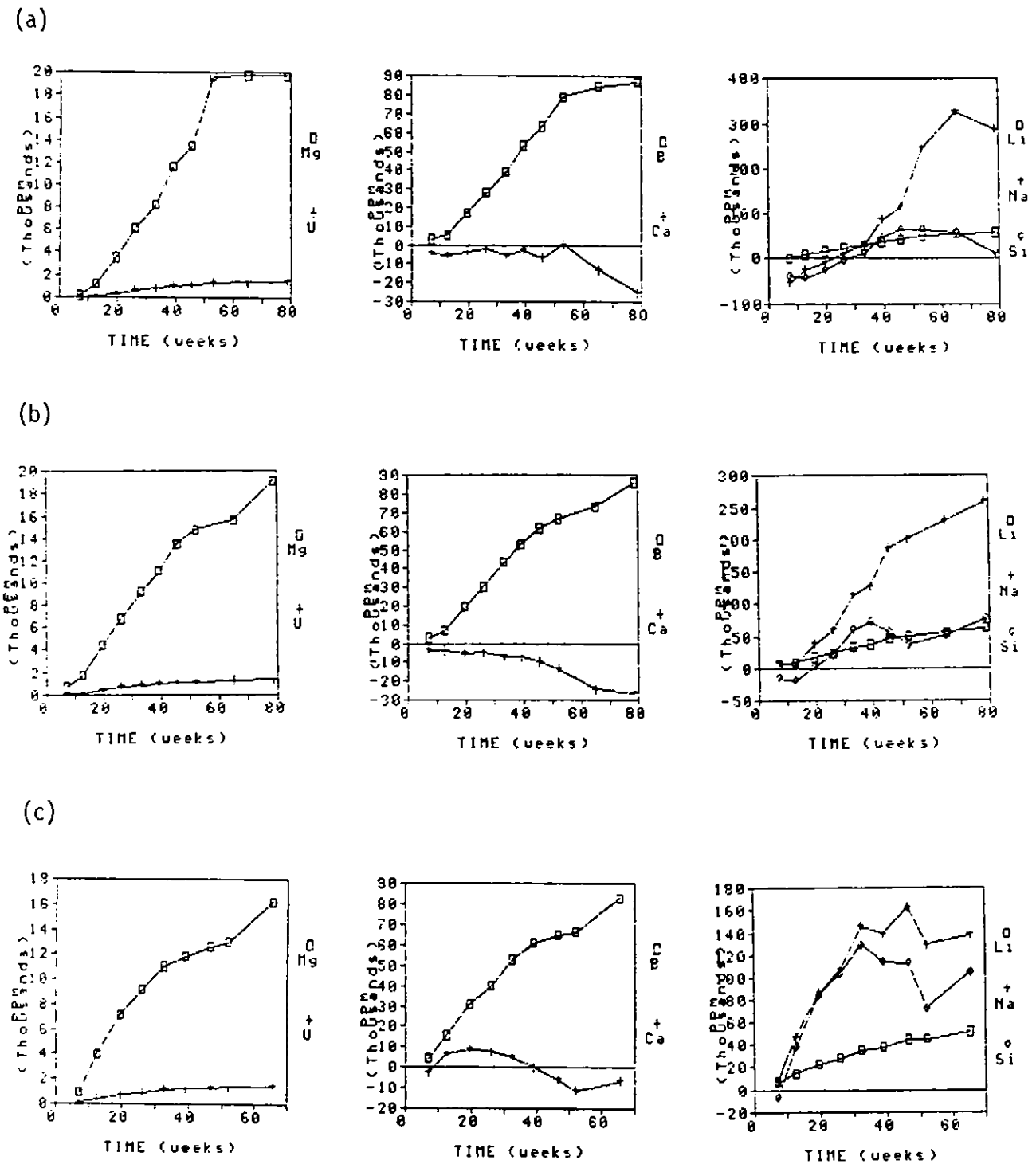

Fig. III-4. Cation Release from the N3 Test Series: (a) N3-9, (b) N3-10, and (c) N3-12

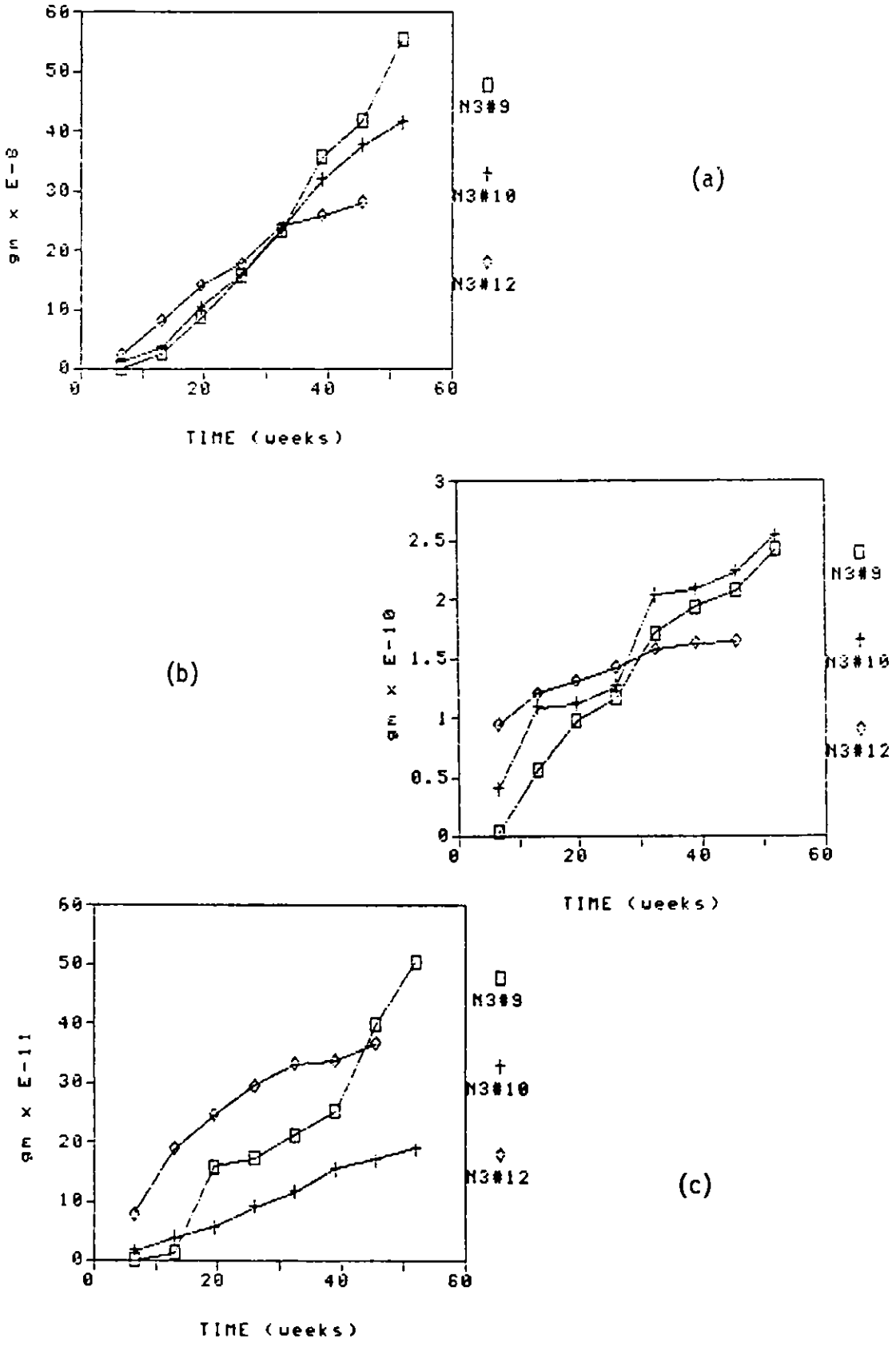

Fig. III-5. Transuranic Release from the N3 Test Series (N3-9, -10, -12): (a) Np, (b) Pu, and (c) Am

2. Parametric Experiments

(J. K. Bates, T. J. Gerding, and A. B. Woodland)

a. Introduction

One key to the applicability of the data generated using the Unsaturated Test is the relationship between the standard conditions used in the test and the eventual conditions encountered in the repository. Since it is likely that repository conditions will vary between individual waste packages, parametric experiments (with Unsaturated Test N2 as the standard method) have been initiated to determine to what degree various factors affect glass reaction. The parametric experiments in progress are listed in Table III-1.

Savannah River Laboratory black frit based 165 glass (see Ref. 4 for composition) has been tested for up to 208 weeks by these procedures. The normalized mass releases (NL) for Li and U are shown in Fig. III-6. Lithium is commonly used to monitor glass reaction because it is released most rapidly from the glass and does not readily form secondary phases or interact with metal components of the test. Uranium is a long-lived actinide present in the glass. The results of experiments from this set form a basis for comparison with subsequent test sets where the test conditions are varied to study parametric effects.

Table III-1. Experimental Conditions Used in Parametric Unsaturated Test Series

Experiment No.	Experimental Parameter(s)
N2	Glass surface area of 13.5 cm^2, drop volume of 0.075 mL, drop interval every 3.5 days, glass in contact with sensitized 304L stainless steel.
P-II	Exclusion of metal contact with glass, standard conditions.
P-III	65% reduction in cast glass surface area, standard conditions.
P-IV	65% reduction in cast glass surface area, 50% reduction in drip volume.
P-V	Drop interval rate increased from 3.5 to 14 days.
P-VIII	Varying degrees of metal sensitization, standard conditions.

b. Results and Discussion

Both the test solutions and the test components (glass and metal) have been examined to describe the reaction process. In Fig. III-6, the P-II and P-V experiments are seen to have the smallest Li and U release. Batch samples from both experiments gained weight, indicating that secondary phases had formed. There was a surface layer composed of a silicon-rich mat with a composition like that of an iron-rich smectite clay. This layer obscured most of the original "as-cut" glass surface. This material probably formed by a combination of precipitation and transformation of altered glass. The major precipitated phases were identified by X-ray diffraction as calcite and gypsum. In the P-II experiments, irregularly shaped grains with a composition very rich in sodium had formed. While this phase has not been positively identified, it may be Na_2CO_3.

The glass reaction in both of these experiments, as measured by the lithium release, is about 50% that for standard test conditions. However, the increase in the drip rate and the lack of a metal retainer result in evaporative processes significantly affecting the formation of phases and the release of elements from the glass. Such evaporative processes are expected to be enhanced under actual repository conditions due to self-heating of the waste.

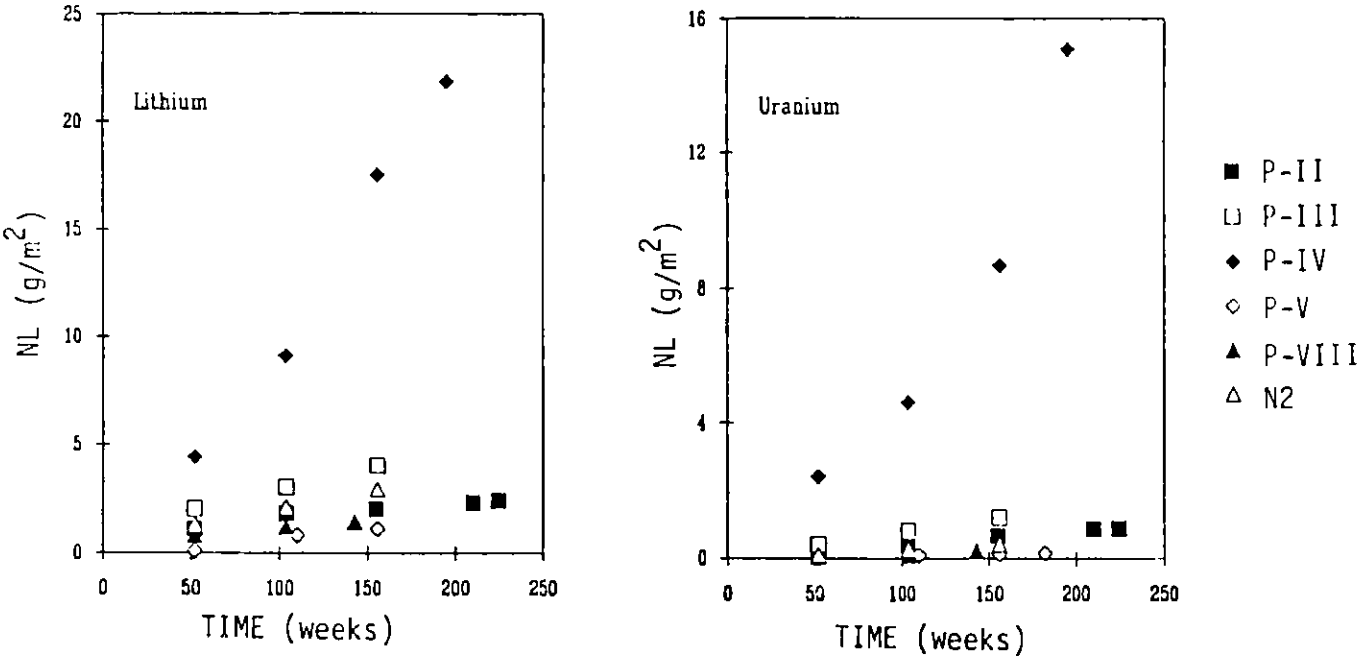

Fig. III-6. Normalized Release of Lithium and Uranium from the Parametric Experiments and the Standard N2 Test

The normalized release in the P-IV experiments is about five times greater than in the P-III experiments and up to ten times greater than in the standard N2 tests. This increased release may be attributable to physical processes occurring on the glass surface. After 26 weeks, the top and bottom surfaces for all samples show some indication of exfoliation in the reacted surface layer. An entire cycle is observable from initial cracking and pulling away from the surface to exfoliation exposing the glass from below. Precipitates are sometimes present in these exposed areas. This process is most advanced on the P-IV samples.

The larger the extent of exfoliation observed on the reacted surfaces, the larger the elemental release. The exfoliated surface layer is not filtered from the test solution, but it is dissolved during an acid soak step and is treated as material available for transport from the waste package. Small pieces of exfoliated layer are sometimes observed in the test solution during sampling.

While the exfoliation is quantitatively related to the erratic and large amount of release that occurs during P-IV and P-III, the cause of the exfoliation is still being investigated. In both of these experimental sets, the top and bottom glass surfaces remained wet with standing water present. Usually P-IV, with the smaller drip volume, had the largest amount of water remaining in contact with the glass. The surface layers are probably unstable in all the experiments, but exfoliated material can only be effectively transported from the glass when the surfaces remain wet and are contacted by intermittent flow.

The P-VIII series of experiments was performed to study the effect of metal sensitization on glass reaction. The standard test conditions utilize partially sensitized metal in contact with the glass. Because the sensitization process degrades the corrosion resistance of the stainless steel, iron from the metal and silicon from the glass react to form iron silicate and iron oxyhydroxide reaction products, which were clearly visible on the test components. To further study the sensitization effect, a low carbon 304L steel was used (0.014 wt % C, compared to 0.028 wt % in the standard test). The steel was treated at 550°C for 24 h and cooled slowly to room temperature. These conditions were also used to

induce sensitization in the standard test. In the 52-week batch experiment, there was evidence of a strong reaction between the metal and glass, as indicated by the accumulation of red-brown rust-like reaction products. The elemental release was similar to that of the standard N2 test. In other P-III experiments, where no evidence of strong reaction was observable, the elemental releases were less. In these glass samples, the top surfaces were dry and the bottom surfaces only damp during sampling. Exfoliation was not as advanced on these samples. This supports the contention that water contact promotes surface layer exfoliation.

c. Conclusions

The Unsaturated Test Method has been used to study the effect of test parameters on glass reaction. Under conditions where evaporative processes dominate (e.g., no metal retainer or extended drop interval), release from the glass is minimized and calcium-rich secondary phases are the dominant reaction products. When varying degrees of sensitization are imparted to the metal retaining sections, elemental release increases by up to twofold, compared to tests performed with nonsensitized metal. Also, iron-rich phases become common. However, when the top and bottom glass surfaces remain wet, the elemental release from the WPA is increased up to a factor of ten. This increase results from the exfoliation of reacted glass layers, followed by transport of these released layers from the glass by intermittent water contact. While some exfoliation release is present under all conditions, it is particularly significant when enough water is present for transport from the glass.

3. Static Leach Experiments
(B. M. Biwer)

The glass surface area/leachant volume (SA/V) ratio is a critical parameter in static leach experiments because it determines the rate at which the solution becomes saturated or approaches steady state with respect to dissolved glass components and the eventual formation of secondary phases. High SA/V ratios are often used to accelerate the attainment of solution saturation, and the factor SA/V t (t = time) is used to compare results attained at different SA/V ratios. For example, a test run for 10 days at an SA/V ratio of 10 m^{-1} (MCC-1 type test[5]) would be predicted to have the same final leachant composition as an equivalent test run for 2 days at an SA/V ratio of 50 m^{-1}. The allure of using such a simple factor to "accelerate" glass reaction based on solution concentration is strong. However, conditions expected in an unsaturated environment complicate this application of SA/V ratio. Important factors to be evaluated with respect to SA/V ratio include those which affect the solution composition independent of simple dissolution of the glass network. One such factor is the presence of silicon in the leachant.

Experiments are in progress to investigate the use of SA/V scaling in various leachants relevant to the tuff repository. Monolithic samples of a synthetic nuclear waste glass (SRL 131) were leached at 90°C in deionized water, a 60 ppm Si solution, and a 120 ppm Si solution. Tests were performed for up to 100 days at SA/V ratios of 10, 50, and 100 m^{-1}. Final elemental solution concentrations have been obtained, and sample characterization is in progress.

Preliminary experiments have shown that the overall extent of reaction for the same time periods decreases with both an increase in SA/V ratio and an increase in the leachant silicon concentration. For example, Fig III-7 shows the boron concentrations of experiments performed with SRL 131 glass leached with deionized water, a 60 ppm silicon solution, and a 120 ppm silicon solution. Note that the boron concentration is lower in the silicon solutions. The preliminary experimental results support the hypothesis that the release rates are limited by solubility rather than by the layer thickness or the existence of a protective layer. Any diffusion limitations due to the reacted layer will be more

pronounced in experiments at lower SA/V ratios, which generate thicker layers. If the release of one element is affected more by the layer than others, the possibility exists that equilibria with secondary phases will be affected, thereby influencing the solution concentration as well.

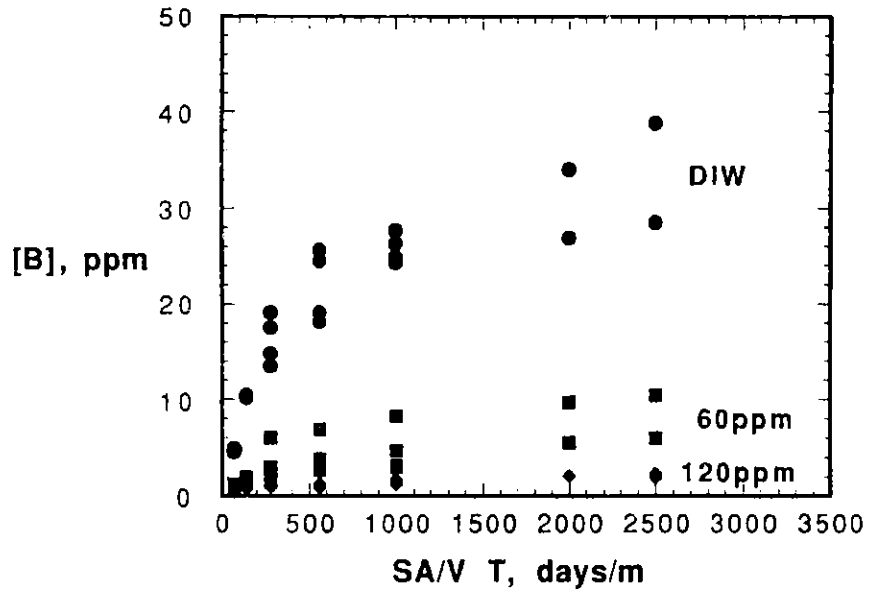

Fig. III-7. Solution Boron Concentration vs. (SA/V)t for SRL 131 Glass Leached in Deionized Water (circle), 60 ppm Si Solution (square), and 120 ppm Si Solutions (diamond)

Slightly higher solution pH values and concentrations of Si (prior to reaching saturation), Li, B, and Na were observed in tests done at 100 m^{-1} than in those done at 50 m^{-1} at equivalent SA/V t. These differences were seen to increase with larger SA/V t in all leachant solutions. Larger surface areas release more alkali and result in higher pH values. The higher pH values promote glass dissolution, which may result in nonuniform acceleration of elemental release and different solution concentrations. These effects could lead to different controlling equilibria (i.e., formation of different alteration products) in experiments performed at different SA/V ratios. For example, preliminary analysis of the reacted samples determined that birnessite ($Mn_7O_{13}{\cdot}5H_2O$) forms as a precipitate on samples reacted in deionized water with an SA/V ratio of 10 m^{-1} but not on samples reacted for equivalent values of SA/V t with an SA/V ratio of 50 m^{-1} or 100 m^{-1}. The use of SA/V t scaling is deemed inappropriate under these conditions.

4. Natural Analogs
(J. J. Mazer)

A relationship between relative humidity (RH) and alteration rates has been described for experimental studies of glasses with complex reaction mechanisms.[6-10] It has been assumed that this RH is unimportant to the relatively simple processes of obsidian hydration.[11] Since obsidian artifacts used in obsidian hydration dating (OHD) have been exposed to a wide range of RH's, a study was initiated to investigate the effects of RH on obsidian hydration by performing carefully controlled hydration experiments at elevated temperatures.

Vapor hydration experiments with three obsidians were performed at 100%, 90%, and 60% RH and temperatures ranging from 150 to 175°C for up to 30 days. The compositions of the three obsidians are given in Table III-2. The experimental method has been described in detail by Ebert.[12] At the termination of an experiment, each sample was thin-sectioned and the hydration layer measured by established procedures.[13]

Hydration rates were derived from linear regression fits to the hydration layer measurements over time. Results are given in Table III-3. At 60% and 90% RH and any one of the three experimental temperatures, the hydration rates are constant, or nearly so, within experimental error. Between 90% and 100% RH there is a significant difference, approximately 30%, between measured hydration rates. The effect of relative humidity is similar at each experimental temperature. Figure III-8 graphically presents the hydration rates as a function of relative humidity at 150 and 175°C. These results demonstrate that relative humidity significantly affects the hydration rates of obsidian.

Table III-2. Obsidians Used in Hydration Experiments

	Coso 4-1	Mule Creek	Orito Quarry
Oxide Weight Percent			
SiO_2	74.9	73.6	72.1
Al_2O_3	14.20	14.34	14.16
Na_2O	4.67	4.62	5.47
K_2O	4.59	4.45	4.33
CaO	0.53	0.65	0.69
MgO	0.02	0.06	0.03
MnO	0.03	0.05	0.06
Fe_2O_3	0.96	0.97	3.17
TiO_2	0.04	0.06	0.19
Element Conc., ppm			
Cu	153	-[a]	-
Zn	47	-	222
Rb	198	-	60
Sr	17	-	19
Y	9	-	36
Nb	23	-	45
Pb	35	-	-
Zr	57	-	458
Ba	-	-	593
H_2O[b]	0.36	0.19	0.15

[a]Dash indicates obsidian not analyzed for given element.
[b]Analyzed using the Penfield method.[14]

It was originally hypothesized that relative humidity effects could be discounted because an obsidian surface is covered by a monolayer of water at RH's as low as 3%.[11,15] Subsequent additions of water to an obsidian/water system were not believed to affect the reaction. However, our results suggest that the diffusivity of water into obsidian is significantly affected by the vapor pressure in contact with a glass surface. Thus, our results support the assertions of others that careful measurements of temperature and relative humidity are necessary to successfully use obsidian hydration dating.[16]

Table III-3. Experimentally Determined Hydration Rates for Three Obsidians

Temp., °C	RH, %	Hydration Rate, $\mu m/days^{1/2}$		
		Coso 4-1	Mule Creek	Orito Quarry
175	100	3.83	2.23	2.08
	90	3.36	1.84	1.58
	60	3.11	1.85	1.50
160	100	2.13	1.35	1.14
	90	1.78	1.20	0.96
	60	1.79	1.17	0.95
150	100	1.38	1.10	1.01
	90	1.26	1.01	0.84
	60	1.25	0.96	0.62

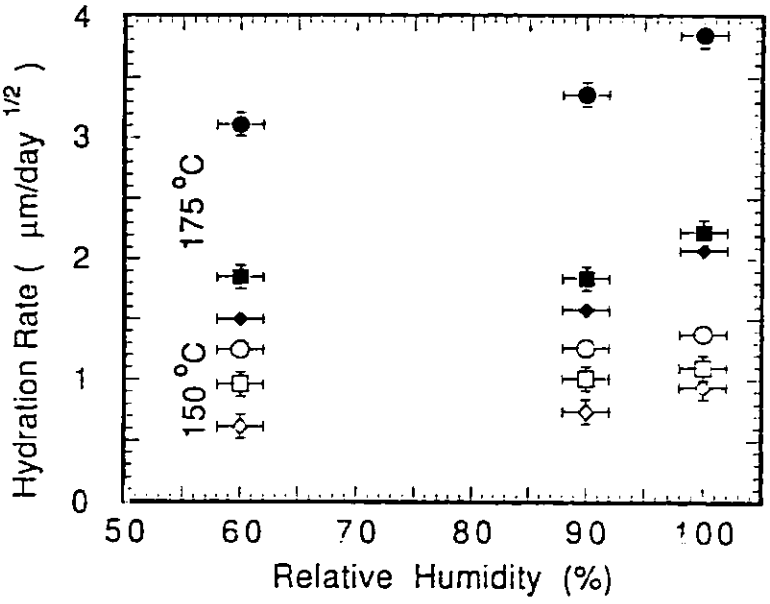

Fig. III-8. Experimentally Determined Hydration Rates as a Function of Relative Humidity at 150 and 175 °C for Three Obsidians: Orito Quarry (diamond); Mule Creek (square); Coso 4-1 (circle)

To better understand how relative humidity affects the obsidian hydration, we considered water sorption on glass surfaces. The amount of water sorbed onto a sample of Coso 4-1 obsidian was gravimetrically determined as a function of relative humidity at 23 °C.[12] Results are plotted in Fig. III-9. Each point represents the mass of water sorbed onto glass at constant relative humidity. Qualitatively, these results show that RH has a similar relationship for water sorption as we observed for hydration rate (Fig. III-8), namely, that the amount sorbed and the measured rate remain constant up to about 90% RH

but increase at higher relative humidities. Hagymassy et al.[17] have measured similar isotherms for water on a large number of simple oxides, which show that the amount of sorbed water increases above 80% RH.

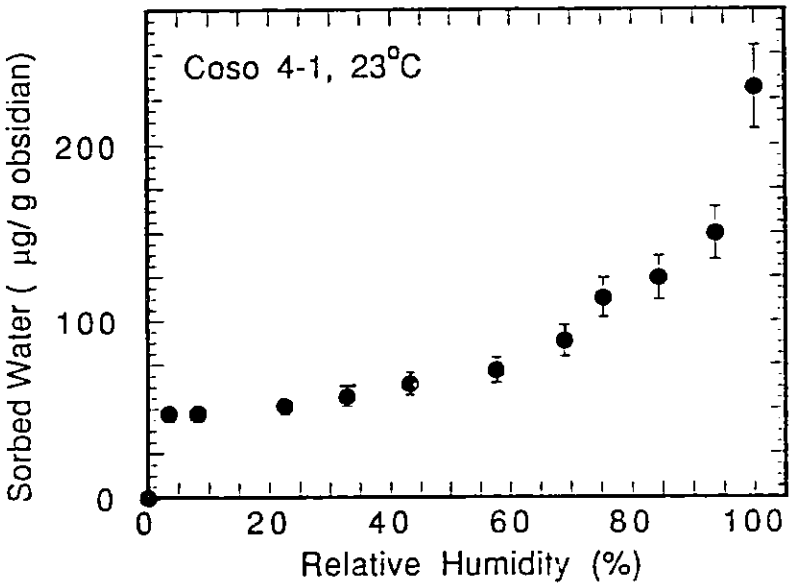

Fig. III-9. Sorption Isotherm Collected at Room Temperature for Coso 4-1 Obsidian (from Ref. 12)

The results suggest that the 50 µg water sorbed onto 100 g glass samples at 3% RH is strongly bonded to surface hydroxyl groups. The amount of sorbed water slowly increases with increasing relative humidity between 3 and about 90% RH. This water forms clusters centered on the hydroxyl groups. Above 90% RH, the amount of sorbed water rapidly increases as the clusters coalesce to form a film covering the entire surface, which corresponds to 4-6 molecular layers of water (monolayers). These results suggest that there is a correspondence between the relative humidity, amount of water sorbed, and the water diffusion rate into the glass. Work is in progress to better understand the compositional effects of obsidians on both their sorptive and reactive properties.

B. Spent Fuel Studies for Yucca Mountain Project

(D. J. Wronkiewicz and E. Veleckis)

The progress made during this reporting period can be subdivided into three related activities: (1) Series 5 spent fuel leach (SFL) tests, (2) tests of matrix dissolution for UO_2 under J-13 water saturated conditions, and (3) unsaturated drip tests between EJ-13 water and UO_2 pellets.

1. Series 5 Spent Fuel Leach Tests

A revised version of the Task Plan for the YMP Series 5 SFL program was completed to conform to new QA Level I formatting rules and to incorporate comments from reviewers. The SFL tests are designed to simulate and monitor the release of radionuclides from spent fuel in the event of possible container breach and infiltration with water. The study is a continuation of previous SFL tests conducted at Hanford Engineering and Development Laboratory in a four series project. The current tests will constitute Series 5 of the project. This test employs a "semi-static" leaching process whereby the bare fuel specimen is immersed in 250 mL of J-13 water within matched stainless steel vessels for periods of up to six months. Both filtered and unfiltered solution analyses are planned for pH and concentrations of

several elements (U, Pu, Am, Np, Cs, Sr, Tc, Se, I, and C). The rate and extent of radionuclide release, under the conditions set by the initial test parameters, will be determined from analytical data collected during the periodic sampling and cycle termination procedures. The experiment was initially slated to begin in early FY 1990, but has been postponed indefinitely due to a directive from LLNL.

2. Saturated Tests with Unirradiated UO_2

Dissolution experiments which utilize a crushed sample obtained from a single UO_2 crystal are planned. This task is designed to investigate the feasibility of using an isotope dilution technique to determine the dissolution rate of a UO_2 matrix in J-13 water. Experimentally, it is similar to the recently completed CMT studies on the dissolution of mixed UO_2 powder in J-13 water (see previous report in this series, Sec. III.B.1). In the present case, however, the solid specimen will consist of homogeneous UO_2 crystals that are crushed to an approximate consistency of the spent fuel. Information gained from these tests will be used to calculate the dissolution rate of the UO_2 matrix based on kinetic models.

The experiments will be carried out in two cycles. In the first cycle, the UO_2 will be leached in pure J-13 water until a steady-state concentration of uranium is established. In the second cycle, the leachant will be replaced with fresh J-13 water that has been spiked with depleted uranium at steady-state concentrations determined from the first cycle. The spiked solution will be assayed for total uranium, ^{235}U, and ^{238}U contents.

Acquisition of pedigreed UO_2 crystals to be used in the tests is being negotiated with J. E. Mendel of the Materials Characterization Center (MCC). Bean-shaped clusters (1/2 to 3/4 in. long) of an old UO_2 melt, showing some single crystal formation, are available. Approximately 100 g of this material will be sent to ANL.

3. Unsaturated Tests with Unirradiated UO_2

A set of experiments, whereby Zircaloy clad-UO_2 pellets have been contacted by dripping EJ-13 water, has been in progress for over 4.5 years. The pellets are cylinders about 1.4 cm in diameter and vary from 0.2 to 3.0 cm in length. The experiments are designed to develop procedures for study of SFL reactions, identify secondary alteration phases, and identify parameters controlling uranium release from the waste package assemblage. The Unsaturated Test Method (Sec. III.A.1) is used with temperatures maintained at 90°C, samples supported by Teflon plates, and variable sample surface areas and water volumes being tested. Four of the original eight experiments have been terminated and the remaining four are continuing.

A pulse of uranium released from the UO_2 solid, combined with the formation of schoepite and dehydrated schoepite ($UO_2 \cdot 2H_2O$ and $UO_2 \cdot 0.8H_2O$, respectively) on the sample surface, characterizes reactions during the first ~30-100 weeks (Fig. III-10). Thereafter, the uranium pulse subsided and a second set of secondary phases formed on the top UO_2 surfaces. These later phases have incorporated cations from the EJ-13 water and include boltwoodite [$K(H_3O)UO_2(SiO_4) \cdot nH_2O$], uranophane [$Ca(UO_2)_2(SiO_3)_2(OH)_2 \cdot 5H_2O$], sklodowskite [$Mg(UO_2)_2(SiO_3)_2(OH)_2 \cdot 5H_2O$], compreignacite [$K_2U_6O_{19} \cdot 11H_2O$], and becquerelite [$CaU_6O_{19} \cdot 10H_2O$]. Nearly all of the uranium leached from the samples was contained in secondary precipitates and/or was sorbed onto the walls of the test vessel.

Experimental results can be described by a sequence of events starting with the oxidative dissolution of the UO_2 matrix and a large pulsed release of uranium from the sample. The alkali/alkaline earth uranyl and uranyl silicate phases that form after ~100 weeks are less soluble than the earlier formed schoepite phases, thus resulting in a decreased rate of uranium release from the sample. The distribution of secondary phases across the sample surface appears to be controlled by the flow patterns of water

across the sample surface. Restricted water flow on the top UO_2 surface, as indicated by clustering of the secondary phases, may facilitate the formation of alkali/alkaline earth uranyl and uranyl silicate phases by allowing evaporative concentration of cations in the EJ-13 water solvent and/or sufficient reaction time for the precipitant phases to form. These experiments will be continued to observe whether any additional phases will form as the reaction process continues.

A second set of four replicate tests has been initiated to investigate reactions between UO_2 pellets and EJ-13 water. This study is similar to that previously described, except that the UO_2 specimens are supported by perforated disks made from 304L stainless steel plates rather than Teflon stands. The study is designed to assess the possible effect of Teflon on uranium mobility and the formation of secondary uranyl phases. After 13 weeks of testing, little reaction occurred except for some dark discoloration of the top UO_2 surfaces. Less than 3 μg of U was released from each of the samples, and cation concentrations of the leachate solutions were relatively unchanged. Based on our results from the previous tests, a large uranium release pulse is not expected until ~26 to 52 weeks.

We are considering additional unsaturated tests that use two alloys (CDA Alloy 715 and Incoloy 825) which are under investigation by the YMP as potential materials for nuclear waste containers. These alloys would be used in the same manner as stainless steel and Teflon plates are used in the present study. These experiments would thus be designed to study interactions between various canister materials and the waste forms, as well as canister compositional effects on uranium mobility and secondary phase formation. Procurement sources for the alloys have been identified, and arrangements have been made for their fabrication to the desired form.

C. Radiation Studies for Yucca Mountain Project

(D. T. Reed)

1. Introduction

The Yucca Mountain Project (YMP) is investigating the feasibility of locating a nuclear high-level waste repository in the tuff formations in southwestern Nevada. The placement of high-level waste containers in the underground facility will perturb the pre-emplacement environment by raising the ambient temperature and exposing the environment to gamma radiation levels that initially may be in excess of 0.1 Mrad/h. The extent of radiolytic alteration of the gas phase present and the nature of the radiolytic products generated are important considerations in evaluating waste package material performance during the early stages of repository history.

The radiation studies being conducted in CMT consist of (1) establishing the extent and nature of radiolytic products generated under repository-relevant conditions, (2) experimentally addressing questionable or unusual results relevant to this task reported in the literature, and (3) performing atmospheric corrosion studies in an irradiated environment.

The emphasis of the radiation studies in this reporting period was on the radiolytic formation of ammonia in oxygen-containing gaseous systems. Three systems were investigated: N_2/H_2 with 0.1% O_2, N_2/H_2O with 0.1% oxygen, and bubbled air.

2. Literature on Radiation Chemistry of Gaseous Ammonia

There has been renewed interest in the gas-phase radiation chemistry of ammonia-containing systems in relation to the performance of copper-based materials in nuclear applications and the E-beam NO_x removal technology. The work being performed at CMT entails evaluating the performance of

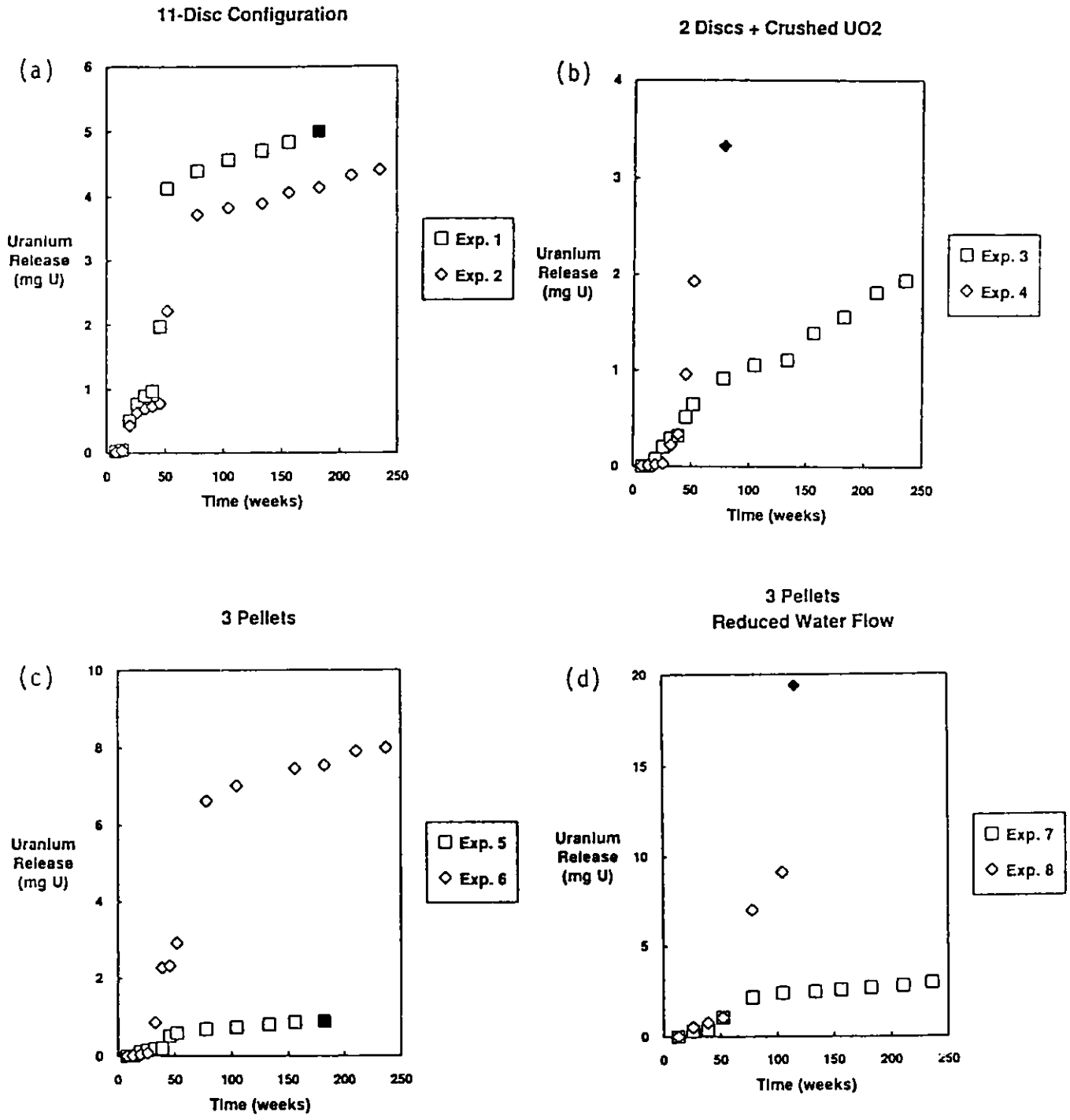

Fig. III-10. Cumulative Release of Uranium from Experiment (a) Nos. 1 and 2 (11 UO_2 disks; 0.075 mL/3.5 day); (b) Nos. 3 and 4 (crushed UO_2 pellet; 0.075 mL 3.5 days); (c) Nos. 5 and 6 (three UO_2 pellets; 0.075 mL/3.5 days); and (d) Nos. 7 and 8 (three UO_2 pellets; 0.0375 mL/7 days). The blocked points indicate that the experiment was terminated.

copper-based materials in irradiated moist-air systems. Ammonia formation in irradiated systems is of concern because ammonia is a known cracking agent for some copper-based materials.

Several studies on the radiation chemistry for ammonia systems have been reported. Schonherr and Schrader[18] reviewed past efforts to establish the steady-state concentrations of ammonia in nitrogen/hydrogen mixtures. The stationary concentration of ammonia formed as the result of radiolysis of a stoichiometric mixture of nitrogen and hydrogen was 4.0 ± 0.1% at doses exceeding 5 x 10^{10} rads. This was set by balancing the net formation and decomposition of ammonia in the system investigated. In radiation chemistry studies of pure ammonia systems,[19,20] the molecular products identified were nitrogen, hydrogen, and, to a much lesser extent, hydrazine. Typical yields (units of molecules/100 eV absorbed dose) obtained were $G(H_2) = 5.0 \pm 1.0$ and $G(N_2) = 1.7 \pm 0.3$, corresponding to $G(-NH_3)$ of 3.4 ± 0.6. Key transients generated in this system are the NH and NH_2 radicals.[21,22]

The effect of oxygen on the formation of ammonia in nitrogen/hydrogen/water vapor systems has, however, not been well established. Oxygen will compete with hydrogeneous species to facilitate the radiolytic oxidation of nitrogen (NO_x formation) rather than its reduction (ammonia formation). This competition has only been studied indirectly. Linacre and Marsh[23] observed the buildup of ammonia in solutions when a mixed-phase deaerated system was irradiated with neutrons and gamma rays. The initial product in this study was NO_x (as dissolved nitrate). In contrast, Sato and Steinberg[24] reported ammonia as the predominant product in gas phase reactions associated with irradiated bubbled-air systems. The role of oxygen, including the ability of oxygen-containing species to inhibit ammonia formation, remains uncertain.

3. Results and Discussion

The objective of our work was to address the following question: can ammonia be generated radiolytically in systems containing oxygen? The three systems studied were (1) 4% H_2O, 96% N_2, 0.1% O_2; (2) 20% H_2, 80% N_2, 0.1% O_2; and (3) air bubbled through 0.1M sulfuric and formic acid.

a. Irradiation of $N_2/H_2O/O_2$ System

The irradiation conditions, the initial and final bulk composition of the gas phase, and the moles of fixation products (ammonia and nitrate) are given in Table III-4 for three runs in the $N_2/H_2O/O_2$ system. The gamma dose rate was between 0.1 and 0.4 Mrad/h, and the absorbed dose was approximately 80 Mrad, corresponding to experiments that were 8-24 days in duration. Experiments were performed in 304L stainless steel vessels at 28 °C (room temperature), 87 °C, and 152 °C. The concentration of the major components in the gas phase was determined by gas chromatography. Fixation products (nitrate, nitrite, and ammonia) were determined by ion-specific electrode analysis of condensate and a rinse of the vessels.

The initial composition of the gas phase was approximately 0.1% oxygen, 4-5% water vapor, and the balance nitrogen. Little change in the nitrogen concentration occurred throughout the course of the irradiation, with approximately 1% being converted to nitrous oxide and NO_x/NH_3. Most of the initial oxygen was converted to nitrous oxide and carbon dioxide (reaction with the stainless steel vessel wall), with some NO_x being formed in the room-temperature experiment. A mass balance analysis indicated that the sum of the oxygen in the oxygen-containing molecular products was greater than that initially present as oxygen. Thus, the water vapor present was an important source of oxygen. It is important to note that oxygen depletion did not occur in any of the three experiments performed.

Table III-4. Irradiation Conditions, Gas Phase Composition, and Moles of Nitrogen Fixation Products in Condensate and Rinse for the $N_2/H_2O/O_2$ System

	AC-1	AC-2	AC-3
Irradiation Conditions			
Temperature, °C	28 ± 2	87 ± 2	152 ± 43
Experiment Duration, h	552.8 ± 0.1	228.9 ± 0.1	212.7 ± 0.1
Dose Rate, Mrad/h	0.13 ± 0.01	0.36 ± 0.02	0.34 ± 0.02
Absorbed Dose, Mrad	72 ± 5	82 ± 5	72 ± 5
Final Composition of the Gas Phase,[a] mol %			
N_2	99.9 ± 0.1	99.8 ± 0.1	99.7 ± 0.1
O_2	0.02 ± 0.005	0.05 ± 0.02	0.06 ± 0.01
N_2O	0.078± 0.005	0.18 ± 0.01	0.12 ± 0.01
CO_2	0.03 ± 0.01	0.03 ± 0.01	0.09 ± 0.01
CO	ND	ND	ND
Fixation Products, mol			
Nitrate in Condensate[b]	$8.2 \pm 0.2 \times 10^{-7}$	$<4 \times 10^{-7}$	$<4 \times 10^{-7}$
Nitrate in Rinse[b]	$<4 \times 10^{-7}$	$<4 \times 10^{-7}$	$<4 \times 10^{-7}$
Ammonia in Condensate	$2.4 \pm 0.2 \times 10^{-7}$	$1.6 \pm 0.1 \times 10^{-7}$	$1.1 \times \pm 0.1 \times 10^{-7}$
Ammonia in Rinse	$1.3 \pm 0.1 \times 10^{-7}$	$1.2 \pm 0.1 \times 10^{-7}$	$1.3 \pm 0.1 \times 10^{-7}$

[a]Initial composition: 99.9 ± 0.1 mol % N_2 and 0.12 ± 0.01 mol % O_2.
[b]A value of $<4 \times 10^{-7}$ mol indicates below detection limits.

With the exception of the room-temperature experiment (AC-1), no nitrate was detected in either the condensate or rinse. This finding suggests that the nitrogen dioxide and nitric/nitrous acid concentrations were not building up as reaction products. In the room-temperature experiment, the nitrate was all in the condensate; thus, the NO_x produced was in gaseous form as either nitric acid or nitrogen dioxide. No nitrite was detected in any of the samples analyzed. At all three test temperatures, significant quantities of ammonia were detected in both the rinse and condensate, with most being in the condensate. Thus, gaseous ammonia was the dominant form of ammonia.

b. Irradiation of $N_2/H_2/O_2$ System

The irradiation conditions, the initial and final composition of the gas phase, and moles of fixation products generated are given in Table III-5 for the experiments involving 0.1% oxygen in an 80% nitrogen-20% hydrogen mixture. The irradiation conditions of these experiments were analogous to those in the $N_2/H_2O/O_2$ experiments.

Gamma irradiation resulted in a decrease of all three of the initial gas components present, even though the data in Table III-5 indicate an apparent increase in mole percent nitrogen. Approximately 10-15% of the hydrogen, over 70% of the oxygen, and less than 1% of the nitrogen initially present were consumed as a result of the gamma radiation absorbed. The nitrogen was primarily converted to ammonia with no detectable amounts of nitrous oxide (<50 ppm) formed. Nitrate may have been observed as a fixation product in the room-temperature experiment, but the response of the ion-specific electrode (ISE) was unusual, leaving open the possibility that another nitrogen oxide species (perhaps nitrite) was present (ammonia does not interfere with the nitrate ISE electrode).

c. Irradiation of Heterogeneous Bubbled Air/Acid Solutions

The results obtained from the gamma irradiation of 0.1N sulfuric and formic acid solutions in the presence of bubbled air are shown in Tables III-6 and -7, respectively. The experimental setup was not designed to trap the irradiation products formed in the gas phase and carried away by the outgoing air. Also shown in the same tables are some data obtained in the absence of bubbled air.

Table III-5. Irradiation Conditions, Gas Phase Composition, and Moles of Nitrogen Fixation Products in Condensate and Rinse for the $N_2/H_2/O_2$ System

	AA-1	AA-2	AA-3
Irradiation Conditions			
Temperature, °C	28 ± 2	87 ± 2	152 ± 3
Experiment Duration, h	577.6 ± 0.1	228.9 ± 0.1	236.4 ± 0.1
Dose Rate, Mrad/h	0.14 ± 0.01	0.36 ± 0.02	0.36 ± 0.02
Absorbed Dose, Mrad	81 ± 5	82 ± 5	85 ± 5
Final Gas Phase Composition,[a] mol, %			
N_2	82.1 ± 0.3	83.6 ± 0.3	82.0 ± 0.3
H_2	17.9 ± 0.3	16.4 ± 0.3	17.9 ± 0.3
O_2	0.011 ± 0.002	0.004 ± 0.001	0.024 ± 0.002
N_2O	ND	ND	ND
CO_2	0.012 ± 0.003	0.008 ± 0.003	0.085 ± 0.003
CO	ND	ND	ND
Condensable Fixation Products, mol			
Nitrate in Condensate	3.9×10^{-6}	$<5 \times 10^{-7}$	$<5 \times 10^{-7}$
Nitrate in Rinse	$<5 \times 10^{-7}$	$<5 \times 10^{-7}$	$<5 \times 10^{-7}$
Total Nitrite	ND	ND	ND
Ammonia in Condensate	1.8×10^{-6}	9.3×10^{-7}	2.5×10^{-6}
Ammonia in Rinse	4.8×10^{-6}	4.8×10^{-6}	3.4×10^{-6}

[a]Initial composition for all three runs: 80.5 ± 0.3 mol % N_2, 19.4 ± 0.3 mol % H_2, 0.10 ± 0.005 mol % O_2.

In the case of sulfuric acid, the concentration of ammonia increases fairly linearly with dose up to ~11.5 Mrad and then remains constant. Although this trend is similar to that seen by Sato and Steinberg[24] under almost similar experimental conditions, the maximum ammonia concentrations obtained in our experiments is much lower than their value (0.12 ppm as N instead of 1.0 ppm as N). In addition, the bubbled-air experiments yielded lower ammonia concentrations than unbubbled experiments. This observation and the appreciable production of nitrate, especially at high doses, in our bubbled-air experiments are in sharp contrast to the observations made by Sato and Steinberg.[24]

The irradiation of 0.1N formic acid solution in the presence of bubbled air was reported by Sato and Steinberg[24] to yield a maximum of 2.5 ppm of ammonia as N. At a dose rate of 2.5 Mrad/h in their experiments, the ammonia concentration reached this value after ~4 h and then decreased to almost zero on further irradiation. The results shown in Table III-7, however, clearly indicate that ammonia concentration becomes measurable only at doses exceeding ~14 Mrad, with no decrease seen upon further irradiation up to ~22 Mrad. The maximum amount of ammonia seen here (0.02 ppm as N) is also much less than Sato and Steinberg's value. In agreement with the results in the sulfuric acid system, higher production of ammonia occurs in the absence of bubbled air than in its presence. Of the two acid systems studied, the highest production of nitrate occurs in formic acid solutions under unbubbled conditions.

Table III-6. Ammonia and Nitrate Concentrations Obtained from 0.1N Sulfuric Acid Solutions Gamma-Irradiated at 25 °C in the Presence and Absence of Bubbled Air. Dose rate ~ 0.1 Mrad/h.

System	Abs. Dose, Mrad	$[NH_3]$ ppm as N	$[NO_3^-]$ ppm as N
Bubbled Air/	2.5	0.03	<0.10
Acid Solution[a]	5.4	0.06	<0.10
	11.5	0.12	0.30
	21.0	0.12	0.59
Air-Saturated	2.3	0.04	<0.10
Acid Solution[b]	4.8	0.04	<0.10
	10.4	0.16	<0.10
	18.9	0.21	<0.10

[a]Air flow rate of 48.8 mL/min.
[b]Irradiated in a 100 mL syringe.

Table III-7. Ammonia and Nitrate Concentrations Obtained from 0.1N Formic Acid Solutions Gamma-Irradiated at 25 °C in the Presence and Absence of Bubbled Air. Dose rate ~ 0.20 Mrad/h.

System	Abs. Dose, Mrad	$[NH_3]$ ppm as N	$[NO_3^-]$ ppm as N
Bubbled Air/	3.6	<0.01 (0.01)[a]	<0.10 (1.20)[a]
Acid Solution[b]	5.6	<0.01	<0.10
	14.2	0.01 (0.06)[a]	<0.10 (2.50)[a]
	22.1	0.02	<0.10

[a]Values in parentheses were obtained in the absence of bubbled air, but the solution was in contact with room air during the entire irradiation period.
[b]Air flow rate of 48.8 mL/min.

4. Conclusions

The experiments completed to date consistently show that ammonia can be generated radiolytically when oxygen is present. The yields observed for the systems studied are given in Table III-8. In the $N_2/H_2/O_2$ mixture, ammonia was the only nitrogen fixation product observed and had a yield that ranged between 0.7 and 0.9 per 100 eV absorbed dose. When 20% hydrogen was replaced with 4% water, both nitrous oxide and ammonia were observed. The presence of nitrous oxide points to the initial formation of nitrogen dioxide since it is a precursor to nitrous oxide. Ammonia yields were substantially lower in the $N_2/H_2O/O_2$ system, ranging between 0.03 and 0.045 per 100 eV absorbed dose. Ammonia was also observed in the the bubbled-air system, confirming the observations reported by Sato and Steinberg,[24] although the yields we observed were consistently lower.

Table III-8. Yield of Nitrogen Fixation Products in $N_2/H_2/O_2$ and $N_2/H_2O/O_2$ Gaseous Systems

Environment	Experimental Designation	Yield, molecules/100 eV		
		Nitrate	N_2O	Ammonia
0.1% O_2 in N_2/H_2O	AC-1	0.1[a]	0.36 ± 0.03	0.045 ± 0.01
	AC-2	<0.06	0.73 ± 0.03	0.03 ± 0.01
	AC-3	<0.06	0.55 ± 0.03	0.03 ± 0.01
0.1% O_2 in N_2/H_2	AA-1	0.51[a]	<0.02	0.85 ± 0.05
	AA-2	<0.06	<0.02	0.73 ± 0.05
	AA-3	<0.06	<0.02	0.73 ± 0.05

[a]Analysis for nitrate was not definitive. This could be an as-yet unknown nitrogenous product.

The results just summarized clearly indicate that hydrogen and/or hydrogeneous transients compete much more effectively with oxygen for atomic nitrogen than previously believed. Further gamma studies are in progress with emphasis on the formation of ammonia as a function of the H_2O vapor/oxygen ratio.

D. Glass Studies for Defense Programs
(J. K. Bates, T. J. Gerding, J. E. Young)

1. Product Consistency Test

The Product Consistency Test (PCT) was developed by Savannah River Laboratory (SRL) to provide confirmation of the consistency of radioactive glass produced by the glass melter of the Defense Waste Processing Facility (DWPF), at Westinghouse Savannah River Co. Three glasses supplied by SRL have been tested: two radioactive, one nonradioactive. The radioactive glasses were designated Can 50 and 165/TK8, and the nonradioactive glass was a sample of ARM-1 glass. The radiation levels associated with the radioactive glasses required that many of the test-related operations be conducted in a shielded facility equipped with remote handling capabilities.

The guidelines for the test procedure were provided by SRL.[25] Implementing the SRL procedure required modifying existing sections and then adding new sections. The purpose of our tests was to evaluate the utility of the procedure in remote facilities. Our results will be compared to results obtained by SRL using the same glass compositions and same procedures.

The PCT procedure calls for reacting (in triplicate) 1.5 g of powdered glass with 15 mL of deionized water (DIW) for seven days at 90°C. At the end of this period, the test solutions are analyzed for glass cations and radionuclides, and the pH is determined. A measure of the sensitivity of the test is whether the solution results for different glasses are different after the seven-day period.

The results of the tests are presented in Tables III-9 through III-13. Table III-9 gives the general test matrix together with results for pH and carbon analyses. Concentration results are given for glass-forming cations in Table III-10, fission-product radionuclides in Table III-11, transuranic elements in Table III-12, and strontium in Table III-13. The results indicate that good precision was obtained for the replicate samples and that the PCT test could distinguish between the different glasses.

Table III-9. Carbon Analysis and pH Results for Glasses Undergoing Radioactive Product Consistency Tests

December 1, 1988 (1409 h) to December 8, 1988 (1209 h)
Temperature 90°C

PCT No.	Vessel No.	Sample Type	Sample Weight, g	DIW Wt., g	Weight Loss, g	Leachate Recovered, g	pH	Carbon Content, ppm		
								Total	Organic	Inorganic[a]
5	182	Blank	-	15.0586	0.0254	14.8857	5.82	0.999	1.739	-0.740[b]
9	192	Blank	-	15.0460	0.0205	14.7884	4.12	1.038	1.409	-0.371[b]
2	183	ARM-1	1.5018	15.0425	0.0307	14.0897	9.56	4.224	2.501	1.723
10	184	ARM-1	1.5089	15.0001	0.0415	14.1210	9.57	3.802	2.133	1.669
4	185	ARM-1	1.5004	15.1584	0.0043	14.1712	9.54	3.989	2.029	1.960
1	186	Can 50	1.5014	15.1070	0.0168	14.0062	9.90	4.758	2.441	2.317
11	187	Can 50	1.5120	15.0505	0.0301	14.0841	9.84	3.416	2.029	1.387
7	188	Can 50	1.5014	15.0237	0.0050	14.1273	9.87	4.935	2.322	2.613
3	189	165/TK8	1.5043	15.1278	0.0482	14.0852	9.33	3.431	1.392	2.039
8	190	165/TK8	1.5093	15.1307	0.0434	14.0387	9.30	3.436	1.570	1.866
12	191	165/TK8	1.5207	15.1752	0.346	14.1400	9.31	2.974	1.370	1.667

[a]Inorganic carbon is calculated by subtracting the amount of organic carbon from that of the total carbon.
[b]Negative results indicate organic carbon present in H_3PO_4 acid used to purge inorganic carbon during analysis.

Table III 10. Filtered Leachate Concentrations for Radioactive Product Consistents Tests

Sample Name	pH Values	Leachate Concentration,[a,b] ppm Al	B	Fe	K	Na	Si	Sr	Li
1.5 Grams of 100-200 Mesh Washed ARM-1 Glass in 15 mL of DIW in Stainless Steel Vessels T = 90°C, t = 7 Day									
PCT 2	9.56	4.9	22	0.00	0.00	46	64	0.010	17
PCT 4	9.54	5.2	22	0.00	0.00	46	64	0.011	16
PCT 10	9.57	5.4	22	0.00	0.00	47	63	0.012	16
Average	9.56	5.2	22	-	-	46	64	0.011	16
Std. Dev.	0.02	0.3	0	-	-	0.6	0.6	0.001	0.6
RSD, %	0.21	5.26	0	-	-	1.30	0.93	9.09	3.75
1.5 Grams of 100-200 Mesh Washed Can 50 Glass in 15 mL of DIW in Stainless Steel Vessels T = 90°C, t = 7 Day									
PCT 1	9.90	6.6	27	4.4	17	91	84	0.00	12
PCT 7	9.87	7.2	28	4.1	17	92	84	0.00	13
PCT 11	9.84	7.4	28	4.2	16	93	85	0.00	13
Average	9.87	7.1	28	4.2	17	92	84	-	13
Std. Dev.	0.03	0.4	0.6	0.2	0.6	1.0	0.6	-	0.6
RSD, %	0.30	5.63	2.14	4.76	3.53	1.09	0.71	-	4.62
1.5 Grams of 100-200 Mesh Washed 165/TK8 Glass in 15 mL of DIW in Stainless Steel Vessels T = 90°C, t = 7 Day									
PCT 3	9.33	21	8.7	3.6	0.00	28	74	0.014	11
PCT 8	9.30	22	8.2	3.3	0.00	27	70	0.012	11
PCT 12	9.31	22	8.5	3.3	0.00	27	70	0.012	11
Average	9.31	22	8.5	3.4	-	27	71	0.013	11
Std. Dev.	0.02	0.6	0.3	0.2	-	0.6	2.3	0.001	0
RSD, %	0.22	2.72	3.53	5.88	-	2.22	3.24	7.69	0
15 mL of DIW in Stainless Steel Vessels									
PCT 5	5.82	0.00	0.00	0.00	0.00	0.00	0.00	0.00	0.00
PCT 9	4.12	0.00	0.00	0.00	0.00	0.00	0.00	0.00	0.00
Average	4.97								
Std. Dev.	1.20								
RSD, %	24.15								
Analytical Detect. Limits[c]		0.1	0.02	0.01	0.5	0.05	0.05	0.0025	0.015

[a]Values listed as 0.00 in the table are less than the detection limit.

[b]These values were determined from dilute HNO_3 strip of vessels at 90°C for ~16 h.

[c]Detection limits are 5x background.

Table III-11. Radionuclide Concentrations[a] in Leachate from Radioactive Product Consistency Tests

Exp No.	Glass Type	^{57}Co		^{60}Co		^{125}Sb		^{134}Cs	
		dpm/mL	mCi/mL	dpm/mL	mCi/mL	dpm/mL	mCi/mL	dpm/mL	mCi/mL
PCT 1	Can 50	37 ± 7	1.7E-8	130 ± 10	5.9E-8	805 ± 57	3.63E-7	32 ± 5	1.4E-8
PCT 7	Can 50	40 ± 7	1.8E-8	108 ± 12	4.9E-8	775 ± 62	3.5E-7	50 ± 10	2.3E-8
PCT 11	Can 50	45 ± 10	2.0E-8	125 ± 13	5.6E-8	780 ± 55	3.5E-7	42 ± 8	1.9E-9
Avg.		41		121		787		41	
Std. Dev.		4.0		11		16		9.0	
RSD, %		9.8		9.1		2.0		22	
PCT 3	165/TK8	0.00		538 ± 38	2.4E-7	1607 ± 177	7.2E-7	0.00	
PCT 8	165/TK8	0.00		543 ± 38	2.4E-7	1578 ± 173	7.1E-7	0.00	
PCT 12	165/TK8	0.00		502 ± 30	2.3E-7	1565 ± 142	7.1E-7	0.00	
Avg.		-		528		1583		-	
Std. Dev.		-		22		22		-	
RSD, %		-		4.2		1.4		-	

Exp No.	^{137}Cs		^{154}Eu		^{155}Eu		^{241}Am	
	dpm/mL	mCi/mL	dpm/mL	mCi/mL	dpm/mL	mCi/mL	dpm/mL	mCi/mL
PCT 1	6483 ± 267	2.9E-6	65 ± 23	2.9E-8	55 ± 8	2.5E-8	60 ± 10	2.7E-8
PCT 7	6225 ± 250	2.8E-6	0.00		0.00		75 ± 12	1.4E-8
PCT 11	6317 ± 250	2.8E-6	0.00		82 ± 25	3.7E-8	57 ± 12	2.6E-8
Avg.	6342		22		46		64	
Std. Dev.	130		38		42		9.6	
RSD, %	2.0		173		91		15	
PCT 3	11967 ± 483	5.4E-6	4133 ± 212	1.9E-6	908 ± 63	4.1E-7	347 ± 38	1.6E-7
PCT 8	11728 ± 483	5.3E-6	4032 ± 242	1.8E-6	995 ± 50	4.3E-7	344 ± 38	1.6E-7
PCT 12	11548 ± 462	5.2E-6	4267 ± 213	1.9E-6	970 ± 58	4.4E-7	332 ± 37	1.5E-7
Avg.	11748		4144		958		341	
Std. Dev.	210		118		45		7.9	
RSD, %	1.8		2.8		4.7		2.3	

[a]These values were determined from dilute HNO_3 strip of vessels at 90°C for ~16 h. The abbreviation dpm/mL = disintegrations per minute per milliliter.

Table III-12. Actinide Concentration in Leachate[a] from Radioactive Product Consistency Tests

Exp No.	Glass Type	Pu-238		Pu-239		Cm-244	
		mCi/mL	mCi Tot.	mCi/mL	mCi Tot.	mCi/mL	mCi Tot.
PCT 3	165/TK8	2.53E-6	3.56E-5	0	0	7.98E-8	1.12E-6
PCT 8	165/TK8	2.62E-6	3.68E-5	0	0	1.39E-7	1.95E-6
PCT 12	165/TK8	2.36E-6	3.33E-5	1.01E-7	1.43E-6	1.57E-7	2.22E-6
Avg.		2.50E-6		3.37E-8		1.25E-7	
Std. Dev.		1.32E-7		5.83E-8		4.40E-8	
RSD, %		53		173		32	
PCT 1	Can 50	3.04E-7	4.26E-6	2.06E-8	2.88E-7	1.30E-6	1.82E-5
PCT 7	Can 50	1.26E-7	1.79E-5	1.18E-8	1.67E-7	1.36E-6	1.92E-5
PCT 11	Can 50	4.34E-7	6.12E-6	0	0	1.06E-6	1.50E-5
Avg.		2.88E-7		1.08E-8		1.24E-6	
Std. Dev.		1.55E-7		1.03E-8		1.59E-8	
RSD, %		54		95		1.3	

[a]These values were determined from alpha counting 10 μL of leachant. No separations were performed on the samples. Because some peaks were not resolved 100%, these peaks were estimated based on linear extrapolation for background subtraction.

Table III-13. Radioactive Strontium Concentration in Product Consistency Test

Exp No.	Glass Type	^{90}Sr dpm/mL	^{90}Sr mCi/mL
PCT 1	Can 50	3.96E3	1.78E-6
PCT 7	Can 50	4.34E3	1.96E-6
PCT 11	Can 50	3.93E3	1.77E-6
PCT 3	165/TK8	2.19E5	9.87E-5
PCT 8	165/TK8	1.94E5	8.74E-5
PCT 12	165/TK8	1.92E5	8.65E-5

2. Defense Waste Glass Studies

The DWPF is scheduled to begin production of radioactive glass early in the 1990s. Prior to startup, the glass producers must demonstrate that they can produce a consistent product, and DOE must indicate how the glass will perform in the storage environment. To assist with the second requirement, we are undertaking two tasks: (1) critical review of parameters that affect glass reaction in an unsaturated environment and (2) long-term testing of fully radioactive glasses made from actual waste taken from the Westinghouse Savannah River Co.

a. Critical Review

The predicted repository environment at Yucca Mountain has been described by the YMP as hydrologically unsaturated with possible air exchange with the neighboring biosphere. We have identified several environmental conditions which may affect the durability of waste emplaced in such an environment over repository-relevant time periods and have reviewed the existing literature to evaluate the state of knowledge regarding the influence of these conditions on the glass reaction. Commonly used experimental methods were also critically analyzed to determine if the data produced will be useful in characterizing the waste stability in the YMP repository.

Although large amounts of liquid water are not expected to contact the waste during the repository lifetime, water vapor or small volumes of transient water may contact the waste at any time after emplacement. We have identified the amount of water contacting the glass waste to be a primary parameter affecting the waste durability. Other primary parameters identified are the waste temperature, radiation fields, glass composition, and secondary or alteration phases that form during glass hydration.

Several conclusions were drawn from our critical review of published results relevant to the influence of these environmental parameters on the glass reaction:

1. A number of empirical models have been proposed to correlate glass composition to the release rate of an element (usually silicon) in a standard leach test. With some ad hoc adjustments, these models can usually predict reaction trends of various glass compositions.

2. Alpha and beta decay may destabilize solid matrices and so reduce durability. Gamma fields produce nitric acid in moist air, which will acidify any liquid water that may accumulate.

3. The glass reaction rate increases with temperature. The stability of secondary phases may be sensitive to temperature.

4. The glass SA/V ratio is an important parameter in leaching tests. A high SA/V ratio is often used to accelerate the approach to leachate saturation, although the glass reaction rate is not itself increased. Difficulties may arise due to complicated pH effects.

5. The glass reaction increases with the relative humidity. The reaction occurs in a thin film of condensed water and results in a very high SA/V ratio. Precipitates may form after only a few days at elevated temperatures due to saturation of the solution after very little glass has reacted.

6. Precipitates or reacted layers may impede the ingress of water and so quench the reaction.

The major conclusion of this study is that, while useful data exist for describing glass behavior in water-saturated systems, few experiments besides those performed in CMT give insight into the reaction in water vapor.

b. Long-Term Leach Tests

Long-term leach tests of glass will be performed using fully radioactive glass produced by mixing glass frit with sludge taken from high-level-waste storage tanks at Savannah River. To prepare for these tests, hot cells at CMT were adapted for glass preparation and testing. Additionally, methods to analyze the reacted glass structure were developed.

The long-term performance of a nuclear waste repository is determined by the stability of the waste form and the mobility of radionuclides contained in the glass. The technique of analytical electron microscopy (AEM) provided the first comprehensive identification of the secondary mineral phases formed during simulated terrestrial weathering of nuclear waste glasses. This technique combines transmission electron microscopy and supporting spectroscopic methods. Data from AEM analysis allow one to obtain a complete description of the reacted glass, from the outermost surface in direct contact with the leachant solution to the reacting front that migrates into the bulk glass.

We have performed SEM and AEM analyses of SRL 131 glass that had been reacted for 546 days at 90°C in deionized water. Figure III-11 shows that six distinct layers form on the glass. For example, manganese and iron oxyhydroxide phases and saponite are precipitated onto the residual glass surface from the leachant solution. In addition, smectites (layers 2 and 3), serpentine (layers 2 and 3), and manganese and uranium-titanium oxyhydroxide layers (layer 1) formed in situ within the glass residual layers, as shown in Fig. III-12. Such detailed analysis of the reacted surface region is very helpful in understanding the glass reaction process.

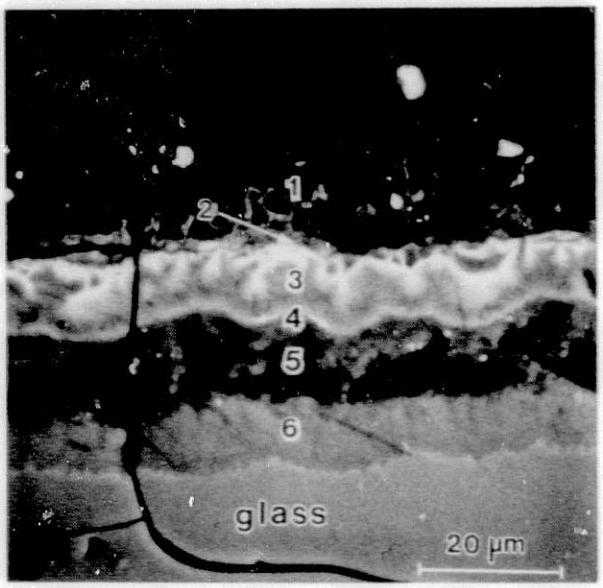

Fig. III-11.

Glass Mixed with Radionuclides and Exposed to Weathering Conditions. Six layers of minerals formed, as shown by numbers 1-6.

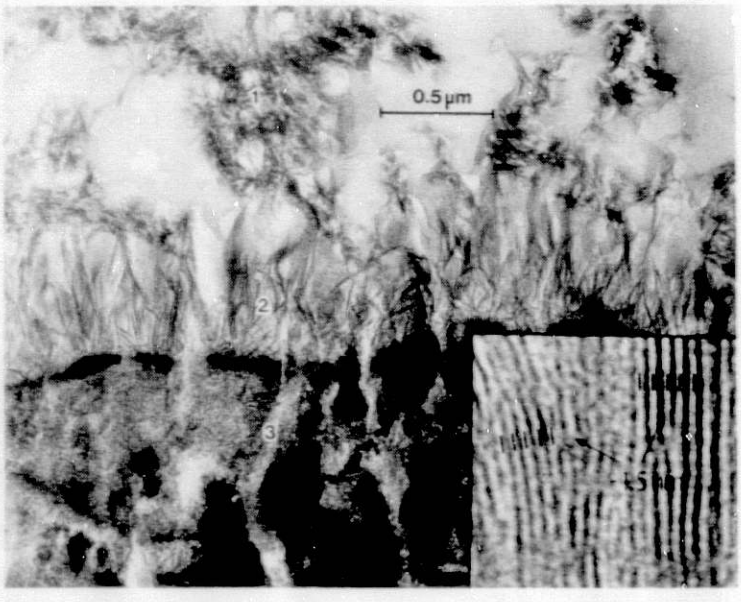

Fig. III-12. High-Resolution Imaging of the First Three Layers of the Glass in Fig. III-11. Inset: a close-up of the second layer's structure

E. Detection and Speciation of Transuranic Elements

(S. Okajima and D. T. Reed)

The detection and speciation of radionuclides in both groundwater systems and systems relevant to their process chemistry are currently receiving considerable attention within DOE. Current emphasis is on evaluating the suitability of the Yucca Mountain site for high-level nuclear waste disposal, determining the near-surface migration and transport of radionuclides at various DOE sites, and minimizing the waste in fuel reprocessing streams by improving on-line monitoring techniques.

At ANL, we have developed and applied both laser photoacoustic spectroscopy (LPAS) and laser-induced fluorescence (collaborative effort with the ANL Chemistry Division) to the detection of radionuclides in systems of interest to DOE. A single-beam differential LPAS system has been assembled within CMT. The details of the system were described previously.[26] The work in this reporting period was focused on continued development of the LPAS technique, with specific emphasis on improving the spectral sensitivity and stability of the LPAS system at temperatures up to 90°C.

1. LPAS Signal Response as a Function of Temperature

Photoacoustic theory for aqueous solutions[27] predicts that the LPAS signal, at elevated temperatures, will be enhanced compared to that at ambient temperature. To test the existing theory, we recorded the LPAS signal of Ho^{3+} in dilute perchloric acid (1.3×10^{-3}M Ho^{3+} in 0.1M $HClO_4$) at 30-90°C. Figure III-13 presents the observed LPAS enhancement with increasing temperature recorded for the Ho^{3+} peak at 485 nm wavelength. The observed LPAS signal was corrected for laser energy fluctuation and normalized to one at 30°C. The enhancement at 90°C (relative to 30°C) is 25% less than theoretically expected.[27] The lower-than-expected LPAS enhancement was most likely due to a reduction in Ho^{3+} peak molar absorbance with increasing temperature. This was experimentally supported by the observed increase in peak width at 90°C.

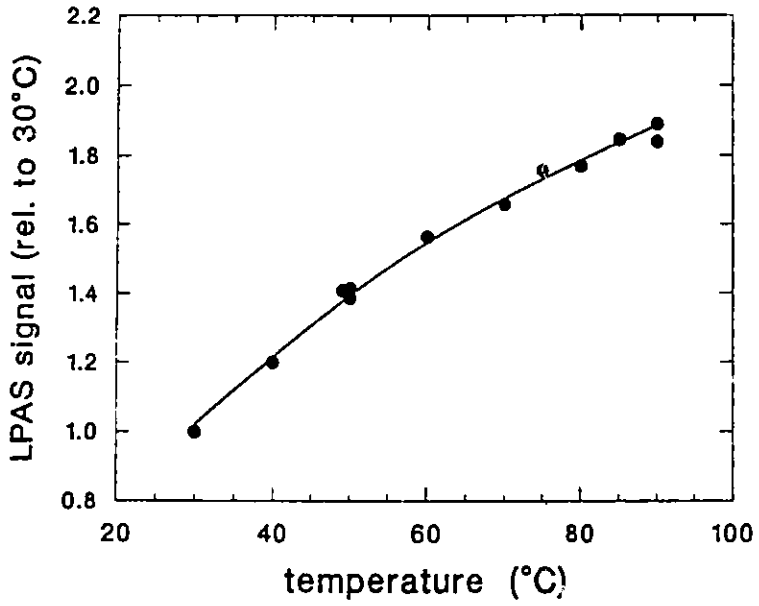

Fig. III-13. Observed LPAS Signal Amplitude at the 485 nm Peak of Ho^{3+} vs. Temperature from a 1.3×10^{-3}M Ho^{3+} in 0.1M $HClO_4$ Solution. Signal normalized to one at 30°C.

In our present LPAS system, a fused silica rod (1-cm dia, 10-cm long) was used to make an acoustic connection between the sample cell and a piezoelectric transducer (PZT). To determine the influence of heat conducted from the sample to the PZT element through the fused silica rod, nitrogen gas was flowed over a portion of the fused silica rod while the LPAS signal amplitude was recorded at fixed laser wavelength for a Ho^{3+}-containing solution held at 90°C. The signal amplitude was found to be independent of gas flow, establishing that transducer heating by conduction through the fused silica rod was not significant.

2. Applicability to On-Line Detection of Uranyl in Nitric Acid Systems

To evaluate the applicability of LPAS to quantitatively analyze uranyl in effluent waste, we investigated the LPAS spectrum of uranyl in nitric acid systems (16 M and 8 M) and water. The laser wavelength range used was 460 to 500 nm, which corresponds to the relatively weak first and second vibrational bands of the uranyl charge-transfer absorption band. The LPAS detection limit for uranyl was estimated to be at least 100 times better than that of more conventional absorption spectroscopy.

Figure III-14 presents the laser pulse energy vs. observed LPAS signal amplitude for uranyl in 8 M nitric acid. The increase in the LPAS signal amplitude is not linear with increasing laser pulse energy. Similar nonlinearity was observed with uranyl in water and 16 M nitric acid. Further analysis of the data in Fig. III-14 indicated that this nonlinearity was due to the increasing importance of two-photon absorption in uranyl at the higher laser pulse energies. The two-photon process responsible for the observed nonlinearity in LPAS signal generation was attributed to the transient absorption that has been observed in flash photolysis investigations.[28]

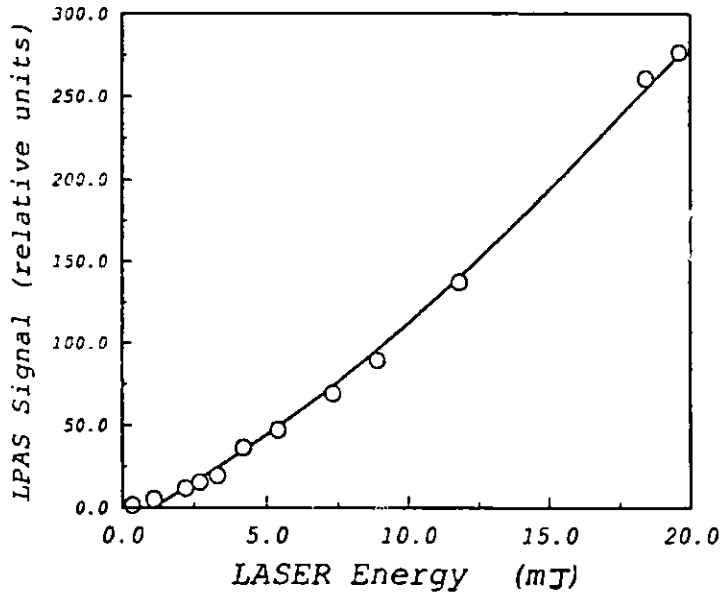

Fig. III-14. Observed LPAS Signal Amplitude at 470 nm vs. Laser Pulse Energy. The sample is 10^{-3}M uranyl in 8M HNO_3 solution.

It is expected that the observed multiphoton process will lead to increased LPAS sensitivity. In the case of uranyl, the LPAS signal amplitude increased by a factor of six due to the presence of the two-photon process. Further investigations into the use of multiphoton processes to improve LPAS sensitivity are underway.

F. Experimental Validation of Performance Assessment for Repository Technology Program
(J. K. Bates and T. A. Abrajano, Jr.)

The objective of this effort for the Repository Technology Program (RTP) is to develop a strategy for validating performance-assessment modeling codes for near-field waste package/groundwater interactions over a range of conditions applicable to the proposed Yucca Mountain repository site. One validation approach is to conduct experimentation based on a laboratory analogue or integrated test methodology, followed by comparison of the experimental results with those predicted by model calculations. Such an approach appears straightforward, but since experimentation is used for both model development and model validation, a clear distinction between the experiments must be maintained such that input used for generating models is not the same input that is used for validating models.

The basis for near-field performance assessment depends on the coupling of sub-models that describe three events: ingress of groundwater, reaction of groundwater with the waste package, and transport of radionuclides through the near-field environment. The experimental strategy revolves around (1) identifying those independent variables that affect each of the three events, (2) identifying the dependent variables that describe the data needs to assess the repository performance, (3) simplifying the overall approach through the use of bounding assumptions, and (4) establishing whether the dependent and independent variables can be measured and/or controlled during experimentation.

Although sub-models for each of the three events are still undergoing development, the dependent and independent variables for each can be identified along with the processes involved (see Table III-14). The effect of all the independent variables on the resultant processes is not known, and a final description is not available concerning either the materials that will comprise the repository (i.e., waste package materials and host rock) or the environment of the waste package and near field. However, enough information is available to allow the validation strategy development to proceed.

The next step is simplification of the experimental strategy by restricting or eliminating independent variables for each of the three events. The types of simplifications that are appropriate for initial model validation experiments are as follows:

1. Control the volume of water available for waste form reaction by experimentally establishing either saturated conditions (the waste package inundated with liquid water) or unsaturated conditions (no direct liquid flow pathway from the waste package to the rock).

2. Fix the composition of the solution contacting the waste package. For example, use J-13 water or J-13 water equilibrated with tuff at the test temperature.

3. Maintain the test at a fixed temperature, excluding localized waste-form heating.

4. Eliminate the container material and associated corrosion products.

5. Induce or accelerate fracture or matrix flow for radionuclide transport by the spatial arrangement of the test components.

6. Use waste forms (glass or spent fuel) that have the poorest performance with respect to radionuclide release.

7. Use waste forms that have not been subjected to aging.

8. Measure only the quantitative release of radionuclides in solution (as opposed to determining the chemical species in solution).

9. Provide as input to the radionuclide transport only the total radionuclide content of the solution (no speciation or fractionation between colloidal and soluble species).

10. Assume that the experimental parameters required to model radionuclide transport are constant with respect to samples of tuff taken from localized areas of the repository horizon. This allows one tuff core to be used in validation testing, while another tuff core is used to measure the independent variables. An alternative simplification would be to assume that crushed tuff could be used in place of tuff core in both modeling and experimentation.

Table III-14. Independent and Dependent Variables Affecting Near-Field Performance

Events	Interactions	Independent Variables[a]	Processes[b]	Dependent Variable
Groundwater Ingress	Rock/Water/Air/ Other Materials	Temperature, time, radiation, rock composition, initial water composition, degree of saturation, other materials	Devitrification hydration, chemical reaction	Solution composition contacting waste
Waste Package Reaction	Humid Air/Metal/ Waste Form/Liquid Water/ Other Materials	Solution composition in, temperature, time, radiation, relative humidity, metal composition and treatment, waste form composition, surface area, volume of water, localized redox environment, nature of reacted layers, glass devitrification, surface roughness, pH, gas composition water flow, glass stress	Metal corrosion, hydration, dissolution, ion exchange	Solution composition after reaction with waste
Radionuclide Transport	Rock/Water/Air/ Radionuclides	Solution composition in, K_d, D_{app}, Pr, γ, b, v_x, hydrodynamic dispersion coefficients, degree of saturation, speciation of radionuclides	Dissolution, complexation, ion exchange, sorption, precipitation	Solution composition after near-field

[a]Symbols are defined as follows:

v_x = average linear velocity of groundwater flow
D_{app} = diffusion coefficient for each radionuclide
K_d = distribution coefficient for each radionuclide
Pr = density of rock
b = fracture half width
γ = radionuclide decay constant

[b]The processes listed are demonstrative and may not be inclusive.

REFERENCES

1. J. K. Bates and T. J. Gerding, *NNWSI Phase II Materials Interaction Test Procedure and Preliminary Results*, Argonne National Laboratory Report ANL-84-81 (1985).

2. J. K. Bates and T. J. Gerding, *One-Year Results of the NNWSI Unsaturated Test Procedure: SRL 165 Glass Application*, Argonne National Laboratory Report ANL-85-41 (1986).

3. J. K. Bates, T. J. Gerding, T. A. Abrajano, and W. L. Ebert, *NNWSI Waste Form Testing at Argonne National Laboratory, Semiannual Report January-June 1986*, Lawrence Livermore National Laboratory Report UCRL-15801-86-1 (1987).

4. J. K. Bates and T. J. Gerding, *Application of the NNWSI Unsaturated Test Method to Actinide Doped SRL 165 Type Glass*, Argonne National Laboratory Report ANL-89/24 (in press).

5. D. M. Strachan, B. O. Barnes, and R. P. Turcotte, "Standard Leach Tests for Nuclear Waste Materials," in *Scientific Basis for Nuclear Waste Management*, Vol. 3, ed., T. G. Moore, Plenum Press, New York, pp. 347-354 (1988).

6. R. F. Bartholomew, P. A. Tick, and S. D. Stookey, "Water/Glass Reactions at Elevated Temperatures and Pressures," J. Non-Cryst. Solids 18&19, 637-642 (1980).

7. T. Yoko, Z-J. Huang, K. Kamiya, and S. Sakka, "Hydration of Silicate, Phosphate, and Borate Glasses in an Autoclave," Rivista della Staz. Sper. Vetro, No. 5, pp.99-104 (1984).

8. T. A. Abrajano, Jr., J. K. Bates, and J. J. Mazer, "Aqueous Corrosion of Natural and Nuclear Waste Glasses. II. Mechanisms of Vapor Hydration of Nuclear Waste Glasses," J. Non-Cryst. Solids 108, 269-288 (1989).

9. M. Tomozawa, S. Ito, and J. Molinelli, "Hygroscopicity of Glasses with High Water Content," J. Non-Cryst. Solids 64, 269-278 (1984).

10. H. Tomozawa and M. Tomozawa, "Diffusion of Water in Borosilicate Glass," J. Non-Cryst. Solids 109, 311-317 (1989).

11. I. Friedman and R. L. Smith, "A New Dating Method Using Obsidian, Part 1: The Development of the Method," Am. Antiq. 25(4), 476-533 (1960).

12. W. L. Ebert, R. F. Hoburg, and J. K. Bates, "The Sorption of Water on Obsidian and a Nuclear Waste Glass," *Phys. Chem. of Glasses* (in press).

13. C. M. Stevenson, W. Freeborn, and B. E. Scheetz, "Obsidian Hydration Dating: An Improved Optical Technique for Measuring the Width of the Hydration Rim," Archaeometry 29, 120-123 (1987).

14. P. G. Jeffery and D. Hutchinson, *Chemical Methods of Rock Analysis*, 3rd Ed., Pergamon Press, New York (1981).

15. I. Friedman, R. L. Smith, and W. D. Long, "Hydration of Natural Glass and the Formation of Perlite," Geol. Soc. Am. Bull. 77, 323-328 (1966).

16. C. M. Stevenson, J. Carpenter, and B. E. Scheetz, "Obsidian Dating: Recent Advances in the Experimental Determination and Application of Hydration Rates," Archaeometry 31, 193-206 (1989).

17. J. Hagymass, S. Brunauer, and R. Sh. Mikhail, "Pore Structure Analysis by Water Vapor Adsorption. I. t-curves for Water Vapor," J. Coll. Inter. Sci. 29, 485 (1969).

18. S. Schonherr and R. Schrader, "Stationary Concentration of Ammonia Reached after Prolonged Radiolysis and by Radiolysis of a Nitrogen-Hydrogen Mixture," Khim. Vys. Energ. 7, 478 (1973).

19. J. A. Eyre and D Smithies, "Primary Yields in the γ-Radiolysis of Ammonia," Trans. Faraday Soc. 66, 2199 (1970).

20. D. B. Peterson, *The Radiation Chemistry of Gaseous Ammonia*, Radiation Chemistry Data Center, Notre Dame, Indiana, NSRDS-NBS-44 (1974).

21. S. Gordon, W. Mulac, and P. Nangia, "Pulse Radiolysis of Ammonia Gas. II. Rate of Disappearance of the $NH_2(X^2B_1)$ Radical," J. Phys. Chem. 75, 2087 (1971).

22. P. B. Pagsberg, J. Eriksen, and H. C. Christensen, "Pulse Radiolysis of Gaseous Ammonia-Oxygen Mixtures," J. Phys. Chem. 82, 582 (1979).

23. J. K. Linacre and W. R. Marsh, *The Radiation Chemistry of Heterogeneous and Homogeneous Nitrogen and Water Systems*, AERE Harwell Report No. 10027 (1981).

24. S. Sato and M. Steinberg, *Radiation Chemical Nitrogen Fixation in Air-Water Systems*, Brookhaven National Laboratory Report BNL-13692 (1969).

25. C. M. Jantzen and N. E. Bibler, "Product Consistency Test Method for Defense Processing Facility (DWPF) Glass," Version 2.1, Savannah River Laboratory (July 14, 1988).

26. M. M. Doxtader, J. V. Beitz, D. T. Reed, and J. K. Bates, *Speciation of Radionuclides in Natural Groundwaters*, Argonne National Laboratory Report ANL-88-5 (1988).

27. J. V. Beitz, M. M. Doxtader, V. A. Maroni, S. Okajima, and D. T. Reed, "High Sensitivity Photoacoustic Spectrometer for Variable Temperature Solution Studies," *Rev. Sci. Instr.* (in press).

28. H. D. Barrows, D. Greatorec, and T. J. Kemp, "Optical and Electron Spin Resonance Detection of Radical Intermediates in the Photooxidation of Organic Molecules in Solution by Transition Metal Ions," J. Am. Chem. Soc. 93, 2539 (1971).

IV. PROGRAM ON PLUTONIUM RECOVERY FROM RESIDUES
(R. D. Pierce)

A. Introduction

The objective of this program is to develop an effective pyrochemical process for the recovery of plutonium from intractable residues. Lawrence Livermore National Laboratory (LLNL) is working jointly with ANL to (1) devise a single economical pyrochemical process capable of recovering plutonium from all the types of scrap and residue now being generated or in storage from previous DOE weapons production operations; (2) minimize waste volumes; (3) remove and concentrate other transuranic (TRU) materials from the wastes so that the bulk of the pyrochemical process effluents can be classified as nontransuranic wastes; and (4) provide a basis for upgrading recycled weapons materials. Savannah River Site (SRS) is working with ANL to develop pyrochemical steps that can be applied in conjunction with existing aqueous processing facilities at SRS to recover plutonium from residues efficiently.

Liquid metals and molten salts at elevated temperature are used as reagents and solvents in the anticipated processes to effect the necessary separations and chemical conversions. Separations are possible because of the differing stabilities of compounds in the molten salt phase in contact with a liquid metal phase. Several residue-recovery flowsheets are under consideration, but all include reduction of PuO_2 in a residue as an initial step. This step is followed by a selective recovery of the plutonium by chemical extraction away from the bulk of the tramp elements, which also are reduced. From the large variety of molten-salt and liquid-metal combinations that exist, zinc-magnesium and copper-magnesium-calcium reduction systems were selected to explore initially. Reference flowsheets, which were prepared based on these systems, formed the basis for the initial research.

Since December 1988, process development and experiments for LLNL have been concentrated on the zinc-calcium based solvent/reductant process because it lends itself to recycle of virtually all the reagents and thereby minimizes waste volumes. In addition, attention is being given to the application of electrochemical steps to minimize reaction products that must be chemically converted for recycle. For example, electrowinning of calcium from CaO reaction product of pyrochemical processes could be employed to avoid generation of excessive salt wastes.

Experiments for SRS have been concentrated on the use of aluminum and aluminum-calcium solvent/reductant systems; however, SRS also supported design work on transfer lines for liquid metals and molten salts for use with pyrochemical process equipment. In addition, reference electrode experiments are underway to develop monitoring instrumentation for reduction and extraction experiments and process control.

To demonstrate the process steps, we are undertaking reduction and extraction experiments with several feed materials: Rocky Flats incinerator ash and ash heel, plutonium-contaminated LECO crucibles, and bomb reduction slag.

This section covers work on development of the zinc-calcium solvent/reductant system, calcium reduction experiments, calcium electrowinning experiments, reference-electrode development experiments, and design work on transfer lines for liquid metals and molten salts used with pyrochemical equipment.

B. Process Development
(R. D. Pierce)

A reference flowsheet for residue processing with the zinc-calcium solvent/reductant system was developed and is summarized in Fig. IV-1. The major process features are as follows:

1. Reduction of the plutonium oxide or other compounds into a liquid zinc-calcium alloy (along with most of the tramp elements from the residue) and selective extraction of the product plutonium from the liquid alloy by solvent electrorefining.

2. Removal of americium as a waste.

3. Concentration of the nontransuranic tramp elements in a zinc waste.

4. Removal of oxygen and recovery of calcium by electrolysis of CaO.

Two variations of this flowsheet are also under investigation: (1) reduction in two steps, with the bulk of the tramp elements reduced ahead of the plutonium so that they will not be present during solvent electrorefining, and (2) substitution of chemical salt-extraction and metal-extraction steps for solvent electrorefining. This latter alternative would improve kinetics but increase the solvent and reactant recycling requirements. Another variation, which is in an earlier stage of development, involves direct electrowinning of liquid plutonium from a salt suspension/solution of the residue to further decrease the reagent recycling requirements.

A material balance flowsheet that follows the reference process in Fig. IV-1 is presented in Fig. IV-2 for an ash-heel feed. The feed and exit streams for this flowsheet are summarized in Table IV-1. For 8.7 kg of residue, the total mass of solid waste is 5.4 kg, most of which is metallic. This waste contains zinc, which is added to the system as $ZnCl_2$ to oxidize excess calcium following the reduction step and to scrub the waste alloy prior to disposal. Calcium, magnesium, americium, and oxygen, which also are present in the residues, are not removed in the waste alloy. Some salt must be discarded to remove calcium, as $CaCl_2$, from the system; CaF_2, which is discarded with the $CaCl_2$, must be replaced in the feed. It is expected that the magnesium will collect with plutonium in the electrorefining step; this magnesium will be distilled from the plutonium and collected for disposal. Americium will be reduced from electrorefiner salt periodically with calcium. The oxygen from the residue forms CO (and CO_2) at a consumable carbon electrode in the recycle electrolysis step. This stream can be decontaminated and disposed of easily.

Although calcium reductant for the residue reduction is generated as a zinc-calcium alloy in the electrochemical reagent-recycle step, a small amount of fresh calcium will be added for reduction of the americium-rich material. If the americium were reduced with a zinc-calcium alloy, slightly less zinc would be discarded in the metallic waste, slightly less salt would be discarded, and no metallic calcium would be added. A disadvantage would be that the americium concentrate would contain zinc.

Development efforts at ANL have been directed toward several aspects of the flowsheet. Preliminary work on the reduction step has focused on assuring that the "intractable" residues are completely digested by the pyrochemical systems. Chemical extraction of the reduced plutonium has been tested, and solvent-electrorefining tests are planned. Argonne is undertaking solvent electrorefining of uranium as part of the Integral Fast Reactor Program. The electrochemical step for calcium and salt

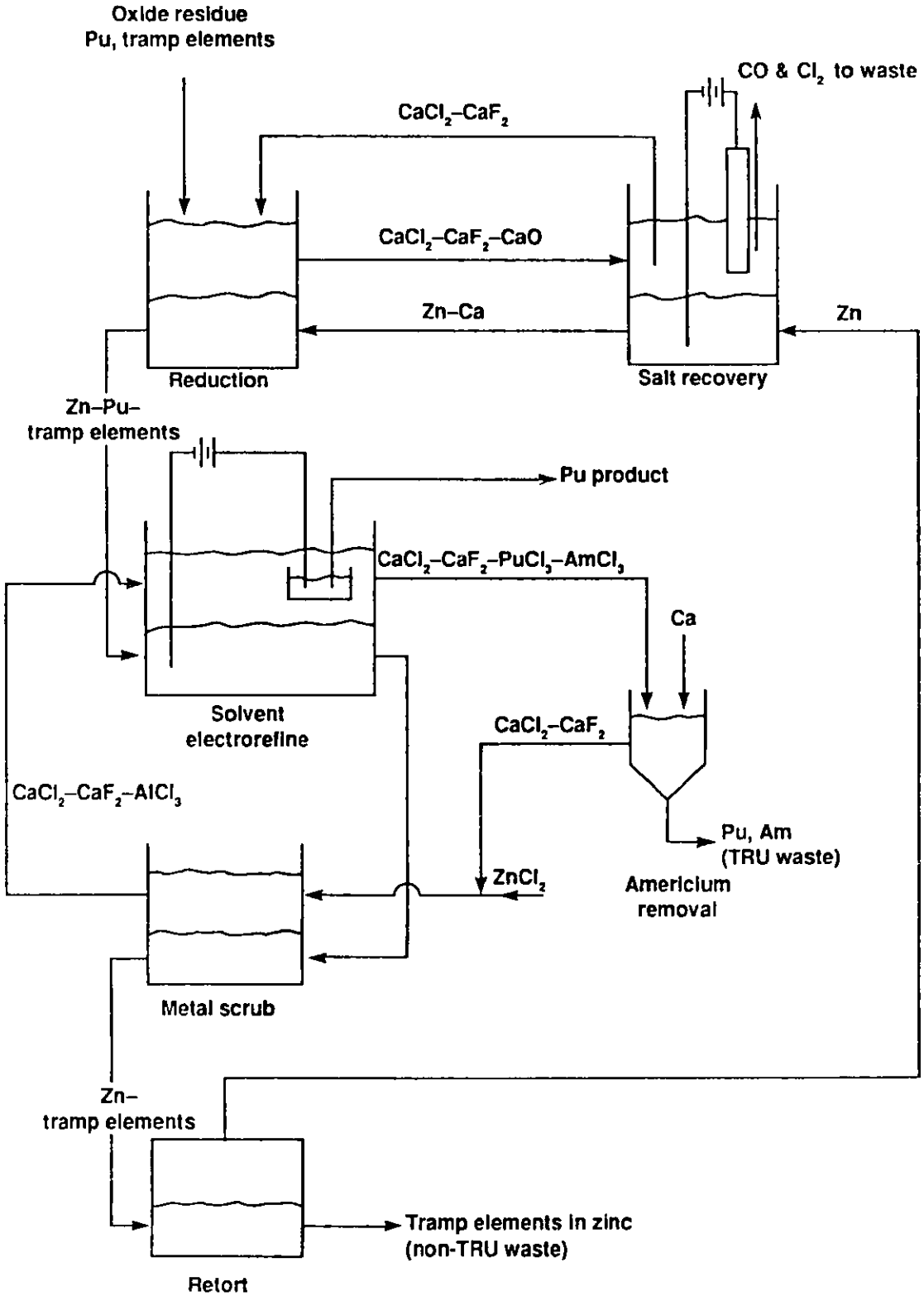

Fig. IV-1. Flowsheet for PuRR Process Using Zn-Ca Solvent/Reductant System

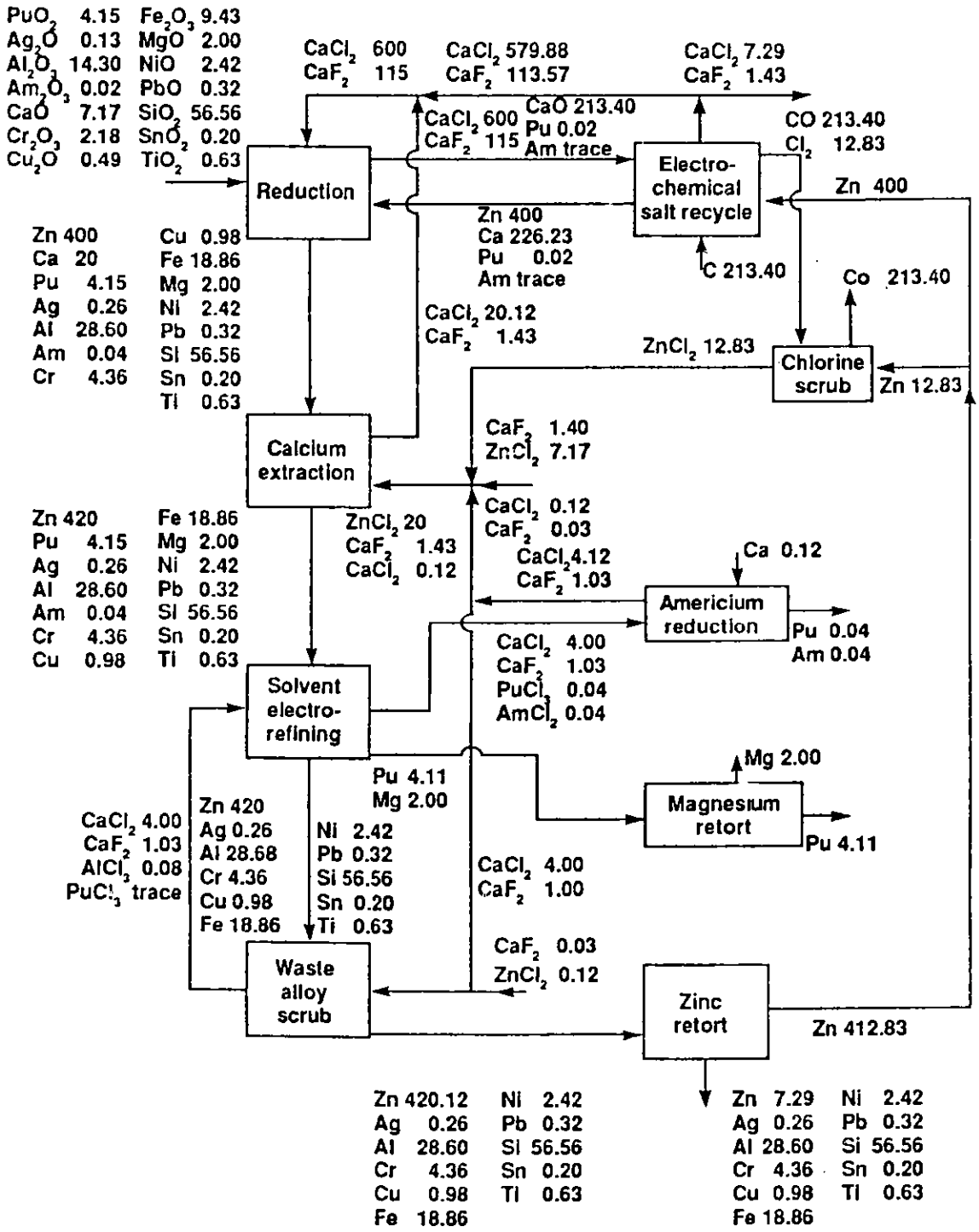

Fig. IV-2. Material Balance Flowsheet for PuRR Process with Ash-Heel Feed. Number of moles given next to elements and compounds.

Table IV-1. Composition of Feed and Exit Streams from PuRR Process with 100 mol Residue Feed (992 g plutonium)

	Amount in Feed Stream			Amount in Exit Stream	
	mol	g		mol	g
Residue			**Zinc Retort Heel**		
PuO_2	4.15	1125	Zn	7.29	477
Ag_2O	0.13	30	Ag	0.26	28
Al_2O_3	14.30	1459	Al	28.60	772
Am_2O_3	0.02	11	Cr	4.36	227
CaO	7.17	402	Cu	0.98	62
Cr_2O_3	2.18	331	Fe	18.86	1052
Cu_2O	0.49	70	Ni	2.42	142
Fe_2O_3	9.43	1506	Pb	0.32	66
MgO	2.00	81	Si	56.56	1590
NiO	2.42	181	Sn	0.20	24
PbO	0.32	71	Ti	0.63	30
SiO_2	56.56	3400		120.48	4470
SnO_2	0.20	30			
TiO_2	0.63	50	**Salt Waste**		
	100.00	8747	$CaCl_2$	7.29	809
			CaF_2	1.43	112
Salt				8.72	921
CaF_2	1.43	112			
$ZnCl_2$	7.29	994	**Gaseous Effluent**		
	8.72	1106	CO	213.40	5975
Metal			**Magnesium Retort**		
Ca	0.12	5	Mg	2.00	49
Carbon			**Americium Reduction**		
C	213.40	2561	Pu	0.04	10
			Am	0.04	10
				0.08	20
			Plutonium Product		
			Pu	4.11	982

recycle is important to avoid excessive waste volumes. Equipment is being readied to resume development of that step, which was investigated briefly as part of an earlier program at ANL.[1] Retorting operations were a routine part of the engineering studies of pyrochemical processing of fast reactor fuels[2] which were performed in the 1960s, and they are believed to require testing, but at a later stage in the process development sequence.

An alternative to an all-pyrochemical process is a head-end process step to convert an intractable material into a form easily dissolved in nitric acid for introduction into existing aqueous processes. Aluminum and zinc alloys of plutonium are expected to be easily dissolved and are convenient reagents for pyrochemical reduction of residues.

C. Calcium Reduction Experiments

(G. K. Johnson, R. D. Pierce, and T. P. Mulcahey)

1. Slag Reduction

The Savannah River Site provided ANL with a slag sample, which is a portion of the "sand, slag, and crucible" residue from bomb reduction of a mixture of PuF_4 and PuO_2 by excess calcium. The SRS provided support to ANL for a preliminary investigation of the pyrochemical recovery of plutonium from the slag.

The approximate compositions of the slag are shown in Table IV-2 from information supplied by Tracy Rudisill, SRS (private communication). Values are given for the assumptions that (1) all the remaining plutonium has been reduced, and (2) the remaining plutonium has not been reduced and is present in the original fluoride-to-oxide ratio of three. Because this slag has been in storage for a long time, the excess calcium may have reacted with air and/or moisture and been oxidized; therefore, values also are given for the assumption that the plutonium was not reduced and all the excess calcium oxidized during storage.

Table IV-2. Approximate Composition of Slag for Calcium Reduction Experiments

	% by Mass		
	If all Pu reduced	If remaining Pu unreduced	If excess Ca oxidized in storage
CaF_2	62.7	59.3	55.4
CaO	15.0	14.2	36.3
Ca	15.3	17.7	0
PuF_4	0	6.9	6.4
PuO_2	0	2.0	1.8
Pu	6.9	0	0

The slag, as-received, consisted of large lumps of gray, rock-like material with some associated loose powder, which was lighter in color. To partition the sample into portions suitable for our experiments, the larger lumps were broken with a hammer into somewhat smaller pieces. When the slag was struck with a hammer, red sparks flew, indicating that the slag still contained calcium metal.

It was assumed that the slag lumps, which are composed mostly of CaO and CaF_2, would be readily soluble in $CaCl_2$ and would not require pulverization. However, the MgO crucibles broke after stirring difficulties were encountered in the first two experiments with slag, and these experiments had to be repeated. It was thus decided to confirm the above assumption. A mixture of 42.7 g slag and 154.0 g $CaCl_2$ was heated in a MgO crucible to 800°C. Probing with the stirrer indicated that the slag lumps were completely digested in about 15 min. After brief stirring, the mixture was cooled and broken out of the crucible. It was observed that the salt had several small balls of calcium on or near the top surface.

Because the bomb reduction process was not expected to yield a homogeneous slag composition and we deliberately used the largest practical lumps of slag, a variable plutonium content between batches was anticipated. Thus, the plutonium content of each slag charge was determined by submitting the entire charge for γ-spectrometric analysis. The results showed plutonium contents between 3.23 and 4.14 mass percent.

Six reduction runs were conducted with the SRS slag, and the salt phase from the least successful run was recontacted with fresh reductant. The first two runs involved the use of Zn-10% Ca (Run SRP-40) and Al-10% Ca (SRP-41) as reductants; then two runs were performed using pure zinc (SRP-42) and aluminum (SRP-43) as the metal phase and the residual calcium in the slag as the reductant. In one of the final two reductions, the aluminum-only run was duplicated except that the mixing intensity was increased stepwise from a low value (SRP-46). For the other run, the zinc-only run was repeated but with a larger zinc volume. For this run (SRP-45), some calcium was added to maintain the same calcium concentration as obtained in the earlier zinc-only run (about 3 wt %). The zinc-10% calcium run (SRP-40) had a poor recovery; therefore, the salt from that run was recharged with fresh reductant and rerun (SRP-44). The experimental conditions and reactants for these runs are summarized in Table IV-3. The furnace well for these experiments was located in an argon-atmosphere glovebox.

During the experiments, filtered samples were withdrawn from the metal phase by using tantalum tubes with tantalum filter frits. Following each experiment, the MgO crucible was removed and broken open. Typically, the salt was composed of two distinctly different-colored regions, a yellow upper portion and a black portion adjacent to the metal. The yellow salt usually was easily cleaved from the black salt and kept separate. The black salt tended to adhere to the metal ingot, and in the case of the aluminum ingots, it coated the ingot on the side and partially on the bottom. Normally, the black salt was removed from the ingot as completely as possible and kept separate. In SRP-42, the black salt layer was too thin to separate from the other phases, and in SRP-44 there was no light-colored salt. Wedge-shaped sections were cut from the ingots for analysis. Analytical results are summarized in Table IV-4.

The uncertainty in analyses of the pie-shaped samples cut from the frozen ingots is high (±50%) because of possible variations in the solute crystallization throughout the ingots. However, both a pie section and the balance of the ingot from Run SRP-42 were submitted for analysis; the indicated plutonium content of the ingot was 0.81 g from the pie-section and 0.82 g from the balance of the ingot. The salts were crushed and quartered for sampling, which has proved reliable. The samples were analyzed by inductively coupled plasma atomic emission spectrometry (ICP). Salt-phase plutonium and americium values were determined by gamma spectrometry.

Material balances range from only 57% (SRP-42) to 141% (SRP-45). Such a wide variation makes quantitative assessment of the results difficult. We have found no evidence for inaccurate analyses of the feed material, but this seems the most likely explanation of the poor material balances. The gamma-spectrometric analyses of the slag feeds were not affected by the sample orientation during counting.

Examination of the data in Table IV-4 shows that, with the possible exception of SRP-43, the plutonium has not been completely transferred into the metal ingot. However, based on analysis of the yellow salt, the reductions would appear to be at least 99.6% complete. Thus, the missing plutonium would be expected to be associated with the black salt phase in some form. Previous examinations of black salts have shown that they contained some of the metal phase. It is probable that, due to the violent agitation in our experiments, some of the metal remains suspended. This suspended metal is expected to have the same plutonium concentration as the bulk metal. Hence, γ-spectrometric analysis of the black salts for plutonium is unreliable unless the metal content of the black salt is also determined. For

Table IV-3. Experimental Details for Slag Experiments[a]

	SRP-40	SRP-44	SRP-41	SRP-42	SRP-43	SRP-45	SRP-46
Metal Charge, g	450.1 Zn 50.7 Ca	450.4 Zn 50.8 Ca	250.0 Al 27.7 Ca	125.2 Zn	125.3 Al	450.2 Zn 14.1 Ca	125.1 Al
$CaCl_2$ Charge, g	154.0	167.9[b]	154.0	154.0	154.0	154.9	154.9
Slag, g	42.70	In Salt	43.06	42.67	43.24	42.58	43.57
Pu in Slag, g	1.77	0.3	1.62	1.42	1.40	1.67	1.66
Am in Slag, μg	136	56	134	119	127	113	118
Stirring Speed, rpm	900[c]	900	900[c]	900	900	900	70 200 460 900
Stirring Time, min	90[c]	60	60[c]	60	60	180	150 200 120 120
Temperature, °C	800	795	800	800	800	800	795 800 785 780

[a]Crucible: 57-mm dia, MgO with 4 fixed MgO baffles; stirrer: Mo-30% W, 29-mm dia flat paddle.
[b]SRP-40 salt.
[c]In the first attempt at these experiments, we were unable to stir at high speed because of some interference. Following the experiments, in which the crucible was broken, the contents were recharged into a second crucible, and the experiment was restarted. Thus, the stirring time and speed are only for the repeat experiment.

Table IV-4. Summary of Analytical Results for Slag Experiments

	SRP-40	SRP-44	SRP-42	SRP-45	SRP-41	SRP-43	SRP-46			
Agitator Speed, rpm	900	900	900	900	900	900	70	200	460	900
Pu in Slag (or Salt),[a] g	1.77	0.29	1.42	1.67	1.62	1.40	1.66	1.58	1.5	1.1
Light Salt, g	95.4	b	176.2	181.9	110.4	125.2	118.1	108.0	106.8	87.2
Pu Content,[a] g	0.0036		0.0021	0.01	0.0017	0.0036	0.02	0.006	0.02	0.015
%of Tot. Pu	0.42		0.15	0.6	0.10	0.41	1.2	0.4	1.3	1.4
Dark Salt, g	87.83	169.7	c	5.9	37.81	48.32	63.2	57.9	33.7	38.4
Tot. Pu Content,[a] g	0.35	0.25		0.003	0.015	0.061	1.69	0.53	0.28	0.15
Entrained Metal,[d] g	1.89 (Zn)	-		0.20 (Zn)	0.063 (Al)	6.09 (Al)	-	-	-	-
Pu in Salt Phase, g	0.34	-		0.002	0.015	0.00	-	-	-	-
% of Tot. Pu	19	86		0.12	0.92	0.00	102	34	19	14
Metal Ingot, g	486	452	104	414	267	126	123	123	116	126
Sol. Pu in Ingot,[e] g	1.36	0.10	1.03	2.46	0.70	1.17	0.11	-	0.75	0.64
Tot. Pu in Ingot,[f] g	1.31	0.10	0.81	2.35	1.13	1.33	-	-	-	1.05
% of Tot. Pu	74	34	57	141	70	95	7	-	50	95
Ca in Ingot,[d] g	56	61	4.2	10.7	31	7.1	5.3	-	5.2	12.9

[a]Based on γ-spectrometric analysis, uncertainty ±10%.
[b]No significant light-colored salt.
[c]Black salt layer was very small and was not kept separate.
[d]Based on ICP analysis, uncertainty ±5 to 10%.
[e]Based on ICP analysis of filtered samples, uncertainty ±10%.
[f]Based on ICP analysis of a pie-shaped portion of ingot, uncertainty ±50%.

experiments SRP-40, SRP-41, and SRP-43, portions of the black salts were dissolved in HCl(aq). In SRP-40, a small amount of residual black material, which was insoluble in HCl(aq), dissolved when HNO_3(aq) was added; ICP analyses were then performed on the resulting solutions for plutonium and metal. For SRP-40, a plutonium content of 0.45 g and a zinc content of 1.89 g were determined. Analysis of this salt by γ-spectrometry had previously given a value of 0.35 g Pu. Although these plutonium results are only in fair agreement, they indicate plutonium content which is much higher than would be expected if it were only due to suspended metal. Although the state of the plutonium in the black salt is unknown, the analyses account for all of the starting plutonium in SRP-40. Also, for experiment SRP-43, the plutonium is accounted for within analytical uncertainty. In this case, the plutonium in the black salt is clearly associated with the entrained aluminum, since the Pu/Al ratio in the salt is the same as in the ingot. Plutonium material balances are low for experiments SRP-41 and SRP-42. For SRP-41, the missing plutonium was not found in the black salt phase, and SRP-42 had no separate dark salt.

A portion of the black salt from SRP-40 was washed free of $CaCl_2$ to increase the relative plutonium content and examined by X-ray diffraction. The analysis failed to identify a plutonium species in the black salt. For Run SRP-44, the bulk of the salt from SRP-40 was contacted with a fresh charge of Zn-10% Ca to determine if the plutonium species in the salt was truly intractable. About 30% of the plutonium was extracted into the metal phase, but the major portion remained in the salt. Further evaluation of the salt residue would be desirable to identify the source of the problem.

The zinc phase for Run SRP-42 was so small that it may have prevented good distribution of the phases with the mixing geometry employed. Accordingly, Run SRP-45 duplicated SRP-42, except with a deeper zinc melt. Additional calcium was added to provide the same calcium concentration (~3%) as in SRP-42. Run SRP-45 apparently was successful because the plutonium left in the salt was small (see Table IV-4); however, the indicated plutonium content of the zinc was 141% of that charged. Filtered metal and metal-ingot analyses agree within 10%.

Run SRP-46 is a duplicate of the successful aluminum-calcium Run SRP-43, except the run was made with a stepwise increase in agitation intensity (see Table IV-3). The mixing intensities were 5×10^{-4}, 1×10^{-2}, 0.1, and 1 times that of SRP-43. At least two hours of agitation was provided at each intensity. The results (see Table IV-4) indicate that the aluminum did not extract all the calcium from the salt until the most intense agitation was provided. Again, the material balance is a problem, but gentle mixing appears inadequate. The high plutonium content of the final salt is disturbing and again suggests (along with the results of SRP-44) that a refractory plutonium phase may occur.

The success of some runs, particularly SRP-43 and -45, indicates that the use of a head-end process step to recover plutonium from slag warrants further investigation. Ingots from these runs should be dissolved in acid to demonstrate that the plutonium is readily available from the Zn or Al ingots. It is important to demonstrate that the salt can be recycled; otherwise, excessive waste volumes will be produced. The unrecovered plutonium of runs SRP-40 and SRP-46 poses a problem that should be investigated. Sampling and analytical procedures should be reviewed to improve the material balances.

2. Ash Heel Reduction
(G. K. Johnson, R. D. Pierce, and T. P. Mulcahey)

Three experiments involving the preparation of an acid-soluble ingot from incinerator-ash heel were completed: two reduction runs (SRP-33 and SRP-36, under an LLNL-sponsored program) to produce a zinc-calcium alloy containing plutonium from ash heel, and one reduction run (SRP-39, under SRS sponsorship) to produce an aluminum-calcium alloy containing plutonium from ash heel. The charges for these runs are summarized in Table IV-5. The ash was generated in a Rocky Flats Plant

Table IV-5. Experimental Details For Ash Heel Experiments[a]

	SRP-33	SRP-36	SRP-39
Metal Charge, g	450 Zn 64 Ca	450 Zn 43 Ca	250 Al 40 Ca
$CaCl_2$ Charge, g	136 $CaCl_2$ 24 CaF_2	136 $CaCl_2$ 24 CaF_2	136 $CaCl_2$ 24 CaF_2
Ash Heel, g	13.7	13.4	13.0
Pu in Ash, g	1.68	1.55	1.51
Am in Ash, μg	3900	3600	3500
Stirring Speed, rpm	900	900	900
Stirring Time, h	2	2	1[b]
Temperature, °C	790	800	800

[a]Crucible: 57-mm dia MgO, with 4 fixed MgO baffles; stirrer: Mo-30% W, 29-mm dia, flat paddle.
[b]Crucible broke and salt leaked out at an unknown time in first attempt; however, agitator had run for 2 h. The salt and metal were reloaded into a new crucible and run for an additional hour.

(RFP) incinerator, and the ash heel was subsequently exposed to multiple nitric acid leaches at RFP. The ash heel was further calcined and sampled at LLNL, and a small batch of the calcined material was sent to ANL. The ANL batch was divided into approximately 13-g portions for use in experiments. The furnace well for these experiments was located in an argon-atmosphere glovebox. Earlier, in Run SRP-16, the reduction and recovery of plutonium from pure PuO_2 were demonstrated with aluminum in the presence of a salt flux. Calcium was employed for the present runs because of the refractory nature of ash heels.

From the analytical results (Table IV-6) for the salts recovered from runs SRP-33, -36, and -39, the reductions appear to have gone to 99.5, 97.5, and 95.9% completion, respectively. The final calcium concentrations for these runs were determined to be 14.8, 9.0, and 6.3 at. %, respectively, which suggest a calcium concentration effect. The difference between the soluble and total plutonium in the metal ingots indicated for each run in Table IV-6 is consistent with our stability experiments on the solubility of plutonium in Zn-Mg and our Zn-Mg reduction experiments on LECO crucibles and raw ash. This difference is attributed to reaction with silicon reduced from tramp silicon compounds to form insoluble $PuSi_2$:

$$Pu_{\text{metal soln}} + 2Si \rightarrow PuSi_2 \qquad \text{(IV-1)}$$

The effect is greater with zinc than with aluminum melts because of the lower activity coefficient for plutonium in aluminum. The acid solubility of this precipitated phase could be important.

The poor material balances again decrease the confidence in the results; however, the ingot and salt analyses indicate that the lower calcium concentration of Run SRP-36 resulted in lower plutonium reduction. The combined effects of calcium and CaO concentrations on the reductions should be examined. The data of Wenz et al.[3] indicate that the solubility of CaO in the reduction salt at 800°C is 9.3 wt %, but for these runs, the CaO concentration would have been about 12 wt % for complete reduction (see Table IV-6). There is mounting evidence that calcium reductions are difficult when the salt becomes saturated with CaO. Shaw[4] has presented data indicating that the solubility of calcium in $CaCl_2$ drops dramatically as the salt becomes saturated with CaO. Soluble calcium may be important in the reduction mechanism. In addition, the ability of the salt to flux the CaO reaction product from the ash surfaces may also be poor for saturated salt.

The americium behavior in these experiments was similar to that of plutonium. The fraction remaining in the reduction salt was similar for both elements in each run. The americium recovered by salt extraction from the two zinc-calcium alloy runs (SPP-33 and -36) is qualitatively similar. The plutonium and americium recovery was higher with the higher calcium concentration of SRP-33. The americium content of the aluminum-calcium ingot of SRP-39 was too low to determine by ICP analysis.

The reductions should be repeated with a larger salt volume to reduce the ultimate CaO concentration to less than saturation. In addition, the effects of calcium concentration should be checked once the effect of CaO saturation is evaluated. A longer reaction time with the recharged materials from SRP-39 would be valuable to determine whether the poor reduction was only a result of a slowed reaction. The acid dissolution of ingots from these runs should be attempted by SRS.

D. Electrolytic Reduction of Calcium Oxide to Calcium Metal

(D. S. Poa, G. K. Johnson, T. P. Mulcahey, and R. D. Pierce)

1. Introduction

In a proposed flowsheet for pyrochemical processing of oxide residues, the reduction step utilizes calcium dissolved in liquid zinc and a cover salt containing $CaCl_2$-15 wt % CaF_2. The reduction reaction is

$$(MO_2)_{Salt} + 2Ca_{Zn} \rightarrow 2\ CaO_{Salt} + M_{Zn} \qquad \text{(IV-2)}$$

where M = plutonium, americium, and tramp elements (e.g., silicon), and the subscript indicates the phase where M is present. The reduction product, CaO, concentrates in the $CaCl_2$-CaF_2 cover salt. When the cover salt nears saturation with CaO (about 17 mol % at 800°C), it must be purified or discarded as radioactive waste. To minimize waste volume from plutonium recovery operations, it is desirable to recycle reagents. Complete or partial recycle of the cover salts and calcium by converting the CaO back to calcium metal would eliminate a large solid waste volume and decrease the calcium and salt feed requirements.

This preliminary study was made to evaluate the electrolysis of CaO in molten $CaCl_2$-15 wt % CaF_2 with a liquid zinc pool cathode and a consumable graphite anode. In the electrolysis, the cathode reaction regenerates calcium metal for recycle to the reduction vessel. The anode reaction yields CO and CO_2 gases. Thus, the oxygen originally associated with the oxidic residue is removed as gases, which can be scrubbed and cleaned for release to the atmosphere. Hence, the waste volume may be significantly decreased.

Table IV-6. Summary of Analytical Results for Ash Heel Experiments

	Zinc-Based Run		Aluminum-Based Run
	SRP-33	SRP-36	SRP-39
Pu in Ash,[a] g	1.68	1.55	1.51
Recovered Salt			
Major Salt Ingot, g	120	180	75
Pu Content,[a] g	0.0033	0.044	0.002
% of total Pu	0.2	2.8	0.13
Am Content,[b] μg	14	92	5
% of total Am	0.4	2.5	0.14
Dark Salt, g			66
Total Pu Content,[c] g			0.084
Entrained Metal,[c] g			4.6
∴ Pu in salt phase, g			0.060
% of total Pu			4.0
Am Content,[b] μg			150
% of total Am			4.3
Salt Outside Crucible[d], g	42		
Pu Content, g	0.0058		
% of total Pu	0.3		
Metal Ingot, g	493	343	260
Soluble Pu in Ingot,[e] g	0.21	0.28	0.90
Total Pu in Ingot, g	1.2[f]	0.90[f]	1.25[g]
% of total Pu	71	58	83
Total Am in Ingot, μg	4670[f]	1140[f]	
% of total Am	120	32	
Ca in Ingot,[h] wt %	9.6	5.7	9.1
at. %	14.8	9.0	6.3
CaO in Salt,[h] wt %	12.4	12.1	11.8

[a]Based on γ-spectrometric analysis, uncertainty ±10%.
[b]Based on γ-spectrometric analysis, uncertainty ±20%.
[c]Based on ICP analysis, uncertainty ±5 to 10%.
[d]Crucible cracked and some salt leaked into Ta secondary crucible.
[e]Based on ICP analysis of filtered samples, uncertainty ±10%.
[f]Based on γ-spectrometric analysis of salt in subsequent salt extraction step, analytical uncertainty ±10% for plutonium and ±20% for americium.
[g]Based on ICP analysis of a pie-shaped portion of ingot, uncertainty ±50%.
[h]Calculated for complete reduction of ash heel.

2. Process Chemistry

The net electrode reactions in this electrolysis are

$$CaO + C \rightarrow Ca^{2+} + CO + 2e^- \quad \text{(IV-3)}$$

or

$$CaO + 1/2\ C \rightarrow Ca^{2+} + 1/2\ CO_2 + 2e^- \quad \text{(IV-4)}$$

at the anode, and

$$Ca^{2+} + 2e^- \rightarrow Ca \quad \text{(IV-5)}$$

at the cathode. The resultant overall reactions are

$$CaO + C \rightarrow Ca + CO \quad \text{(IV-6a)}$$

and

$$CaO + 1/2\ C \rightarrow Ca + 1/2\ CO_2 \quad \text{(IV-6b)}$$

The actual electrode processes may be more complicated, and various side reactions are possible.

Based on the standard free energies of formation (unit activities for all the reacting species), the following decomposition potentials (E_d°) at 800°C were calculated:

$CaO \rightarrow Ca + 1/2\ O_2$ (g)	$E_d^\circ = 2.68$ V	(IV-7)
$CaO + C \rightarrow Ca + CO$ (g)	$E_d^\circ = 1.80$ V	(IV-8)
$CaO + 1/2\ C \rightarrow Ca + 1/2\ CO_2$ (g)	$E_d^\circ = 1.66$ V	(IV-9)
$CaCl_2 \rightarrow Ca + Cl_2$ (g)	$E_d^\circ = 3.28$ V	(IV-10)
$CaF_2 \rightarrow Ca + F_2$ (g)	$E_d^\circ = 5.36$ V	(IV-11)

The decomposition potentials of reactions IV-8 and -9 are enough lower than those of reactions IV-10 and -11 that selective decomposition of CaO in molten $CaCl_2$-CaF_2 salt is possible.

3. Experimental

The electrolysis experiments were conducted in a helium glove-box facility, with the moisture level below 3 ppm and the oxygen level below 10 ppm.

A laboratory-scale cell was constructed for verifying the feasibility of the concept. The cell design is shown schematically in Fig. IV-3. The cell vessel was a MgO crucible having an inside diameter of 89 mm, a depth of 152 mm, and a wall thickness of 1.5 mm. The magnesia crucible contained the electrolyte, the electrodes, and a paddle stirrer (molybdenum-30 wt % tungsten). The cathode was a pool of liquid zinc with a tungsten wire (1.6-mm dia) electric conductor. The collection of calcium metal product directly in a liquid zinc pool is convenient for recycling to the reduction vessel.

Two different arrangements of graphite anodes were used in the preliminary electrolysis experiments. Two 12.5-mm-dia graphite rods bound together were used for the initial two experiments, while the subsequent four experiments employed a hollow graphite tube, as shown in Fig. IV-4. This

design facilitated the collection of product-gas samples. The slots on the lower edge of the tube anode were originally provided to prevent excessive accumulation of product gases in the inner void space of the tube stopping gas formation. The slots were omitted after the first run to increase the gas pressure available to force gas into the gas sample bottles and to conserve electrode use since the used end was cut off when there was significant reduction in electrode thickness.

The cell was placed inside a graphite secondary container, which was then positioned in a furnace well in the floor of the glovebox. A calibrated Chromel-Alumel thermocouple was inserted in a hole in the wall of the graphite secondary container.

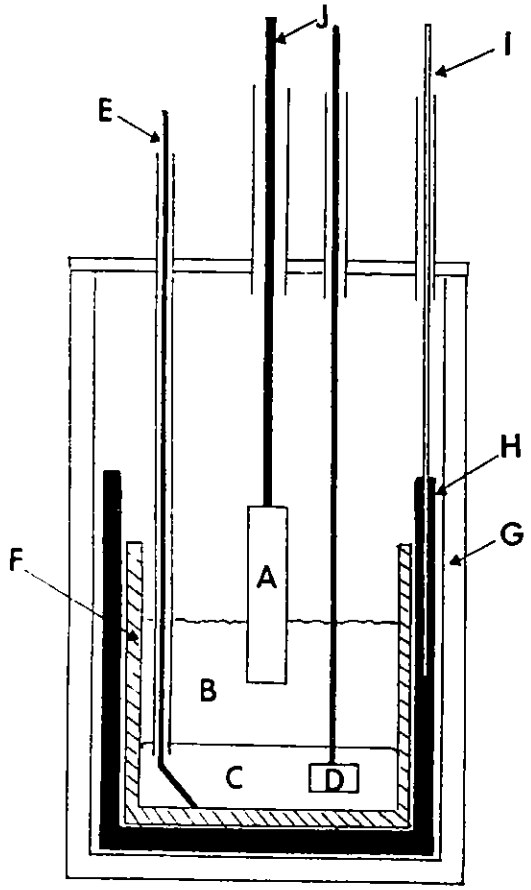

Fig. IV-3.

Electrochemical Cell Used for Electrolysis of CaO. (A) Graphite anode, (B) electrolyte, (C) liquid zinc cathode pool, (D) paddle stirrer, (E) cathode contact lead, (F) magnesia crucible, (G) furnace well, (H) graphite secondary container, (I) thermocouple, (J) anode contact lead.

The $CaCl_2$ used in these experiments was polarographic-grade material obtained from the Anderson Physics Laboratory (Urbana, IL). The CaO and CaF_2 were reagent-grade materials. The zinc metal was of 99.99% purity, obtained from Belmont Metals Inc. (Brooklyn, NY). The anode substrate material was grade ECV graphite rods obtained from Union Carbide Corp. (Cleveland, OH).

A Hewlett Packard Model 6282 A DC power supply provided the DC current for the electrolysis. The cell voltage and current were monitored with a Fluke Model 8800 A and a Model 8000 A DMM, respectively. The cell voltage and current during electrolysis were also recorded by a Gould Model 110 strip-chart recorder. The paddle stirrer was driven by a Cole-Parmer Model 4380-00 bench stirrer motor.

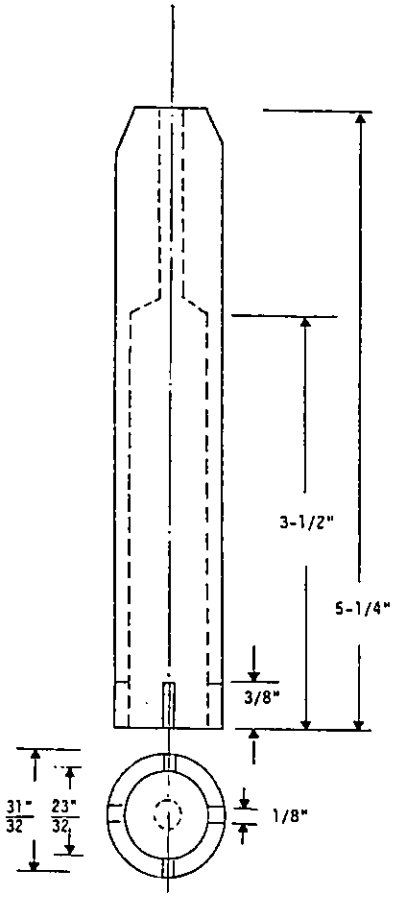

Fig. IV-4.

Schematic of Graphite Tube Anode (gas collection electrode)

Prior to the electrolysis experiment, the graphite cell components, including the anode rods and the secondary container, were preheated and degassed in a vacuum furnace (AVS Model No. HMF-12-12-12-1300 Horizontal Vacuum Furnace, Advanced Vacuum Systems, Inc., Ayer, MA) at 1000 °C. The MgO crucible was preheated at 225 °C for about 16 h in air.

The electrolysis experiments consisted of the following steps:

(a) The cell was initially loaded with 835 g zinc metal, 250 g $CaCl_2$, and 43 g CaF_2, as well as a CaO amount which was varied from run to run.

(b) The loaded cell was heated to about 785 °C. After the crucible contents had melted, the melt was stirred for about 2 h with a flat paddle at about 200 rpm.

(c) The cathode conductor rod and the anode were installed in the cell. The graphite anode was lowered into the salt phase to about 6 mm above the zinc-salt interface. (The reacting surface area for the anodes was approximately 18 cm^2 for the rod type and 28 cm^2 for the hollow-tube type.)

(d) After about 10 min on open circuit, electrolysis was initiated. The cell operated in a constant current (1.5 to 4.5 A) mode. Based on the original anode surface area, the current density ranged from 54 to 161 mA/cm^2. During electrolysis, the operating current was periodically adjusted to ensure that the cell voltage did not exceed 2.7 V,

which is the calculated reversible $CaCl_2$-decomposition potential under the cell conditions. However, in the product-gas collection runs, during the final period (1 to 1-1/2 h) of electrolysis, the cell voltage was deliberately brought up to the range of 2.7 to 3.3 V to determine whether any appreciable amount of chlorine gas could be collected in the effluent gas.

(e) The current- and potential-time curves were recorded during electrolysis. Samples of effluent gas were collected at predetermined periods of electrolysis and analyzed for CO, CO_2, and Cl_2.

(f) At the conclusion of electrolysis, the graphite anode and the cathode conductor rod were withdrawn from the cell. Filtered samples of the molten zinc cathode alloy were taken and analyzed for calcium.

(g) After the cell had been cooled to room temperature, the solidified salt phase and metal ingot were visually examined, and for certain runs, samples were taken and analyzed.

4. Results and Discussion

Of the six experimental runs, the graphite anodes were solid rods for the first two and hollow tubes for the other four. The estimated current efficiencies for these six runs are summarized in Table IV-7. The current efficiencies were determined by comparing the calcium content in the zinc phase (based on chemical analyses of filtered samples) with the amount that could be liberated by the integrated current with an efficiency of 100%. Following are observations obtained from the experimental results:

(a) At constant current, the cell voltage drifted slowly but consistently upward with time of electrolysis.

(b) As shown in Table IV-7, current efficiencies for the first two runs are much higher than those of the next two. Thus, the possible effect of the anode shape should be investigated further.

(c) For the more dilute CaO conditions of Runs 5 and 6, excessive anode polarization was observed. Gentle stirring with Run 5 dropped the potential significantly at a given current; therefore, gentle agitation was provided for Run 6, which had a current efficiency of 22%.

(d) In Run 1, after the melt was cooled and solidified, a very thin shiny metal layer was separated at the zinc-salt interface. The calcium metal content in this layer was 4.2 wt %, which was much higher than that in the bulk zinc cathode phase (0.53 wt %). This suggests that phase separation occurred during cooling.

(e) In Runs 2-4, a 1/2- to 1-cm layer of salt containing graphite and numerous gas bubbles occurred at the surface of the electrolyte. This salt layer might have caused some short circuiting between the anode and cathode, which would decrease current efficiency. For future experiments, cells will be designed to eliminate or decrease such carbon layer effects.

Table IV-7. Analytical Results for Filtered Molten Zinc Cathode Samples and Current Efficiencies Calculated Based on Calcium Concentration in Zinc Cathode

Run No.	Anode Type	Approx. Reacting Anode Surface Area, cm^2	Initial CaO Charge, g	Integrated Current, Ah	Electrolyte Agitation, rpm	Final Ca in Zinc Cathode, wt %	Final Ca in Zinc Cathode, g	Current Efficiency, %
1 (Dry-21)	Graphite rods	18	29	8.25	0	0.53	4.4	72
2 (Dry-22)	Graphite rods	18	29	13.02	0	0.71	5.9	61
3 (Dry-23)	Hollow graphite tube	28	29	11.47	0	0.36	3.0	35
4 (Dry-25)	Hollow graphite tube	28	34	14.36	0	0.30	2.5	23
5 (Dry-26)	Hollow graphite tube	28	6	2.7[a]	0	0.27[b]	2.2[b]	116[b]
6 (Dry-27)	Hollow graphite tube	28	~6[c]	14.25	100	2.28	2.3	22

[a]Apparently high anode polarization could only draw relatively low current.
[b]Analysis suspect, possible salt ($CaCl_2$-CaF_2) contamination.
[c]Salt from Run 5 was reused with an additional 3 g of CaO.

Table IV-8 gives the analytical results of effluent gas samples from three runs. As shown in this table, both CO and CO_2 gases were produced during electrolysis. However, no chlorine gas was detected in these gas samples, including those collected when the cell was operated at a voltage range of 2.7 to 3.3 V. The CO_2/CO ratio in all the three gas samples collected in Run 3 was approximately 1, while for the four gas samples collected in Run 4, this ratio ranged from 3.3 to 6.1, increasing consistently with time of electrolysis. These differences in CO_2/CO ratio might have resulted from the complicated heterogeneous reactions and kinetics occurring at the anode, which are not well understood. It also is uncertain whether there was significant gas composition shift outside the cell by Boudouard reaction ($2CO \rightarrow CO_2 + C$).

Table IV-8. Analytical Results of Effluent Gas Samples

Run No.	Sample No.	Comp., %				
		He	CO	CO_2	Cl_2	Other
3[b](Dry-23)	1	99.6	0.30	0.10	ND[a]	ND
	2	97.7	1.06	1.25	ND	ND
	3	95.2	2.4	2.3	ND	ND
4[c](Dry-25)	1	90.5	2.2	7.3	ND	ND
	2	94.0	1.1	4.9	ND	ND
	3	90.5	1.7	7.8	ND	ND
	4	81.5	2.6	16.0	ND	ND
6[d](Dry-27)	1	98.5	0.9	0.54	ND	ND
	2	94.9	5.4	9.7	ND	ND
	3	>99.9	≤0.016	<0.005	ND	ND

[a]Not detected.

[b]For Run 3, we collected gas sample No. 1 during the initial 1-1/2 h period of electrolysis, sample No. 2 during the next 1-1/2 h period, and sample No. 3 during the final 1-2/3 h period.

[c]For Run 4, gas sample No. 1 was collected during the initial 2-1/2 h period of electrolysis. Then, the cell was on open circuit overnight. After restarting the electrolysis, we collected gas sample No. 2 during the initial 2-1/3 h period, gas sample No. 3 during the following 2 h 55 min, and sample No. 4 during the final 1 h 14 min.

[d]For Run 6, we collected gas sample No. 1 during the initial 2-h period of electrolysis, sample No. 2 during the next 1-1/2 h period, and sample No. 3 during the following 1-1/2 h period of electrolysis.

Post-test examination of the cell components revealed that the MgO crucible, the Mo-W alloy paddle stirrer, and the tungsten cathode electric-conductor rod were all in good condition. In addition, the boron nitride (BN) used for electrically insulating the cathode conductor rod in the first two runs was severely attacked by the salt phase during electrolysis, while the alumina tube (Grade 998 Al_2O_3, McDanel Refractory Co., Beaver Falls, PA), which replaced the BN insulator for Runs 3 through 6, suffered no apparent attack by the melts.

5. Conclusions

The results of these electrolysis experiments are encouraging and demonstrate that CaO dissolved in molten $CaCl_2$-CaF_2 can be electrolyzed to produce calcium dissolved in a liquid zinc cathode. However, the results are still preliminary, and additional laboratory-scale studies are needed. In

future experiments, efforts will be made to investigate the effect on the current efficiency of CaO concentration in the salt phase, especially when the concentration is low (i.e., below 2 wt %); stirring the salt phase during electrolysis; and anode design. Also to be investigated are changes in cell design to avoid the carbon contamination of melts.

E. Reference Electrode Experiments

(D. S. Poa, R. D. Pierce, G. K. Johnson, and T. P. Mulcahey)

A reference electrode for use in a zinc-alloy/molten-salt system is being developed. Two scoping experiments were performed to test a simple zinc electrode contained in a porous MgO tube, which has pores that fill with salt but will not permit metal entry. A concentration cell is established between the reference electrode and an alloy being measured. The electrode is immersed in a $CaCl_2$-CaF_2 cover salt over the alloy of interest. Because of the volatility of zinc, a small amount of cover salt is also charged to the reference electrode.

1. Zinc Electrode

The first experiment (Run DRY-18) investigated the effect of the MgO tube porosity on the zinc electrode performance. Each MgO tube (5-mm ID and 10-mm OD) was initially filled with 1.0 g zinc and 1.0 g salt. The reference electrodes showed a strong potential change with the calcium concentration of the zinc alloy in which the reference electrode was immersed and a weak dependence on temperature in the range of 700 to 800°C.

The test results indicate that the tube porosity has a strong effect on the stability of the electrode potential. A reference electrode using a MgO tube with a medium porosity (medium density) showed only a slight decrease in potential from 1.31 to 1.28 V after 30 min in a Zn-7.2 wt % Ca melt. With a reference electrode using a high porosity (low density) tube, the cell potential dropped from 1.26 V to 0.68 V in the same period. After about 16 h of immersion in the alloy, both electrodes approached a relatively stable potential of 0.4 to 0.5 V.

Reversing the polarity of the cell for a period by imposing a small current (50 to 100 μA) had no effect on cell potential. This suggests that the decrease in cell potential was not due to a reversible charge-transfer reaction in the electrode. Addition of 1.0 g zinc to the medium-density MgO electrode increased the potential from 0.50 to 1.20 V. Thus, the potential change was a result of a shift in the composition of the zinc in the reference electrode. Because calcium has a finite solubility in the salt phase, it is likely that calcium was diffusing from the zinc alloys to the zinc reference electrode under a concentration gradient.

Tubes of higher density will be sought for future testing, and the area of the tube that is porous also may be decreased. These changes will reduce the rate of change of the reference electrode composition and the associated drift in potential. For the duration of an experiment, the potential of an electrode from the medium-density MgO should be sufficiently stable to follow the progress of the chemical or electrochemical reaction of interest, and until less porous tubes are available, the medium-density tubes will be used. In addition, a zinc-calcium reference electrode alloy will be selected with a significant calcium concentration to give an interpretable potential signal with greater stability. Figure IV-5 presents calculated cell potentials as a function of the calcium concentration in the reference alloy and illustrates the extreme sensitivity of the electrode potential at low concentrations of calcium. This curve also illustrates why the rate of potential change in our tests decreased markedly at around 0.4 to 0.5 V.

2. Electrode Response

The second experiment investigated the potential change as calcium, magnesium, and aluminum are extracted sequentially from a zinc alloy by incremental additions of $ZnCl_2$ to the cover salt. Instead of pure zinc, Zn-3.8 wt % Ca alloy was used as the reference alloy. One gram of this alloy was charged to a medium-density MgO reference electrode tube. The melt alloy being studied initially was 575 g of approximately 3.6 wt % Ca, 0.3 wt % Mg, 0.9 wt % Al, and 95.2 wt % Zn; the Ca-Mg-Zn alloy from Run DRY-18, with added aluminum, was used for this experiment. (The magnesium came from attack of the MgO crucible by calcium during DRY-18.) This alloy was covered with $CaCl_2$-CaF_2 cover salt and maintained at about 735 °C for the test.

Before the $ZnCl_2$ additions were made, the cell potential ranged randomly from 0.007 to 0.03 V. A low potential was expected because of the nearly identical calcium content of the electrode and the melt. A 20-g addition of $ZnCl_2$ resulted in a potential change to -0.024 V. A second 20-g $ZnCl_2$ addition dropped the potential to -0.05Ɛ V. A third addition of 20-g $ZnCl_2$ dropped the potential to -1.17 V. In 45 min, the cell potential drifted to -1.09 V. At this time, a 10-g addition of $ZnCl_2$ was inserted, and the potential dropped to -1.15 V. Over the next five hours the potential drifted to -0.20 V.

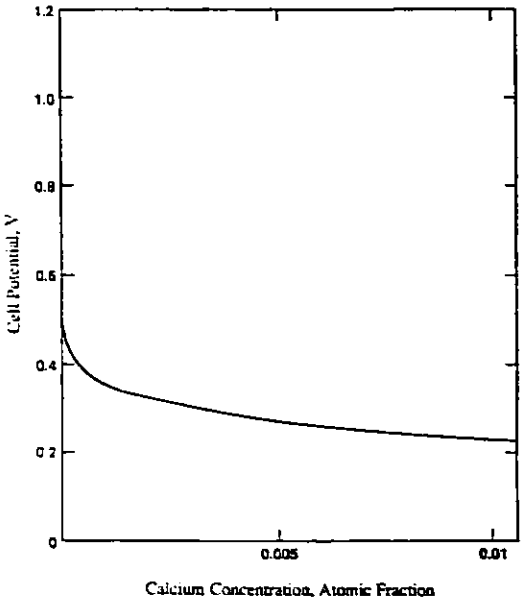

Fig. IV-5.

Cell Potential versus Calcium Concentration in Reference Electrode

Expected potentials for the extraction are presented in Table IV-9. A comparison of these data with the experimental results indicates that the calcium content of the melt was less than expected, and that the third $ZnCl_2$ addition was enough to react the balance of the calcium and all the magnesium. With that assumption, the observed potentials agree well with predictions. The final potential was established by the aluminum in the melt, but as calcium was being extracted from the reference alloy, the signal drifted toward zero. This again illustrated the importance of an electrode with more resistance to diffusion through the salt bridge.

Table IV-9. Calculated Potentials for Extraction Run with Zn-Ca-Al-Mg-Alloy

	Potential,[a] V
Initial[b]	-0.006
1/3 Calcium Removed	-0.039
2/3 Calcium Removed	-0.091
All Calcium Removed	-0.67
3/4 Magnesium Removed	-0.73
All Magnesium Removed	-1.12

[a]Versus Zn-3.8 wt % Ca reference.
[b]Initial charge: 550 g Zn, 21 g Ca (72 g), 1.7 g Mg (10 g), and 5 g Al (25 g), where numbers in parentheses are $ZnCl_2$ equivalent.

F. Calculations of Americium Distribution between Liquid Plutonium and Molten NaCl-KCl (I. Johnson)

We have analyzed the experimental data reported by Mullins et al.[5] on the distribution of americium between liquid plutonium and a molten equimolar mixture of NaCl and KCl (at 971-1048 K). The objective was to verify the conclusion of these authors that the americium exists in the divalent state in the molten salt mixture and to estimate the activity coefficient of $AmCl_2$ in the molten salt mixture. This analysis is possible because Mullins et al. fully reported the experimental data, a practice often not followed in many current publications. It was found that these data support a divalent oxidation state for most of the americium in the molten salt mixture, and that the activity coefficient of $AmCl_2$ is about 10 times that of $PuCl_3$ in the NaCl-KCl salt mixture.

In this system, the following equilibrium reactions are expected:

$$Am + PuCl_3 = AmCl_3 + Pu \qquad \text{(IV-12)}$$

$$3Am + 2PuCl_3 = 3AmCl_2 + 2Pu \qquad \text{(IV-13)}$$

from which the following equilibrium constant relations may be derived:

$$\frac{a_{Pu}\, a_{AmCl_3}^3}{a_{Am}\, a_{PuCl_3}^3} = K_{3a} \qquad \text{(IV-14)}$$

$$\frac{a_{Pu}^2\, a_{AmCl_2}^3}{a_{Am}^3\, a_{PuCl_3}^2} = K_{2a} \qquad \text{(IV-15)}$$

in which the a's are activities, and the K's are thermodynamic equilibrium constants. By substituting into Eqs. IV-14 and -15 the product of atom (mole) fractions, X_i, and the activity coefficients, γ_i (i.e., $a_i = X_i\gamma_i$) and combining the activity coefficients with the equilibrium constants, we obtained two equations of the same form as Eqs. IV-14 and IV-15 but with the a's replaced by X's and the two new equilibrium constants given by the relations:

$$K_3 = K_{3a}\frac{\gamma_{Am}\gamma_{PuCl_3}}{\gamma_{Pu}\gamma_{AmCl_3}} \qquad \text{(IV-16)}$$

$$K_2 = K_{2a}\frac{\gamma_{Am}^3\gamma_{PuCl_3}^2}{\gamma_{Pu}^2\gamma_{AmCl_2}^3} \qquad \text{(IV-17)}$$

These equations yield the following relation for the americium distribution coefficient:

$$D_{Am} = K_3 D_{Pu} + K_2^{1/3} D_{Pu}^{2/3} \qquad \text{(IV-18)}$$

The two terms on the right-hand side of Eq. IV-18 are proportional to the contribution of trivalent and divalent americium to the species present in the molten salt mixture. The values of D_{Am} computed from Eq. IV-18 were compared with the experimental values. The constants K_3 and $K_2^{1/3}$ were computed on the assumption that all activity coefficients in Eqs. IV-16 and -17 are equal to one (ideal solutions). The computed values were larger than the experimental values by a factor which increased from about 1.4 to 1.6 as the concentration of $PuCl_3$ increased. The experimental data could not be fit to an equation of the form suggested by Eq. IV-18 with reasonable values for the two constants. However, the data could be fit to an empirical relation whose parameters were close to what is expected if only the second term on the right-hand side of Eq. IV-18 is significant. In this case, the power of D_{Pu} is not exactly 2/3 but varies from about 0.63 to 0.69, and the value of K_2 is about 70-90% smaller than the theoretically computed value (if γ's are equal to one).

Two observations need to be explained: namely, the first term on the right-hand side of Eq. IV-18 does not appear to be significant, and the empirical constants are different from the expected values. The computed values of the standard free energies of Eqs. IV-12 and -13 are about -7 and -25 kcal/mol, respectively. Since the values of the free energies of formation of $PuCl_3$, $AmCl_3$, and $AmCl_2$ all have large uncertainties, the computed value of the standard free energy of Eq. IV-12 could be smaller; a combined error of 4 to 5 kcal/mol would not be unreasonable. While such an error (in the "right" direction) could make the contribution of the trivalent form of americium insignificant, it would have a smaller effect on the predicted contribution of the divalent form of americium. This appears to be a situation in which high accuracy (uncertainties of ± 1 kcal/mol) in the thermodynamic data are required to make a definitive decision based on theoretical computations.

Considering the scatter of the experimental data in Fig. IV-6, the deviation of the power of D_{Pu} from exactly 2/3 as required by Eqs. IV-18 (a slope of 2/3 in Fig. IV-6 in which the logarithms of the two

distribution coefficients are plotted) is not unexpected. It is reasonable to assume that the 2/3 power is appropriate for the analysis of these data. Therefore, the values of $K_2^{1/3}$ were computed from the experimental data on the assumption that the 2/3 power dependence on D_{Pu} was correct. An example of the results obtained for the data at 1003 K is shown in Fig. IV-7. Similar results were obtained for the other two temperatures; however, the scatter is even greater. These values of $K_2^{1/3}$ are smaller than the values computed on the assumption that all of the activity coefficients are equal to one and decrease as the mole fraction of $PuCl_3$ increases. In addition, the $K_2^{1/3}$ computed from the experimental data decreased as the temperature increased, whereas the values computed from the free energies of formation increased with higher temperature. Since K_2 involves not only the thermodynamic equilibrium constant, K_{2a}, but also the product of four different activity coefficients, this difference in temperature dependence may be the result of different temperature dependences for the free energies of formation and the activity coefficients.

The ratio of the activity coefficients of americium and plutonium in the metallic phase can probably be safely assumed to be close to one. The value for γ_{Pu} must be close to one for these very dilute solutions of americium in plutonium (the metallic phase is almost pure plutonium). The values of γ_{Am}, while possibly not exactly one, would be expected to be constant (Henry's law followed). Therefore, the difference between the observed and theoretical values of $K_2^{1/3}$ is principally due to the two salt activity coefficients.

To study the possible effect of variations in the salt activity coefficients on $K_2^{1/3}$, γ values for $PuCl_3$ were computed for each of the experimental data sets and used to compute the γ value for $AmCl_2$ on the assumption that Eq. IV-13 applies (a slope of exactly 2/3 and the theoretical values of K_{2a} were used). It was found that the average γ values for $AmCl_2$ were 10.4 times the value γ for $PuCl_3$. Since the γ values for $PuCl_3$ in the NaCl-KCl salt system (for the range of $PuCl_3$ concentrations and temperatures examined) are estimated to be 0.001-0.002, γ values for $AmCl_2$ are 0.01 to 0.02. When this result is substituted into Eq. IV-17 it is found that

$$K_2^{1/3} = K_{2a}^{1/3} \frac{1}{10.4(\gamma_{PuCl_3})^{1/3}} \qquad \text{(IV-19)}$$

If the γ values for $PuCl_3$ are 0.001 and 0.003 (the range found for the data at 1003 K), $K_2^{1/3}$ varies from 0.96 to 0.67 times $(K_{2a})^{1/3}$. If the γ values for $AmCl_2$ and $PuCl_3$ were both equal to the γ values for $PuCl_3$ found for this system, the extraction of americium from plutonium would be almost ten times larger. Various salt effects were noted when the effect of changing the composition of the "inert" salt used to dilute the $PuCl_3$ was studied. These are due to the differences in the effect of the salt composition on the activity coefficients of $AmCl_2$ and $PuCl_3$.

If the extraction of americium from plutonium involved the formation of the trivalent $AmCl_3$ in the molten salt, the extraction with $PuCl_3$ would be significantly smaller than observed. For example, for the present series of experiments, computed values of D_{Am} would be about 25% of the observed values. In addition, there would be a smaller dependence on the inert diluent salt used. This effect is predicted from the observations that the difference in the ionic radius of Pu^{3+} and Am^{3+} is very small, and deviations from ideal behavior are dependent on the differences between the ionic radii and charge of the solute and solvent cations. On the other hand, both the ionic radii and charge are different for Pu^{3+} and Am^{2+} cations; hence, the effect of diluent salts on their activity coefficients is expected to be different, as found in this study. For the experimental data analyzed, because the concentration of both $PuCl_3$ and $AmCl_2$ in the molten salt is small, the salt effects are dominated by the properties of the NaCl-KCl solvent

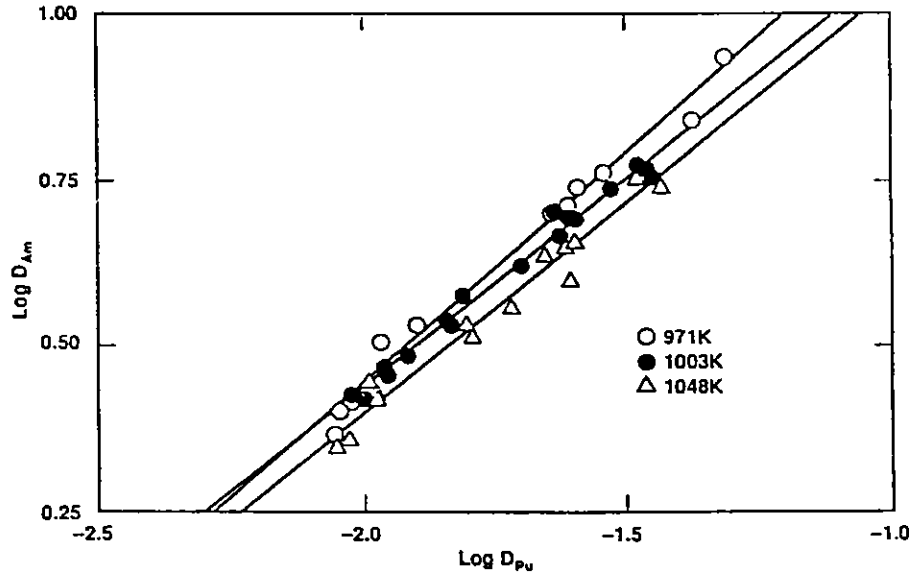

Fig. IV-6. Distribution of Americium between Plutonium and NaCl-KCl at 971, 1003, and 1048 K

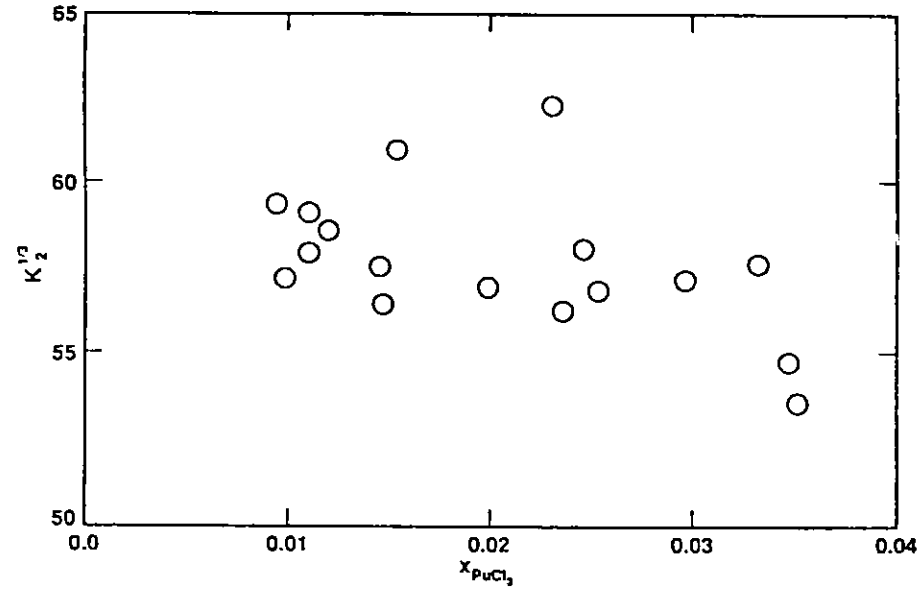

Fig. IV-7. Equilibrium Constant ($K_a^{1/3}$) for Americium Extraction from Plutonium by $PuCl_3$ in NaCl-KCl at 1003 K

salt. When the $PuCl_3$ concentration is increased, as has been the case in studies using pure $PuCl_3$ to very dilute solutions in an "inert" diluent salt, the effect of $PuCl_3$ as a "solvent" salt on the activity coefficient of $AmCl_2$ must be considered. As the salt approaches pure $PuCl_3$, its activity coefficient will approach one, while the activity coefficient of $AmCl_2$ will approach its value as a dilute solute in molten $PuCl_3$, which is likely to be less than one. This will lead to values of K_2 larger than K_{2_a} and, hence, enhanced extraction of americium from plutonium.

This analysis of the experimental data reported by Mullins et al. confirms their conclusion that $AmCl_2$ is the main product formed by the extraction of americium from liquid plutonium by $PuCl_3$ dissolved in a molten equimolar mixture of NaCl-KCl. The observed dependence of the americium distribution coefficient on the plutonium distribution coefficient indicates that the activity coefficient of $AmCl_2$ in this salt mixture is about 10 times that of $PuCl_3$. The analysis method developed for these experiments should be useful in understanding the salt effect observed when different diluent salts are used.

G. Design of Pyroprocessing Transfer Line

(T. P. Mulcahey and G. K. Johnson)

In practical pyroprocessing schemes, it is often desirable to optimize time and reagent use by transferring molten metals or salts from a crucible in one furnace to one in another furnace so that additional process steps can be pursued or a liquid can be transferred to a mold where cooling can take place. Argonne-developed pressure and vacuum pyrochemical liquid-transfer hardware and techniques have been used from 1950 to the present in accomplishing these liquid transfers at temperatures up to 800°C.

The development effort undertaken for SRS was to design, build, and test a transfer line for the pyroprocessing facilities, which will employ a glovebox being fabricated by Los Alamos National Laboratory (LANL) for SRS. The initial phase was to develop a preliminary design for application in the glovebox, based on the designs previously used by ANL, and to build a prototype unit that could eventually be tested at ANL and SRS. The initial phase also included effort to obtain the Mo-30 wt % W tubing proposed for the design.

1. Overall Design

The preliminary SRS Transfer line design developed in this report period was based on earlier CMT designs for walk-in-hood furnaces and bell-jar furnaces (operated in air and in inert-atmosphere gloveboxes) used in developing pyrochemical processes in the 1960s. These earlier transfer lines typically weighed ~45 lb (~20 kg), and the major structural components were constructed from 304 stainless steel (SS) and Mo-30 wt % W. The heaters for these units were single-wire, SS sheath, MgO-insulated units, which were hand wrapped around 3/4-in. (~2 cm) Mo-W tube. They were separated from the 304 SS outside shell for the transfer line by high-temperature mineral fiber insulation. Four separate heat zones maintained the transfer line above freezing temperatures for the liquids being transferred. The unit was lifted and positioned by a hoist but could be handled manually if necessary. The units were shaped in the form of a "U," with one leg shorter than the other. The most extensive development was done on lines with 27 in. (69 cm) between center lines and leg lengths of 27 and 42 in (69 and 107 cm). The Mo-W tube was made by gun drilling (with a 1/2-in. drill) 4 ft (1.2 m) into each end of a 3/4 in. (2-cm) dia, 8-ft (2.4-m) long rod and then bending the resulting tube.

The SRS transfer line was designed to transfer material between two "below-floor-level" furnaces in the LANL glovebox. Because significantly less material is to be transferred than for the earlier CMT design, a smaller diameter Mo-W tube could be used. The selection of a 1/2 in. (1.3 cm) OD x 1/4 in.

(0.6 cm) ID tube for the design was based on a compromise among adequate bore to avoid plugging, minimization of transfer line mass, and appropriate bore for the scale of the experiments. Also, the difficulty in drilling the tubing in the lengths required increases as the hole size decreased.

The legs of the proposed SRS transfer line, shown in Fig. IV-8, were approximately 32-in. (81-cm) and 24-in. (61-cm) long, and the distance between them was ~28 in. (~70 cm); however, the section between the legs was sloped toward the receiving section at a rate of about 1/2 in. per foot (4 cm per meter) to promote draining of liquid left in the line after completion of a transfer.

The design allowed the intake to be raised from the bottom of the ceramic crucible in the furnace to a point at least 2 in. (5 cm) up from the bottom so that the amount of material left in the crucible, after completing a transfer, could be changed when desired.

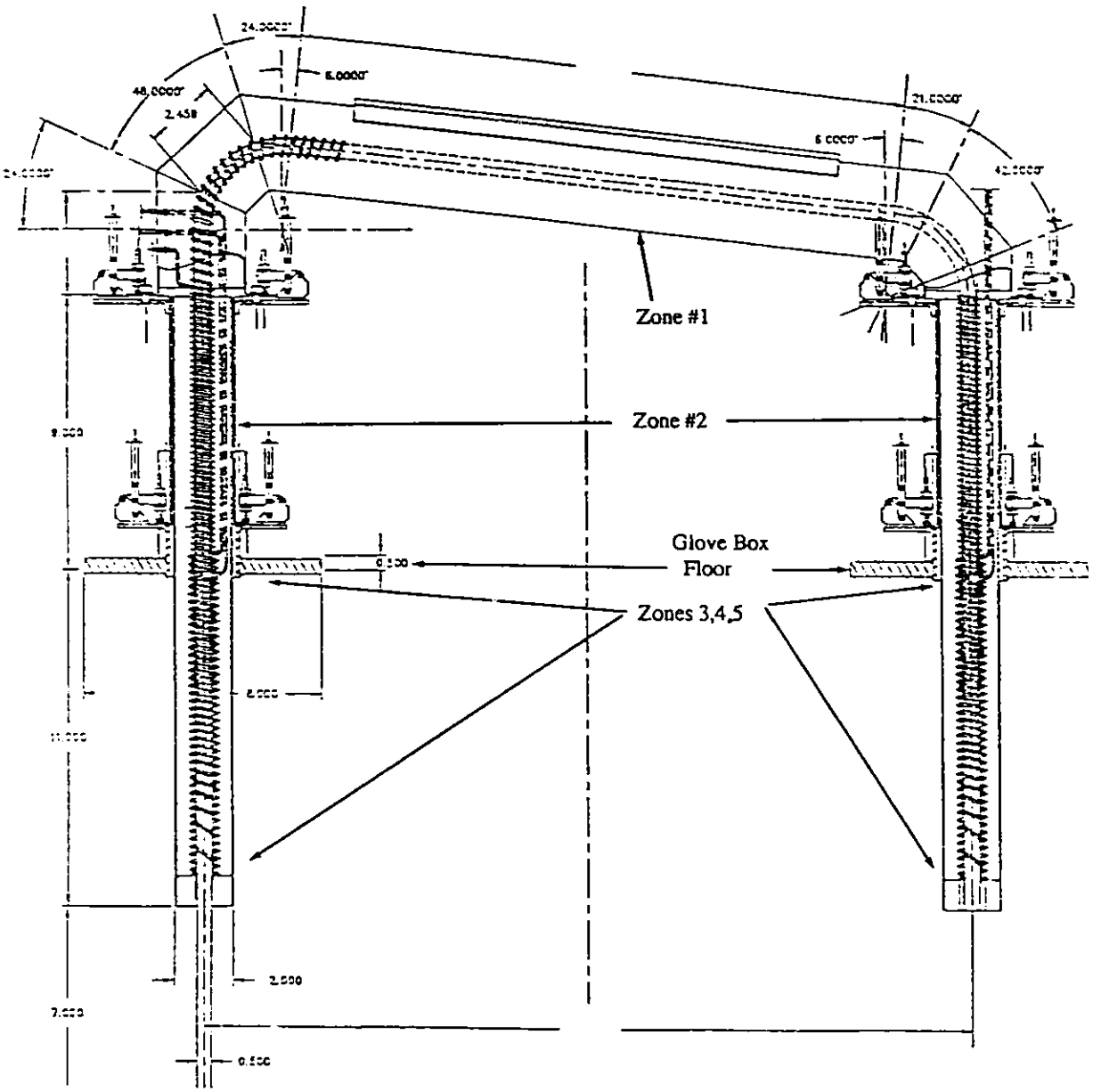

Fig. IV-8. Engineering Drawing for Proposed SRS Transfer Line

2. Heater Design and Testing

For the SRS design, it was decided to use spiral-wound, Inconel-sheathed, two-wire Nichrome heaters. These heaters are readily available and allow simpler lead configuration than for single-wire heaters. However, the two-wire design may be less reliable than the one-wire design previously used and may require steps to minimize thermal cycling.

We identified a heater vendor (ARi Industries, Inc) who can provide 1/2-in. (1.3-cm) ID heater coils of 1/8-in. (0.3-cm) dia sheathed heaters wound with any desired number of coils/inch, coil length, and fit on the 1/2-in. (1.3-cm) coil. As a help in defining the heater design and as a check on vendor and heater performance, a 1/2-in. (1.3-cm) ID coiled heater was procured and tested on a 304 SS tube. Fiberfax was wrapped around the coil on the tube, and the internal temperature along the length of the tube and the applied power were monitored. The tests were performed in a hood with the tube, heater, and insulation contained in a bag so that the tests could be performed in three different atmospheres: air, argon, and helium. Tests in the different atmospheres were needed to establish power-temperature relationships to assure that the assembled prototype could be tested, if necessary, with an appropriate melt transfer in a glovebox or hood with air, argon, or helium atmosphere.

For simulation of the portion of the prototype transfer line that would be exposed to a room-temperature glovebox environment, the heater with appropriate thickness of insulation was placed in a 3-in. (8-cm) dia SS tube in air and heated until the center tube was approximately steady at 850°C. The power required was ~130 W for heating a 16-in. (41-cm) long section of tube in air with a heater coil of ~3 turns per inch. This compares favorably with power measurements reported earlier,[6] considering that additional insulation was used in the present experimental section. The exterior surface temperature was monitored along the 3-in. (8-cm) OD tube and ranged up to 126°C, while the internal [1/2-in. (1.3-cm) OD tube] temperature was 844°C.

The experiment was repeated with argon and helium atmospheres. The power required for the argon atmosphere test was ~120 W, with an internal temperature of 857°C and surface temperatures up to 125°C. The power required for the helium atmosphere test was not determined directly. At the end of the experiment, the interior tube temperature was 780°C (and rising slowly) and the power applied was 3.3 times that in the argon experiment. The experiment was terminated for fear that the heater wire would exceed its maximum temperature and fail prematurely. The 3-in.(8-cm) OD tube surface temperature was 128°C, with an interior tube temperature of 616°C. This suggested that the surface temperature in a helium atmosphere test might rise excessively with an interior [1/2-in. (1.3-cm) OD tube] temperature of 850°C.

The same experiments were performed with the appropriate insulation in a 2-in. (5-cm) OD section of SS tubing. The results with this decreased insulation indicated that, at an approximately steady-state interior temperature of 850°C, the exterior tube temperature ranged up to 240°C at a power of 185 W in an argon atmosphere.

Since part of the SRS transfer line may consist of a 2-in. (5-cm) tube contained in a 2 1/2-in. (6.3-cm) SS tube, the experiment was repeated with this tube arrangement. The steady-state power required to achieve 850°C interior temperature increased slightly, but the indicated surface temperature was about 120°C. The test results were not quantitatively what was expected because of the crude nature of these experiments. Nevertheless, they did qualitatively indicate that the exposed surface temperature was significantly lower than that for the 2-in. (5-cm) tube alone.

A decision was made to design the SRS heaters to match heat losses in five different heat zones:

Zone 1: 3-in. (8-cm) dia exterior tube exposed to argon glovebox atmosphere (see Fig. IV-8).

Zone 2: 2-in. (5-cm) dia interior tube and 2 1/2-in. (6.3-cm) dia exterior tube exposed to glovebox atmosphere.

Zone 3: 2 1/2-in. (6.3 cm) dia exterior tube exposed to the higher temperatures existing below floor level in furnace well.

Zone 4: 2-in. (5-cm) dia exterior tube in a temperature transition zone ranging in exterior temperature from Zone 3 to near the top of the furnace heater assembly.

Zone 5: 2-in. (5-cm) dia exterior tube that can extend through the furnace heater support structure.

The design resulted in the specification of four heater designs to meet the needs of the five heat zones. Zones 2, 3, 4, and 5 are identical in each leg of the transfer line. Heat requirements of Zone 1 would be satisfied by a heater design of three turns/inch wound clockwise with tangential lead termination and with a length equal to 1/2 the 3-in. (8-cm) dia cover tube. Two heaters were selected to cover all of Zone 1 so that a lower voltage to the heaters would be maintained, and the potential for ionization of the expected argon operating/test atmosphere would be minimized.

Heat requirements of Zone 2 would be satisfied by a heater design of about five turns/inch (clockwise with tangential termination lead that could be bent at the time of assembly to match the design lead path).

Because of the lack of knowledge of the temperature profile below the glovebox floor (in the SRS furnace well), the heater requirements for the lower three zones of each of the two legs were believed best satisfied by two full-length heaters, one wound for uniform heat generation, and the other wound for variable heat generation. This arrangement would also satisfy an operational consideration of keeping the transfer line hot while it is removed from the furnace wells, if this is deemed desirable. One heater, clockwise wound, with variable spacing (see Fig. IV-9) would be mounted on the 1/2-in. (1.3-cm) tube. The other heater, wound counterclockwise, would be slipped over the first and have four turns/inch. Both legs of the transfer line would be heated identically, and power for the matching heaters in each half of the transfer line could be controlled in parallel to satisfy the required temperature conditions.

3. Design Revision

A design review for our pyroprocessing transfer line was held on September 6, 1989, at SRS. The conclusion from the design review was that our preliminary design must be modified because of operational headroom/weight restrictions for handling the unit in the LANL glovebox. The weight of the unit was estimated to be greater than one or two men could lift (the lifting restriction in a glovebox at SRS is 7.2 kg or 16 lb per person), and there did not appear to be enough headroom in the box for a hoist.

A subsequent ANL review of the preliminary design indicated that the transfer line could be reduced in weight and shortened. However, the amount of weight reduction is limited by the need for some structural support for the Mo-W tube, which is brittle in the cold condition (<200°C). In addition, there is a minimum weight for the Mo-W parts in the design. (Specific gravity of Mo-W is ~12.)

The estimated weight of the Mo-W tube and end protector/gas seals for the ANL design for SRS was about 11 lb (5 kg). This could be decreased somewhat by reducing the length of the protector/seal parts and the overall length of the "U"-shaped design. Additional weight savings could be obtained by using thinner stainless steel materials and eliminating the 3-in. (8-cm) dia housing for the horizontal segment of the U-tube, but the weight of a transfer line probably cannot be reduced to the 16-lb (7.2 kg) limit so that one person could lift the line unassisted in the glovebox. However, the weight might be reduced below 32 lb (14 kg) so that two people could handle the transfer line.

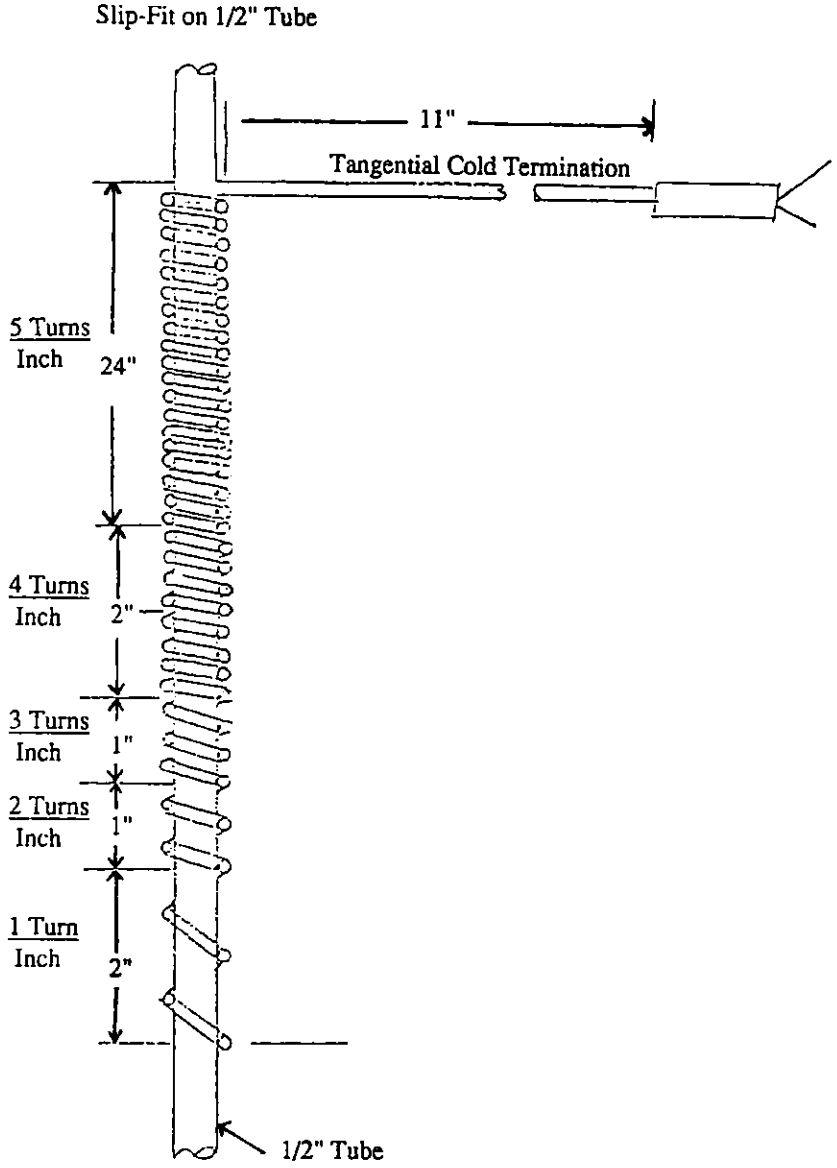

Fig. IV-9. Engineering Drawing for Variable-Spaced Heater

4. Tubing Manufacture

The program continuation plans called for procurement and manufacture of Mo-30 wt % W components, including the necessary tubing. A vendor search was made for anyone willing to attempt to make small orders of 1/2-in. (1.3-cm) OD x 1/4-in. (0.6 cm) ID tubing. One was found, but program funds were depleted before tubing could be obtained.

APPENDIX

Calculations for Distribution of Americium between Plutonium and NaCl-KCl

The details of the numerical computations are given in this appendix. Two sets of computations dependent on information not found in the paper by Mullins et al.[5] are involved in this analysis. The first is the computation of the thermodynamic equilibrium constants, while the second is the computation of the activity coefficients of $PuCl_3$ in the molten NaCl-KCl salt mixture. By giving more details of these computations, some of the uncertainties in the thermodynamic data can be stated so that the conclusions of this analysis can be more realistically evaluated.

The numerical values for the free energies and two thermodynamic equilibrium constants (K_{3a} and K_{2a}) are given in Table A-1. The free energy data for $PuCl_3$ were obtained from data selected for the solid by the IAEA[7] and the enthalpy of fusion estimated by Rand.[8] The thermodynamic data for the two americium chlorides are from a recent assessment by us. The free energy values given in Table A-1 are for the liquid chlorides (super cooled if necessary), and the subscripts 3 and 2 refer to the trivalent or divalent americium chloride.

The activity coefficients of $PuCl_3$ in the equimolar NaCl-KCl salt mixture were computed from the relations developed by Gohil et al.[9] for the excess free energies of the three binary systems ($PuCl_3$-NaCl, $PuCl_3$-KCl, NaCl-KCl) as a function of composition and temperature and the Toop[10] relation for estimating excess free energies in ternary solutions. The Toop relation is exact for regular systems and has been found to be a good approximation for more complex systems.

The numerical details of the computations are given in Table A-2, which is a copy of the relevant parts of the spreadsheet.

Table A-1. Thermodynamic Equilibrium Constants and Free Energies at 971, 1003, and 1048 K

	971 K	1003 K	1048 K
ΔG_f,kcal/mol			
$PuCl_3$	-176.5	-175.1	-173.2
$AmCl_3$	-183.7	-182.6	-181.0
$AmCl_2$	-125.9	-125.2	-124.4
ΔG_3,kcal/mol	-7.26	-7.48	-7.79
K_{3a}	43.1	42.5	42.2
ΔG_2,kcal/mol	-24.6	-25.5	-25.8
K_{2a}	3.48×10^5	3.58×10^5	3.79×10^5
$K_{2a}^{1/3}$	70.4	71.0	72.4

Table A-2. Data for the Distribution of Pu and Am between Liquid Pu and Molten NaCl-KCl. (Summary of Computations, 7/12/89)

Mol. Fraction				Activity Coeff.			
$PuCl_3$	$AmCl_2$	Am	D_{Am}	$PuCl_3$	$AmCl_2$	Ratio	K_2 obs
T=698°C							
0.00874	0.000191	8.25E-05	2.31	0.001079	0.01359	12.59	54.49
0.00899	0.000197	7.80E-05	2.52	0.001085	0.01276	11.76	58.24
0.00936	0.000195	7.50E-05	2.60	0.001094	0.01277	11.68	58.48
0.01070	0.000219	6.86E-05	3.19	0.001125	0.01159	10.31	65.65
0.01250	0.000204	6.03E-05	3.38	0.001168	0.01244	10.65	62.74
0.02277	0.000244	4.85E-05	5.02	0.001445	0.01438	9.95	62.55
0.02443	0.000220	4.27E-05	5.15	0.001495	0.01505	10.06	61.15
0.02557	0.000240	4.38E-05	5.47	0.001530	0.01482	9.69	63.04
0.02858	0.000252	4.35E-05	5.78	0.001626	0.01573	9.67	61.87
0.04231	0.000233	3.35E-05	6.95	0.002130	0.02036	9.56	57.23
0.04900	0.000255	2.97E-05	8.59	0.002421	0.01978	8.17	64.13
					Ave.	10.37	60.87
					Std. Dev.	1.18	3.19
T=730°C							
0.00940	0.000189	7.17E-05	2.64	0.001360	0.01471	10.81	59.30
0.00982	0.000197	7.51E-05	2.62	0.001372	0.01535	11.19	57.13
0.01091	0.000214	7.37E-05	2.90	0.001403	0.01508	10.75	59.05
0.01095	0.000208	7.30E-05	2.85	0.001404	0.01539	10.96	57.89
0.01191	0.000223	7.31E-05	3.05	0.001432	0.01542	10.77	58.52
0.01448	0.000230	6.75E-05	3.41	0.001508	0.01626	10.78	57.45
0.01465	0.000229	6.78E-05	3.38	0.001514	0.01662	10.98	56.37
0.01537	0.000237	6.30E-05	3.77	0.001536	0.01553	10.11	60.90
0.01991	0.000348	8.34E-05	4.18	0.001682	0.01767	10.50	56.88
0.02312	0.000242	4.80E-05	5.05	0.001793	0.01685	9.40	52.24
0.02373	0.000222	4.79E-05	4.64	0.001815	0.01881	10.36	56.20
0.02469	0.000237	4.82E-05	4.92	0.001850	0.01846	9.98	57.98
0.02548	0.000235	4.79E-05	4.91	0.001878	0.01906	10.15	56.74
0.02969	0.000202	3.69E-05	5.47	0.002039	0.02002	9.82	57.06
0.03323	0.000260	4.36E-05	5.95	0.002183	0.02078	9.52	57.53
0.03473	0.000229	3.93E-05	5.82	0.002246	0.02229	9.92	54.67
0.03514	0.000268	4.67E-05	5.74	0.002264	0.02290	10.12	53.49
					Ave.	10.36	57.61
					Std. Dev.	0.52	2.02
T=775°C							
0.00878	0.000184	8.27E-05	2.23	0.001783	0.02033	11.40	52.37
0.00932	0.000186	8.10E-05	2.29	0.001803	0.02073	11.49	51.75
0.01028	0.000204	7.36E-05	2.77	0.001838	0.01852	10.08	58.66
0.01049	0.000194	7.38E-05	2.62	0.001845	0.01988	10.78	54.77
0.01057	0.000194	7.28E-05	2.67	0.001848	0.01968	10.65	55.39
0.01554	0.000307	8.97E-05	3.42	0.002035	0.02115	10.39	54.98
0.01605	0.000293	8.94E-05	3.28	0.002055	0.02268	11.04	51.59
0.01896	0.000339	9.30E-05	3.64	0.002174	0.02370	10.90	51.25
0.02203	0.000234	5.36E-05	4.36	0.002304	0.02275	9.87	55.51
0.02425	0.000209	4.64E-05	4.50	0.002403	0.02420	10.075	3.68
0.02473	0.000148	3.70E-05	3.99	0.002425	0.02780	11.46	47.00
0.02513	0.000215	4.66E-05	4.60	0.002443	0.02448	10.02	53.65
0.03328	0.000221	3.86E-05	5.73	0.002843	0.02623	9.23	55.39
0.03669	0.000211	3.79E-05	5.57	0.003026	0.03004	9.93	50.41
					Ave.	10.52	53.32
					Std. Dev.	0.67	2.75

REFERENCES

1. R. E. Barbetta et al., "Molten Salt Recycle, Electrolysis of CaO in Molten Salt," *Chemical Engineering Division Fuel Cycle Programs Quarterly Progress Report April-June 1979*, Argonne National Laboratory Report ANL-79-99, pp. 34-41 (1980).

2. R. D. Pierce and Leslie Burris, Jr., "Pyroprocessing of Reactor Fuels," in *Reactor Technology Selected Reviews*, ed., L. E. Link, U. S. Atomic Energy Commission, Division of Technical Information, TID 8540, pp. 411-476 (1964).

3. D. A. Wenz, I. Johnson, and R. D. Wolson, J. Chem. Eng. Data, 14(2) 250-252 (1968).

4. S. J. Shaw, Ninth Annual Pyrochemical Workshop, October 17-19, 1989, Alexandria, VA (1989).

5. L. J. Mullins, A. J. Beaumont, and J. A. Leary, J. Inorg. Nucl.Chem. 30, 147 (1968).

6. D. E. Grosvenor, I. O Winsch, W. E. Miller, G. J. Bernstein, and R. D. Pierce, *Engineering and Equipment Design and Application of Corrosion-Resistant Heated Transfer Tubes for Liquid Metals and Salts*, Argonne National Laboratory Report ANL-7522, Table II, p. 12 (December 1968).

7. J. Fuger et al., *The Chemical Thermodynamics of Actinide Elements and Compounds, Part 8, The Actinide Halides*, International Atomic Energy Agency, Vienna (1983).

8. M. H. Rand, *Plutonium Physico-chemical Properties of Its Compounds and Alloys*, International Atomic Energy Agency, Vienna, Special Issue No. 1 (1966).

9. D. D. Gohil, T. G. Chart, and M. H. Rand, *Calculated Phase Equilibria for the KCl-NaCl-$PuCl_3$ System*, National Physical Laboratory Report DMA (D) 519 (March 1986).

10. G. W. Toop, Trans. Met. Soc. AIME 233, 850 (1965).

Distribution for ANL-91/26

Internal:

J. K. Bates (5)
J. E. Battles
G. J. Bernstein
B. M. Biwer
P. E. Blackburn
R. A. Blomquist
L. Burris
D. J. Chaiko
D. B. Chamberlain
Y. I. Chang
L. S. H. Chow
J. M. Copple
W. L. Ebert
P. A. Finn
A. K. Fischer
E. C. Gay
T. J. Gerding
D. W. Green
J. E. Harmon
E. P. Horwitz
J. C. Hutter
R. J. Jaskot
C. E. Johnson (5)
G. K. Johnson
I. Johnson
T. R. Johnson
J. P. Kopasz
J. Laidler
L. Leibowitz
R. A. Leonard
M. A. Lewis
M. J. Lineberry
P. S. Maiya
J. J. Mazer
C. C. McPheeters
W. E. Miller
F. C. Mrazek
T. P. Mulcahey
P. A. Nelson
A. E. Newman
S. Okajima
R. D. Pierce
D. S. Poa
D. T. Reed
M. C. Regalbuto
R. T. Riel
M. F. Roche
J. Sedlet
W. B. Seefeldt
J. L. Settle
S. M. Smidt
M. J. Steindler
R. K. Steunenberg
D.-K. Sze
S.-W. Tam
C. E. Till
Z. Tomczuk
L. E. Trevorrow
G. F. Vandegrift (10)
E. H. Van Deventer
M. A. Vest
L. C. Walters
R. D. Wolson
D. J. Wronkiewicz
D. G. Wygmans
ANL Patent Dept.
ANL Contract File
TIS Files (3)

External:

DOE-OSTI, for distribution per UC-500 (102)
ANL Library (2)
Manager, Chicago Operations Office, DOE
A. Bindokas, DOE-CH
J. Haugen, DOE-CH
A. L. Taboas, DOE-CH/AAO
Chemical Technology Division Review Committee Members:
- S. Baron, Brookhaven National Laboratory, Upton, NY
- N. Jarrett, Noel Jarrett Associates, Lower Burrell, PA
- L. Newman, Brookhaven National Laboratory, Upton, NY
- J. Stringer, Electric Power Research Institute, Palo Alto, CA
- J. B. Wagner, Arizona State University, Tempe, AZ
- R. G. Wymer, Oak Ridge National Laboratory, Oak Ridge, TN
- E. B. Yeager, Case Western Reserve University, Cleveland, OH

M. G. Adamson, Lawrence Livermore National Laboratory, Livermore, CA
J. Allison, USDOE, Environmental Restoration and Waste Management, Germantown, MD
J. T. Bell, Oak Ridge National Laboratory, Oak Ridge, TN
S. E. Berk, USDOE, Office of Fusion Energy, Germantown, MD
N. E. Bibler, Westinghouse Savannah River Co., Aiken, SC
W. Bourcier, Lawrence Livermore National Laboratory, Livermore, CA

D. F. Bowersox, Los Alamos National Laboratory, Los Alamos, NM
L. Brewer, University of California, Berkeley, CA
M. H. Campbell, Westinghouse Hanford Co., Richland, WA
K. A. Chacey, USDOE, Office of Waste Management, Germantown, MD
R. G. Clemmer, Battelle Pacific Northwest Laboratories, Richland, WA
M. O. Cloninger, Yucca Mountain Project Office, Las Vegas, NV
M. S. Coops, Lawrence Livermore National Laboratory, Livermore, CA
D. Cubicciotti, Electric Power Research Institute, Palo Alto, CA
H. Ted Davis, University of Minnesota, Minneapolis, MN
J. Dennison, Dennison Environmental, Woburn, MA
M. Dinehart, Los Alamos National Laboratory, Los Alamos, NM
M. Duff, USDOE, Office of Waste Operations, Germantown, MD
C. W. Frank, USDOE, Office of Technology Development, Germantown, MD
L. R. Greenwood, Battelle Pacific Northwest Laboratories, Richland, WA
W. S. Groenier, Oak Ridge National Laboratory, Oak Ridge, TN
K. Hain, USDOE, Office of Technology Development, Germantown, MD
R. R. Hobbins, EG&G Idaho, Inc., Idaho Falls, ID
J. O. Honeyman, Westinghouse Hanford Operations, Richland, WA
L. J. Jardine, Lawrence Livermore National Laboratory, Livermore, CA
J. J. Jicha, USDOE, New Production Depart., Washington, DC
R. T. Jubin, Oak Ridge National Laboratory, Oak Ridge, TN
D. A. Knecht, Westinghouse Idaho Nuclear Co., Idaho Falls, ID
M. Levenson, Menlo Park, CA
S. C. T. Lien, USDOE, Office of Technology Development, Germantown, MD
T. B. Lindemer, Oak Ridge National Laboratory, Oak Ridge, TN
Los Alamos National Laboratory, Los Alamos, NM
A. Malinauskis, Oak Ridge National Laboratory, Oak Ridge, TN
W. H. McVey, USDOE, Division of LMFBR Fuel Cycle Projects, Germantown, MD
R. Morissette, Science Applications International Corp., Las Vegas, NV
A. C. Muscatello, Los Alamos National Laboratory, Los Alamos, NM
L. Nelson, Sandia Corp., Albuquerque, NM
J. Nelson, Westinghouse Hanford Co., Richland, WA
M. O'Hara, Martin Marietta Energy Systems, Oak Ridge, TN
D. R. Olander, University of California, Berkeley, CA
A. L. Olson, Westinghouse Idaho Nuclear Co., Inc., Idaho Falls, ID
D. A. Orth, Westinghouse Savannah River Co., Aiken, SC
V. M. Oversby, Lawrence Livermore National Laboratory, Livermore, CA
M. Palmer, Los Alamos National Laboratory, Los Alamos, NM
R. Palmer, West Valley Nuclear Services, West Valley, NY
G. Pfennigworth, Martin Marietta Energy Systems, Oak Ridge, TN
L. Reichley-Yinger, Columbus, OH
R. L. Ritzman, Electric Power Research Institute, Palo Alto, CA
C. Russomanno, USDOE, Civilian Radioactive Waste Management, Washington, DC
P. S. Schaus, Westinghouse Hanford Co., Richland, WA
M. W. Shupe, USDOE, Office of Technology Development, Germantown, MD
D. Stahl, Science Applications International Corp., Las Vegas, NV
I. R. Tasker, IIT Research Institute, Bartlesville, OK
D. W. Tedder, Georgia Institute of Technology, Atlanta, GA
T. A. Todd, Westinghouse Idaho Nuclear Co., Inc., Idaho Falls, ID
USDOE, Office of Basic Energy Sciences, Washington, DC
S. Yarbro, Los Alamos National Laboratory, Los Alamos, NM